DISSERTATION

submitted to the

Combined Faculties for the Natural Sciences and for Mathematics

of the Ruperto-Carola University of Heidelberg, Germany

for the degree of

Doctor of Natural Sciences

Presented by

Mariona Rabionet Roig, *Llicenciada en Química*

Born in: Canet de Mar, Spain

Oral examination: February 14th 2011

Ceramide Synthase 3

and its Essential Role in

Skin Barrier Function and Male Fertility

Referees:

Prof. Dr. rer. nat. Walter Nickel

Prof. Dr. rer. nat. Roger Sandhoff

Examiners:

Prof. Dr. rer. nat. Peter Angel

Prof. Dr. rer. nat. Sabine Strahl

For Michael

This work has been carried out from September 2006 to September 2010
at the departement of Cellular and Molecular Pathology in the working group of
Lipid Pathobiochemistry of the Deutsches Krebsforschungszentrum in Heidelberg.

This PhD thesis was supported by the Deutsche Forschungsgemeinschaft
projects SA 1721/1-1 and 1721/2-1.

List of figures

List of tables

Summary

The functional specialization of sphingolipids (SLs) is determined by their structural diversity and their unique expression patterns according to cell type and degree of differentiation. Ultra long chain (ULC) SLs characterized by an *N*-acyl moiety longer than 26 carbon atoms in length are primarily expressed in mature male germ cells and epidermal keratinocytes. To unveil the functional role of these unconventional SLs, it is necessary to define their biosynthetic requirements at the molecular level.

In mammals, fatty acids are incorporated into SLs at the stage of ceramide synthesis by a family of six homologue enzymes, the ceramide synthases (CerS1–6). By analyzing the expression levels of the CerS family in skin, as well as in juvenile and in “germ cell-free” testis, solely CerS3 mRNA distinctively correlated with the presence of ULC-SLs. As found *in vitro,* the synthesis of ceramides with cerotoyl-(26:0) and montanoyl-residues (28:0) required CerS3, as demonstrated by a non-radioactive and detergent-free enzymatic assay established in living human cells expressing CerS3. For this purpose, activated ULC-acyl-CoAs as assay substrates and ceramide internal standards for mass spectrometric quantifications were specifically synthesized.

The crucial role of CerS3 in the synthesis of ULC-SLs could be further confirmed with CerS3 deficient mice. Mass spectrometric analysis of epidermal extracts established acyl-CoAs ranging from 24 to 36 carbon atoms in length as substrates of CerS3 *in vivo*. CerS3 deficiency resulted in a complete loss of ceramides with acyl-chains longer than 24 carbon atoms, including all ω-hydroxy-ULC-ceramides. Consequently, the total epidermal ceramides were drastically reduced by 90% leading to a severe impairment of the epidermal permeability barrier and ultimately to premature neonatal death.

The metabolic defect of CerS3 mice gave rise to a multitude of alterations associated with the maturation and terminal cornification of keratinocytes. At the *stratum granulosum* (SG), diminished size in filaggrin-containing granules and reduced number of loricrin-containing granules were accompanied by aberrant processing of filaggrin and decreased levels of loricrin. At the *stratum corneum* (SC), remnants of glycogen, nuclear material and organelle structures were detected at the

first corneocyte layers. CerS3$^{d/d}$ mice exhibited a markedly thickened and compact SC that could be associated with the persistence of corneodesmosomes, eventually resulting from the reduced expression of the protease cathepsin D at the SG and SC. Additionally, the defective degradation of corneodesmosomes led to the distinctive persistence of the embryonic peridermal layer in newborn mutant epidermis. Furthermore, CerS3 deficient mice exhibited disorganized lamellar sheets that yield the formation of non-lamellar lipid agglomerates, rather than building up evenly distributed lipid unit lamellar structures.

The compromised skin integrity of mutant mice facilitated the severe invasion of pathogens evidenced by the increased microbial growth and the formation of *pseudohyphae* prior to colonization by *Candida albicans* on cultured skin biopsies.

In summary, these results demonstrated the prerequisite of a functional CerS3 for the generation of ULC-SLs, which play an essential role in skin barrier function and male fertility. The phenotypic alterations derived from the *in vivo* depletion of CerS3 suggested in addition a crucial regulatory function that could be encoded within the homeobox domain. Taken all together, these findings established the basis for the identification and diagnosis of potential human skin disorders associated with a CerS3 dysfunction.

Zusammenfassung

Die funktionelle Spezialisierung von Sphingolipiden (SL) wird durch ihre strukturelle Vielfalt und durch die spezifischen Expressionsmuster in Abhängigkeit von Zelltyp und Grad der Differenzierung festgelegt. Ultra-langkettige ("Ultra Long Chain", ULC) SL, die sich durch einen *N*-Acylsubstituenten mit einer Kettenlänge vom mehr als 26 C-Atomen auszeichnen, werden primär in reifen männlichen Keimzellen und Keratinozyten der Epidermis exprimiert. Um die funktionelle Rolle dieser ungewöhnlichen SL zu verstehen, ist es notwendig, zuerst ihre Biosynthese auf einer molekularen Basis zu begreifen.

Bei Säugetieren werden Fettsäuren von einer Familie von 6 homologen Genen, den sog. Ceramidsynthasen (CerS1–6), während der Ceramidsynthese in SL eingebaut. Mit der Bestimmung der Expressionslevel dieser CerS-Familie in der Haut, sowie im juvenilen und „keimzellenfreien“ Hoden konnte einzig die CerS3-mRNS mit dem Vorkommen der ULC-SL korreliert werden. Die *In vitro*-Synthese von Ceramiden mit Cerotin- (26:0) oder Montansäureresten (28:0) setzt die CerS3-Aktivität voraus. Dies konnte anhand eines erstmalig etablierten, nicht-radioaktiven und detergenzfreien, enzymatischen Tests, basierend auf vitalen humanen Zellen die CerS3 exprimieren, nachgewiesen werden. Zu diesem Zweck wurden ULC-acyl-CoA als Substrate sowie Ceramide mit verkürzter Sphingoidbase speziell synthetisiert, und die letzteren als interne Standards für massenspektrometrische Quantifizierung eingesetzt.

Die bedeutende Rolle von CerS3 bei der Synthese von ULC-SL konnte durch Untersuchungen an CerS3-defizienten Mäusen weiter untermauert werden. Differenzielle massenspektrometrische Untersuchungen wiesen Acyl-CoA mit einer Kettenlänge von 24 bis 36 Kohlenstoffen als Substrate von CerS3 *in vivo* aus. CerS3-Defizienz führte zu einem kompletten Verlust der Ceramide mit einer Kettenlänge von mehr als 24 Kohlenstoffatomen, einschließlich aller ω-Hydroxy-ULC-Ceramide. Die Gesamtzahl aller Ceramide der Epidermis war um 90% reduziert, was zu einer starken Beeinträchtigung der Wasserpermeabilitätsschranke der Epidermis und letztlich zu einem vorzeitigen neonatalen Tod führte.

Der metabolische Defekt der CerS3-Mutanten äußerte sich in einer Vielzahl von phänotypischen Veränderungen in Reifung und terminaler Verhornung der Keratinozyten. Im *Stratum granulosum* (SG) wurde eine Reduktion in der Größe der Filaggringranula als auch der Loricringranula beobachtet, begleitet von einer fehlerhaften Prozessierung des Filaggrins und einem Abfall des Loricringehaltes im SG. In den ersten Korneozytenschichten des *Stratum corneum* (SG) konnten Reste von Gykogen, Zellkernmaterial und Organellen nachgewiesen werden. CerS3$^{d/d}$-Mäuse zeigten ein deutlich verdicktes und kompaktes SC. Ursache hierfür ist wohl die Persistenz von Corneodesmosomen, bedingt u.a. durch eine niedrige Konzentration der Protease Cathepsin D im SG und SC. Weiterhin führte der defiziente Abbau von Corneodesmosomen zum Erhalt des Periderms auf der Haut von neugeborenen Knockout-Tieren. Zusätzlich wiesen CerS3-defiziente Mäuse ungeordnete lamelläre Lipidschichten auf, die zur Bildung von nichtlamellaren Lipidagglomeraten führten und nicht zu den gleichmäßig gespreiteten, lamellär strukturierten Lipideinheiten zwischen den Corneozyten.

Die in ihrer Funktion kompromittierte Haut der Mutanten erleichterte in Biopsiekulturen erhöhtes mikrobiologisches Wachstum von Pathogenen/ *Candida albicans*, die Bildung von invasiven Pseudohyphen und anschließende Kolonisierung in tiefere Schichten.

Zusammenfassend zeigen diese Ergebnisse die Notwendigkeit einer intakten CerS3 für die Bildung von ULC-SL, die eine essentielle Rolle in der Funktion der Hautbarriere und bei der männlichen Fortpflanzung spielen. Die phänotypischen Veränderungen, die durch Abwesenheit intakter CerS3 *in vivo* hervorgerufen werden, deuten auf eine zusätzliche regulatorische Funktion dieses Proteins hin, die innerhalb der Homeobox-Domäne kodiert sein könnte.

Die vorliegenden Resultate sind Grundlage für die Identifikation und Diagnose potentieller menschlicher Hauterkrankungen, die auf einer CerS3 Fehlfunktion beruhen könnten.

1. Introduction

1.1. Sphingolipids

Sphingolipids (SLs) were first described by Johann L.W. Thudichum as natural chemical constituents of the brain (Thudichum, 1884). Today, sphingolipids and their glycosylated derivatives are best described by their structural properties. Ceramide is the core of most sphingolipids and serves as the anchor of glycosphingolipids (GSLs) in the outer leaflet of the cellular plasma membrane. Biochemically, ceramide is an amino alcohol composed of a fatty acid linked by an amide bond to a long chain base (LCB), most commonly sphingosine (Figure 1). On the other hand, glycosphingolipids are amphiphatic molecules composed of the hydrophobic ceramide backbone and a hydrophilic oligosaccharide chain. Together with sphingomyelin (SM), a ceramide with a phosphorylcholine head group, these are the major type of sphingolipids ubiquitously expressed in all eukaryotic cells, as well as some prokaryotic organisms and viruses.

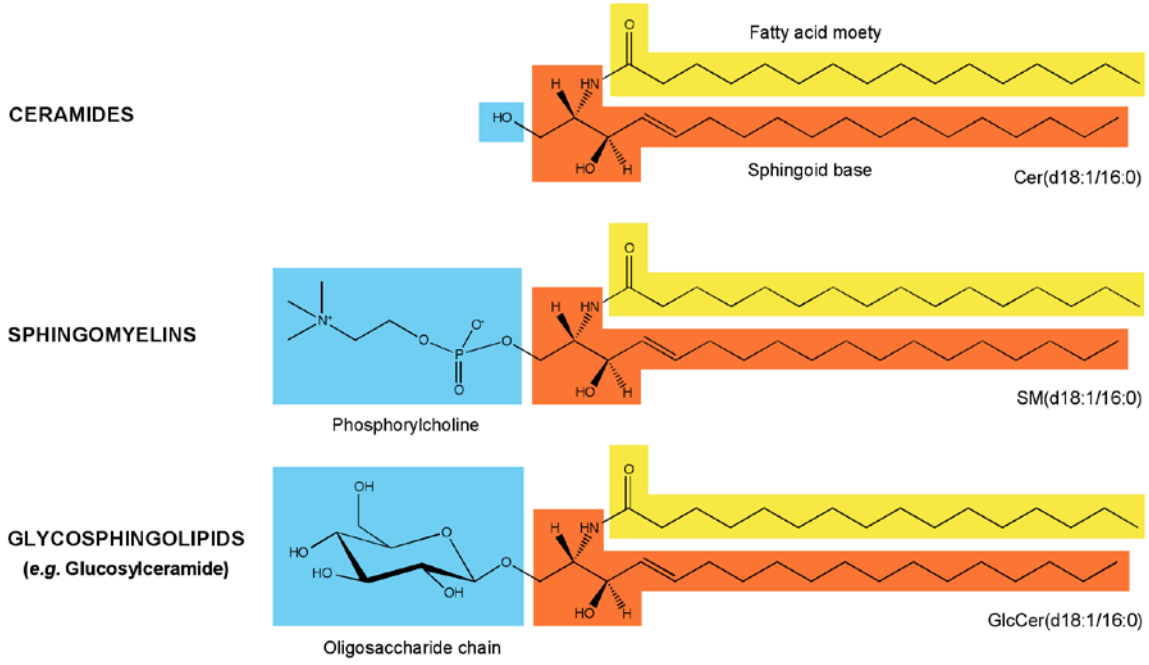

Figure 1. Structure of major sphingolipid classes.
Ceramides, glycosphingolipids and sphingomyelins are biosynthesized via the condensation of an activated fatty acid with a sphingoid base linked by an amide bond, and are represented here by a palmitoyl moiety (yellow) and a sphingosine base (orange), respectively.

The structural diversity of sphingolipids is a prerequisite for their functional specialization in different tissues or cell types. The fatty acid moiety differs in chain length and various degrees of saturation, hydroxylation, and esterification, which contributes significantly to this structural complexity. This remarkable diversity is further enhanced by the combination of naturally occurring long chain bases, mainly sphingosine, sphinganine (dihydrosphingosine) and phytosphingosine (4-hydroxysphinganine). However, more than 60 species of sphingoid bases have been reported [(Karlsson, 1970), for review see (Pruett et al., 2008)]. The heterogeneity of sphingolipid structures peaks with the great variation of carbohydrate moieties, with around 500 structures already characterized. In combination, this huge molecular diversity creates thousands of different structures, whose functions are just starting to be elucidated.

Sphingolipids have been shown to be expressed in a unique cell-type specific manner. Their expression patterns are determined by cellular differentiation, degeneration, development, cell cycle and viral or oncogenic transformations (Hakomori, 1981; Majoul et al., 2002; Muramatsu, 2000).

In the extracellular side of the plasma membrane, sphingolipids have been reported to be involved in a wide variety of cellular processes including adhesion, proliferation and transport. These are facilitated either by direct lectin binding (Yang et al., 1996), direct contact to membrane receptors and transporters (Yamashita et al., 2003), or eventually establishing platforms for concentrating these proteins within the membrane (Lang, 2007).

Glycosphingolipids can act as recognition molecules for toxins, viruses and bacteria at the cell surface, where their complex oligosaccharide chain serve as a binding site for these pathogens (Schnaar, 1991). Furthermore, simple sphingolipids, namely ceramide, sphingosine and sphingosine-1-phosphate (S1P), have been shown to function as bioactive molecules in a large variety of signaling events (Lahiri and Futerman, 2007). Ceramide and S1P appear to have opposite roles in signaling transduction pathways. While ceramide has been shown to induce apoptosis by regulating the activity of some proteins to which it binds, *e.g*. kinase suppressor of Ras, phospholipase A_2 or cathepsin D (Heinrich et al., 1999; Ruvolo, 2003), the latter

has been implicated in cell proliferation and differentiation (Spiegel and Milstien, 2003).

Sphingolipids also play a role in the pathogenesis of diverse diseases, being the most prominent the inherited lysosomal storage diseases caused by the malfunction of enzymes involved in sphingolipid catabolism (Kolter and Sandhoff, 1999). Furthermore, sphingolipids contribute to the development of a multitude of diseases including neurodegenation (Grimm et al., 2005), cancer progression (Hakomori, 1996), diabetes (Aerts et al., 2007; Stratford et al., 2004) and pathogen invasion (Arikawa et al., 2002; Bibel et al., 1992).

1.2. Ultra long chain sphingolipids

In mammalian cells, the most abundant fatty acid (FA) moieties incorporated into membrane lipids range between 16 and 24 carbon atoms in length. In sphingolipids, they are primarily saturated or monounsaturated, whereas polyunsaturated fatty acids are additionally expressed in phosphoglicerolipids and cholesterol esters. Generally, fatty acid residues of 14 to 20 carbon atoms in length are denominated as long chain fatty acids (LC-FAs), whereas acyl residues with 22 to 26 carbon atoms are refered in this study as very long chain fatty acids (VLC-FAs) (Figure 2).

VLC-FAs have been found in most human tissues, generally bind by an amide linkage to sphingolipids, or esterified to cholesterol esters and phospholipids (Poulos, 1995). Sphingolipids containing VLC-FAs (VLC-SLs) are enriched in certain tissues, particularly in myelin sheaths of the brain (O'Brien and Rouser, 1964; Pakkala et al., 1966) and in kidney (Sandhoff et al., 2002), where they mostly occur as their α-hydroxylated derivatives.

Sphingolipids containing acyl residues with a chain length of 28 to 36 carbon atoms have also been found in mammalian cells (Poulos, 1995; Sandhoff, 2009), and are denominated here as ultra long chain sphingolipids (ULC-SLs). Despite the constitutive expression of VLC-SLs, the occurrence of ultra long chain SLs is restricted to testis/spermatozoa, and the epidermis. In epidermal keratinocytes, ULC-sphingolipids up to 36 carbon atoms in length are mainly saturated or monounsaturated, whereas in the testis ULC-SLs are polyunsaturated (Figure 2).

Structurally, ULC-SLs differ greatly from their shorter chain homologues. These differences might be required for their functional specialization. The composition and function of ULC-SLs in both tissues will be described in detail in the following sections, and is the topic discussed throughout this study.

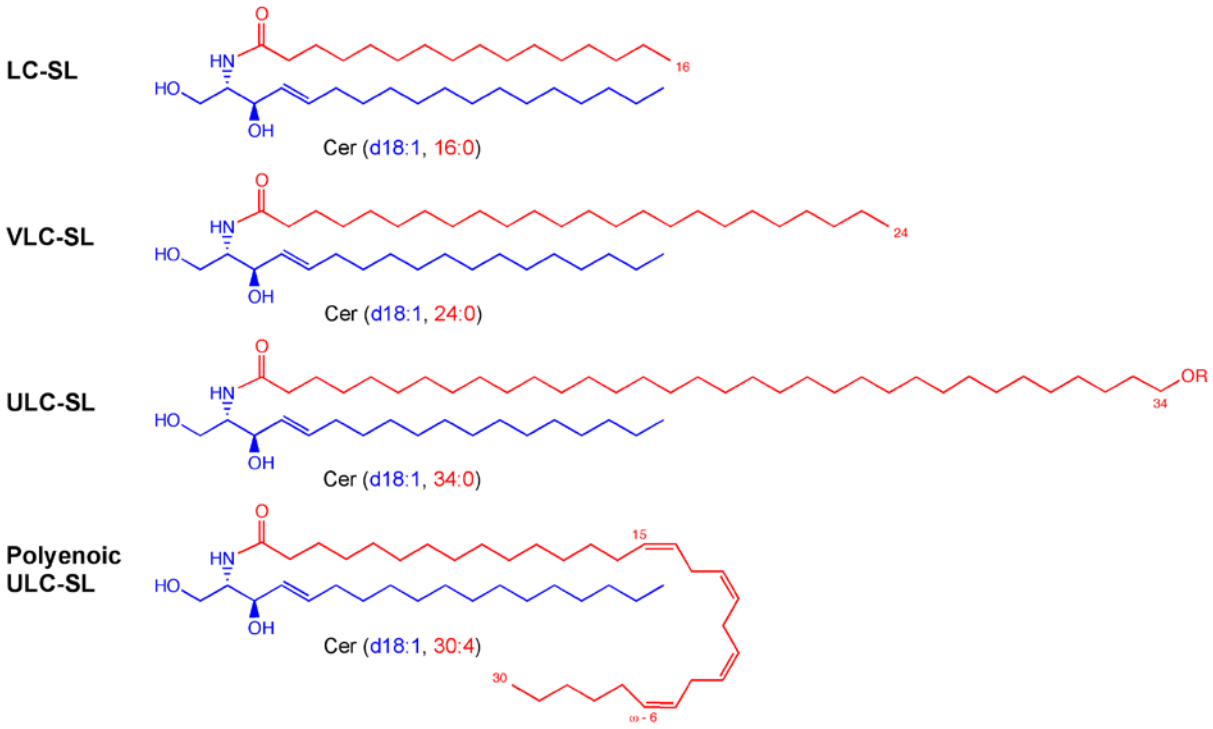

Figure 2. Comparison of sphingolipid structures differing by the carbon chain length and saturation of their fatty acid residues.

The majority of sphingolipids found in the plasma membrane of mammalian cells contains saturated long chain (LC-) and very long chain (VLC-) fatty acid residues ranging primarily between 16 to 24 carbon atoms. Ultra long chain (ULC-) sphingolipids with a fatty acid moiety of 28 to 36 carbon atoms are exclusively found in the epidermis and the testis. Epidermal sphingolipids, mostly ceramides and glucosylceramides, contain primarily saturated (or monounsaturated) ULC-acyl moieties of 30–36 carbon atoms. Most epidermal ULC-SLs are hydroxylated or esterified with linoleic acid or to proteins of the cornified envelope at the C_{ω} position of their fatty acid residue. Testicular ULC-acyl residues range from 28 to 32 carbon atoms and possess multiple unsaturations (4 to 6). They are mostly incorporated into complex GSLs.

The rod outer segments (ROS) of the retina have been reported to contain the highest levels of ULC-FAs (Poulos, 1995). Aveldaño and co-workers could show that these polyunsaturated (4–6 double bonds) fatty acids (PUFAs) ranging from 30 to 36 carbon atoms were incorporated into phosphoglycerolipids, namely phosphatidylcholine (Aveldano and Sprecher, 1987). In 2010, Brush and colleagues could demonstrate the expression of ULC-PUFAs in acidic GSLs. However, the authors failed to detect ULC-PUFAs incorporated into neutral sphingolipids, including sphingomyelin (Brush et al., 2010). The function of ULC-PUFAS glycosphingolipids in retina has not yet been clarified, however Brush and colleagues speculated on a possible role of ULC-SLs or ULC-PUFA glycosphingolipids in the pathogenesis of the retinal Stargardt disease (STDG3). Patients suffering this autosomal dominant disease carry mutations in the elongation of very long chain fatty acid 4 gene (*Elovl4*), which have been involved in the synthesis of ULC-FAs (*vide infra*). Although the pathogenesis of STDG3 is more likely to be caused by the lack of ULC-PUFA phosphatidylcholines in the membrane of photoreceptor cells (McMahon et al., 2007b), retinal ULC lipids are beyond the main focus of this study.

1.3. Metabolism of ultra long chain sphingolipids

1.3.1. Sphingolipid metabolism and topology

De novo synthesis of sphingolipids is initiated in the cytosolic face of the endoplasmic reticulum (ER) via the condensation of the amino acid L-serine with an activated fatty acid. This first acylation is catalyzed by the pyridoxalphosphate dependent serine palmitoyltransferase (SPT) and is the rate-limiting step of the sphingolipid synthetic pathway (Figure 3). The mammalian SPT complex is a heterodimer composed of three subunits (SPTLC1–3), and exhibits the highest specificity towards palmitoyl-CoA (16:0-CoA), thereby generating a long chain base (LCB) of 18 carbons, 3-ketosphinganine (Hornemann et al., 2007). The ketone moiety of this intermediate is subsequently reduced by a NADPH-depending reductase yielding sphinganine.

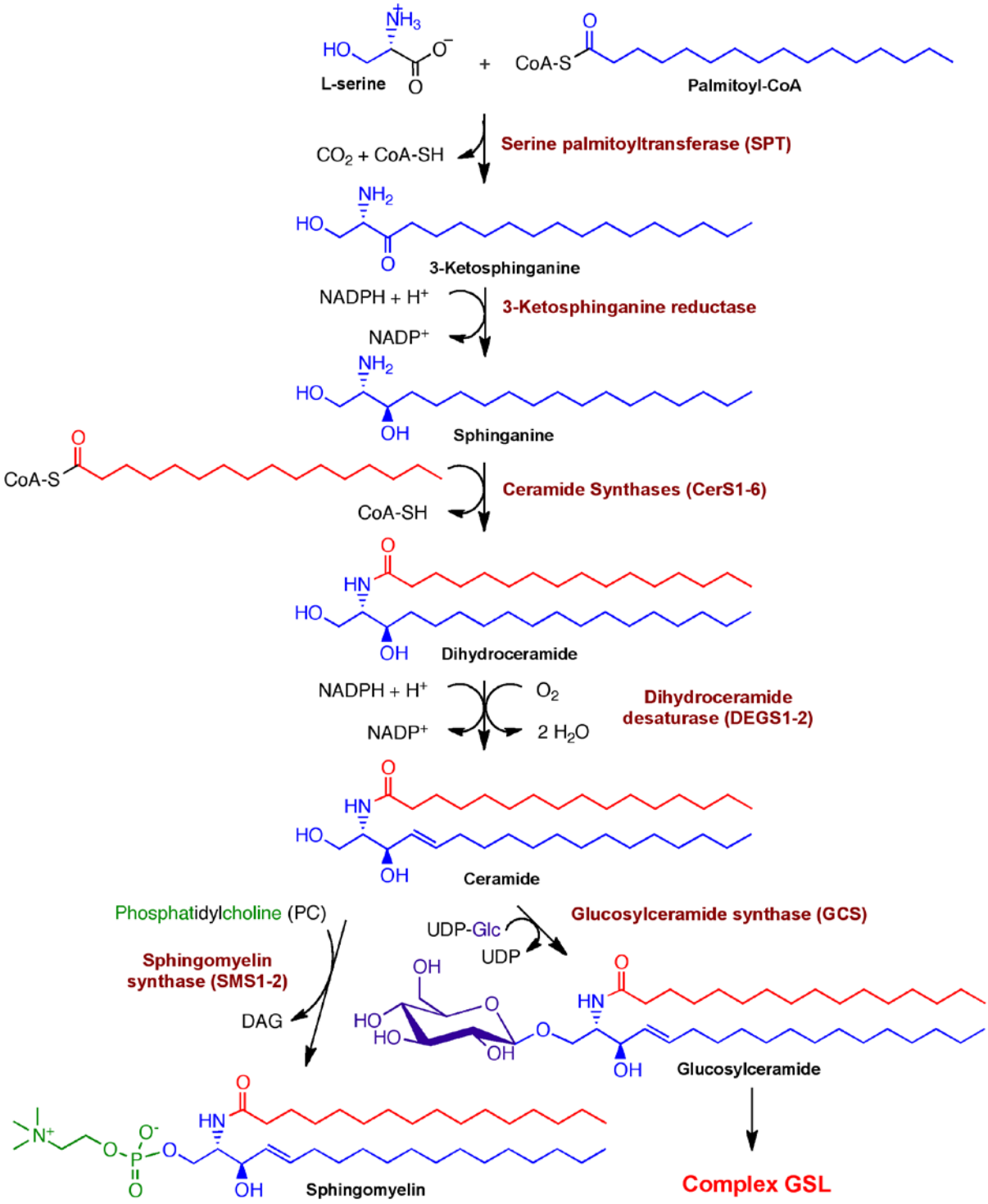

Figure 3. *De novo* sphingolipid biosynthesis.

The enzymes involved in sphingolipid biosynthesis are integral membrane proteins localized within the ER and the Golgi apparatus (here shown in dark red). The primary LCB contained in the majority of SLs and GSLs is derived from the intermediate (2S,3R)-2-aminooctadecane-1,3-diol, namely sphinganine.

N-acylation of sphinganine with an activated fatty acid proceeds leading to the formation of dihydroceramide. Likewise, sphingosine generated via the "salvage pathway" can be directly acylated to produce ceramide (Figure 4). The condensation of these and other endogenous long chain bases with a fatty acid – activated as a coenzyme A derivative – is facilitated by the ceramide synthases (CerSs, officially Lass). To fulfill the synthesis of the great variety of naturally occurring (dihydro)ceramides, which mainly differ in the chain length, hydroxylation and number of unsaturations of their fatty acid moieties, a family of six homologue enzymes is required in mammals, CerS1–6. This key step in the sphingolipid metabolic pathway will be extensively discussed during this study. Finally, dihydroceramide synthesized via the *de novo* pathway is dehydrogenated to ceramide by the dihydroceramide desaturase.

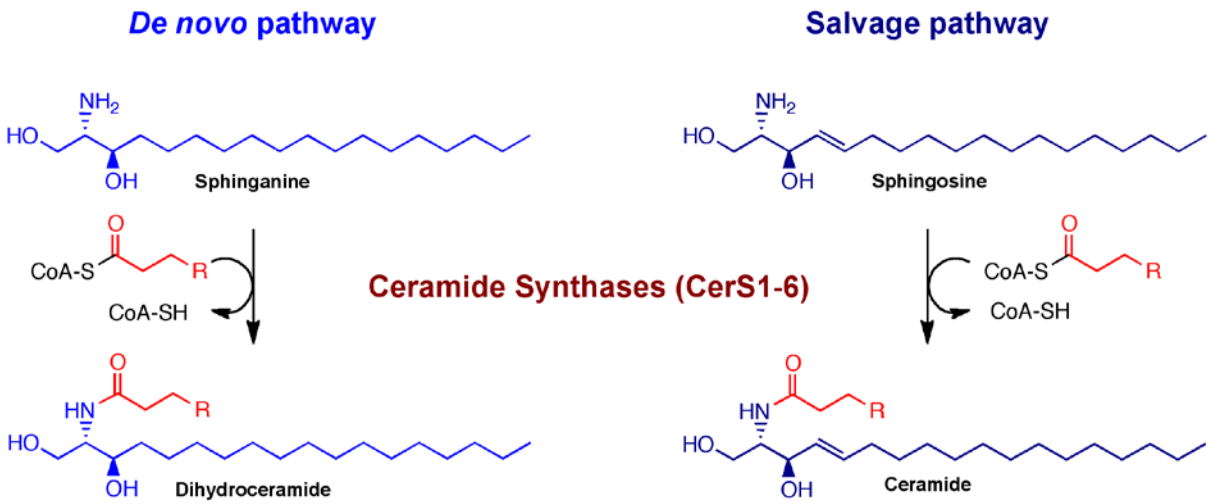

Figure 4. *De novo* and salvage (dihydro)ceramide synthesis catalyzed by the ceramide synthases.
CerSs facilitate the acylation of D-erythro-sphinganine derived from the de novo synthesis, as well as D-erythro-sphingosine from the salvage pathway to generate D-erythro-dihydroceramide and D-erythro-ceramide, respectively.

Ceramide is a key metabolite required in a huge variety of cellular processes and is the common precursor for all complex glycosphingolipids and sphingomyelins. Most enzymes involved in the ceramide metabolic pathway have been reported to be

membrane-bound proteins localized in the cytosolic side of the ER (Mandon et al., 1992; Michel and van Echten-Deckert, 1997). However, as the biosynthesis of GSLs and SMs takes place in the Golgi apparatus, ceramide must be efficiently transported from the ER to the Golgi compartment (Figure 5). This transfer occurs via a vesicular and a non-vesicular protein-mediated manner (Perry and Ridgway, 2005).

The majority of complex GSLs are derived from the simplest GSL, glucosylceramide (GlcCer). The glucosylation of ceramide is catalyzed by glucosylceramide synthase (GCS, officially UGCG) and takes place in the cytosolic side of the cis-Golgi cisternae (Futerman and Pagano, 1991; Jeckel et al., 1992), or potentially in a sub-compartment of the ER (Ardail et al., 2003). A vesicular flow is thought to be the major transport mechanism to deliver ceramide to the Golgi apparatus for the synthesis of complex GSLs. For further processing, GlcCer must translocate to the luminal side of the Golgi compartment. There, it is converted into lactosylceramide (LacCer) and maybe further glycosylated to generate all complex GSLs (Lannert et al., 1998).

Instead, the galactosylation of ceramide leading to GSL of the gala series takes place in the luminal leaflet of the Golgi apparatus (Sprong et al., 1998). The synthesis of galactosylceramide (GalCer) is catalyzed by the ceramide UDP-galactosyl-transferase (CGT, officially UGT8). GalCer is primarily expressed in the brain and the kidney, where it is also sulfated.

SM synthesis requires the transport of Cer from the cytosolic side of the ER to the luminal side of the Golgi. This transfer is thought to be mediated mainly by the ceramide transfer protein (CERT) (Hanada et al., 2003). In the Golgi, sphingomyelin synthase (SMS) catalyzes the transfer of phosphorylcholine from phosphatidylcholine (PC) to ceramide. To date, two SMS isoforms have been described in mammals, SMS1 and SMS2, the former being ubiquitously expressed and localized exclusively in the Golgi apparatus, and the latter specifically expressed in round spermatids and early elongated spermatids of the testis and additionally localized at the plasma membrane (Huitema et al., 2004; Igarashi, 2010; Lee et al., 2007; Mitsutake et al., 2010).

Ultimately, newly synthesized sphingolipids are delivered to the plasma membrane where they influence membrane functions.

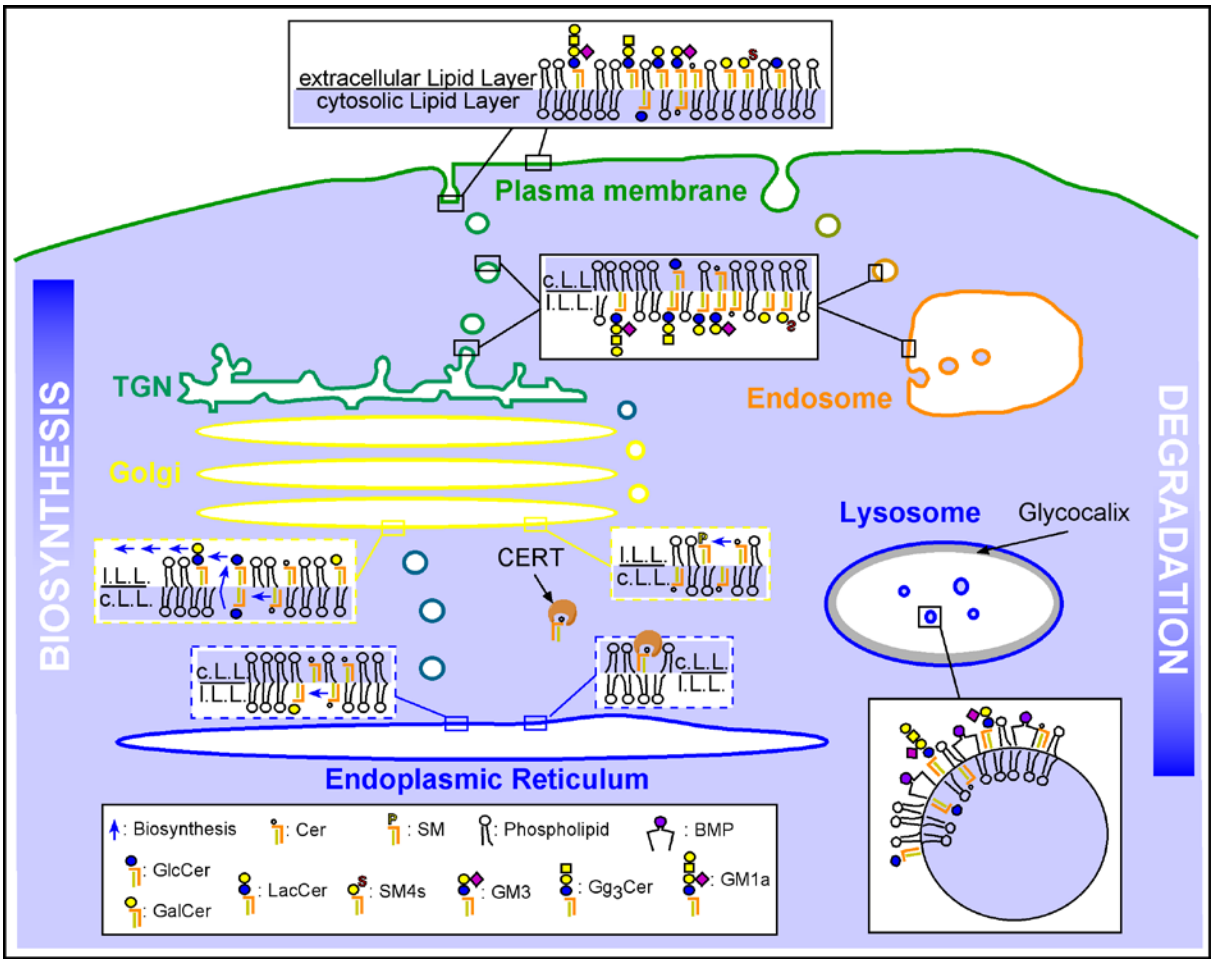

Figure 5. Schematic representation of sphingolipid metabolism.
The biosynthesis of GSL and SM occurs in the ER and the Golgi apparatus of mammalian cells and involves vesicular and non-vesicular protein-mediated transport. Sphingolipid processing and trafficking occurs primarily in the trans-golgi-network (TGN) previously to be exocytosed to the plasma membrane. Sphingolipid catabolism takes place in the lysosomes, where water-soluble hydrolases sequentially degrade their carbohydrate residues. Sphingolipids require the endocytic pathway involving early and late endosomes prior to reach the catabolic lysosomal machinery. Scheme modified from (Sandhoff, 2007).

Sphingolipids are constitutively degraded in the lysosomes by water-soluble hydrolases that sequentially cleave off their carbohydrate residues. Simple sphingolipids, namely ceramide and sphingomyelin, are degraded by specific lysosomal ceramidases and sphingomyelinases. For their degradation, sphingolipids at the PM are internalized by endocytosis, sorted in endosomes and delivered into

intraendosomal vesicles to the lysosomes. Once degraded, their building blocks might serve for the synthesis of newly required metabolites.

1.3.2. Synthesis of ultra long chain sphingolipids

Unconventional ULC-SLs require an additional synthetic machinery to complete their biosynthesis. On one hand, a fatty acid elongation system capable of synthesizing activated fatty acids with a chain length up to 36 carbon atoms is required. In mammals, the elongation of fatty acids beyond the length of 16 carbon atoms is catalyzed by members of the *elongation of very long chain fatty acids* gene family, the *Elovl* genes. On the other hand, ULC-FAs have to be incorporated into a sphingoid base for the generation of ULC-SLs. Therefore, a ceramide synthase with a high affinity towards activated ULC-FAs is additionally required.

1.3.2.1. The elongation of very long chain fatty acids family (Elovl)

Fatty acids up to 16 carbon atoms are sequentially elongated in two carbon atom steps by the cytosolic fatty acid synthase (FAS) protein complex. The primary end-product is palmitate (16:0), which after activation to its coenzyme A derivative is translocated to the ER. There, the fatty acid elongation of LC-, VLC- and ULC-FAs is achieved during a four-step reaction cycle, where members of the *Elovl* gene family encode for the first regulatory condensing enzyme (Figure 6). Elovl proteins employ malonyl-CoA as an acyl donor for the addition of two-carbon units to a fatty acyl-CoA, and thereby generating 3-ketoacyl-CoA by means of decarboxylation. The 3-ketoacyl-CoA reductase catalyzes the reduction of the carbonyl group to alcohol yielding 3-hydroxyacyl-CoA. Dehydration follows resulting in the synthesis of *trans*-2-enoyl-CoA, which is finally reduced to generate the elongated fatty acyl-CoA (for a description of fatty acid nomenclature see supplemental Table A1 and A2).

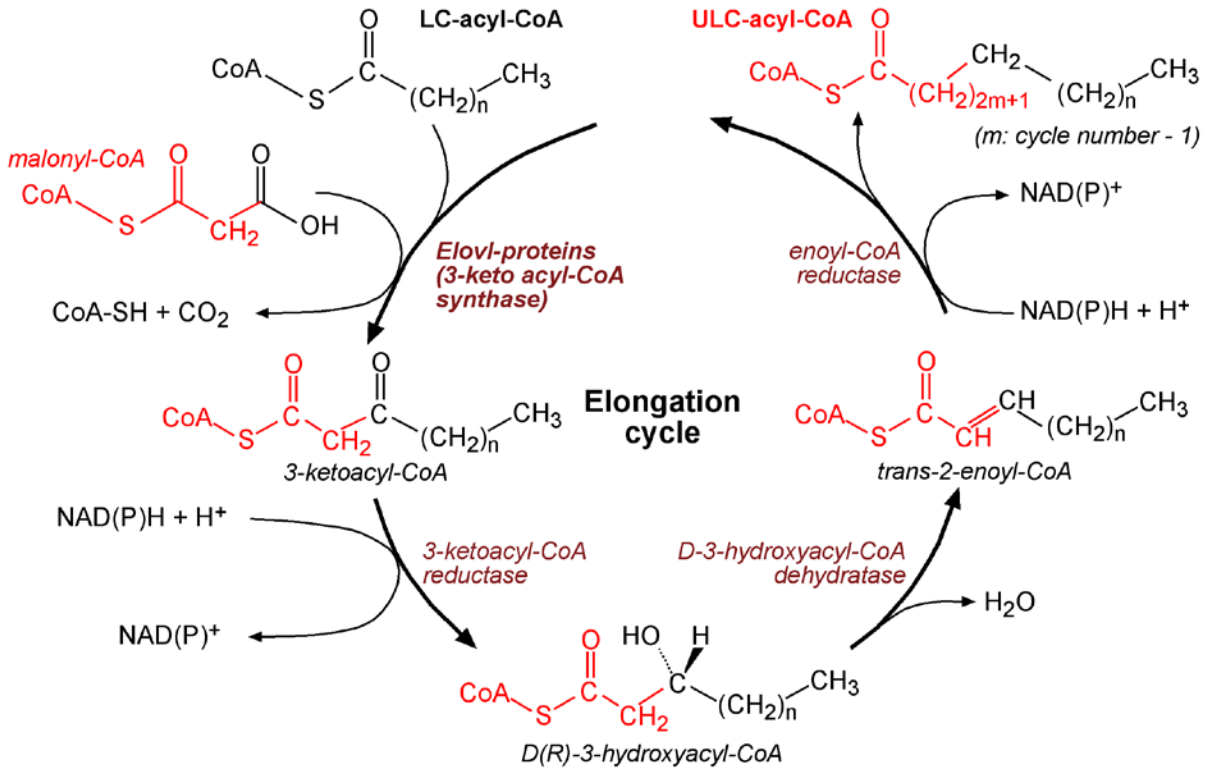

Figure 6. Synthesis of LC-, VLC- and ULC-CoAs.
Elovl proteins residing in the ER catalyze the rate-limiting step of the fatty acid synthesis consisting of the condensation of a precursor fatty acid with malonyl-CoA. The formed 3-ketoacyl-CoA derivative is reduced, dehydrated and further reduced resulting in the formation of a fatty acyl-CoA with an additional two-carbon unit in its chain.

In mammals, the *Elovl* gene family consists of seven members (*Elovl1–7*), which are reported to be localized within the ER membrane. Their tissue expression and substrate affinity regulates the specific fatty acid species expressed in each cell type. At the beginning of this study, reliable data concerning the distinct distribution and substrate specificity of these enzymes in eukaryotic cells was rather limited. To date increasing numbers of reports including studies in transgenic mice are available (Table 1). In summary, the synthesis of saturated and monosaturated LC-CoAs seems to be facilitated by Elovl6, which produces stearoyl-CoA (18:0), and by Elovl1, Elovl3, and Elovl7, that take over to generate VLC-CoAs. Polyunsaturated LC- and VLC-CoA biosynthesis from essential fatty acid precursors is catalyzed by Elovl2 and Elovl5 (Guillou et al., 2009).

Enzyme Name	Previous Names[1]	Tissue mRNA expression	Fatty acyl-CoA substrate	
			Carbon number	Unsatura.[2]
Elovl1	Ssc1	Brain, ub.[3]	18-24	S, M
Elovl2	Ssc2	Testis, liver	20-24	P
Elovl3	Cig30	BAT[4], WAT[4], seb.glands[4], liver	18-24	S, M
Elovl4	-	Retina, brain, skin	28-30	S, P
Elovl5	Helo1	Liver, testes, ub.	18-20	P
Elovl6	-	Liver, WAT, ub.	16	S, M
Elovl7	-	Kidney, pancreas, ub.	18-24	S, M

[1] Ssc1: sequence similarity to Cig30 1; Ssc2: sequence similarity to Cig30 2; Cig30: cold-inducible glycoprotein of 30 kDa; Helo1: homolog of yeast long chain polyunsaturated fatty acid elongation enzyme

[2] Unsaturations. S: saturated; M: monounsaturated; P: polyunsaturated.

[3] Ubiquitously expressed.

[4] BAT: brown adipose tissue; WAT: white adipose tissue; Seb. glands: sebaceous glands.

Table 1. Tisssue distribution and substrate specificity of the Elovl proteins.
Tissue expression and substrate preferences of the Elovl proteins described in this table were obtained from (Guillou et al., 2009; Leonard et al., 2004). Lipid profile changes due to depletion of Elovl3 is associated with triacylglycerides (Westerberg et al., 2004).

Recent studies indicate that the biosynthesis of ULC-CoAs seems to be restricted to Elovl4 expression. The highest transcript levels are found in retina, brain, skin, and to a lesser extent in the testis (Mandal et al., 2004). *In vivo* depletion of Elovl4 revealed an essential requirement of ULC-CoAs in epidermal sphingolipids. Elovl4 mutant mice exhibited a depletion of ω-hydroxy-ceramides with fatty acyl residues of 28 and longer carbon atoms in their chain length. Additionally, an accumulation of ceramides with 26 carbon acyl residues suggested cerotoyl-CoA (26:0-CoA) to be a *bona fide* Elovl4 substrate (Li et al., 2007). In 2008, *in vitro* studies using overexpressing cells could show that Elovl4 is required for the synthesis of saturated and polyunsaturated ULC-CoAs (Agbaga et al., 2008). To date, no other elongase has been reported to have affinity towards both saturated and unsaturated fatty acids.

1.3.2.2. The ceramide synthase family (CerS)

Acyl-CoAs are incorporated into sphingolipids at the stage of ceramide sythesis (see Figure 3 and 4). This acylation of a spingoid base is catalyzed by the ceramide synthase (CerS) family, which operates in the “salvage pathway” to generate ceramide, in addition to the *de novo* synthetic pathway yielding dihydroceramide (*vide supra*).

Ceramide synthases were originally denominated longevity assurance genes (*Lass*, still their official gene name) for their replication capacity upon its deletion and for their role in determining yeast longevity (D'Mello N et al., 1994). Since the yeast *Lag1* gene was discovered, several of their homologues have been identified in a wide variety of eukaryotic organisms, including mammals (supplemental Table A3). Whereas one enzyme solely appears to encode for a ceramide synthase in *D. melanogaster* (Bauer et al., 2009), three homologues are required in *C. elegans* (Menuz et al., 2009) and *S. cerevisiae* (Schorling et al., 2001; Vallee and Riezman, 2005). In mammals, six homologue genes constitute the ceramide synthase family (CerS1–6). CerSs exhibit a tissue specific distribution, in addition to distinct preferences towards the chain length and saturation grade of their acyl-CoA substrates (Table 2). Thus, their tissue expression pattern determines the distinct ceramide composition possible in each cell type. For instance, CerS1 is primarily expressed in the brain, where it catalyzes the formation of ceramide preferentially containing a stearic acid moiety, the major ceramide species in this organ (Venkataraman et al., 2002).

Currently, the preferences for ULC-CoAs have not been appointed to any of the ceramide synthases. However, their substrate affinity was either determined in overexpressing cells lacking ULC-CoAs, or in *in vitro* ceramide synthase assays with acyl-CoA substrates ranging from 16 to 26 carbon atoms. Nevertheless, CerS2 and CerS3 seem to preferentially incorporate acyl-CoAs with the longest carbon atom chains included in those studies. Interestingly, CerS3 is exclusively expressed in testis and skin (Laviad et al., 2008), both tissues being the major source of ULC-CoAs. Therefore, we hypothesized that CerS3 could be a potential candidate responsible for the generation of ceramides containing ULC-CoAs. The investigation of the ceramide synthase(s) involved in the biosynthesis of ULC-SLs, as well as the

functional role of these unconventional sphingolipids are the major topics to be discussed in this study.

Enzyme Name	Previous Names[1]	Tissue mRNA expression	Acyl-CoA substrate	References for substrate affinity
CerS1	Lass1, Uog1	Brain, skeletal muscle	18	(Venkataraman et al., 2002)
CerS2	Lass2, Trh3	Kidney, liver	22-24	(Laviad et al., 2008)
CerS3	Lass3, T3L	Testes, skin	18-24	(Mizutani et al., 2006)
CerS4	Lass4, Trh1	Liver, heart, skin	18-22	(Riebeling et al., 2003)
CerS5	Lass5, Trh4	Ub.[2]	16-18	(Riebeling et al., 2003)
CerS6	Lass6, Trh1-like	Intestine, kidney, ub.	14-16	(Mizutani et al., 2005)

[1] Lass: longevity assurance homolog; Uog1: upstream of GDF1; Trh: translocating chain-associating membrane protein homolog; T3L: Trh3-like protein.
[2] Ubiquitously expressed.

Table 2. Tisssue distribution and substrate specificity of the CerS proteins.
Tissue expression was summarized from (Laviad et al., 2008).

1.4. Expression of ultra long chain sphingolipids

1.4.1. The testis

The testis consists of highly convoluted loops of the seminiferous tubules embedded in interstitial tissue. The former functional compartment is required for sperm cell formation, whereas the main function of the latter involves hormone production.

In the coiled loops of the seminiferous tubules, spermatozoa are continuously produced from differentiated germ cells after each spermatogenic cycle (Figure 7). The supporting Sertoli cells are required during spermatogenesis to deliver nutrients to germ cells, as well as for maintenance of the integrity of the seminiferous epithelium, regulation of differentiating germ cells, and for the phagocytosis of residual bodies left by spermatids upon transformation into spermatozoa. Additionally, Sertoli cells are crucial for the establishment of the blood-testis barrier

(BTB), a junctional complex that generates the physical barrier separating the seminiferous epithelium into an adluminal and a basal compartment.

On the other hand, Leydig cells in the insterstitium are the endocrine cells responsible for androgen production, mainly testosterone. Additionally, myeloid cells are localized in the interstitium enclosed within the lymphatic endothelium.

1.4.1.1. The spermatogenic cycle

Spermatogenesis is a complex and highly regulated process by which diploid spermatogonia differentiate into mature haploid spermatozoa. This transformation takes place in the seminiferous tubules and involves three stages known as spermatocytogenesis, spermatidogenesis and spermiogenesis. During spermatocytogenesis, spermatogonial stem cells (SG) located at the basal lamina are subjected to numerous mitotic divisions within a highly proliferative phase. These rapid successive divisions generate different type A spermatogonia that can be distinguished by the amount of chromatin in the nuclear envelope. Sequentially, spermatogonia initiate various differentiation steps leading to type B spermatogonia, followed by the formation of primary spermatocytes (SC), *i.e*. preleptotene and leptotene spermatocytes (plSC and lSC). These primary spermatocytes initiate the long lasting prophase of the first meiotic division, and thereby entering the stage of spermatidogenesis. During this phase, primary spermatocytes migrate through the active blood testis barrier to the adluminal compartment, which distinct milieu favors the development of meiosis I leading to the formation of the secondary spematocytes. There, pachytene spermatocytes (pSC) enter the second meiotic division ending in the formation of haploid spermatids with a unique genetic rearrangement. Spermiogenesis proceeds with the transformation of round spermatids (rST) into elongated spermatids (eST) and finally into fully differentiated spermatozoa (Sza). This requires massive morphological changes of the spermatids, including the development of the flagellum required for motility, the formation of an acrosome membrane containing digestive enzymes necessary for fertilization, nuclear transformation, and elimination of excess cytoplasm by the excretion of a residual body (rb).

Spermatozoa generated with each spermatogenic cycle must be released into the lumen of the seminiferous tubules during a process known as spermiation. Following, spermatozoa are transported into the epididymis were their maturation is completed.

The complete spermatogenic cycle requires five mitotic and two meiotic divisions. Only the first mitotic division generates two separated daughter cells. All subsequent divisions of differentiating germ cells generate sister cells that remain connected by intercellular bridges due to an incomplete cytokinesis, and thereby sharing one unique cytosol and plasma membrane.

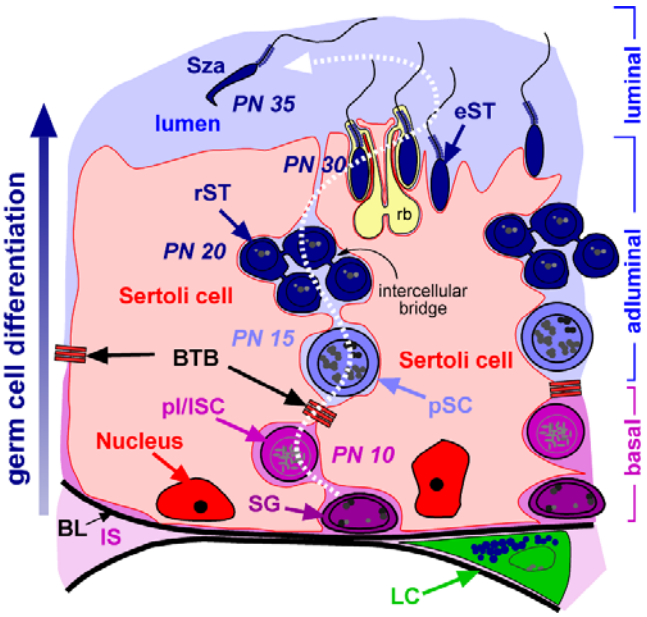

Figure 7. Schematic representation of the spermatogenic cycle in mice.
In the seminiferous tubules of the testis, spermatogonial stem cells (SG) adhered at the basal lamina (BL) proliferate generating spermatogonia type B that differentiate into preleptotene and leptotene spermatocyte (pl/ISC), which are the most differentiated germ cells present at post natal day (PN) 10. These primary SCs must traverse the blood-testis barrier (BTB) and further differentiate into pachytene spermatocytes (pSC), which are present at PN 15 of the first spermogenic cycle. At PN 20, the first round spermatids (rST) are formed and 10 days later the tubules contain significant amount of elongated spermatids (eST). These must further differentiate to generate spermatozoa (Sza), which are released into the lumen of the tubules from PN 35 onwards, and transported into the epididymis where they acquire full maturation. In the interstitium (IS) between adjacent tubules, androgen producing Leydig cells (LC) are located. Scheme modified from (Sandhoff, 2009).

1.4.1.2. Testicular polyenoic ultra long chain sphingolipids

In addition to simple sphingolipids, *i.e.* ceramides and sphingomyelins, mouse testis express complex glycosphingolipids of the ganglio (Gg-) and the globo (Gb-) series. In previous work of our department, the comparison of GSL patterns of fertile and infertile mouse models led to the finding of a novel class of complex GSLs (Sandhoff et al., 2005). Structural analysis of these 8 novel molecules revealed a fucose residue attached to their ganglio-series oligosaccharide chains. Interestingly, the novelty relied on the fatty acid residue incorporated in these complex GSLs, being almost exclusively polyunsaturated (4 to 6 double bonds) and with a chain length of 28 to 32 carbon atoms (Figure 8). Previously, sphingolipids containing ULC-PUFA residues have only been described as minor components incorporated into sphingomyelin of various mammals (Robinson et al., 1992).

Investigations of the specific GSL expression patterns of fertile GM3/Siat9$^{-/-}$ and infertile GM2S/Galgt1$^{-/-}$ mice linked the presence of the neutral subset of fucosylated GSL (FGSL) containing the ULC-PUFA moieties to be required for male fertility in mice (Sandhoff et al., 2005). Infertile mice lacking this neutral subset due to a genetic disruption of the GM2S/Galgt1$^{-/-}$ developed multinucleated giant cells at the stage of spermatid formation. The intercellular bridges connecting the sister spermatids were lost, leading to an arrest of spermatogenesis in these mutant mice. Whereas lack of these unconventional fatty acid residues, and/or lack of the complex fucosylated carbohydrate structure of this neutral FGSL are required for male fertility, is still to be elucidated.

Therefore cell-stage expression patterns of ULC-PUFA sphingolipids, in addition to the identification and *in vivo* depletion of the CerS(s) responsible for their biosynthesis, will be required to get insight into the molecular function and specific role of ULC-SLs in spermatogenesis.

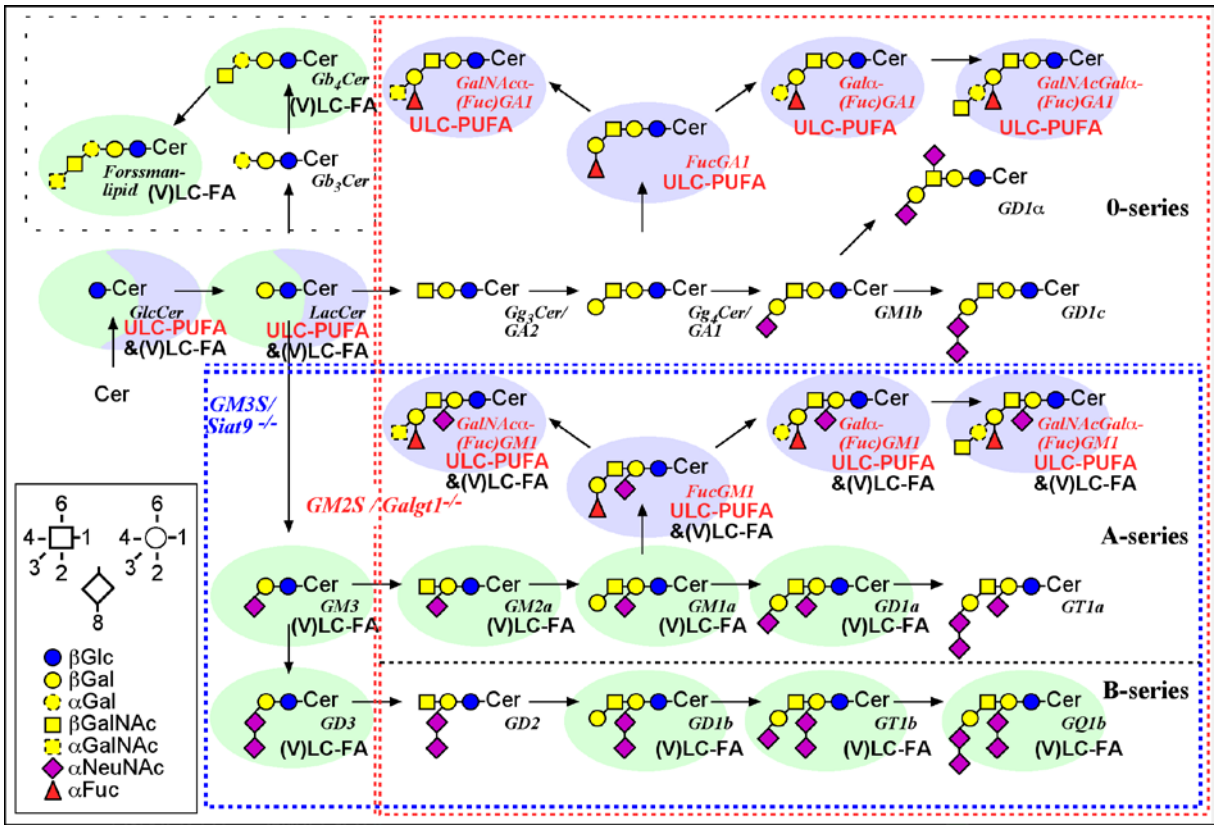

Figure 8. GSL structures expressed in mouse testis.
Testicular GSL structures are respresented within their synthetic pathways of the ganglio- and globo-series. GSLs absent in fertile GM3S/Siat9$^{-/-}$ and infertile GM2S/Galgt1$^{-/-}$ mice are enclosed in a blue and red square, respectively.

1.4.2. The epidermis

The mammalian skin is composed of two morphologically distinct layers: the overlying *epidermis*, which provides the primary barrier against desiccation, xenobiotics and pathogens; and the underlying *dermis*, which provides the strength and flexibility of the skin and accounts for the majority of its thickness. The latter is mostly constituted of fibroblasts, which secrete the connective tissue matrix mainly composed of collagen fibrils and elastin fibres. Instead, the primary cells of the epidermis are keratinocytes, which undergo progressive differentiation, maturation and cornification from the basal lamina to the outermost superficial cell layer (Figure 9).

1.4.2.1. Epidermal structure and keratinocyte differentiation

Epidermal differentiation is a highly dynamic process where keratinocytes are continuously regenerated from the proliferative *stratum basale* and shed upon their terminal stage of cornification. During this process, keratinocytes must undergo a series of profound changes involving their complete cellular structure and composition (Figure 9).

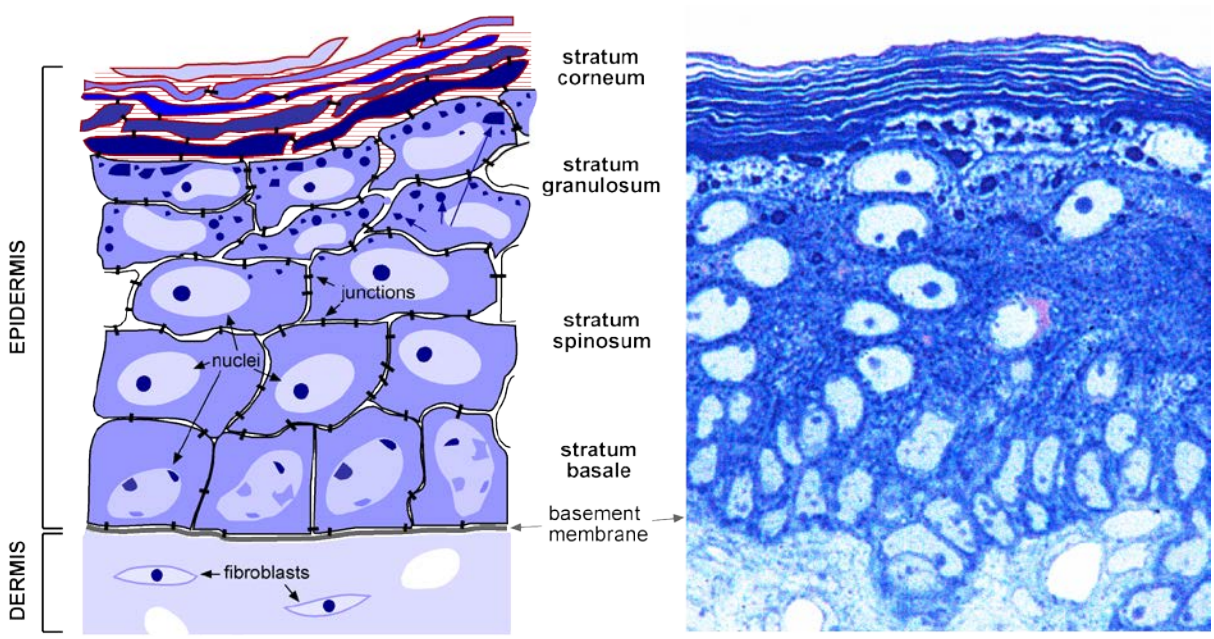

Figure 9. The epidermal structure.

The epidermis is a self-renewing tissue, where keratinocytes at the stratum basale progressively differentiate and migrate through the stratum spinosum and the stratum granulosum to terminally differentiate in the stratum corneum, where they finally shed during desquamation. Right, PAS-methylene blue-Azur II staining of neonatal mouse skin. KG: keratohyalin granules. Scheme (left) modified from (Sandhoff, 2009).

Keratinocytes residing at the *stratum basale* (SB) are characterized by the expression of keratins K5 and K14. These structural proteins, together with microtubules and microfilaments, constitute the cytoskeleton of basal epithelial cells. Upon leaving the basal lamina, keratinocytes become less proliferative and begin their apical migration reaching the *stratum spinosum* (SS). At the spinous layers, a complete new set of structural proteins is synthesized, mainly K1 and K10. At a more

advanced stage starts the synthesis of lipids and early structural proteins (involucrin, transglutaminases) required for the formation of the cornified envelope (CE). The cornified envelope consists of a highly cross-linked protein structure that replaces the plasma membrane of terminally differentiated keratinocytes, *i.e.* corneocytes. These structural proteins of the CE are covalently bound to the corneocyte-lipid envelope (CLE), and together provide the primary and essential epidermal barrier (Candi et al., 2005). In parallel to the synthesis of lipids and enzymes required for the establishment of the CE and CLE, the formation of the secretory lamellar body organelle (LB) occurs at the upper SS layers. The main function of this unique multifunctional organelle is to deliver lipids, enzymes, antimicrobial peptides, among other metabolites, and secrete them primarily at the interface of the upper epidermal layers, *i.e.* the *stratum granulosum* (SG) and the *stratum corneum* (SC) (Elias et al., 2006).

At the SG, the keratinocyte maturation proceeds with the expression of loricrin and profilaggrin, main constituents of the keratohyalin granules (KG), which structural proteins will be incorporated to the CE. The most profound changes during keratinocyte differentiation occur between the maturation of nucleated keratinocytes of the SG to enucleated corneocytes of the SC. At this interface, the majority of lamellar bodies secrete their contents, transglutaminases (TGs) cross-link proteins that generate the CE (involucrin, loricrin) and organelles of the viable epidermal layers are progressively degraded.

Morphologically, keratinocytes develop a flattened shape concomitantly with their differentiation yielding the squamous corneocytes. This terminally differentiated keratinocytes are devoid of nuclei, organelles and plasma membrane. Instead, the highly cross-linked proteins of the CE serve as a scaffold where lipids of the CLE are covalently bound.

The terminal keratinocyte differentiation leads to a highly regulated proteolytic process of specialized cell-cell junctions, *i.e.* corneodesmosomes, that concludes in the desquamation of the outermost corneocytes. The proteolytic cleaveage of corneodesmosomes requires the degradation of secreted extracellular corneosomal proteins (*i.e.* corneodesmosin), as well as of specific cadherins (*i.e.* desmogleins) by various proteases (*i.e.* kallikreins and cathepsins). The altered expression of

proteases, or alteration in the concentration of protease inhibitors, and other factors such as calcium concentration, pH and water content, results in a defect in corneocyte shedding, thereby altering desquamation leading to various pathologies (*e.g.* ichthyoses).

1.4.2.2. Embryonic epidermis and the periderm

At the initial embryonic stages of development, a transient epidermal layer known as *periderm* is formed from the embryonic ectoderm. During the early embryonic period, the epidermis consists of two cell layers, the inner proliferative basal keratinocytes and the outer periderm cells. At the embryonic/fetal transition, the basal keratinocytes start to stratify leaving the periderm cell layer at the epidermal surface. Peridermal cells cease to divide and increase in surface area, while characteristic blebs are being formed. Later in fetal development, complete stratification is reached with the formation of a thin stratum corneum underneath the peridermal cell layer. Nuclear degradation of peridermal cells proceeds with the subsequent disaggregation of the periderm, a process that occurs concomitantly with the barrier formation (Hardman and Byrne, 2006). In mice, the epidermal barrier is estimated to develop from embryonic day E16.5 to be completed at E18.5 (in mice born at day 19) (Hardman et al., 1998).

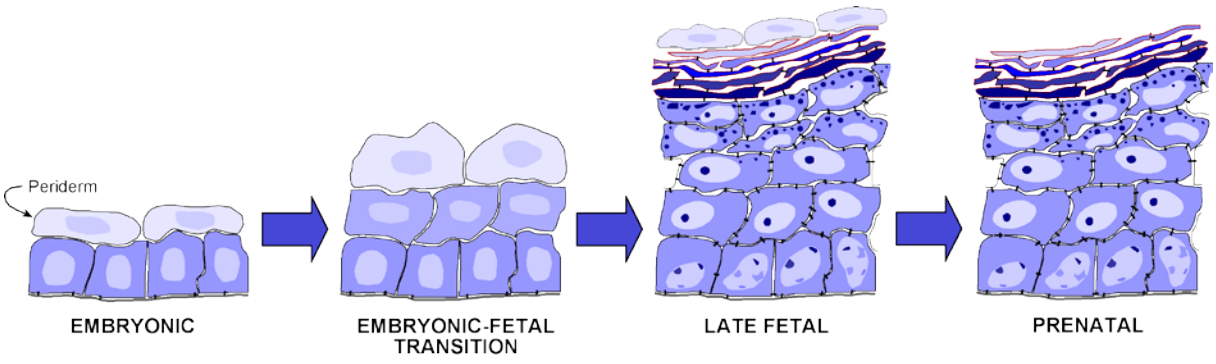

Figure 10. Development of embryonic epidermis.
Epidermis develops from the embryonic ectoderm by subsequent stratification of basal keratinocytes. The transient peridermal layer located at the surface might serves as a protective layer for the developing epidermis. Present until the late fetal stage (P < 16.5), the periderm disaggregates during the prenatal period (P > 18.5).

Although the function of the periderm is not completely understood, its role as a protective layer for embryonic skin has been suggested. The fact that the periderm is sealed with tight junctions supports this hypothesis. Differing from epidermal tight junctions, peridermal cells express claudin-6 (Morita et al., 2002). Keratins, namely K6, K16 and K17, are additionally expressed in this transient epidermal layer (Hardman and Byrne, 2006).

1.4.2.3. Stratum corneum pH

Along with the keratinocyte terminal differentiation, a remarkable pH gradient is established. In humans, the initial neutral pH (~6.8) at the lower SC decreases with cornification reaching an acidic pH (~4.5–5.3) at the surface of the SC. The generation of this “acid mantle” is influenced by exogenous as well as endogenous mechanisms. Whereas exogenous sources such as microbial metabolism or lactate formation from sweat appear to contribute to a minor extent to the pH gradient, the endogenous formation of free fatty acids from phospholipids, in addition to the proton secretion from the Na^+/H^+ antiporter at the keratinocyte PM, and the trans-urocanic acid production are the major contributors of the acidic pH. This acidic mantle at the surface of the SC is required to modulate SC integrity and cohesion, to provide resistance to antimicrobial activity, and to maintain the epidermal permeability barrier homeostasis (Fluhr and Elias, 2002).

1.4.2.4. Intercellular junctions of the epidermis

The epidermis contains various types of cell-cell junctional complexes, that are required for maintaining cellular adhesion, controlling transport of solutes and foremost, regulate the epidermal barrier function. Epidermal intercellular junctions are comprised of communication junctions (gap junctions), mechanical junctions (adherens junctions and desmosomes) and tight junctions.

Communication junctions are commonly denominated as gap junctions and are composed of two transmembrane half-channels*, i.e.* connexons, each consisting of an assembly of six connexins that form a continuous channel between neighboring cells thereby directly connecting their cytoplasms (Figure 11). The channel created by connexons is about 2 to 4 nm, thus enabling the passage of ions and small

molecules up to 1 kDa. By regulating the flow of these molecules, gap junctions are directly involved in the chemical communication between neighboring cells forming a functional synchronized syncytium (Haftek et al., 2006).

Mechanical junctions are involved in cellular adhesion by connecting intracellular cytoskeletal proteins of adjacent cells. The adherens junctions (*zonulae adherentes*) connect F-actin filaments via the classical cadherin-catenin complexes between two neighboring cells. Instead, desmosomes (*maculae adherentes*) are keratin-associated protein complexes that are distinctive of epidermal tissues.

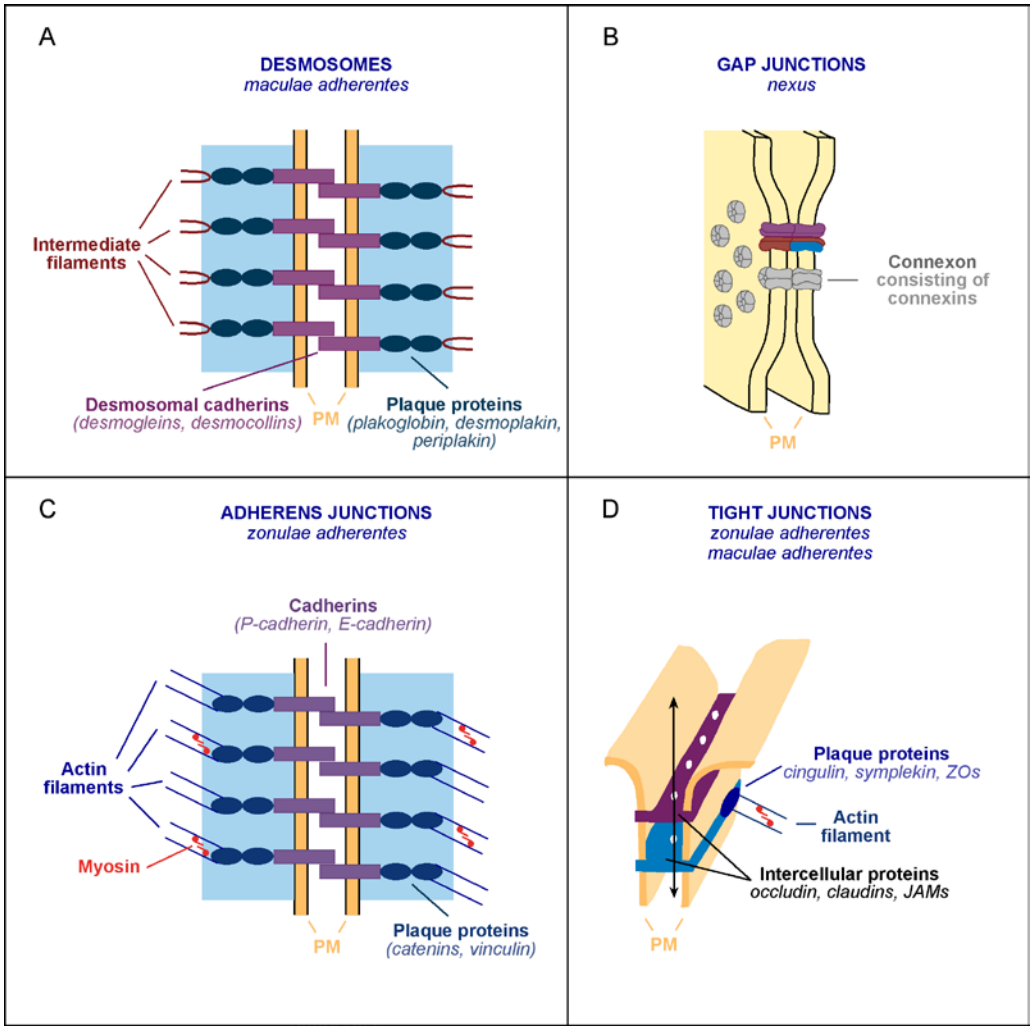

Figure 11. Epidermal intercellular junctions.
Model describing mechanical junctions (desmosomes and adherens junctions, A and C), communication junctions (gap junctions, B) and tight junctions (D), including the major proteins associated with each junctional complex. PM: Plasma membrane; ZOs: Zonula occludens proteins. Modified from (Lüllmann-Rauch, 2003)

The intercellular connections of actin-associated adherens junctions are constituted by transmembrane cadherins that form calcium dependent homodimers with cadherins of adjacent cells (Figure 11). Epidermal cell cohesion is achieved by anchoring the intracellular portion of these cadherins (P-cadherin and E-cadherin) to intracellular catenins (α-catenin, β-catenin, γ-catenin/plakoglobin and δ-catenin). The intercellular space created by this cell-cell junction is about 15 to 20 nm. Adherens junctions are distributed over the entire viable layers of mammalian epidermis (Brandner et al., 2010).

Desmosomes are junctional protein complexes built up by the desmosomal cadherins (desmogleins and desmocollins) and the intracellular plaque proteins (plakoglobin and desmoplakin) (Figure 11). Intercellular cadherins serve as anchor sites for the attachment of adjacent cells. They span across the PM of nucleated keratinocytes or through the CE of corneocytes, binding to the intermediate filaments (keratins) via the plaque proteins.

Keratinocyte maturation modulates the number, size and composition of desmosomes. At the SB, desmosomes increase upon differentiation to the SS. At the interface between SG and SC, desmosomes undergo a series of profound changes including the integration of the junctional complexes into the CE. These morphological changes lead to the formation of the corneodesmosomes. At the first layers of the SC, *i.e. stratum compactum*, corneodesmosomes are almost evenly distributed over the entire surface of the corneocytes. As cornification advances, non-peripheral corneodesmosomes distributed at basal and apical regions, are first degraded by LB-secreted proteases. In the upper SC, *i.e. stratum disjunctum*, the degradation of peripheral corneodesmosomes distributed at the lateral regions is initiated, resulting in a weaker cell cohesion that ultimately leads to the shedding of the outermost superficial corneocytes (Haftek et al., 2006).

The process of desquamation involves the proteolytic degradation of corneodesmosomal proteins. Several proteases have been implicated in this process, mainly proteins of the kallikrein family (KLK7 and KLK5) and the cathepsin family (CTSL2, CTSL-like, CTSD and CTSE-like). Protease inhibitors have also been implicated in the regulation of corneocyte exfoliation, among them elafin, antileukoproteinase and SPINK-5 are the most prominent. Additionally, several other

factors have been shown to influence cell cohesion at the SC, such as water content, SC pH and depletion of extracellular calcium (Haftek et al., 2006). Deregulations and alterations of the desquamation process can lead to several pathological conditions, *e.g.* Netherton syndrome (Schmuth et al., 2007).

Whereas adherens junctions and desmosomes mechanically couple the intracellular cytoskeleton of neighboring cells and thereby regulate cell adhesion, tight junctions are primarily responsible for sealing adjacent cells and controlling the paracellular transport. Tight junctions (*zonulae occludentes*) from two adjacent cells form paired strands or fibrils, which contain aqueous pores, thus enabling the diffusion of selected ions and small molecules (Figure 11). In addition, tight junctions (TJs) separate the apical and the basal plasma membrane domains thereby blocking the lateral diffusion of proteins and lipids (Morita et al., 2002).

The debate regarding the occurrence of typical TJ structures in mammalian epidermis has been ongoing for several decades. This controversy reached its end with the recent reports from the Tsukita and Franke groups describing TJs and TJ-related structures in stratified mammalian epithelia (Langbein et al., 2002; Morita et al., 2002). In addition to typical TJ structures (*zonulae occludentes*), characterized by their “kissing points” at the electron microscopical level, they identified “lamellated TJs” (*coniunctiones laminosae*), “sandwhich junctions” (*iuncturae structae*), extended close-contact junctions (occludens junctions), among other structures. These junctional complexes were often found interspersed between desmosomal junctions (Langbein et al., 2002).

At the molecular level, tight junctional complexes are comprised of transmembrane and plaque proteins. Occludin, claudins and junctional adhesion molecules (JAMs) have been reported among the transmembrane proteins found in epidermal tight junctions. These intercellular proteins are associated with scaffolding plaque proteins such as cingulin, symplekin, *zonula occludens* proteins (ZO-1, ZO-2, ZO-3), *etc*. The latter *zonula occludens*-associated proteins have been demonstrated to directly bind to the F-actin cytoskeleton (Brandner and Proksch, 2006). The molecular composition of the tight junctional transmembrane and plaque proteins is widely diverse and varies according to cell types, as well as their degree of differentiation. In particular, the expression pattern of the extensive claudin protein family has been

reported to be highly tissue specific (Tsukita et al., 2001). Their composition and ratio of expression have been shown to modulate TJ permeability and ion selectivity (Furuse et al., 2001). However, the essential role of TJ in the epidermal permeability barrier was not established until it could be demonstrated that claudin-1 deficiency resulted in rapid postnatal lethality due to a tremendous transepidermal water loss (TEWL) in mice (Furuse et al., 2002).

Differing from the wide distribution of adherens junctions within the living layers of the epidermis, the expression of *zonulae*-TJs is restricted to the SG layer. Typical *zonulae*-TJ structures are distributed continuously around the cell-cell borders of granular keratinocytes (Furuse et al., 2002). In addition, less developed TJ complexes known as *maculae occludentes* have also been reported at the SG layer. Their distribution was focussed in a series of discrete sites around the cell-cell borders of granular keratinocytes (Morita et al., 1998).

In diseased skin, TJ expression exhibits a broadened distribution that included keratinocytes of the SS layer. Altered expression of TJ proteins have been demonstrated in psoriasis, ichthyosis vulgaris, various eczema, but also in tumors and in regenerating skin after wounding (Brandner and Proksch, 2006; Kirschner et al., 2010a).

1.4.2.5. Epidermal permeability barrier

The primary function of the epidermis is to provide a defensive barrier against pathogenic microbes, mechanical and chemical insults, and most importantly to provide terrestrial vertebrates with a barrier against desiccation. This essential permeability barrier primarily resides in the SC, where corneocytes are embedded in lipid lamellar sheets that form the corneocyte-lipid envelope. These highly hydrophobic lamellae are mostly composed of ceramides (Cer), cholesterol (Chol) and free fatty acids (FFA), estimated to contain 50%, 25% and 10% of the total lipid mass, respectively (Werzt, 2006). The near equimolar ratio of these major components of the CLE is critical for the proper maintenance of the epidermal permeability barrier (Holleran and Takagi, 2006). Alterations of this ratio, as well as the variation within their species, have been linked to a multitude of skin diseases such as atopic dermatitis and psoriasis (Imokawa et al., 1991; Motta et al., 1993).

Minor components of the lipid lamellae include cholesterol sulfate, which is required for proper desquamation (Elias et al., 1984), and free long chain bases, resulting from the degradation of ceramide, which might be necessary for inhibiting pathogenic microbial growth (Bibel et al., 1992; Veerman et al., 2010).

The formation of the epidermal permeability barrier is initiated with the synthesis of lipids required for the formation of the CLE and their precursors, which take place at the ER and the Golgi compartments of mostly keratinocytes of the upper SS and SG (Figure 12). These secretory lipids and their precursors are packed in disk-like form lipid layers, together with hydrolytic enzymes (*e.g.* glycosidases, proteases), and other proteins into lamellar bodies. These stacks of lipids mostly consist of cholesterol and the precursor species of glucosylceramides, sphingomyelins, and glycerophospholipids, required for the formation of intercellular ceramides and FFAs (Freinkel and Traczyk, 1985). Analysis on the composition of these precursor lipid species revealed that glucosylceramides are specially enriched of a unique ULC-ω-hydroxy fatty acid moiety esterified with linoleic acid at the ω-position (Abraham et al., 1985). In contrast, the acyl moieties of sphingomyelins have non-hydroxy fatty acids up to 26 carbon atoms, or α-hydroxy-LC-FA residues (Uchida et al., 2000).

Following the synthesis and recruitment of lipids and proteins into LB, these organelles translocate apically towards the plasma membrane of the uppermost keratinocytes of the SG. A deficiency or malfunction of this multifunctional organelle has severe consequences. Mutations in the ATP-binding cassette transporter A12 protein, ABCA12, required for the proper lipid transport in LB, leads to the fatal human disorder of Harlequin ichthyosis causing a defective barrier function and neonatal death (Akiyama et al., 2005; Kelsell et al., 2005).

At the interface, LB fuse with the PM and secrete their content in the extracellular space (Madison, 2003). There, LB-derived lamellar sheets are organized parallel to the PM, where conventional plasma membrane lipids are successively replaced by the lamellar sheets of the CLE. The formation of the mature CLE requires the attachment of ω-hydroxy-ULC-glucosylceramides to the carboxy residues of proteins in the outer surface of the CE (Holleran and Takagi, 2006). Previous ω-esterification to fatty acids like linoleic acid appears to be crucial for this process, as lack of sphingolipids containing these ω-esterified FAs in CGI-58 deficient mice also leads to

a strong decrease in protein bound sphingolipids (Radner et al., 2009). *In vitro*, the transesterification of ω-hydroxy-ULC-ceramides from their linoleic esters onto glutamine residues of involucrin has been demonstrated for transglutaminase 1 (TG1) (Nemes et al., 1999). However, patients with TG1 deficiency exhibit sporadic normal CLE structures, therefore this enzyme might not be solely responsible for the attachment of ω-hydroxy-ULC-sphingolipids to the CE (Elias et al., 2002).

The CE proteins involved in the covalent attachment of ω-hydroxy-ULC-sphingolipids *in vivo* remain elusive. Although involucrin, envoplakin and periplakin have been suggested substrates for ceramide attachment, other structural proteins have not been discarded as possible substrates (Marekov and Steinert, 1998). In mice, the *in vivo* depletion of involucrin develop normal CE (Djian et al., 2000), therefore other additional proteins might be responsible for the linkage to the CLE.

At the extracellular space, the lipid lamellae are elongated and fuse resulting in the formation of uninterrupted lipid sheets. This fusion of short lipid stacks has been suggested to occur edge-to-edge (Landmann, 1986), and might be mediated by the extracellular processing of precursor polar lipids (mainly glucosylceramide and phospholipids) that generate the highly hydrophobic constituents of the CLE (Coderch et al., 2003).

The final step for barrier formation requires the hydrolysis of precursor lipids by secreted acid hydrolyses. In particular, glucosylceramides are converted into ceramides by β-glucocerebrosidase (Holleran et al., 1994b). The formation and processing of glucosylceramide is an imperative for a functional epidermal barrier, as has been demonstrated in the keratinocyte specific deletion of glucosylceramide synthase (Jennemann et al., 2007) and in a mouse model for Gaucher disease with a defective β-glucocerebrosidase (Doering et al., 1999b; Holleran et al., 1994a). The hydrolysis of GlcCers appears to require the activation of β-glucocerebrosidase by saposins. The *in vivo* deficiency of prosaposin, common precursor of these small glycoproteins, exhibits abnormal lamellar membrane maturation (Doering et al., 1999a).

The processing of protein bound ω-hydroxy-ULC-glucosylceramides leads to the maturation of the CLE. However, the processing of sphingomyelin by acid sphingomyelinase, as well as the breakdown of phospholipids by phospholipase A_2

to generate FFAs, has been shown to be critical for epidermal barrier homeostasis. The hydrolysis of precursor lipids has an optimum acidic pH, exhibiting extremely reduced enzymatic activities at neutral pH (Holleran and Takagi, 2006).

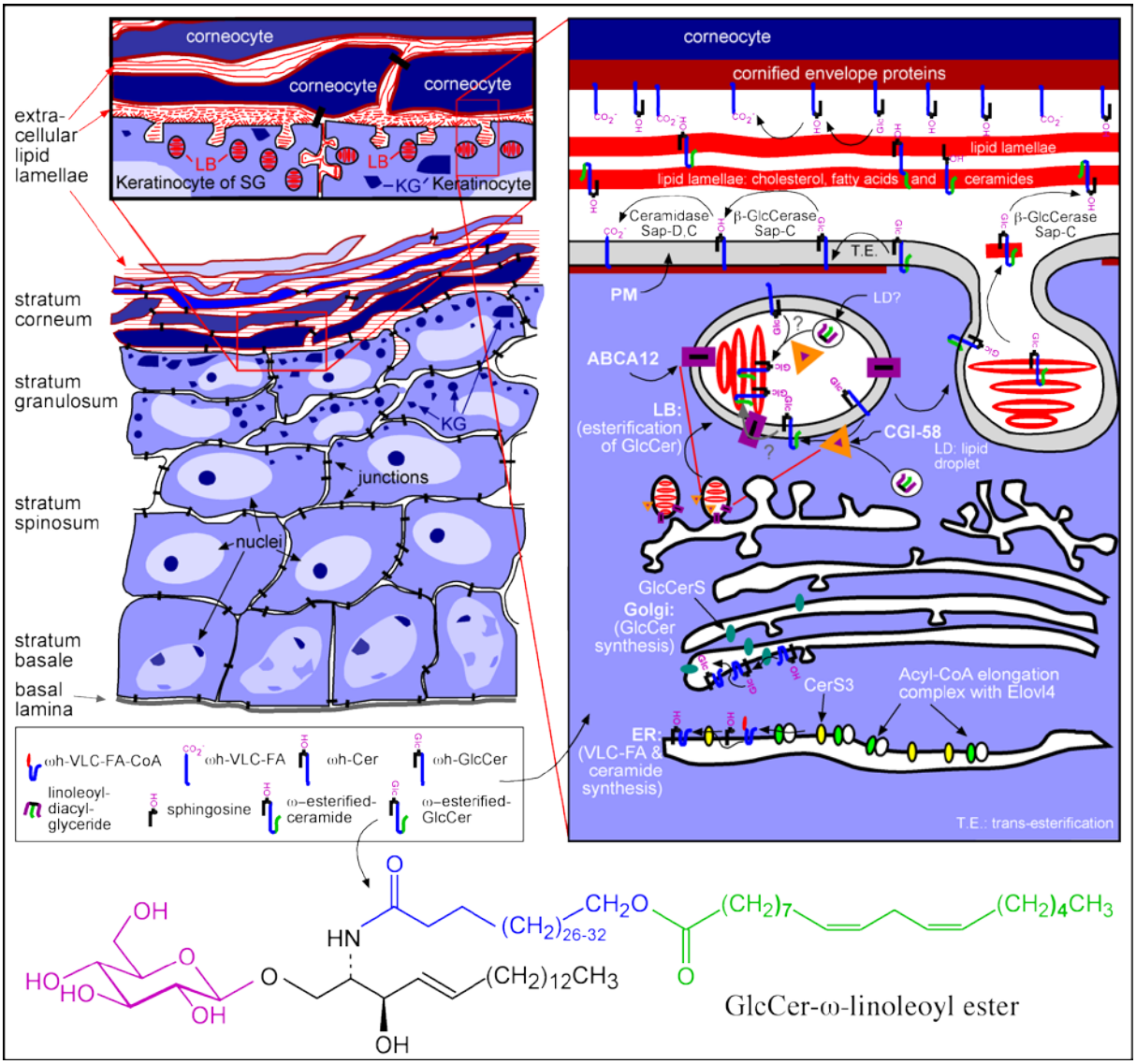

Figure 12. Establishment of the epidermal permeability barrier.

The epidermal permeability barrier is primarily localized at the SC. The highly hydrophobic lipid lamellae together with the CLE are required for the proper function of the epidermal barrier against desiccation. The lamellar bodies have an essential function involving the transport and secretion of precursor lipids to the interface, which are further processed to generate the CLE, i.e. the lipid sheets within the interstices. Modified from (Sandhoff, 2009).

Although a significant progress has been achieved in the last decades to elucidate the metabolic requirements for the formation of the CLE, the precise steps for ULC-FA elongation, ω-hydroxylation and ω-*O*-esterification are still unresolved, regarding the enzymes and their intracellular localization. The specific regulation of these processes, as well as the precise biogenesis, transport and secretion of LB is a prerequisite for understanding the pathogenesis of a multitude of skin diseases.

1.4.2.6. Epidermal ultra long chain sphingolipids

Ceramides are the main class of sphingolipids expressed in the mature CLE, as well as in the lipid lamellae of the SC. Although at least twelve major classes of ceramide species have been identified (Uchida and Hamanaka, 2006), the characterization of human SC ceramides by LC-ESI-MS/MS resulted in the identification of 342 ceramide species (Masukawa et al., 2008).

SC ceramides derived from sphingosine can be classified according to their acyl residue: *NS* for non-hydroxy-FA, *AS* for α-hydroxy-FA, *OS* for ω-hydroxy-FA, *POS* for ω-hydroxy-FA bound to protein and *EOS* for ω-hydroxy-FA esterified primarily to linoleic acid (Figure 13).

Sphingosine is not the exclusive LCB expressed in epidermal ceramides. In addition, phytosphingosine and 6-hydroxy-sphingosine are common LCBs found in human epidermis. The molecular diversity generated by the presence of various LCBs is further enhanced by mostly variations within the chain length of the acyl moieties and the hydroxylation of the sphingoid base and the acyl residue.

The ω-hydroxy-ceramides esterified with linoleate (EOS) are the most common SC ceramides. They contain primarily saturated or monounsaturated ULC-acyl moieties of 30 to 36 carbon atoms. In humans, the linoleate residue (18:2, ω-6) is the major FA linked to EOS, which contributes with 95% of total EOS. In contrast, mice epidermis contains 45% of linoleate esters linked to the ω-hydroxyl group (Uchida and Hamanaka, 2006). In essential fatty acid deficiency (EFAD) oleate (18:1, ω-9) residues have been shown to replace linoleate, with a consequent decrease in the epidermal permeability barrier (Melton et al., 1987).

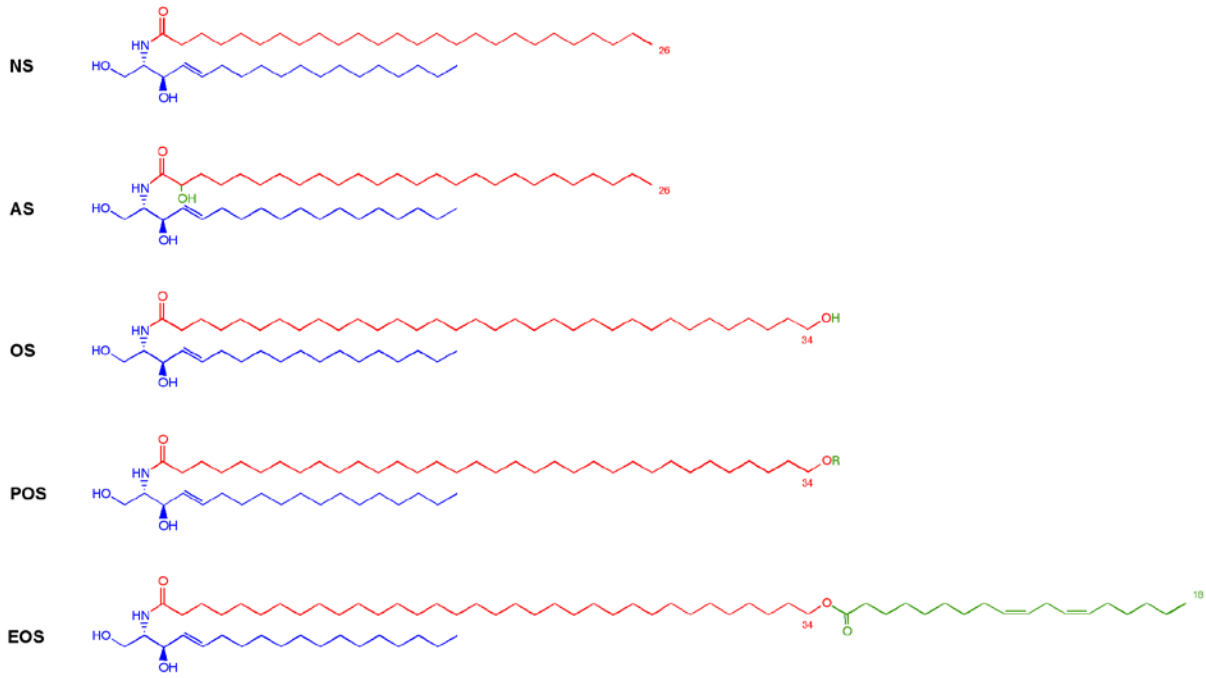

Figure 13. Major classes of epidermal ceramides.
Non-hydroxy and α-hydroxy-ceramides mainly contain acyl moieties with a carbon chain length up to 26 carbon atoms. The majority of ω-hydroxy-ceramides incorporate saturated or monounsaturated ULC-acyl residues ranging from 30 to 36 carbon atoms.

The biosynthesis of ω-hydroxy-ceramides esterified to carboxy residues of CE proteins (POS) is essential for epidermal barrier homeostasis. Likewise to EOS, these ceramide species mainly contain saturated or monounsaturated ULC-acyl moieties (Coderch et al., 2003). The precursor of both ceramide classes has been shown to be exclusively glucosylceramide (Uchida and Hamanaka, 2006). In contrast, non-hydroxy and α-hydroxy epidermal ceramides appear to be derived from SM species (Uchida et al., 2000). The acyl residues incorporated into NS and AS ceramides are mostly saturated and contain 16, 18, 24 or 26 carbon atoms in their acyl chains (Coderch et al., 2003), however they do not contain ULC-acyl moieties.

Although hydroxy fatty acids account for about 40% of SC ceramides, the enzyme(s) involved in the synthesis of α-hydroxy-Cers are not yet resolved. *In vitro* studies demonstrated that FA2H increased α-hydroxy-Cers levels upon keratinocyte

differentiation, however *in vivo* deletion of this gene did not exhibit obvious alterations of the permeability barrier suggesting another enzyme being involved in the biosynthesis of α-hydroxy-Cers (Hama, 2009; Meixner, 2009).

The multiple regulatory functions of ceramides in cell cycle, apoptosis and cellular differentiation have been demonstrated for various cell types, including keratinocytes (Geilen et al., 1997). In the epidermis, the essential role of ceramides in the formation and maintenance of the permeability barrier is currently being established. However, whether epidermal ceramides have a functional role in regulating keratinocyte differentiation and/or apoptosis is yet undetermined.

1.5. Hypothesis and aims

Complex glycosphingolipids and ceramides containing ULC-PUFA moieties were first described in mature mouse testis by Sandhoff et al. Interestingly, the neutral subset of this class of GSLs correlates with male fertility in mice. The functional role of these unconventional testicular sphingolipids has not been yet elucidated, however understanding the biosynthetic requirements of ULC-sphingolipids is a prerequisite in order to gain a deeper insight into their role in cellular functions.

ULC-acyl moieties are incorporated to sphingoid bases by a yet unidentified ceramide synthase homologue. Preliminary work demonstrated that CerS3 is strongly expressed in testis and skin, both being the only mammalian tissues containing ULC-sphingolipids (Sandhoff et al., unpublished data). Hence, we hypothesized that CerS3 might be involved in the synthesis of these ULC-ceramides, which are the common precursor for all complex ULC-glycosphingolipids.

To confirm the role of CerS3 or any other CerSs in the biosynthesis of ULC-sphingolipids, transcriptional analysis of the individual members of the CerS family will be performed to determine whether CerS3 or another CerS is coexpressed with testicular ULC-PUFA sphingolipids. For these studies, germ cell-stage specific and “germ cell-free” mice testes will be analyzed.

The identified CerS(s) responsible for catalyzing ULC-sphingolipid formation will be further characterized regarding their genetic structure, topology and subcellular localization.

To demonstrate the *in vitro* capacity for ULC-ceramide biosynthesis, the identified CerS(s) will be subjected to enzymatic assays. The substrate specificity of the corresponding CerS(s) towards ULC-CoAs in favor of LC- and VLC-CoAs will be determined. To carry out these enzymatic assays, living mammalian cells expressing CerS(s) with recombinant GFP proteins will be generated and supplemented with various acyl-CoAs including ULC-CoAs.

In parallel, the *in vivo* depletion of CerS3 is being established in our department. Mice carrying a genetic alteration of the CerS3 gene will provide a valuable tool to clarify the role of this enzyme in ULC-ceramide biosynthesis. In addition, this dysfunctional CerS3 mouse model will unveil new insights into the biological functions of its specific ceramide species in the skin and the testis.

2. Materials and methods

2.1. Materials

2.1.1. Chemicals

All reagents used in this study for routine analysis were obtained from the following commercial sources: Sigma, Carl Roth, Fluka, AppiChem, Gerbu and Merck. The grade of these chemicals were pure for analysis.

For cloning, restriction enzymes were obtained from Invitrogen and New England Biolabs (NEB). For synthesis of organic compounds, solvents and reagents were purchased from Fluka, except for coenzyme A obtained from American Radiolabelled Chemicals, dimethylketene methyl trimethylsilyl acetal and triethylamine from Sigma, and sphingosine (d17:1), which was acquired from Avati Polar Lipids. For ceramide synthase assay, activated fatty acids with coenzyme A with an acyl moiety ranging from 16 to 26 carbon atoms were also acquired from Avanti Polar Lipids. For cell culture, supplements were purchased from Invitrogen. All other chemicals were used and purchased as indicated in the corresponding sections.

2.1.2. Basic equipment

General consumables for molecular biology and cell culture were purchased from Eppendorf, Gilson, Greiner and BD Biosciences.

2.1.3. Buffers and solutions

All stock buffers and solutions were prepared using either Aqua ad injectabilia Braun or double distilled autoclaved water.

Solutions for molecular biology - I	
TAE buffer (50x) 2 M Tris/AcOH pH 8.0 0.1 M EDTA	**EB buffer** (1x) 10 mM Tris/HCl pH 8.5
Xylene cyanol loading buffer (10x) 0.001% xylene cyanol (w/v) 50% glycerol (v/v) 20mM Tris/HCl pH 7.5	**Crystal violet loading buffer** (10x) 0.02% crystal violet (w/v) 50% glycerol (v/v) in H_2O

Solutions for molecular biology - II	
TE buffer (1x) 10 mM Tris/HCl pH 8.0 1 mM EDTA	**Restriction digest buffer** [1] (1x) 50 mM Tris-HCl pH 8.0 10 mM $MgCl_2$ 100 mM NaCl
Ligation buffer [1] (5x) 250 mM Tris-HCl pH 7.6 50 mM $MgCl_2$ 5 mM ATP 5 mM DTT 25% polyethylene glycol-8000 (w/v)	**PCR buffer** [1] (10x) 200 mM Tris-HCl pH 8.8 100 mM KCl 100 mM $(NH_4)_2SO_4$ 20 mM $MgSO_4$ 1% Triton X-100 (w/v) 1 mg/ml nuclease-free BSA

Solutions for Western blot - I	
Hypotonic lysis buffer [1] (1x) 50 mM HEPES-NaOH 0.5 mM DTT 1x protease inhibitors mixture [2]	**Digitonin lysis buffer** [1] (1x) 20 mM HEPES-NaOH pH 7.4 25 mM KCl 250 mM sucrose 2 mM $MgCl_2$ 0.5 mM DTT 1x protease inhibitors mixture [2] 1% digitonin [2,3] (w/v)
Resolving gel buffer (8x) 3 M Tris-HCl pH 8.8 0.1% SDS (w/v)	**Stacking gel buffer** (4x) 0.5 M Tris-HCl pH 6.8 0.1% SDS (w/v)
Lämmli loading buffer [1] (4x) 40% glycerol (v/v) 0.02% bromophenol blue (w/v) 250 mM Tris pH 6.8 8% SDS (w/v) 0.4 M DTT	**Running buffer** (10x) 250 mM Tris 1.92 M glycine 1% SDS (w/v)
Transfer buffer (10x) 250 mM Tris 1.92 M glycine	**Transfer-MeOH buffer** [4,5] (1x) 1x transfer buffer 20% CH_3OH (v/v)

Solutions for Western blot - II	
PBS buffer (10x) 1.4 M NaCl 27 mM KCl 0.1 M Na_2HPO4 18 mM KH_2PO4 pH 6.8	**PBS-Tween® buffer** (1x) 1x PBS 0.1% Tween® 20 (v/v)
Ponceau red 0.5% Ponceau red (w/v) 1% AcOH (v/v)	**Blocking buffer** [4,5] (1x) 5% skimmed milk (w/v) in PBS-T

Solutions for affinity purification of an antibody	
Coupling buffer (1x) 0.5 M NaCl 0.2 M $NaHCO_3$ pH 8.3	**Acetate buffer** (1x) 0.1 M NaOAc 0.5 M NaCl pH 4.0
20 mM Natrium phoshate buffer (1x) 0.2 M NaH_2PO_4 x H_2O (stock A) 0.2 M Na_2HPO_4 x 7 H_2O (stock B) 28 ml stock A + 72 ml stock B + 900 ml H_2O pH 7.2	**Eluate solution-1** (1x) 70 mM glycine pH 2.7 0.6 mM phosphate buffer pH 2.7
Eluate solution-2 (1x) 100 mM glycine pH 2.0	**Eluate solution-3** (1x) 30% glycerol (v/v) in 10x PBS pH 11.7

Other buffers and solutions	
Thermolysin buffer [1] (500 µg/ml) 10 mM HEPES pH 7.4 142 mM NaCl 6.7 mM KCl 0.43 mM NaOH 1 mM $CaCl_2$	**Lowry complex reagent** [5] (1x) 2% Na_2CO_3 (w/v) in 0.1 M NaOH + 0.01% $CuSO_4$ in H_2O + 0.02% Na,K tartrate in H_2O
Citrate buffer (1x) 25 mM sodium citrate 0.5% *N*-laurylsacrosine (w/v) pH 7.5	**Guanidin thiocyanate buffer** (10x) 1x citrate buffer [6] + 4.23 M guanidin thiocyanate + 0.2 M 2-mercaptoethanol

[1] Store at – 20 ºC.
[2] Add freshly.
[3] Digitonin solution (10%) was prepared by dissolving the powder in boiling water and keeping the solution at 95 ºC for 10 min.
[4] Store at + 4 ºC.
[5] Freshly prepared.
[6] Freshly sterile filtered.

2.1.4. Plasmids

Name	**Gene of interest**	**Resistance**	**Size** (bp)	**Source**
pEGFP-N1	EGFP	Kan^r	4733	Clontech
hElovl2-EGFP – pReceiver-M03	human Elovl2	Amp^r	7190	Genecopoeia (EX-W1503-M03)
hElovl4-tGFP – pCMV6-AC-GFP	human Elovl4	Amp^r	7502	Origene (RG206248)
hCerS3 – pReceiver-M02	human CerS3	Amp^r	6913	Genecopoeia (EX-T7111-M02)
pRevTRE2-EGFP	MoMuLV-derived retroviral vector encoding EGFP	Amp^r	7198	Kindly provided by Prof. Dr. W. Nickel

2.1.5. Restriction endonucleases

Plasmid	**Restriction endonucleases**		**Company**
	5’ – prime	**3’ – prime**	
hCerS2-EGFP	HindIII	EcoRI	Invitrogen
hElovl2-EGFP	EcoRI	BamHI	Invitrogen
mCerS3-EGFP	EcoRI	BamHI	Invitrogen
pRevTRE2-mCerS3-EGFP	BamHI	AgeI	Invitrogen, NEB
pRevTRE2-hCerS3-EGFP	BamHI	AgeI	Invitrogen, NEB

2.1.6. DNA and protein ladders

Type of ladder	Range	Comapny
1 kb DNA ladder	506–12216 bp	Invitrogen
100 bp DNA ladder	100–2072 bp	Invitrogen
PageRuler™ plus prestained	10–250 kDa	Fermentas
Precision plus protein all blue standards	10–250 kDa	Bio-Rad Laboratories

2.1.7. Technical devices

Basic instrumentation used regularly in this study included incubator, oven, centrifuge, microwave, water bath, pH meter, autoclave and horizontal shaker. Other technical devices used are summarized in the following table:

Instrument	Company
Instruments used for molecular biology	
2720 Thermal cycler - PCR	Applied Biosystems
Avanti J-25 centrifuge	Beckman
GelDoc™ 2000 Gel Documentation System	Bio-Rad Laboratories
SM-30 Control rotary shaker	Neolab
Ultrospec 2000 UV/Visible Spectrophotometer	Pharmacia Biotech
Instruments used for cell biology	
Centrifuge 5417R and 5415C	Eppendorf
FACS Calibur	BD Biosciences
FACS Vantage Diva and FACS Aria I cell sorters	BD Biosciences
Instruments used for immunoblotting	
Mini-PROTEAN 3 Cell electrophoresis system	Bio-Rad
Sonifier 250	Branson
Sonorex Super RK 102H - Sonicator	Bandelin

Instruments used for lipid analysis	
Alpha 1-2 - lyophilizer	Christ
Evaporator	Liebisch
Linomat IV	Camag
Scanning densitometer CS-9301	Shimadzu
Varifuge 3.0 R	Heraeus Sepatech
VG micromass model Quattro II	Waters
Instruments used for RNA analysis	
2100 Bioanalyzer	Agilent Technologies
Glass-Col® grinder	Glass-Col®
Light Cycler® 2.0 system	Roche Diagnostics
Ultra Turrax® T25 basic	IKA Labortechnik
Instruments used for microscopic analysis	
Biorevo BZ-9000	Keyence
DTK 1000	DSK Microslicer
Leica CM 3050S	Leica
Leica DM-RBE microscope	Leica
Leica TCS-SL confocal scanning system, with microscope DMRE and Leica confocal software, Version 2.61	Leica
Leica Ultracut UCT	Leica
Leica Ultracut UCT equipped with a Leica EMFCS	Leica
Microm HM 340E	Thermo Scientific
Microm HM 355S	Microm
Zeiss EM 906E	Zeiss
Other instruments	
Tewameter TM300	Courage-Khazaka Electronics
Thermomixer comfort	Eppendorf

2.1.8. Cell lines

2.1.8.1. Bacterial and fungal strains

E. coli derived DH5α bacterial strain was used for most cloning procedures. Subcloning efficiency DH5α competent cells (Invitrogen, 18265-017) were used for regular subcloning experiments, whereas library efficiency DH5α competent cells (Invitrogen, 18263-012) were used for ligation reactions. Low copy number CopyCutter™ EPI400™ *E. coli* cells (Epicentre®, C400CH10) were used exclusively to enable the amplification of hElovl4-tGFP plasmid DNA.

To examine the vulnerability of CerS3$^{d/d}$ skin against microbial infections, *Candida albicans* (ATCC 90028) were used.

2.1.8.2. Eukaryotic cell lines

The following cell lines and clones were used in this study:

- HEK-293T: Human embryonic kidney 293 cells expressing SV40 large T-antigen. Provided by Prof. Dr. Walter Nickel.
- HeLa: Human cervix carcinoma derived cell line with epithelial-like morphology.
- HeLa$_{mCAT1\text{-}rtTA2\text{-}M2}$: Clone originated from HeLa cells stably transfected with mCAT1 (murine cationic aminoacid transporter 1), rtTA2-M2 (optimized reverse tetracycline-controlled transactivator), and a truncated version of CD2 (cluster of differentiation 2). This clone was kindly provided by Prof. Dr. Walter Nickel.
- HeLa$_{mCAT1\text{-}rtTA2\text{-}M2\text{-}hCerS3\text{-}eGFP}$: Clone originated from HeLa$_{mCAT1\text{-}rtTA2\text{-}M2}$ stably transfected with hCerS3-eGFP.
- HeLa$_{mCAT1\text{-}rtTA2\text{-}M2\text{-}mCerS3\text{-}eGFP}$: Clone originated from HeLa$_{mCAT1\text{-}rtTA2\text{-}M2}$ stably transfected with mCerS3-eGFP.
- HeLa$_{mCAT1\text{-}rtTA2\text{-}M2\text{-}eGFP}$: Clone originated from HeLa$_{mCAT1\text{-}rtTA2\text{-}M2}$ stably transfected with eGFP.
- K9: Immortalized cell line derived from murine primary Leydig cells.

2.1.9. Mouse lines

Mouse strain	Tissue analyzed	Source
C57/BL6	Brain, colon, liver, skin, testis	Charles River
$CerS2^{gt/gt}$	Skin	Kindly provided by K. Willecke
$CerS3^{d/d}$	Skin	Generated by R. Jennemann
$GM2AP^{-/-}$	Testis	Kindly provided by R.L. Proia
Kit^{W-v}/Kit^{W}	Testis	The Jackson Laboratory (stock number 100410)

2.1.10. Media

2.1.10.1. Media for bacterial culture

LB medium	**SOC medium**
1% tryptone (w/v)	2% tryptone (w/v)
0.5% yeast extract (w/v)	0.5% yeast extract (w/v)
1% NaCl (w/v)	10 mM NaCl
pH 7.0	2.5 mM KCl
	10 mM $MgCl_2$
	10 mM $MgSO_4$
	20 mM glucose

LB-agar medium for plates was prepared by adding 1.5% bacto-agar in LB medium. Growth media were autoclaved and supplemented with antibiotics for selective growth of bacteria carrying the plasmid with the adequate resistance. Antibiotics used in this study were ampicillin (100 µg/ml) or kanamycin (50 µg/ml).

2.1.10.2. Media for cell culture

RPMI growth medium [1,2]	**DMEM growth medium** [1,4]
1x RPMI 1640	1x DMEM
+ 10% FCS [3] (v/v)	+ 10% FCS [3] (v/v)
+ 2 mM L-glutamine	+ 2 mM L-glutamine
+ 10 mM HEPES	+ 100 U/ml penicillin
+ 50 U/ml penicillin	+ 100 µg/ml streptomycin
+ 50 µg/ml streptomycin	

DMEM growth medium [1,5]	**MBS-medium** [1]
1x DMEM + 15% FCS [3] (v/v) + 4 mM L-glutamine + 15 mM HEPES + 100 U/ml penicillin + 100 µg/ml streptomycin	DMEM + 7% modified bovine serum (w/v) + 25 µM chloroquine in PBS

[1] Stored at 4 ºC.

[2] For culture of HeLa cells.

[3] FCS was heat inactivated for 30 min at 56 ºC prior to be used as a supplement.

[4] For culture of HEK-293T cells.

[5] For culture of K9 Leydig cells.

Additional solutions used for cell culture were:

RPMI 1640 (1x) Roswell Park Memorial Institute medium (Sigma, R0883)

DMEM (1x) Dulbecco's modified Eagle's minimal essential medium (Lonza, BE12-604F)

D-PBS (1x) Duldecco's phosphate buffered saline (Sigma, D8537)

Trypsin (10x) 0.25% trypsin (Gentaur) + 0.5 mM EDTA

Trypan blue (1x) 0.4% trypan blue + 0.81% NaCl + 0.06% KH_2PO_4

2.1.11. Multi-component systems ("Kits")

Multi-component system	**Company**
Agilent RNA 6000 nano reagents	Agilent
ECL Western blotting analysis system	Amersham GE Healthcare
Light Cycler® FastStart DNA master SYBR green I	Roche Diagnostics
MBS mammalian transfection kit	Stratagene
pVPack vectors kit	Stratagene
Qiagen plasmid maxi kit	Qiagen
QIAprep spin miniprep kit	Qiagen
QIAquick gel extraction kit	Qiagen
QIAquick PCR purification kit	Qiagen
TURBO DNA-free™ kit	Ambion

2.1.12. Primers

2.1.12.1. Primers used for analytical polymerase chain reaction (PCR)

The tissue distribution of *Cers3* was analyzed with the following primers:

Gene		Primer sequence	T_a (ºC)	Product size (bp)
CerS3 – cDNA [1]	F	5' – TCT GGG AGG TTT GGA ATG AC – 3'	55	687
	R	5' – CGC CAC ATT GTG CTT CAA – 3'		
mGapdh	F	5' – ACT CCC ACT CTT CCA CCT TC – 3'	55	156
	R	5' – GGT CCA GGG TTT CTT ACT CC – 3'		

[1] To analyze *Cers3* expression 30 cycles of denaturation-annealing-elongation of the cDNA template were used.

2.1.12.2. Primers used for preparative PCR

The following primers were used to generate mammalian expression plasmids:

Plasmid		Primer sequence	T_1, T_2 (ºC) [1]	Product size (bp)
mCerS3-EGFP	F [2]	5' – ATG TTT CAG ACG TTT AGA AAA TGG TT – 3'	56	1171
	R [2]	5' – CGC CAC ATT GTG CTT CAA – 3'		
	F	5' – TAT ATA GAA TTC GCC ACC ATG TTT CAG ACG TTT AGA AAA TGG TTC TGG – 3'	56, 62	1181
	R	5'– TAT ATA GGA TCC GTA CGG CCA TGC TGA CCA TTG GCA ATG – 3'		
hCerS2-EGFP	F	5' – CAG GAT GCT CCA GAC CTT GT – 3'	53	1164
	R	5' – GCA GCT GGA ATA ATG GTT CA – 3'		
	F	5' – TAT ATA AAG CTT GCC ACC ATG CTC CAG ACC TTG TAT GAT TAC TT – 3'	54, 62	1171
	R	5' – TAT ATA GAA TTC GGT CAT TCT TAC GAT GGT TGT TAT TGA GGA TG – 3'		
hElovl2-EGFP	F	5' – TAT ATA GAA TTC GCC ACC ATG GAA CAT CTA AAG GCC TTT GAT GAT G – 3'	54, 63	920
	R	5' – TAT ATA GGA TCC GTT TGT GCT TTC TTG TTC ATC ACT CCA TTT – 3'		

Plasmid	Primer sequence		T_1, T_2 (ºC) [1]	Product size (bp)
pRevTRE2-mCerS3-EGFP	F	5' – TAT ATA GGA TCC GC CAC CAT GTT TCA GAC GTT TAG AAA ATG GTT CTG G – 3'	56, 66	1181
	R	5' – TAT ATA ACC GGT GTA CGG CCA TGC TGA CCA TTG GCA ATG – 3'		
pRevTRE2-hCerS3-EGFP	F	5' – TAT ATA GGA TCC GCC ACC ATG TTT TGG ACG TTT AAA GAA TGG TTC TGG – 3'	56, 66	1181
	R	5' – TAT ATA ACC GGT GTA TGG CCA TGC TGG CCA TTG GGA ATG – 3'		

[1] T_1 is the annealing temperature used for 10 cycles in order to bind the primer nucleotides complementary to the template cDNA. T_2 corresponds to the annealing temperature of the full-length primers including the overhang nucleotides and was used for an additional 15 cycles.
[2] F and R stands for forward and reverse primer, respectively.
Restriction sites are shown underlined.

2.1.12.3. Primers used for quantitative real time PCR (qRT-PCR)

The expression of ceramide synthase genes in testicular RNA was determined using the following primers:

Gene	Primer sequence		T_a (ºC)	Product size (bp)
mCers1	F	5' – TGA CTG GTC AGA TGC GTG A – 3'	55	93
	R	5' – TCA GTG GCT TCT CGG CTT T – 3'		
mCers2	F	5' – TCA TCA TCA CTC GGC TGG T – 3'	55	90
	R	5' – AGC CAA AGA AGG CAG GGT A – 3'		
mCers3	F	5' – ATC TCG AGC CCT TCT TCT CC – 3'	55	128
	R	5' – CTG GAC GTT CTG CGT GAA T – 3'		
mCers4	F	5' – TGC GCA TGC TCT ACA GTT TC – 3'	55	132
	R	5' – CTC GAG CCA TCC CAT TCT T – 3'		
mCers5	F	5' – TCC ATG CCA TCT GGT CCT A – 3'	55	147
	R	5' – TGC TGC CAG AGA GGT TGT T – 3'		
mCers6	F	5' – GGG TTG AAC TGC TTC TGG TC – 3'	55	138
	R	5' – TTT CTT CCC TGG AGG CTC T – 3'		

To study the mRNA expression levels of the ceramide synthase family in the skin of CerS3$^{-/-}$, the primers detailed above were used, with the exception of *CerS3*, where primers within exon 7 and 8 were used.

Gene	**Primer sequence**		**T_a** (ºC)	**Product size** (bp)
mCers3Δ7	F	5' – GGT CAC TGG TGT TTA GCC TGA – 3'	55	128
	R	5' – GGT CCC ACT GCG AAT GTA AT – 3'		

For the evaluation of expression levels of enzymes involved in fatty acid elongation and desaturation, the primers summarized as follows were used.

Gene	**Primer sequence**		**T_a** (ºC)	**Product size** (bp)
mElovl1	F	5' – GGT GGG GGA TAA AAA TTG CT – 3'	56	106
	R	5' – CCA AGG GCA GAC AAT CCA TA – 3'		
mElovl2	F	5' – GAC GCT GGT CAT CCT GTT CT – 3'	56	105
	R	5' – GCT TTG GGG AAA CCA TTC TT – 3'		
mElovl3	F	5' – TTT GCC ATC TAC ACG GAT GA – 3'	56	84
	R	5' – CGT GTC TCC CAG TTC AAC AA – 3'		
mElovl4	F	5' – GGG ATC ATA CAA CGC AGG AT – 3'	56	118
	R	5' – CTC AAC GCC TTT CGA TAC AA – 3'		
mElovl5	F	5' – CTC TCG GGT GGC TGT TCT T – 3'	56	98
	R	5' – AGA GGC CCC TTT CTT GTT GT – 3'		
mElovl6 [1]	F	5' – ACA ATG GAC CTG TCA GCA AA – 3'	60	119
	R	5' – GTA CCA GTG CAG GAA GAT CAG T – 3'		
mElovl7	F	5' – ATC GAG GAC TGT GCG TTT TT – 3'	60	81
	R	5' – GGC GAG GAC ATG AGG AGA TA – 3'		

[1] Primer sequence reported by (Wang et al., 2006).

The endogeneous *Cers* transcript levels of $HeLa_{mCAT1\text{-}rtTA2\text{-}M2}$ cells were examined with the following primers:

Gene	**Primer sequence**		**T_a** (°C)	**Product size** (bp)
hCers1	F	5' – TGC CTG ACA TCC CCT TCT AC – 3'	60	90
	R	5' – ACG CCA CGA TGT ACA GGA AC – 3'		
hCers2	F	5' – ACG CAG TGA CCG GGA AGA AAC AGA – 3'	64	150
	R	5' – TGG GAG GCA GCT GGA GTA ATG GTT – 3'		
hCers3	F	5' – TCT TGC AGG TCC TTC ACC TT – 3'	65	102
	R	5' – CCT CGT CAT CAC TCC TCA CA – 3'		
hCers4	F	5' – TTC AAC GGG CTT CTG ATG TT – 3'	60	97
	R	5' – CCA TCT GGC CCT TCT TCA T – 3'		
hCers5	F	5' – CCT AAT TGC ACG GAT TGC TT – 3'	63	109
	R	5' – TGT GCA GGT GGT CAC ATC TT – 3'		
hCers6	F	5' – TCA GCT GAT GCT CTT CTG GA – 3'	63	91
	R	5' – CCA CGG CAA ACA TAA CAA AC – 3'		

Primers used for the expression analysis of antimicrobial peptides:

Gene	**Primer sequence**		**T** (°C)	**Product size** (bp)
mBD1 / Defb1	F	5' – GGT GTT GGC ATT CTC ACA AGT C – 3'	60	99
	R	5' – GGT ATT AGA TGG GCA GCT GGA G – 3'		
mBD2 / Defb2	F	5' – TGC TGC CTC CTT TTC TCA TAT ACC A – 3'	60	78
	R	5' – GTG GTC AAG TTC TGC TTC GTA TC – 3'		
mBD3 / Defb3	F	5' – ATG CTG GAA TCG GTG CAT TGG CA – 3'	64	138
	R	5' – CTT CAT GGA GGA GCA AAT TCT GGT GT – 3'		
mBD4 [1] */ Defb4*	F	5' – CAC ATT TCT CCT GGT GCT GCT – 3'	64	52
	R	5' – GAT AAT TTG GGT AAA GGC TGC AA – 3'		
mCamp	F	5' – CTT CAA CCA GCA GTC CCT AGA CA – 3'	60	53
	R	5' – GAT CCA GGT CCA GGA GAC GGT A – 3'		

[1] BD4 primer sequence reported by (Dorschner et al., 2003).

For all experiments Gapdh was used to normalize the relative values of the target genes under the following conditions:

Gene	Primer sequence		T (ºC)[b]	Product size (bp)
mGapdh	F	5' – ACT CCC ACT CTT CCA CCT TC – 3'	55	156
	R	5' – GGT CCA GGG TTT CTT ACT CC – 3'		
hGapdh	F	5' – CAA CTA CAT GGT TTA CAT GTT C – 3'	60	181
	R	5' – GCC AGT GGA CTC CAC GAC – 3'		

2.1.12.4. Primers used for mouse genotyping

Gene	Primer sequence		T_a (ºC)	Product size (bp)
CerS3 – wt [1]	F	5' – ACA TAT CTC CCT TTG CCC TGA TG – 3'	58	315
	R	5' – ATA ATT GCA AGA GAC GGC AAT GA – 3'		
CerS3 – ko [1]	F	5' – ACA TAT CTC CCT TTG CCC TGA TG – 3'	58	272
	R	5' – GAC AGC CCT GAA ATG TAT CAT GC – 3'		
CerS3 – cDNA [2]	F	5' – TCT GGG AGG TTT GGA ATG AC – 3'	55	687 [3], 594 [4]
	R	5' – CGC CAC ATT GTG CTT CAA – 3'		

[1] Primers used for routine genotyping of CerS3$^{-/-}$ mice.
[2] Primers used for the analysis of CerS3 mutant transcript from skin cDNA.
[3] Product size for wild type CerS3 transcript.
[4] Product size for mutant CerS3 transcript lacking exon 7.

2.1.13. Antibodies

Primary Antibodies – I					
Antibody	**Host/ligand - Clonality**[1]	**Application**[2]	**Dilution**	**Supplier (Clone)**	**Order num.**
β-Actin	rabbit – p	WB	1:1000	Santa Cruz	sc-1616-R
F-Actin	TRITC-Phalloidin	Cryo SM	1:600	Sigma	P1951
Filaggrin	rabbit – p	WB	1:1000	Covance	PRB-417P
		Unfix. cryo	1:10		

Primary Antibodies – II					
Cathepsin D	rabbit – p	WB	1:500	DakoCytomation	A0561
		Cryo SM	1:100		
		Paraffin	1:100-200		
CerS3	rabbit – p	Cryo SM	1:500	PickCell Laboratories	Custom-made[3]
		Paraffin	1:1000		
Cholesterol	Filipin	Cryo SM	10 µg/ml	Sigma	F9765
		Unfix. cryo	10 µg/ml		
Cingulin	Guinea pig – p	Unfix. cryo	1:2000	Provided by L.Langbein	-
Claudin-1	rabbit – p	WB	1:100	Thermo Scientific	RB-9209
		Cryo SM	1:20		
		Unfix. cryo	1:10		
		Paraffin	1:20		
Dansyl[4]	rabbit – p	Unfix. cryo	1:100	Invitrogen	A6398
Desmoglein 1/2	mouse – m	WB	1:100	Progen (DG3.10)	61002
		Cryo SM	1:5		
		Paraffin	1:10		
Desmoplakin 1/2	mouse – m	WB	1:50	Progen (DP447)	651155
		Cryo SM	Undil.		
		Paraffin			
GFP	rabbit – p	WB	1:1000	Genetex	GTX26556
Golgin-97	mouse – m	ICC	1:200	Molecular Probes	A-21270
Involucrin	rabbit – p	WB	1:100	Thermo Scientific	RB-10288
		Cryo SM	1:150	Covance	PRB-140C
		Paraffin	1:100		
Kalilkrein 5	rabbit – p	WB	1:100	Abgent	AP6324b
Ki67	rat – m	Paraffin	1:200	Dako (TEC-3)	M7249
Lamp1	rabbit – p	ICC	1:200	Acris	SP5446P
Loricrin	rabbit – p	WB	1:1000	Covance	PRB-145P
		Cryo SM	1:150		
		Paraffin	1:100		
Lipids	nile red	Unfix. cryo	5 µg/ml	MP Biomedicals	151744
Ox-Phos Complex IV Subunit I	mouse – m	ICC	1:400	Molecular Probes	A6403

Primary Antibodies – III					
PDI	mouse – m	ICC	1:400	Acris	SM5075
Plakoglobin	mouse – m	WB	1:200	Progen (PG 5.1)	65105
Transgluta-minase 1	rabbit – p	WB	1:4000	Abcam	ab86589

[1] m: monoclonal, p: polyclonal

[2] Cryo SM: cryo-semithin sections; ICC: immunocytochemistry; Unfix. cryo: unfixed cryo-sections; WB: Western Blot.

[3]: Custom-made against a peptide located at the C-terminus of the mouse CerS3.

[4]: Against monodansylcadaverine for *in situ* transglutaminase 1 assay.

Secondary Antibodies					
Antibody	**Host/ligand**	**Application**[1]	**Dilution**	**Supplier**	**Order num.**
Alexa Fluor® 546 anti-rabbit	goat	ICC	1:400	Molecular Pobes	A11035
Alexa Fluor® 488 anti-guinea pig	goat	IHC	1:200	Molecular Pobes	A11073
Biotinylated anti-rat	Rabbit	Paraffin	1:200	Vector Laboratories	BA-4001
Cy3™- anti-mouse	donkey	ICC / IHC	1:200 / 1:1000	Jackson Dianova	715-165-150
Cy3™- anti-rabbit	donkey	IHC	1:1000	Jackson Dianova	711-165-152
Mouse-HRP	goat	WB	1:1000	Santa Cruz	sc-2005
Rabbit-HRP	goat	WB	1:1000	Santa Cruz	sc-2004

[1] ICC: immunocytochemistry; IHC: immunohistochemistry; WB: Western Blot

2.2. Methods

2.2.1. Cloning and molecular biology

2.2.1.1. Directional cloning

For the generation of mammalian expression plasmids, cDNA from mouse or human biopsies (*e.g.* testis for CerS3 or kidney for CerS2) provided the DNA template used for the amplification of the gene of interest by means of PCR. Primers used for enhancing the target gene coincided with the beginning of the 5' prime cDNA sequence (including the starting codon) as the forward primer, and the 3' prime cDNA sequence (without terminal codon) as the reverse primer. Directional cloning of the amplified fragment DNA containing the gene of interest was achieved by inserting overhangs via a second PCR amplification that will be able to create *cohesive ends* upon restriction endonuclease digestion (Figure 14).

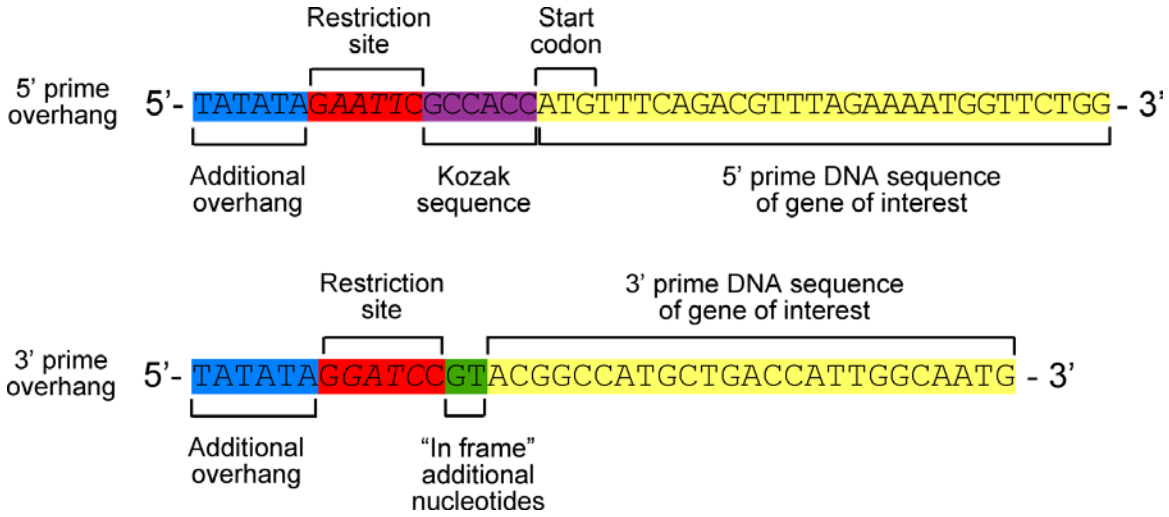

Figure 14. Strategy design for cloning in frame.
Forward primer included an additional overhang sequence, an adequate restriction site for the insertion into the target vector, the Kozak sequence, and the beginning of the 5' prime cDNA sequence of the gene of interest. Contrarily, reverse primer lacked the Kozak consensus, and instead two additional nucleotides were inserted. These nucleotides were required for having the protein product in frame with its C-terminal tag. CerS3 overhang primers serve as an example for cloning in frame into an EGFP encoding vector.

Oligonucleotide linkers used for the generation of overhang termini primarily contained the specific recognition sites for endonucleases with some additional overhang nucleotides required for many restriction enzymes to efficiently cleave DNA. The Kozak consensus sequence was additionally inserted prior to the starting codon to favour translation of the engineered protein. For generating fusion proteins with tagged vectors (*e.g.* EGFP and HA), care was taken that the C-terminus of the protein of interest was in frame with the following tagged encoding sequence.

Once the PCR product containing the restriction sites was generated and purified, enzymatic digestion with endonucleases was performed in parallel with vector DNA, thus generating unpaired nucleotide termini of both insert and vector DNA. The cohesive end termini of insert and vector DNA could then be ligated, and subsequently transformed into competent bacteria for DNA amplification.

Afterwards, plasmid DNA was isolated and analyzed by agarose electrophoresis and nucleotide sequencing. One single clone carrying the gene of interest was then retransformed in bacteria, which was grown in a large volume of culture medium to obtain stocks of plasmid DNA. The complete cloning strategy is detailed in Figure 15.

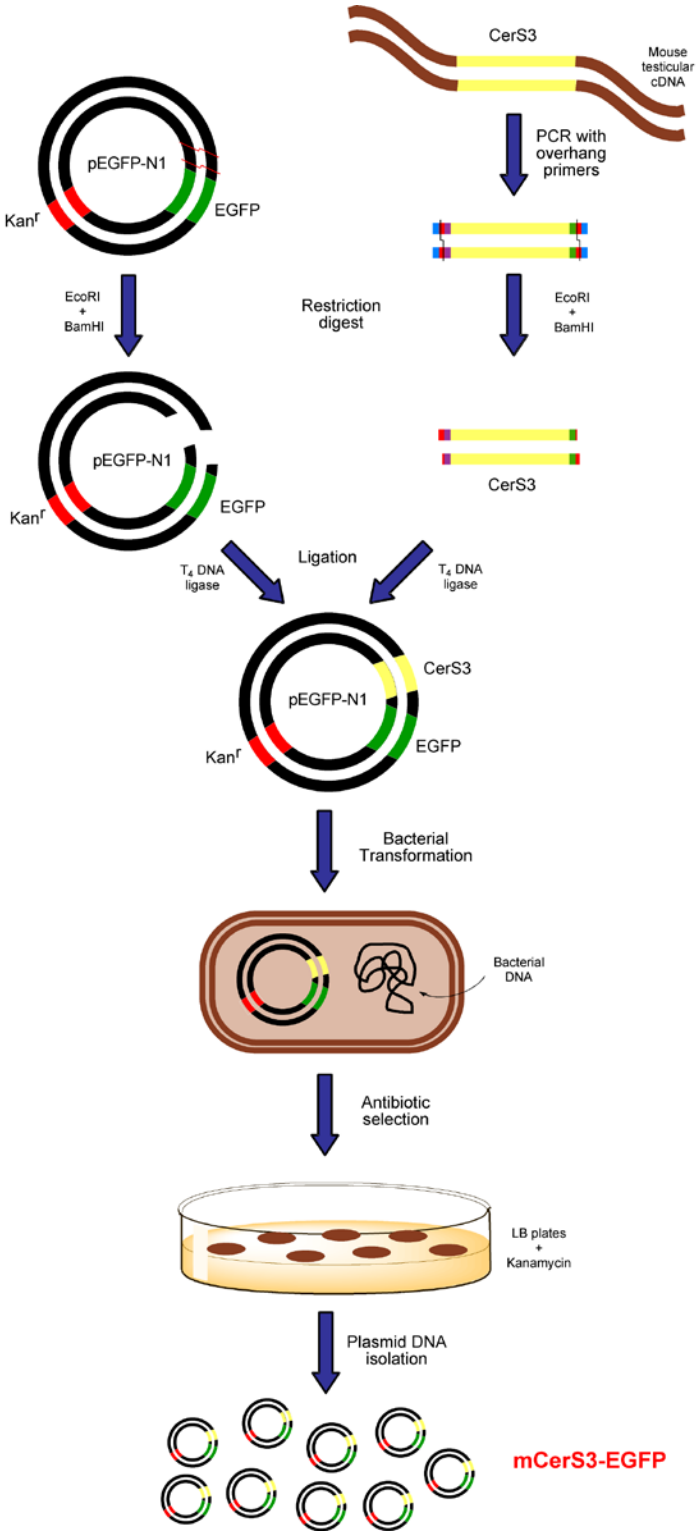

Figure 15. Directional cloning of a DNA fragment into vector DNA.
Generation of mCerS3-EGFP serves as an example for directional cloning. Mouse CerS3 flanked with EcoRI and BamHI sites was inserted into pEGFP-N1 vector, and transformed into competent bacteria.

Following this procedure, mCerS3-EGFP and hCerS2-EGFP were generated by inserting the corresponding cDNAs into the *N*-terminus of the pEGFP-N1 vector. For CerS3, EcoRI and BamHI sites were introduced to the amplified 1.2 kbp DNA template using overhang primers with these unique restriction sites. Similarly, full-length *CerS2* cDNA was cloned into pEGFP-N1 by HindIII/EcoRI sites. Additionally, hElovl2 encoding plasmid was subcloned into pEGFP-N1 via the EcoRI and BamHI sites.

For retroviral transduction, mCerS3-EGFP and hCerS3 plasmids were further subcloned into pRevTRE2-EGFP. Both genes were inserted using primers flanked with BamHI and AgeI sites.

The sequences of all constructs were verified by nucleotide sequencing. DNA sequencing was performed by the sequencing laboratory of the DKFZ.

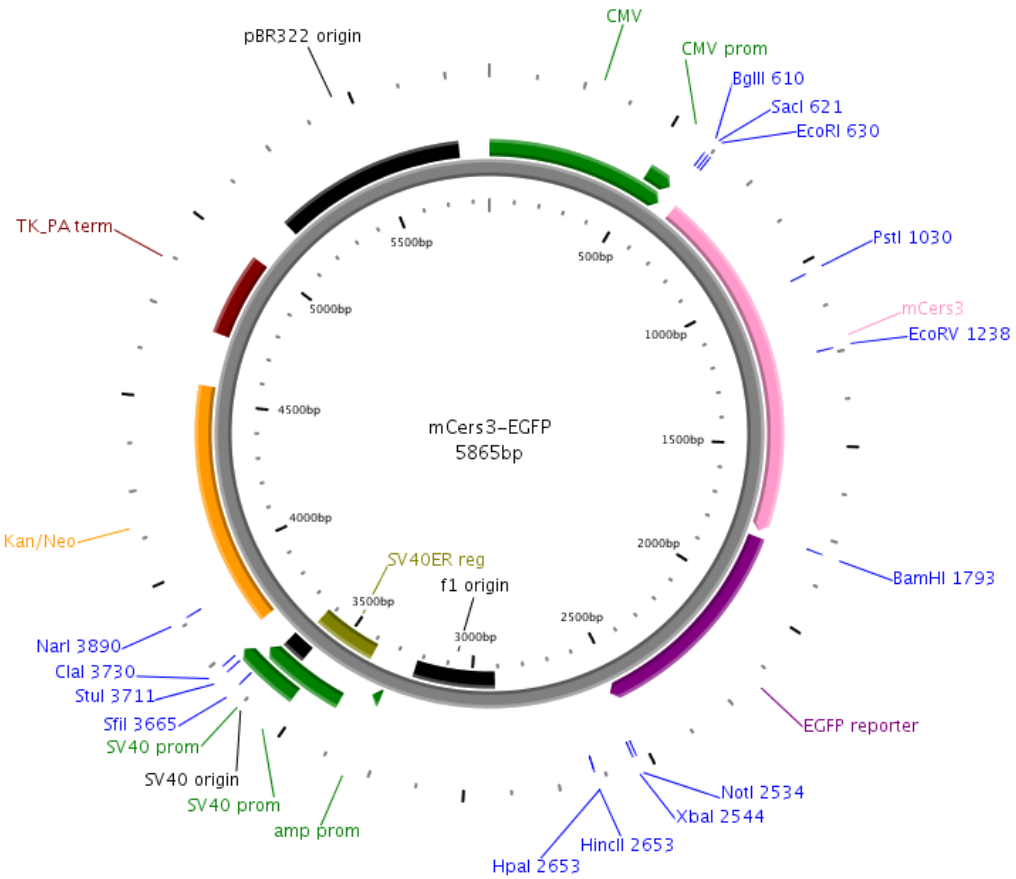

Figure 16. Plasmid map from generated mCerS3-EGFP.
CerS3 was inserted at the N-terminus of an enhanced GFP tag plasmid via the EcoRI-BamHI restriction sites.

2.2.1.2. Polymerase chain reaction (PCR)

PCR were performed to amplify specific DNA fragments containing the gene of interest from cDNA templates, as well as to introduce overhangs containing specific restriction sites that will generate “sticky ends” via endonuclease digestion, as described above.

For cloning, four PCR reactions performed in a final volume of 50 µl were combined in order to obtain larger amounts of DNA. All PCR products were generated using proofreading *Pfu* DNA polymerase (Promega). The general protocol used for preparative PCR was the following:

PCR reaction (50 µl):	
Buffer with 20 mM Mg^{2+}(10x)	5 µl
$MgCl_2$ (25 mM)	0–3 µl
dNTP mix (10 mM each)	1 µl
Forward primer (15 µM)	1 µl
Reverse primer (15 µM)	1 µl
cDNA template	10 pg–1 µg
Pfu DNA polymerase (3u/µl)	0.25 µl
H_2O	up to 50 µl

PCR program	T (ºC)	time
1. Denaturation	95	2 min
2. Denaturation	95	15–30 s
3. Annealing	T_1,T_2	30 s
4. Elongation	72	2min/1kbp
(Steps 2 to 4 are repeated for 10 cycles with T_1 and 15 cycles with T_2)		
5. Final elongation	72	5 min
6. Cooling	4	∞

The annealing temperature (T_a) was determined by the primer pair of each reaction, according to the length and the guanine/cytosine content of the oligonucleotides. For preparative PCR using overhang primers, two different annealing temperatures were used. The T_a used for the first 10 cycles (T_1) allowed the binding of the nucleotides complementary to the template cDNA. T_2 was used for an additional 15 cycles and corresponded to the annealing temperature of the full-length primers including the overhang nucleotides. For analytical PCR using primers complementary to the DNA template, 35 cycles were run with an adequate T_a.

The primer sequence and annealing temperatures used to generate DNA fragments by analytical and preparative PCRs are detailed in section 2.1.12.1. and 2.1.12.2, respectively.

2.2.1.3. Purification of PCR products

DNA fragments generated by PCR were purified using the QIAquick PCR purification kit following the manufacturer's recommendations. This purification method is based on the adsorption of DNA to a silica membrane, which takes place in the presence of high salt concentrations, achieved by mixing the DNA with a binding buffer. Oligonucleotides (up to 40 bp), enzymes and other impurities do not bind to the membrane allowing the decontamination of the DNA. An additional washing step with an ethanol-based buffer is able to remove the additional salts. For all applications, DNA was eluted from the silica-based columns with 50 µl of provided EB buffer.

2.2.1.4. Electrophoretic separation of DNA fragments by agarose gels

DNA fragments were separated in agarose gels by electrophoresis using TAE buffer (1x). For small fragments (50 to 500 bp) agarose gels of 2% were used, while for the separation of larger fragments (0.5 to 10 kbp) lower percentage gels were preferred (0.8–1.5%). Gels were prepared by dissolving the agarose in TAE buffer with the help of a microwave oven. To visualize DNA fragments, ethidium bromide (final concentration 1 µg/ml) was added to the cooled solution, before being poured into the gel chamber. Xylene cyanol loading buffer (10x) with glycerol was added to the DNA samples before being electrophoresed at 80–120 V. In order to estimate the size of the DNA fragments, DNA ladder of either 100 bp or 1000 bp were loaded in parallel with DNA samples. Bands corresponding to the DNA fragments were visualized and documented with GelDoc^{TM} 2000 Gel Documentation System.

2.2.1.5 *Digestion of DNA by restriction endonucleases*

Plasmid DNA and fragment DNA containing the gene of interest (insert) were digested in parallel with sequence specific endonucleases in order to create "sticky ends". The enzymatic reaction was performed overnight at 37 ºC (optimal temperature for all enzymes used) to assure the complete cleavage of the DNA. A control digestion with plasmid DNA lacking restriction enzyme was performed in order to distinguish between linearized and circular plasmid DNA, and to confirm the complete linearization of the digested plasmid in further analysis with agarose gels.

The restriction digest was performed as follows:

Restriction digest (70 µl):	
Assay buffer (10x)	7 µl
Plasmid DNA / Insert DNA	~ 3–5 µg / whole purified PCR product
Restriction enzyme (5–10 U/µl)	5 µl
H_2O	up to 70 µl

The cloning strategy was designed to insert the DNA encoding for the gene of interest into the plasmid with two different restriction sites, in order to have the insertion of the fragment in the correct direction. Therefore, two restriction enzymatic reactions were necessary. After the first digest, an aliquot was analyzed by agarose electrophoresis to assure the complete linearization of the plasmid DNA, and subsequently the DNA was purified with QIAquick PCR purification kit. Following, the second restriction digest was performed, and the plasmid and insert DNA containing the "sticky ends" were purified by extracting the bands from agarose gels (described below). Thus, traces of circular plasmid DNA that could still be present were removed due to the different mobility with the linear conformation during gel electrophoresis.
The restriction endonucleases used for the generation of each expression plasmid are summarized in section 2.1.5.

2.2.1.6. Extraction of DNA fragments from agarose gels

For purification of DNA fragments carrying "sticky ends", extraction of the DNA from agarose gels with crystal violet dye were preferred. Crystal violet (final concentration 1.5 µg/ml) in TAE buffer (1x) was used instead of ethidium bromide, thus DNA bands could be visualized without being exposed to ultraviolet light, which might produce DNA damage or release of the single stranded nucleotides of the "sticky ends". After electrophoresis, DNA fragments were excised from the gels, and extraction was performed using QIAquick gel extraction kit according to the instructions of the manufacturer. This purification method shares the same principle as the QIAquick PCR purification kit (see section 2.2.1.3.). DNA was eluted with 50 µl EB buffer.

2.2.1.7. Ligation of DNA fragments

Plasmid and insert DNA with complementary "sticky ends" were enzymatically ligated with T4 DNA ligase, which binds the 5'-phosphate end of one nucleotide (or DNA fragment) with the 3'-hydroxyl end of the other nucleotide (or the other DNA fragment) by a phosphodiester linkage. All ligation reactions were performed overnight at 16 ºC with a final volume of 20 µl and using 5 units of ligase. In general, the following protocol was used:

Ligation reaction (20 µl):	
Ligation buffer (5x)	4 µl
Plasmid DNA	3–30 fmol
Insert DNA	9–90 fmol
T4 DNA ligase (5 U/µl)	1 µl
H_2O	up to 20 µl

For a successful ligation, a molar ratio of 3:1 insert to plasmid was used. Two control ligations were performed in parallel, one lacking DNA ligase and a second lacking insert DNA. The amount of bacterial colonies after transformation with these negative controls indicated the success of the cloning procedure.

2.2.1.8. Bacteria culture and storage

E. coli-DH5α competent bacteria (either subcloning or library efficiency) were used for cloning procedures. Transformed bacteria were grown in LB medium (Luria-Bertani broth or Lysogeny broth) with constant shaking (225 rpm) or in LB plates, at 37 ºC with the required antibiotics.

Competent bacterial cells were frozen with a mixture of dry ice/ethanol and stored at – 80 ºC.

2.2.1.9. Bacterial transformation with plasmid DNA

For the transformation of *E. coli* with DNA from ligation reactions, library efficient DH5α competent cells were used. Cells were thawed on ice and a 100 µl aliquot of bacteria for each ligation was transferred into 14 ml snap-cap polypropylene tubes (Falcon 2059). Following manufacturer's recommendations, ligated DNA was diluted 1:5 with TE buffer, and 1 µl of the dilution was homogeneously dispensed in the

bacteria. Gentle tapping proceeded, and subsequently bacteria were incubated on ice for 30 min. Bacterial transformation was achieved by heat-shock for 45 s in a water bath kept at 42 ºC. After 2 min on ice, transformed bacteria were allowed to grow in 900 µl of SOC medium with a constant shaking of 225 rpm at 37 ºC for 1 h. Various dilutions (non, 1:10 and 1:100) of the bacterial culture were plated onto selective LB-agar plates and incubated overnight at 37 ºC.

For subcloning of plasmid DNA, generally subcloning efficiency DH5α were used. However, the amplification of hElov4-tGFP plasmid DNA required the usage of low copy number CopyCutter™ EPI400™ *E. coli* due to DNA instability in DH5α cells. A slightly modified protocol was followed according to the instructions of the manufacturer.

2.2.1.10. Extraction of plasmid DNA from bacteria – "Mini-preparation"

To analyze which bacterial colonies grown in LB plates were successfully transformed with the plasmid encoding the gene of interest, DNA from ten colonies was extracted. Plasmid DNA was isolated using the QIAprep spin miniprep kit following the instructions of the manufacturer. Briefly, a single bacterial colony after overnight growth in selective LB-agar plates was inoculated in LB medium (4 ml) with the adequate antibiotic: ampicillin (100 µg/ml) or kanamycin (50 µg/ml). *E. coli*-DH5α cells were grown overnight at 37 ºC and 225 rpm in a rotary-shaker (SM-30 Control). Snap-cap polypropylene tubes (Falcon 2059) were used for the bacterial culture, allowing exchange of oxygen during the incubation time. Cells were harvested by centrifugation at 8000 rpm for 3 min using a table-top microcentrifuge. Subsequently, bacterial cells were resuspended and lysed using a modified alkaline lysis method. After neutralization with a high salt concentration buffer, plasmid DNA was cleared of genomic DNA, proteins, cell debris and others by centrifugation at 13,000 rpm. The lysate containing the plasmid DNA was then ready to bind to a silica-based membrane. Several washing steps proceeded to remove salts and other contaminants. Finally, purified plasmid DNA was eluted from the silica membrane column with 50 µl of EB buffer. All steps required for the extraction were performed at room temperature.

To evaluate which of the colonies carried the plasmid with the correct insertion of the DNA fragment, analytical restriction digestions (1h, 37 ºC) were performed and analyzed by agarose gel electrophoresis. Plasmid DNA with the correct size of cleaved fragments after analytical restriction digest was analyzed by nucleotide sequencing in order to assure that no mutation occurred during the cloning process.

2.2.1.11. Extraction of plasmid DNA from bacteria – "Maxi-preparation"

For purification of larger amounts of plasmid DNA, the Qiagen plasmid maxi kit was used. This DNA preparation was performed once the accuracy of the plasmid sequence was confirmed. Generally, 1 µl of plasmid DNA (from mini-preparation) was retransformed into *E. coli*-DH5α cells, as described in section 2.2.1.9. After transformation, the approximately 1 ml SOC medium containing the transformed bacteria was diluted 1:200 with selective LB medium, and incubated overnight at 37 ºC under constant shaking. Bacterial cells were then harvested by centrifugation at 6000 $\times$ *g* using an Avanti J-25 centrifuge (Beckman). DNA extraction proceeded following the instructions provided. In general, cells were resuspended, lysed according to a modified alkaline lysis method, and finally neutralized. Proteins, genomic DNA and other impurities were cleared by centrifugation at 20,000 $\times$ *g*. Differing from mini-preparation, plasmid DNA in low salt conditions was allowed to bind to an anion-exchange resin column. Sequentially, DNA was washed and eluted from the columns using a high-salt concentration buffer. Isopropanol precipitation of the DNA allowed the removal of the salts and concentration of DNA into a pellet, which was further washed and finally dissolved in a suitable volume of water or EB buffer.

2.2.1.12. Determination of nucleic acid concentration (DNA and RNA)

Nucleic acid concentration was determined according to the amount of light absorbed when exposed to ultraviolet light at a wavelength of 260 nm. The absorbance (A) of analyzed samples was measured with Ultrospec 2000 photometer (Pharmacia Biotech). Concentration could be calculated according to the Lambert-Beer's law, taking into account that the extinction coefficients for double-stranded DNA and single-stranded DNA/RNA are 0.020 and 0.027 $(\mu g/ml)^{-1}cm^{-1}$, respectively. Integrity

assessment of analyzed samples was determined by the ratio of absorbance at A_{260nm} vs A_{280nm}, the latter corresponding to the wavelength at which proteins absorb light. The optimal $A_{260/280}$ ratio for pure DNA is approximately 1.8, while for pure RNA is ~ 2.

2.2.2. Cell culture and transfection

2.2.2.1. Culture of eukaryotic cells

HeLa cells were grown in RPMI-1640 medium (Sigma, R0883) supplemented with 10% inactivated fetal calf serum, 2 mM L-glutamine, 10 mM HEPES, with or without 50 U/ml pencillin and 50 µg/ml streptomycin. Instead, HEK-293T and K9 Leydig cells were cultured in DMEM growth culture media with supplements (see 2.1.10.2.). Cells were maintained in monolayer cultures in a humidified atmosphere of 5% CO_2 at 37 °C, and were subcultured twice a week with trypsin-EDTA (0.25% in PBS).

2.2.2.2. Freezing and thawing of eukaryotic cells

To create stocks, cells in growth phase were trypsinized and harvested at 1000 × *g* for 5 min. Cells were then resuspended in freezing media consisting of 90% FCS and 10% DMSO, transferred into cryotubes (Nalgene) and kept for long time storage at – 80 ºC.

For the repropagation of frozen cellular stocks, cryotubes were placed in a water bath at 37 ºC until cells were thawed. Cells in freezing media were directly diluted 1:12 with prewarmed growth medium in a 75 cm^2 tissue culture flask. After cellular attachment, medium was exchanged to remove residual DMSO. Cells were passaged at least once before being used for experiments.

2.2.2.3. Transfection of eukaryotic cells

Transient transfection of plasmid DNA into HeLa cells was achieved by means of lipofection. HeLa cells were seeded in 6-well plates either 24 or 48 h prior to transfection. Highly confluent cells (90–95%) were then transfected with the optimal amount of plasmid DNA (previously tested for each plasmid) using Lipofectamine™ 2000 reagent (Invitrogen) according to manufacturer's recommendations. Thus, plasmid DNA (4 µg) was complexed with transfection reagent with a ratio optimized

for each transfection in order to minimize cytotoxicity. DNA-cationic lipid complexes in serum-free RPMI medium were administered drop-wise to the cells, which were then incubated at 37 ºC for 4 h. Subsequently, medium was exchanged by growth medium with FCS. Analyses were performed genrally after 24 h of overexpression.

Transfection efficiencies were determined by flow cytometric analysis according to the fluorescence signals generated from the overexpression of EGFP fusion proteins.

For subcellular localization studies, HeLa cells (2.5×10^5) were transfected 24 h after seeding with mCerS3-EGFP and control pEGFP-N1 using Lipofectamine™ at a 1:2.5 ratio (µg DNA/µl Lipofectamine™). Double transfections with mCerS3-EGFP and either hEovl2-EGFP or hElovl4-tGFP were performed with 3:0.75 and 4:2 ratios, respectively. For ceramide synthase assays, $HeLa_{mCAT1\text{-}rtTA2\text{-}M2}$ cells (1×10^5) were seeded 48 h prior to transfection with hCerS2-EGFP and control EGFP with a ratio of 1:2.

2.2.2.4. Generation of stable cell lines

Stable cell lines expressing CerS3-EGFP (mouse and human), as well as EGFP (control), were generated by retroviral transduction using genetically modified HeLa cells ($HeLa_{mCAT1\text{-}rtTA2\text{-}M2}$). The infection of these cells in order to achieve inducible transgene expression of CerS3 required the production of viral particles in a packaging cell line, HEK-293T. These virions were generated via the triple transfection with 1) a MoMLV (Moloney murine leukemia virus) derived retroviral vector encoding the gene of interest from the doxycycline/transactivator responsive element (pRevTRE2-EGFP), together with 2) *gag-pol* (pVPack-GP) and 3) *envelope (*pVPack-Eco), the latter vectors are both responsible for the formation of the viral proteins. While the former encodes the *gag* and *pol* genes required for the synthesis of proteins of the core capsid and for the reverse transcriptase and integrase, the latter encodes the ecotropic viral envelope protein (limited to infection of murine hosts), which facilitates infection of the target $HeLa_{mCAT1\text{-}rtTA2\text{-}M2}$ cells by direct interaction with cell-type specific receptors (mCAT1). On the other hand, the non-replicating retroviral vector contains all the *cis* regulatory elements necessary for the transcription of CerS3, as well as an extended version of the viral packaging signal required for the viral CerS3 RNA transcript to be packaged into infectious virions.

Previous integration of mCAT1 (murine cationic aminoacid transporter 1) and the doxycycline-sensitive transactivator rtTA2-M2 (optimized reverse tetracycline-controlled transactivator) allowed the generation of inducible HeLa cells expressing the gene of interest, as already described (Engling et al., 2002). Thus, viral particles produced by HEK-293T cells enabled the infection of the modified HeLa cells expressing the murine receptor protein (mCAT1) required for the infection of the murine leukemia virus, and consequently enabled the stable integration of CerS3.

The expression of the gene of interest takes place under induction with doxycycline (dox), making use of the Tet-On inducible expression system. In this system, doxycycline is required for binding to the tetracycline-controlled transactivator (rtTA2-M2), expressed by the modified HeLa cells. This transcription factor binds to the tetracycline-responsive element (TRE), encoded in the MLV-retroviral vector and thereby activates the transcription of the downstream gene of interest, CerS3-EGFP.

CerS3-EGFP expressing cells were isolated by fluorescence-activated cell sorting (FACS) selecting for the EGFP-derived fluorescence. These populations were cultured for 7 days in the absence of doxycycline and then selected for negative fluorescence signals. Following an additional 7 days induction with doxycyline, single cell clones were sorted by EGFP-derived fluorescence. Three stable cell lines were generated following this procedure: *mCerS3* regarding $HeLa_{mCAT1\text{-}rtTA2\text{-}M2\text{-}mCerS3\text{-}eGFP}$, *hCerS3* for $HeLa_{mCAT1\text{-}rtTA2\text{-}M2\text{-}hCerS3\text{-}eGFP}$, and *control* for $HeLa_{mCAT1\text{-}rtTA2\text{-}M2\text{-}eGFP}$ expressing cells.

These cell lines were produced using the pVPack vectors and the transfection MBS mammalian transfection kit (Stratagene), following the instructions of the manufacturer.

2.2.2.4.1. Production of viral particles

Viral particles were produced by cotransfection of the plasmids encoding viral proteins together with the plasmid encoding the gene of interest. HEK-293T cells were used as a packaging cell line for producing the virions after transfection via the calcium phosphate method.

Plasmid DNA was prepared for transfection by mixing 1.5 µg of each of the required plasmids: the MLV plasmid encoding the gene of interest (pRevTRE2-mCerS3-EGFP, pRevTRE2-hCerS3-EGFP, or control pRevTRE2-EGFP), the pVPack-GP and pVPack-Eco. To this mixture, 1 ml ethanol (100%) and 100 µl NaOAc (3 M) were added, following 30 min incubation at – 80 ºC. Vector DNA was pelleted at 13,000 rpm in a cooled table-top centrifuge for 10 min, the supernatant was discarded and the DNA was washed once more with ethanol (70%). The DNA was collected at 13,000 rpm for 5 min, and the pellets were kept overnight at 4 ºC.

HEK-293T cells (~ 40% confluent) were seeded in growth medium 24 h prior to transfection. Shortly before transfection, growth medium was exchanged by MBS (modified bovine serum) containing DMEM medium. DNA was prepared for $Ca_3(PO_4)_2$ transfection by resuspending the air-dried pellet in 225 µl water supplemented with 25 µl solution I and 250 µl solution II of the MBS transfection kit. After 10 min incubation at room temperature, the DNA solution was added drop-wise to the cells and homogeneously distributed. Cells were incubated for 3 h at 37 ºC until transfection medium was exchanged by growth medium supplemented with 25 µM chloroquine. The use of chloroquine leads to reduced degradation of the DNA and thereby increasing the efficiency of the gene transfer. After an additional incubation for 6 h, medium was exchanged by growth medium without chloroquine and cells were incubated overnight. This medium was once more exchanged after 24 h by 2 ml of fresh growth medium and cells were then incubated at 37 ºC and 5% CO_2 for additional 48 h.

2.2.2.4.2. Retroviral transduction

$HeLa_{mCAT1\text{-}rtTA2\text{-}M2}$ cells expressing the murine surface receptor and the reverse tetracycline transactivator were seeded in 6-well plates 24 h before transduction.

Viral particles produced by HEK-293T cells and released into the medium for 48 h were collected with a syringe. About 50% of the supernatants (1 ml) were directly added to the target HeLa cells (~ 40% confluent) through a sterile 0.45 µm filter. Sequentially, DEAE-dextran solution (final concentration 10 µg/ml) was added and the cells were then transferred into an incubator at 37 ºC for 3 h. Subsequently, the medium was exchanged by growth medium and cells were incubated for 72 h.

Reagents and buffers required for retroviral transduction were provided by Prof. Dr. Walter Nickel of the Biochemie Zentrum der Universität Heidelberg (BZH) of University of Heidelberg.

2.2.2.4.2. Selection of clones by fluorescence-activated cell sorting (FACS)

$HeLa_{mCAT1\text{-}rtTA2\text{-}M2}$ cells transduced with CerS3 encoding retroviral particles were splitted and induced with 2 µg/ml doxycycline. Following 40 h incubation at 37 ºC, fluorescence positive cells were isolated using FACSVantage Diva cell sorter.

For sorting, cells were detached from the culture plates using a mild dissociation buffer consisting of PBS with 0.5 mM EDTA. Cells were then harvested, washed with chilled PBS, and resuspended in FACS buffer (PBS with 0.5 mM EDTA and 1.5% FCS). Prior to cell sorting, cell suspensions were directly filtered with a cell strainer placed in the cap of sterile polystyrene tubes (BD Falcon 352235).

Three cell lines expressing mCerS3-EGFP, hCerS3-EGFP and EGFP were obtained. These populations were cultured for an additional 7 days in the absence of doxycycline to turn off the transcription of the transgene. Sequentially, populations were selected for negative fluorescence signals. Following an additional 7 days induction with doxycycline, single cell clones were sorted by EGFP-derived fluorescence with FACSAria I cell sorter. Single clones were propagated and analyzed according to doxycycline response by flow cytometry.

Sorted cells were directly placed in growth medium containing antibiotics (50 U/mL penicillin, 50 µg/mL streptomycin and 50 µg/ml gentamycin), and immediately transferred into culture plates.

Sorting of the cells was performed by Dr. Steffen Schmitt and Klaus Hexel from the Flow Cytometry Core Facility of DKFZ.

2.2.2.5. Analysis of transfection rates by flow cytometry

Transient expression rates of transfected cells, as well as induced transgene expression of stable cell lines were analyzed by flow cytometry using FACSCalibur. Taking advantage of the expression of the gene of interest as a fusion protein with EGFP tags, transfection rates could be measured according to the fluorescence signal.

For analysis, cells were harvested and pelleted at 1000 × *g* in facs tubes (BD Falcon 352054). Supernatant was discarded and cell pellets were resuspended in chilled PBS. Cell suspensions were kept from light at 4 ºC until transfection rates were determined. Acquisition and analysis were performed using BD CellQuest Pro software.

2.2.3. Western blot

2.2.3.1. Preparation of total protein lysates

2.2.3.1.1. Eukaryotic cell culture lysates

Cells in culture were trypsinized and harvested at 106 × *g* for 5 min at 4 ºC. Cell pellets were then washed with chilled PBS and resuspended in hypotonic lysis buffer. After 30 min incubation on ice, cells were lysed by sonication (Sonorex Super RK 102H) at 35 Hz for 5 intervals of 30 s. Total protein lysates were cleared of both nuclei and cell debris by centrifugation at ~ 21,000 × *g* for 15 min. Supernatants were then transferred into a clean tube, and kept at – 80 ºC until further use.

2.2.3.1.2. Tissue biopsy lysates

Skin biopsies were incubated at 58 ºC for 6 min in PBS containing 10 mM EDTA in order to separate dermis from epidermis. Skin was then transferred into ice cold PBS-EDTA solution and epidermis was obtained by peeling off the dermis. Epidermis in digitonin lysis buffer was homogenized by sonication (Branson sonifier 250) using 5 pulses every 30 s for 5 min. Lysates containing epidermal proteins were cleared by centrifugation at ~ 21,000 × *g* for 15 min.

2.2.3.2. Determination of protein concentration by BRADFORD assay

Protein concentration in total lysates were determined according to the Bradford method (Bradford, 1976). This method is based on the shift of absorption of coomassie brilliant blue G-250 upon binding to proteins.

Briefly, protein-dye solutions were prepared by mixing either 2.5 or 5 µl of lysate with Bradford reagent up to 1 ml. To determine the protein concentration, a dilution series of BSA standards ranging from 0 to 10 µg/µl dissolved in Bradford reagent was prepared in parallel. The absorbance of protein-dye mixtures was measured at

the absorption maximum (595 nm), and the protein content was calculated by interpolating the absorbance measured from the BSA standard curve.

2.2.3.3. *SDS-polyacrylamide gel electrophoresis (SDS-PAGE)*

Proteins were separated according to their molecular weight in 7–10% SDS-polyacrylamide gels. To cast the discontinuous gels, the solutions for the resolving and the stacking gel were prepared as indicated below. The resolving gel was then poured between glass plates separated by 1.5 mm and was allowed to polymerize for about 30 min. On top a stacking gel of 3.45% polyacrylamide was poured, and a comb was placed to create wells. Polymerization of the stacking gel was terminated at 4 ºC. The composition of the stacking and resolving gels used in this study was the following:

Stacking gel	
	3.45%
4x Stacking gel buffer	1.875 ml
30% Acrylamide/ bisacrylamide[1]	862.5 µl
10% APS[2]	56.25 µl
TEMED	15 µl
H_2O	4.76 ml

Resolving gel		
	7%	10%
8x Resolving gel buffer	1.875 ml	1.875 ml
30% Acrylamide/ bisacrylamide	3.5 ml	5.0 ml
10% APS	150 µl	150 µl
TEMED	9.9 µl	9.9 µl
H_2O	9.47 ml	8.0 ml

[1] Rotiferase gel 30, 37.5:1 (Carl Roth)

[2] Ammonium persulfate (APS) is a radical initiator that triggers the polymerization of the gels, therefore it is added shortly before the gels are poured.

Protein samples were denatured prior to electrophoresis by the addition of 4x Lämmli buffer containing 8% SDS and sequentially incubated at 95 ºC for 5 min. Equal amounts of protein (50 µg) were electrophoresed at ~ 35 mA during the separation in the stacking gel and at ~ 45 mA in the resolving gel.

2.2.3.4. Immunoblotting

After electrophoresis, proteins were transferred onto nitrocellulose membranes. For transfer, 0.45 µm membranes were placed on gels and covered with 3 pieces of Whatmann paper and a sponge on each side. These stacks were assembled in a bath of chilled transfer buffer (1x) containing methanol. Electrotransfer of proteins to the membranes were carried out at ~ 170 mA for 4 h on ice. Subsequently, membranes were stained with Ponceau red to assess the quality of the transfer, the equality of the loading of the SDS-PAGE and to indicate the position of the lanes in case that cutting the membranes was required. Following the transfer, membranes were blocked generally with 5% skimmed milk in PBS-Tween®. Blocking was performed at room temperature for 1 h. Afterwards, membranes were incubated with primary antibodies in 3% skimmed milk-PBS-Tween®. Binding of primary antibodies was carried out under constant rotation overnight at 4 ºC. On the following day, unbound antibodies were washed from the membranes 3 times with PBS-Tween® for 10 min. Coupling of HRP-conjugated secondary antibodies was performed at r.t. for 45–60 min. Then, membranes were washed 3 more times for 10 min each with PBS-Tween®. The working dilutions of primary and secondary antibodies used in this study are listed in the table of section 2.1.13. Finally, proteins were detected by enhanced chemiluminescence using an ECL-detection kit (Amersham GE Healthcare) following the instructions of the manufacturer.

2.2.3.5. Purification of antibodies by affinity column chromatography

Polyclonal CerS3 antibody against the mouse protein was generated by PickCell Laboratories. Thus, a synthethic peptide against our self-designed epitope (CGGKETEYLKNGLGTNRHLIANGQHGR) located at the *C*-terminus was used to immunize rabbits. Serum containing the polyclonal antibody was purified by affinity chromatography using the peptide coupled to *N*-hydroxysuccinimide (NHS)-activated sepharose.

For the coupling, 500 µl of sepharose beads preactivated with NHS were loaded into a polypropylene column (Thermo Scientific, 29922), where solvent was drained and beads were washed with 10 ml of 1 mM HCl. Subsequently, sepharose beads were preconditioned with 5 ml coupling buffer (0.2 M $NaHCO_3$, 0.5 M NaCl, pH 8.3),

prior to be transferred with 1 ml of coupling buffer into an eppendorf tube. Beads were then pelleted and mixed with the peptide (3.7 mg) freshly dissolved in 500 µl coupling buffer. The coupling reaction was performed overnight at 4 ºC with constant rotation. After completion of the coupling, non-reacted groups were blocked with 0.2 M glycine pH 8.0 for 2–3 h at 4 ºC. Afterwards, the sepharose beads were transferred back into the column and washed first with 3 ml of 0.1 M Tris-HCl buffer (pH 9.0), followed by washing with 3 ml of 0.1 M NaOAc with 0.5 M NaCl buffer (pH 4.0). These buffers were alternated to wash two more times the sepharose beads. The column containing the peptide-sepharose beads was stored at 4 ºC until further used in 2 ml PBS containing 0.05% NaN_3 to prevent microbial contamination.

To affinity purify the serum containing polyclonal antibodies, serum was diluted 1:2 with PBS and pelleted down to remove unsoluble particles. Subsequently, peptide-sepharose beads were incubated with the serum in a 50 ml Falcon tube maintaining constant rotation overnight at 4 ºC. Afterwards, the beads were transferred into a polypropyene column where the solvent was eluted. Sepharose beads were washed with 20 mM natrium phosphate buffer (10 ml), and the purified antibody was eluted with a low pH glycine buffer in phosphate buffer (pH 2.7) directly into 175 µl of 1.5 M Tris-HCl (pH 8.8). Sequentially, the beads were washed with another 10 ml of phosphate buffer. The “washing-eluates” were collected, pooled and incubated overnight at 4 ºC with the peptide-sepharose beads. Afterwards, beads were transferred once more into the column, washed with phosphate buffer and eluted with glycine buffer. Both glycine eluates were collected, pooled and concentrated using an Amicon Ultra 15 centrifugal device (Millipore, UFC 9 030 08) at 4000 $\times$ *g* for 20 min.

In addition, CerS3 antibody was eluted from the column with a pH 2.0 glycine buffer directly into 700 µl of 1.5 M Tris-HCl pH 8.8. Following the washing of the column with 10 ml of phosphate buffer, the rest of the CerS3 antibody was eluted with 30% glycerol in 10x PBS into 700 µl of 1.5 M Tris-HCl pH 6.8.

Each of the three eluates were concentrated and washed twice with PBS. The purified antibody concentration was determined by absorbance at 320 nm. If the concentration was lower than 1 mg/ml, BSA was used to stabilize the solution. The eluate corresponding to the glycine buffer pH 2.7 exhibited the highest

concentrations. Aliquots were prepared from the purified CerS3 antibody solutions and stored at – 20 ºC and at 4 ºC. The latter aliquots contained 0.05% NaN_3.

All solutions used during this procedure were used chilled at 0–4 ºC and were sterile filtered.

2.2.4. Chemical synthesis of organic compounds

2.2.4.1. Synthesis of ultra long chain acyl-CoAs (ULC-Acyl-CoAs)

For the synthesis of montanoyl-CoA (28:0) and melissoyl-CoA (30:0), fatty acids (100 µmol) were dissolved in dry tetrahydrofuran (THF, 4 ml). Equimolar amounts of *N*-hydroxysuccinimide and dicyclohexylcarbodiimide were added at room temperature and the reaction was kept under nitrogen for 12 h.

The activated fatty acids were coupled to the polysilylated form of coenzyme A, which was generated *in situ* as described (Lucet-Levannier et al., 1995). Thus, the trilithium salt of coenzyme A was passed through a Dowex-50 ion exchange column acidified with 1 M HCl and subsequently lyophilized. The resulting free CoA (26 µmol) was dissolved in dry acetonitrile (2 ml). Dimethylketene methyl trimethylsilyl acetal (650 µmol) was added and the resulting solution was stirred for 16 h under nitrogen. After removal of all volatiles using a nitrogen stream, the polysilylated coenzyme A was dissolved in 1 ml dry THF.

To a stirred solution of activated fatty acid (39 µmol) in THF containing CsF (1.3 mmol) and dicyclohexano-18-crown-6 (0.13 mmol), the coenzyme A solution was added dropwise and the reaction mixture was stirred for 4 h at room temperature. The crude mixture was acidified with an equal volume of 10 mM KH_2PO_4 (pH 5.5), and the organic solvent was removed using a nitrogen stream. Afterwards, the aqueous phase was desalted using a reverse phase C18 column (see 2.2.6.4.) and the final product was eluted with methanol. For quantification, mass spectrometric analyses with acyl-CoAs of known concentrations were performed (see 2.2.6.8.).

2.2.4.2. Synthesis of internal standards for ESI-MS/MS

2.2.4.2.1. Synthesis of ceramides(d17:1) standards

Fatty acids were activated by converting them into their respective *N*-hydroxysuccinimide esters as described above (see 2.2.4.1.). The activated fatty acids (40 µmol) were then condensed with d17:1-sphingosine (10.5 mmol) in a final volume of 4 ml dry THF. The reaction was catalyzed by triethylamine (4 µl) for 1–2 days at r.t. under an inert atmosphere.

2.2.4.2.2. Purification of internal standards by flash-column chromatography

The crude ceramide products were purified by silica gel flash-column chromatography using mixtures of hexane/isopropanol/water of increasing polarity as a solvent system.

For preparative chromatography, a column of 20 mm in diameter with a fritted glass filter was used. A layer of sea sand was placed on top of the glass filter, following by 12 g of silica gel (LiChroprep Si 60, 40–43 µm, Merck) used as a stationary phase. The column was tightly packed by the application of vacuum, and a second layer of sea sand and glass wool were mounted on top of the stationary phase. Afterwards, the column was flushed with elution solvent using vacuum to force the solvent through the silica, and therefore solvate the column. Subsequently, the crude products dissolved in the minimum amount of elution buffer were loaded onto the column. Hexane/isopropanol/water (90/9.5/0.5 or 93/7/0.1) mixture was used as starting elution solvent system. Fractions of ~ 4–6 ml of eluate were sequentially collected into separate glass tubes until 100 ml for each of the 4 solvents mixtures with increasing polarity were used. The final elution mixture was hexane/isopropanol/water 83/15/1.

In order to locate the fractions containing the purified products, an aliquot of every third fraction were loaded onto a thin layer chromatography (TLC) plate (see 2.2.6.9.). Fractions containing the purified ceramides were pooled and dried under a nitrogen stream. To quantify the synthesized ceramides, a dilution series of the purified products were separated on a TLC plate and bands were analyzed by densitometry as described below.

2.2.5. Ceramide synthase enzymatic assay

A non-radioactive enzymatic assay in living mammalian cells was established in order to evaluate the substrate specificity of CerS3 (and CerS2) towards acyl-CoAs. Therefore, HeLa cells stably transfected with mouse and human CerS3, EGFP-control, as well as *untreated* cells ($HeLa_{mCAT1\text{-}rtTA2\text{-}M2}$) were seeded onto 6-well plates with a density of 1×10^5 cells/well with or without induction with 2 µg/ml doxycycline. These inducible cell lines were generated by retroviral transduction as described in section 2.2.2.4.

Forty-eight hours after seeding, *untreated* cells were transfected with hCerS2-EGFP and incubated for 4 h at 37 ºC (for transfection see 2.2.2.3.). The assay was started by exposing the cells to media containing a mixture of saturated acyl-CoAs, namely 16:0, 18:0, 24:0, 26:0 and 28:0 (10 µM each) and d17:1-sphingosine (6 µM).

The latter was stored in an organic solvent mixture of $CHCl_3/CH_3OH/H_2O$ (10/10/1) at – 20 ºC, therefore the solvent had to be removed prior addition to the cells. To assure the complete solution of the relative lipophilic reagents in the aqueous medium, the dried solvents were dissolved in growth medium and sonication was applied for 5 min at r.t. (Sonorex Super RK 102H, Bandelin).

The assay was finalized upon 20 h of reaction by harvesting the cells. Afterwards, lipids were extracted and quantified as described in section 2.2.6.

2.2.6. Lipid analysis

2.2.6.1. Sample preparation

Cells grown in tissue culture plates were trypsinized and harvested at 106 × *g* for 5 min at 4 ºC. Cell pellets were then washed with chilled PBS and dried with 1-propanol under nitrogen flow.

For the extraction of epidermal lipids, skin biopsies from the back of CerS3 deficient mice and control littermates were rapidly dissected and snap-frozen in liquid nitrogen before being stored at – 80 ºC. Skins were thawed and epidermis were isolated by treating the biopsies with 500 µg/ml thermolysin buffer for 2 h at 37 °C (Germain et al., 1993). Afterwards, epidermis was separated from dermis, cut into small pieces, and lyophilized (Alpha 1-2, Christ).

2.2.6.2. Lipid extraction by modified BLIGH and DYER method

Sphingolipids were extracted according to Doering et al. with slight modifications (Doering et al., 1999a; Jennemann et al., 2007). In general, lipids were isolated using mixtures of $CHCl_3/CH_3OH/H_2O$.

In particular, dried pellets from cultured cells were extracted with 2 ml 10/10/1 (v/v/v) solvent mixture at 37 ºC for 15 min with occasional sonication. After centrifugation at ~ 2000 × *g* for 10 min, supernatants were collected and pellets were then reextracted once more with 10/10/1 solvent mixture, and finally with a 30/60/8 (v/v/v) solvent mixture.

For the extraction of epidermal free lipids, ~ 3 mg of dried weight epidermis cut in small pieces was extracted once with $CHCl_3/CH_3OH/H_2O$ 30/60/8, then with 10/10/1 and finally with $CHCl_3/CH_3OH$ 2/1 (v/v/v) as described. Each extraction step was performed at 50 ºC for 15 min under sonication.

Supernatants were combined and dried under a nitrogen flow at 37 ºC. In parallel, pellets were dried and kept at 4 ºC for further analysis.

2.2.6.3. Removal of phospholipids by mild alkaline methanolysis

Combined lipid extracts were subjected to methanolic mild alkaline hydrolysis (0.1 M KOH in CH_3OH) for the removal of phospholipids. The saponification of cell culture extracts was performed at 37 ºC for 2 h, while epidermal extracts required 4 h at 50 ºC for complete hydrolysis. Sequentially, saponified lipid extracts were neutralized with glacial AcOH and solvent was removed under a mild nitrogen flow.

2.2.6.4. Desalinization by reverse-phase chromatography (RP-18)

Saponified lipid extracts were desalted by reverse phase chromatography prior to being analyzed either by TLC or ESI-MS/MS. Thus, columns packed with C18 material (Porasil silica 125Å 55–105 µm) were preconditioned consecutively with 3 times CH_3OH and 2 times with 0.1 M KCl. Salt-containing samples were dissolved in ddH_2O to a final concentration of 0.1–0.2 M KCl by brief sonication before being loaded into the columns. Following the loading of the samples, vials were washed twice with 0.1 M KCl, sonicated and loaded as well into the columns. Lipids bound to the column were then washed 3 times with ddH_2O. Finally, sphingolipids were eluted

with CH_3OH and dried under a nitrogen flow. In case of desalinization of epidermal ceramides, an additional washing step with ddH_2O was performed prior to elute the lipids with CH_3OH into the original sample tubes, and subsequently dried under a nitrogen flow.

Desalting of saponified lipids from cultured cells was performed using freshly prepared Pasteur pipettes. For tissue extracts, 100 mg of packing material was loaded into 5 ml polypropylene reusable columns. To assure complete removal of previous lipid extracts, polypropylene columns were carefully washed with 2 x 4 ml $CHCl_3$, 1 x 4 ml $CHCl_3/CH_3OH$ 1:1, 1 x 4 ml CH_3OH, 1 x 4 ml CH_3OH /H_2O 1:1, and finally equilibrated with 2 ml 0.1 M KCl.

2.2.6.5. Extraction of protein-bound sphingolipids

Protein-bound sphingolipids from epidermal biopsies were extracted from the pellets obtained after extraction of free lipids. Pellets were “washed” 3 times with 2 ml of 100% CH_3OH for 5 min and 2 times with 2 ml of 95% CH_3OH at 60 °C for 2 h to remove residual free lipids. Treatment of the residual pellets with 1 ml of 1 M KOH in 95% methanol at 60 °C for 2 h cleaved ester linkages and released protein-bound sphingolipids. Supernatants were neutralized with AcOH and desalted using RP-18 columns as described above.

2.2.6.6. Extraction of fatty acids

Fatty acids rich in ULC-acyl moieties were isolated from GM2AP$^{-/-}$ mice testes by acid hydrolysis, as previously described (Valianpour et al., 2003). Following homogenization and lyophilization of the biopsies, fatty acids were hydrolyzed at 90 ºC for 2 h with 10 ml of $CH_3CN/HCl_{conc.}$ 4/1 (v/v). Testicular fatty acids were then extracted with the double amount of n-hexane. The upper organic phase was separated and dried under a nitrogen flow. For cell culture experiments, isolated fatty acids corresponding to 2 mg of wet weight were dissolved first in ethanol (1 mg wet weight / 1 µl ethanol), following intensive vortexing and finally dissolved in 2 ml of culture media.

2.2.6.7. Protein determination according to LOWRY

Pellets obtained after lipid extraction were used for determination of their protein content according to the method of Lowry (Lowry et al., 1951).

This colorimetric assay is based on the redox-reaction of peptide bonds with $CuSO_4$ under basic conditions and the subsequent reduction of Folin-Ciocalteu reagent by Cu^+. First, proteins dissolved in alkaline conditions react with Cu^{2+} forming a tetradentate Cu^{2+} complex with the amino groups of peptide bonds. Subsequently, Cu^{2+} is reduced by certain peptide side chains. This reaction is stabilized by tartrate. Upon addition of the Folin-Ciocalteu reagent containing a mixture of phosphomolybdate and phosphotungstate (Mo^{6+}/W^{6+}), reduction to heteropolymolybdenum blue (Mo^{5+} and Mo^{6+}) takes place, which is detectable at a maximum of 750 nm.

Therefore, pellets were dissolved in 1 M NaOH at 50 ºC for 4 h with occasional sonication. To determine the protein concentration, a standard curve was prepared with BSA (0–20 µg) in 0.1 M NaOH. Sample aliquots and BSA standards were dissolved in 0.1 M NaOH to a final volume of 300 µl. Complex reagent (1.5 ml) containing Na_2CO_3, $CuSO_4$, and tartrate was added to each sample. Copper complexes were allowed to form by incubating the samples 10 min at room temperature. Subsequently, 150 µl of Folin-Ciocalteu reagent were added, followed by a brief vortexing. Protein complexes were then incubated 45 min at r.t. in the dark, and protein content was measured by spectrophotometry at 750 nm.

2.2.6.8. Quantification by electrospray ionization tandem mass spectrometry (ESI-MS/MS)

Sphingolipid quantification was performed by tandem mass spectrometry using a triple quadrupole instrument (VG micromass model Quattro II, Waters) equipped with a nano electrospray source, as previously described (Jennemann et al., 2007; Sandhoff et al., 2005). Equivalent lipid samples regarding the protein content were dissolved in 5 mM NH_4OAc in CH_3OH. Prior to being analyzed, internal standards were added to the aliquots.

Synthesized montanoyl- and melissoyl-CoA were also quantified by mass spectrometry. An equimolar mixture of 16:0, 18:0, 20:0, 24:0 and 26:0-CoA of known

concentration were used as internal standards to determine the concentration of the acyl-CoAs.

Sphingolipids, as well as fatty acids and acyl-CoAs were detected with precursor ion scans and neutral loss modus, respectively. The acquisition parameters and the internal standards used for quantification are compiled in the following table:

Lipid	Scan modus	*m/z*	Specific scan for	Collision energy (eV)	Internal standards
Acyl-CoA	Neutral loss	507	Phosphato-ADP	37	16:0-CoA,18:0-CoA 20:0-CoA,24:0-CoA 26:0-CoA
Cer (d17:1)	Precursor ion	250	Sphingoid base (d17:1)	44	Cer (d17:1,19:0) Cer (d17:1,25:0)
Cer (d18:1)	Precursor ion	264	Sphingoid base (d18:1)	50	Cer (d18:1,14:0) Cer (d18:1,19:0) Cer (d18:1,25:0) Cer (d18:1,31:0)
GlcCer (d18:1)	Precursor ion	264	Sphingoid base (d18:1)	50	GlcCer (d18:1,14:0) GlcCer (d18:1,19:0) GlcCer (d18:1,25:0) GlcCer (d18:1,31:0)
α-Hydroxy-fatty acids	Neutral loss	46	Carbonyl	30	Not quantified
SM	Precursor ion	184	Phosphoryl-choline	35	SM (d18:1,14:0) SM (d18:1,19:0) SM (d18:1,25:0) SM (d18:1,31:0)

All ESI-MS/MS measurements were performed by Prof. Dr. Roger Sandhoff from DKFZ in Heidelberg.

2.2.6.9. Thin layer chromatography (TLC)

Ceramide internal standards were analyzed and quantified by thin layer chromatography. After purification of internal standards with column chromatography, 20 µl of every third fraction of the eluate were spotted on double-sided HP-TLC silica plates (Silicagel 60 F_{254}, Merck) using a Linomat IV (Camag). Separation was carried

out by running the TLC from both sides with $CHCl_3/CH_3OH$/glacial AcOH (188/11/1) in a horizontal chamber. Bands were then made visible by developing the TLC plate in 10% $CuSO_4$ in 8% H_3PO_4 (10 min at 180 ºC). The fractions containing the purified ceramides were pooled and dried under a nitrogen stream.

For quantification, a dilution series of the purified products were spotted on a HP-TLC together with standards of known concentration and separated with $CHCl_3/CH_3OH$/glacial AcOH (188/11/1). After development with $CuSO_4$ reagent, quantification of the bands was performed by densitometric scanning using a TLC scanner (Shimadzu CS-9301).

For epidermal extracts, lipids corresponding to 0.5 mg dry weight were spotted on a TLC plate and separated using a complex solvent system that included four different solvent mixtures. First, $CHCl_3/(CH_3)_2CO$ (1/1) was used to run the plate up to 4 cm of a 20 cm TLC plate, followed by $CHCl_3/CH_3OH$/glacial AcOH (60/35/8) run up to 7 cm, $CHCl_3/CH_3OH$/glacial AcOH (190/9/1) to 12 cm and finally n-hexane/methyl t-buthyl ether/glacial AcOH (90/10/1) up to the top. Lipids were then visualized using $CuSO_4$ reagent.

Total mRNA expression analysis

2.2.7.1. Isolation of total RNA from tissue and eukaryotic cells

Total RNA was extracted with phenol, guanidinium thiocynate and chloroform according to Chomczynski and Sacchi, either with the ready-to-use Tryzol® reagent or with a modified Chomczynski and Sacchi method (Chomczynski and Sacchi, 1987).

2.2.7.1.1. RNA isolation by modified CHOMCZYNSKI and SACCHI *method*

Juvenile mice testes (PN 5–25) were homogenized on ice in 3 ml of freshly prepared guanidinium thiocyanate buffer. Total RNA was then extracted with 300 µl of NaOAc (2 M, pH 4), 3 ml of Roti-Aqua-Phenol (Carl Roth), and 600 µl of $CHCl_3$/isoamyl alcohol 24/1 (Sigma), with thorough mixing by inversion after the addition of every reagent. The suspension was incubated 15 min on ice, following by a centrifugation step at 15,000 × *g* for 30 min at 4 ºC. The upper aqueous phase containing the RNA was then transferred into a fresh tube, separated from the DNA and proteins present

in the lower phenol phase. Subsequently, 3 ml of isopropanol (100%) were added and RNA was precipitated overnight at – 20 ºC. A second precipitation step was performed by collecting the RNA pellet at 15,000 × *g* for 20 min, following the addition of 2 ml guanidinium thiocyanate buffer and 2 ml isopropanol, and overnight precipitation at – 20 ºC. After collection of RNA at 15,000 × *g* for 20 min, a washing step with 600 µl of 70% ethanol (– 20 ºC) was performed. Finally RNA was collected once more with 20 min centrifugation at 18,000 × *g*, and the pellet was then solubilized in ddH_2O. Isolated RNA was flash frozen in liquid nitrogen and kept at – 80 ºC.

2.2.7.1.2. RNA isolation by Tryzol® reagent

Tryzol® reagent (Invitrogen), a ready-to-use monophasic solution of phenol and guanidinium thiocyanate, was used to isolate total RNA from cultured cells as well as from tissue biopsies (e.g. testes, skin), according to manufacturer's instructions.

Cultured cells grown in monolayer in a 6-well plate were directly lysed with 1 ml of Tryzol® reagent. For the isolation of RNA from tissue, biopsies were homogenized in 1 ml Tryzol® per 50–100 mg of tissue. Skin biopsies were disrupted using a glass-teflon grinder (Glass-Cool®), while disruption of testes was performed using a power homogenizer (Ultra Turrax® T25 basic). Sequentially, homogenates were incubated for 5 min at r.t. to enable complete cell lysis. RNA was extracted with the addition of 0.2 ml $CHCl_3$ (per 1 ml of Tryzol®), followed by a thorough mixing, and an incubation step of 3 min at r.t. Following, phase separation was performed at 12,000 × *g* for 15 min, and the upper aqueous phase containing RNA was collected into a fresh tube. RNA precipitation was performed with 0.5 ml isopropanol, and RNA was pelleted at 12,000 × *g* for 10 min. To wash the RNA pellet, 1 ml ethanol (75%) was used, and RNA was finally collected at 7,500 × *g* for 5 min, and solubilized in DEPC or Braun water. All centrifugation steps were performed at 4 ºC.

2.2.7.2. DNAse digestion

Contaminating DNA was removed from RNA isolates using TURBO DNA-free™ Kit (Ambion). Thus, 10 µg of RNA dissolved in 15 µl of ddH_2O were incubated for 30 min

at 37 ºC with 1 µl of DNase I and 1x DNase buffer. Following enzymatic treatment, 2 µl of DNase inactivation reagent were added, and after 2 min incubation at r.t., contaminants were pelleted at 10,000 × *g* for 2 min. Finally, purified RNA was transferred into a fresh tube.

2.2.7.3. RNA integrity assessment *with RNA6000 nanochip*

RNA integrity was analyzed by electrophoresis using an Agilent RNA 6000 nanochip according to the description of the manufacturer. The nanochip was evaluated with 2100 Bioanalyzer (Agilent Technologies) using the *eukaryote total RNA assay*. The RNA integrity number (RIN) was used to determine the quality of the isolated RNA. RIN is an algorithm calculated by the software according to the complete electrophoretic trace of the RNA sample. Maximum RNA quality is defined by RIN values equal to 10, and ratios between 28S/18S of rRNA equal to 2.

2.2.7.4. Synthesis of double stranded cDNA

Reverse transcription of RNA into single stranded (ss) cDNA was performed with Superscript® II. Briefly, 3 µg of isolated RNA diluted in 14 µl of ddH_2O were mixed with 1 µl of oligo-$dT_{12\text{-}18}$ primer (0.5 µg/µl) and 1 µl of dNTP mixture (10 mM). The samples were heated to 65 ºC for 5 min prior the addition of 4 µl of first strand buffer (5x) and 2 µl of DTT (100 mM). After incubating the samples for 2 min at 42 ºC, 1 µl of Superscript® II (200 u/µl) was added, and reverse transcription was performed for 1 h at 42 ºC.

Sequentially, double stranded (ds) cDNA was synthesized from freshly prepared single stranded cDNA. To the ss cDNA was added 30 µl of second strand buffer (5x), 3 µl of dNTP mixture (10 mM), 4 µl DNA Polymerase I (10 u/µl), 1 µl of DNA ligase (10 u/µl), and 1 µl of RNAse H (2 u/µl) to a final volume of 153 µl with ddH_2O. The reaction mixture was incubated for 2 h at 16 ºC. To assure blunt end of the ds cDNA termini, 2 µl of T4 DNA polymerase were added to the newly synthesized ds cDNA. Afterwards, samples were incubated for 10 more min at 16 ºC in order to allow the enzymatic reaction of the polymerase. Finally, ds cDNA was purified using the QIAquick PCR purification kit (see 2.2.1.3) and eluted from the silica-based membrane with 50 µl of ddH_2O.

All enzymes used for reverse transcription were purchased from Invitrogen.

2.2.7.5. Quantitative real time PCR (qRT-PCR)

Quantification of gene expression by real time PCR was performed using the LightCycler® 2.0 system (Roche Diagnostics). For the amplification and detection of the gene of interest, the LightCycler® FastStart DNA Master SYBR Green I was used in combination with specific primers for the target genes and 1:10 dilution of the synthesized cDNA. Generally, optimal amplification of target genes required divalent cations in a final concentration of 2.5 mM. The real time PCR reactions were set as follows:

Real time PCR reaction (20 µl):	
H_2O	12.8 µl
$MgCl_2$ (25 mM)	1.2 µl
Primers (5 µM each)	2 µl
cDNA template (1:10)	2 µl
LightCycler® SYBR Green	2 µl

Program	T (ºC)	time
1. Denaturation	95	10 min
2. Denaturation	95	15 s
3. Annealing	T_a	5 s
4. Elongation	72	10 s
(Steps 2 to 4 are repeated for 45 cycles)		
5. Denaturation	95	0 s
6. Annealing	65	15 s
7. Melting	95	0 s
8. Cooling	40	30 s

The PCR reaction mixtures were loaded in LightCycler® glass capillaries, and the qRT-PCR was performed immediately. A negative control was loaded in each PCR to assure no contamination of the samples. Amplicons of the target gene were generated during the 45 denaturation-annealing-elongation cycles (programs 2–4). Following, melting curves of the amplified fragments were generated (programs 5–8) in order to evaluate the integrity of the products. Reactions were performed with biological triplicates and technical duplicates.

Primers were designed exon-spanning and localized at the 3'-prime region using Primer3 (v 0.4.0). Generally, amplicon size was between 50 and 200 bp, and the GC content was set to 45–55%. To exclusively enhance the target homologue gene, blast analysis and multiple sequence alignment (ClustalW, v 1.83) were performed to evaluate the homology of the primer with the other homologue family members. The sequence and annealing temperatures of the primers used in this study are listed in

section 2.1.12.3. Amplicons were further analyzed by agarose electrophoresis to assure the amplification of the appropriate products.

Quantification of the gene expression was calculated using the $\Delta\Delta C_T$ method (Livak and Schmittgen, 2001), normalizing relative C_T values to the expression of the housekeeping gene, Gapdh.

2.2.8. Animal experiments

2.2.8.1. Animal care

Animals were kept under specific pathogen-free conditions in barrier facilities, where a 12 h light / 12 h dark cycle was maintained. Mice were housed in groups up to five animals at a controlled temperature of 22 ºC. They were fed regular laboratory chow diet and water, supplied *ad libitum*.

2.2.8.2. Genotyping

CerS3$^{-/-}$ mice were genotyped by PCR using genomic DNA isolated from tail biopsies. For routine extraction of genomic DNA, about 0.3 cm tails were digested overnight at 56 ºC with 100 µl of DirectPCR® Lysis Reagent (PeqLab) supplemented with 2.5 µl of proteinase K (Sigma). Heat inactivation of the enzyme was performed at 85 ºC for 45 min prior to the PCR. Reactions were performed using 1 µl of DNA from tail digestion in a final volume of 50 µl, as described in section 2.2.1.2. Amplification of specific products corresponding to wild type and mutant allele were performed with primers listed in section 2.1.12.4., and using Taq DNA polymerase (5 Prime). Agarose gel electrophoresis was performed to analyze the fragments obtained from PCR, as described in section 2.2.1.4.

To corroborate the generation of a truncated CerS3 transcript lacking exon 7, isolated cDNA from skin of mutant and wild type animals (for methods see 2.2.7.1-4.) was used to specifically amplify a PCR product between exon 6 and the immediate 3'UTR (primers listed in 2.1.12.4.).

2.2.8.3. Skin permeability assay

Permeability of skin was tested by hematoxylin diffusion essentially as described (Vasireddy et al., 2007). In brief, euthanized embryos and newborn animals were

fixed in CH_3OH for 5 min, washed with PBS and incubated in hemalaun solution (Roth, T865.3, according to Mayer) for 40 min at room temperature. Excess hemalaun was removed by several thorough washes with PBS. After hematoxylin staining, images of the animals were taken using a digital camera.

2.2.8.4. Determination of transepidermal water loss (TEWL)

Transepidermal water loss was measured using a Tewameter TM300 (Courage-Khazaka Electronics) as described (Herrmann et al., 2003).

2.2.8.5. Epidermal pH

Epidermal pH was determined by direct contact of humidified pH-indicator strips (pH 5.2–7.2, Merck) to the skin of mice.

2.2.9. Pathogenic infection experiments

2.2.9.1. Culture of mouse skin

Skin biopsies from the back of newborn animals were maintained viable on collagen gels partially submerged in DMEM medium (Lonza, BE12-604F) supplemented with 50 U/ml penicillin and 50 µg/ml streptomycin (Gibco). Collagen gels were prepared as previously described (Stark et al., 2006). Thus, type I collagen was isolated from tail tendons of young rats and lyophilised. To a 4 mg/ml solution of collagen in 0.1% AcOH was added 10% of 10x Hank's balanced salt solution (Gibco) titrated with 5 M NaOH and 10% of DMEM medium. The mixture was allowed to jellify in PET-membrane filter inserts (Falcon) for 1 h at 37 ºC, following the addition of 12 ml DMEM medium in each of the deep-wells (BD Biosciences, BD 355467).

2.2.9.2. Pathogenic infection

Candida albicans (ATCC 90028) was grown overnight in LB medium. Prior to infection, yeast concentration was determined by cell counting using a Neubauer chamber. Afterwards, cells were pelleted by centrifugation and resuspended in PBS to a concentration of 10^9 cells/ml. *C. albicans* (1 µl, 1×10^6 cells) was inoculated to the center of the skin biopsy and incubated at 30 ºC for the specified time.

2.2.9.3. Determination of pathogenic growth

Infected skin biopsies were flushed with 10 ml PBS. An aliquot of these suspensions (100 µl) were plated in two different dilutions on Sabouroud agar plates (BioMérieux). Multiple serial dilutions had been previously performed to determine optimal conditions. After 24 h incubation at 37 °C, colonies were counted and concentrations were determined as CFU/ml. Technical triplicates from biopsies of four mice were analyzed.

Pathogenic infection and growth studies were performed by Rene Karayilan and Prof. Dr. Alexander Dalpke at the department of Medical Microbiology and Hygiene of University of Heidelberg.

2.2.10. Microscopy

2.2.10.1. Light and electron microscopy

Specimens for ultrastructural analyses were prepared as previously described with slight modifications (Komljenovic et al., 2009). Embryonic and neonatal CerS3$^{d/d}$ and control mice were anesthetized and transcardially perfused for 15–30 min at r.t. The freshly prepared fixative solution contained 2.5–4% glutaraldehyde in 0.1 M sodium cacodylate buffer (pH 7.6) and saturated picric acid (300 µl per 100 ml fixative solution), in addition to 2% polyvinylpyrrolidone (PVP, Polyvidon 25, MW 25,000, Merck) and 0.05% $CaCl_2$. Fixed skin from the interscapular region of the back was dissected and embedded in agar (extrapure, Merck) in order to preserve the periderm and the entire layers of the stratum corneum. Following, sections of 80 to 150 µm thickness were prepared using a microslicer (DTK 1000).

One series of samples were incubated in alkaline diaminobenzidine (DAB) for 30–60 min for enhancement of membrane staining, and postfixed with 1% buffered OsO_4 in sodium cacodylate buffer (pH 7.6) containing 1.5% potassium ferrocyanide for 20–30 min, followed by osmification without ferrocyanide for an additional 40–60 min.

A second series of specimens were treated, after one osmification step with 1% buffered OsO_4 for 90 min, with 1% tannic acid (low molecular galloyl glucose, LMGG,

Mallinckrodt laboratories) in 0.1 M sodium cacodylate buffer (pH 7.0), as described (Simionescu and Simionescu, 1976).

Fixed on superfrost®, slides were immersed in freshly prepared HIO_4 (5% aq. sol.) for oxidation at 60 ºC (2x 30 min), rinsed with ddH_2O for 30 min and dried at 85 ºC. En-block staining with 1% uranyl actetate proceeded for 20–30 min prior to dehydration in graded ethanol and embedding in Epon 812. Subsequently, serial semithin Epon sections of 0.5–1 µm thickness were prepared (Leica Ultracut UCT).

For light microscopical analysis, semithin sections were stained with periodic acid-Schiff (PAS) (Schroeder et al., 1980) without counterstaining or followed by a modified Richardson solution containing methylene blue-Azur II. Briefly, Epon sections were immersed in a freshly prepared HIO_4 solution (5% aq. sol.) at 60 ºC for $2 \times$ 30 min, rinsed in ddH_2O for 30 min and dryed at 85 ºC. Sections were then incubated with Schiff solution for 90 min at 60 ºC, with an additional rinsing and drying step. Subsequently, samples were counterstained with 0.5% methylene blau/Azur II (1:1) in 0.5% aqueous borax solution for 3–5 min at r.t. Specimens were finally rinsed with ddH_2O and dryed at 85 ºC. To visualize epidermal glycogen, specimens were exclusively stained with PAS without counter-staining.

For ultrastructural analysis, series of ultrathin Epon sections were prepared and stained with lead citrate prior to be analyzed with an electron microscope (Zeiss EM 906E).

For pathogenic studies, infected skin biopsies from CerS3 deficient mice and controls were fixed together with collagen gels with 4% formalin for 24 h at r.t. and subsequently embedded in paraffin. Sections (Microm, HM 355S) of 1 µm thickness were prepared and deparaffinized by short sequential immersions in xylene, ethanol solutions (100%, 96%, 80% and 70%) and water. Sections were then immersed in 0.75% HIO_4 for 10 min, carefully rinsed with water and incubated in Schiff solution for 5 min. Following rinsing and drying steps, biopsies were then counterstained with hemalaun solution (Roth, according to Mayer). Sections were dehydrated by subsequent immersions in ethanol solutions of increasing concentrations (70–100%), followed by immersion in xylene. Sections were then mounted with Vitro-Clud (Langenbrink) and analyzed using a Leica DMLB microscope.

Specimen preparation and ultrastructural analyses were performed in cooperation with Ingrid Kuhn-Krause and Prof. Dr. Karin Gorgas at the department of Anatomy and Cell Biology of University of Heidelberg. The PAS staining of infected skin biopsies was performed with the technical assistance of Gabriele Schmidt from DKFZ in Heidelberg.

2.2.10.2. Immunohistochemistry of mouse newborn skin

Neonatal mice were transcardially perfused with 3–4% paraformaldehyde (PFA) solution in 0.1 M PBS (pH 7) containing 2% PVP for 15–30 min at r.t. Skin samples were dissected, postfixed with fixative solution for additional 30–60 min at 4 ºC and rinsed with PBS containing 2% PVP. Sections were prepared as follows.

Ultracryosemithin sections. Microslicer sections of 600 µm thickness were cryo-protected in sequential sucrose solutions (0.1 M PBS, pH 7.6 with 10% PVP) of increasing concentrations (10%, 20%, 30% and 2.3 M) prior to be frozen in precooled isopentane with liquid nitrogen. Subsequently, ultracryosemithin sections of 0.6–0.8 µm thickness were prepared with a Leica Ultracut UCT equipped with a Leica EMFCS. F-actin, loricrin and involucrin were localized following this protocol.

Cryosections. After anesthesia, unfixed skin biopsies from the back of newborn animals were quickly placed onto an aluminium foil and frozen in pre-cooled isopentane with liquid nitrogen and embedded in tissue block. Cryosections of 3–5 µm thickness were obtained with a Leica CM 3050S and subsequently fixed with acetone for 10 min at r.t. For the detection of claudin 1, sections were subjected to an antigen retrieval with 10 mM sodium citrate and 0.5% Tween-20 (pH 6.0) for 20 min at 96 ºC. Instead, cingulin and filaggrin were permeabilized with 1% Triton X-100 in PBS (v/v) for 5 min and then blocked for 30 min with 10% FCS. For nile red, filipin and transglutaminase detection of unfixed cryosections a modified protocol was used (*vide infra*).

Paraffin. Fixed specimens were dehydrated in a graded ethanol series and embedded in Paraplast Plus. Paraffin sections of 3–5 µm thickness were obtained with a Microm HM 340E, then deparaffinized and subjected to antigen retrieval as described *(vide supra*). Cathepsin D, desmoglein 1/2, desmoplakin, Ki67 (*vide infra*), loricrin, and CerS3 were detected with this protocol.

In situ extraction of protein-bound sphingolipids on paraffin sections was performed to detect desmoglein, loricrin and involucrin antigens. Thus, sections were deparaffinized with xylene (2 x 30 min) and immersed in 100% ethanol (2 x 10–15 min). Protein-bound epidermal sphingolipids were then extracted with mild alkaline methanolysis (0.1–1M KOH in 100% CH_3OH) for 1–2 h at r.t., slightly modified as described in section 2.2.6.5. Afterwards, sections were washed in CH_3OH (3 x 2 min) and finally immersed in 100% ethanol for 10 min. Subsequently, sections were dehydrated by immersion in sequential ethanol solutions of decreasing concentrations and water, prior to be subjected to an antigen retrieval.

For detection of antigens, sections were incubated with primary antibodies for 1–16h at 4 ºC or at r.t. Subsequently, sections were washed and incubated with secondary antibodies for 1 h at r.t. Following another washing step, nuclear staining was performed with DAPI (20 ng/ml, Sigma). Sections were then mounted in DakoCytomation fluorescent mounting medium.

The *in situ* detection of transglutaminase activity in skin biopsies was performed as described with slight modifications (Yanagi et al., 2010). Shortly, unfixed cryosections of 3–5 µm thickness were air-dried for 30 min at r.t and washed with PBS (2 x 5 min) to remove the tissue block. Sections were blocked with 1% BSA in 100 mM Tris-HCl (pH 7.4) for 30 min, following 1 h incubation with 12 µM monodansylcadaverine (Sigma) in 100 mM Tris-HCl (pH 7.4) containing 5 mM $CaCl_2$. For negative controls, EDTA was added into the substrate buffer to a final concentration of 20 mM. The enzymatic reaction was stopped by incubation of PBS containing 10 mM EDTA for 5 min. Two additional washing steps were performed with PBS for 5 min, prior to incubation for 3 h with the primary antibody dissolved in 12% BSA-PBS. Sections were then washed with PBS (3 x 5 min) and incubated for 45 min with the secondary antibody in 12% BSA-PBS. Following nuclear staining, specimens were mounted in Fluoromount-G. All steps were performed at r.t.

Lipids were detected with nile red and filipin using unfixed cryosections, as previously reported with slight modifications (Goritz et al., 2007; Greenspan et al., 1985). For cholesterol staining using filipin, sections were left to air-dry and washed prior to be immersion-fixed in 4% phosphate-buffered formalin. Sections were then

washed with ddH_2O and PBS, and subsequently incubated with freshly prepared filipin solution (10 µg/ml in PBS with 1% DMSO) for 2 h at r.t. Substrate was then washed with PBS and ddH_2O, and finally mounted in Fluoromount-G. To visualize neutral and polar lipids using nile red, sections were air-dried and sequentially incubated with a freshly prepared solution containing 5 µg/ml of nile red in 75% glycerol. This solution was prepared from a 500 µg/ml stock solution of nile red dissolved in acetone. After 5 min incubation, sections were mounted and directly visualized.

For immunofluorescence studies, sections were analyzed with the fluorescence microscope Biorevo BZ-9000 (Keyence). For negative controls, PBS was used instead of primary antibodies.

Keratinocyte proliferation was assessed in paraffin sections with detection of Ki67 antigen using a DakoAutostainer. Following permeabilisation, blocking and binding with primary antibody, sections were incubated with a biotinylated anti-rat antibody and detected with alkaline phosphatase-labelled streptavidin (1:200, Vector Laboratories, SA-5100).

Terminal dUTP nick-end labeling (TUNEL) was performed on unfixed skin biopsies embedded in paraffin wax using the *in situ* cell death detection kit (Roche, 11 684 817 910), following the recommendations provided by the manufacturer. Afterwards, biopsies were counter-stained with hematoxylin prior to being analyzed using a Leica DM-RBE microscope.

Sample preparation and immunohistochemical stainings were performed with major help of Ingrid Kuhn-Krause, Claudia Schmidt and Prof. Dr. Karin Gorgas.

2.2.10.3. Immunohistochemistry of cell cultures

For subcellular localization of CerS3, HeLa cells were seeded and transfected on sterile 12 mm glass coverslips placed in 6-well plates. Following 24 h after transfection, cells were washed 3 times with chilled PBS. Cells were then fixed with 3.5% PFA for 5 min on ice, following 10 min at r.t. Afterwards, cells were washed with chilled PBS (3x for 5 min), following permeabilization with CH_3OH (– 20 ºC) for 6 min (Brock et al., 1999). Subsequently, cells were washed once more with PBS (3x for 5 min), before blocking for 1 h with 3% BSA-PBS. Binding of primary antibodies was

performed for 1.5 h at r.t. After three washing steps, incubation of secondary antibodies for 45 min followed. Primary and secondary antibodies were diluted in 1.5% BSA-PBS. Afterwards cells were washed once more and nuclear staining was performed with Draq5™ (Biostatus) in PBS for 10 min. Finally, cells were washed with PBS (4x for 5 min) and mounted with Fluoromount-G. Immunofluorescence images were acquired with Leica TCS-SL microscope and analyzed with Leica Confocal software (version 2.61) by Tjeerd Sijmonsma from DKFZ in Heidelberg.

2.2.11. Statistical analysis

All data concerning animal experiments included a minimum of 3 mice per group. *In vitro* experiments were performed at least in 3 independent experiments. All statistical analyses were performed using *Student t* test, and differences among groups were considered significant for $p < 0.5$ (*), $p < 0.1$ (**) and $p < 0.01$ (***).

3. Results

3.1. Transcriptional analysis of the ceramide synthases in murine testis and skin

Previous studies with fertile and infertile mouse models led to the finding of a novel class of fucosylated GSLs, whose expression of the neutral subset strictly correlates with fertility in mice. The acyl moieties of this main class of testicular GSLs are almost exclusively comprised of ultra long chain polyunsaturated fatty acids (ULC-PUFAs) (Sandhoff et al., 2005). To gain deeper insight into the function of these unusual GSLs, we aimed first to identify the ceramide synthase homologue/s responsible for the incorporation of these ULC-acyl residues into the ceramide backbone.

3.1.1. *Cers3* is exclusively expressed in tissues containing ULC-sphingolipids

The mammalian ceramide synthase family is composed of six homologue genes (*Cers1–6*). Currently, five of these enzymes have been reported to incorporate specifically a subset of acyl-CoAs, which differ in the length of their hydrocarbon chain. The affinity for ULC-FAs has not been appointed to any of the investigated ceramide synthases. Yet neither the tissue, nor substrate specificity of CerS3 had been determined at the starting point of this study. However, it is CerS3 that was found in our department to be strongly expressed in mature mouse testis (Sandhoff et al., *unpublished results*). To confirm these preliminary results, and to investigate the *Cers3* expression in other tissues, PCR analyses from mouse cDNA were performed (Figure 17).

The highest *Cers3* expression was found in testis, confirming previous results and succeeding studies (Laviad et al., 2008; Mizutani et al., 2006). To a lesser extent, *Cers3* was additionally expressed in mouse skin. Interestingly, both testes and skin are the only mammalian tissues reported to contain major concentrations of ULC-sphingolipids. Otherwise, *Cers3* cDNA could not be amplified from either brain, liver or colon.

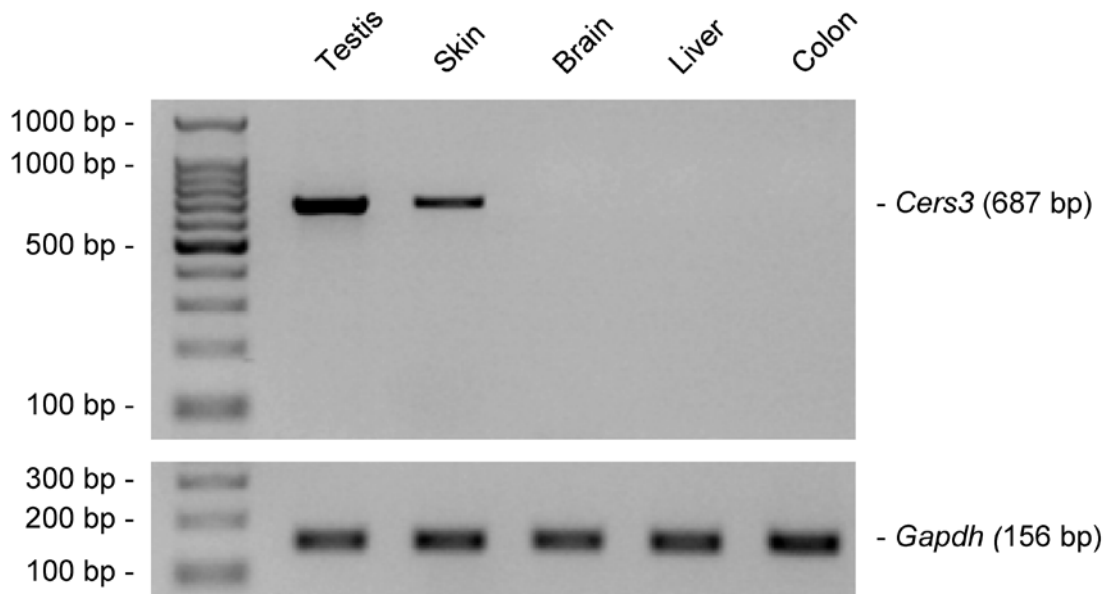

Figure 17. Tissue distribution of *Cers3* cDNA.
Agarose gel electrophoresis of Cers3 DNA products obtained by PCR analyses from diverse mouse tissues. The expression of Gapdh was used as a loading control.

The substrate specificity of the ceramide synthase homologues has been already characterized in several studies, including a recent study on the substrate preference of CerS3 (Mizutani et al., 2006). However the length of acyl-CoAs included in all previous studies ranged between 14 and 26 carbon atoms without including ULC-acyl-CoAs. Nevertheless, the longer acyl-CoAs included in these studies, 24- and 26-CoA, were best incorporated by CerS2 and CerS3. To elucidate whether CerS2 and CerS3 or any other CerS homologue plays the leading role in the synthesis of ULC-sphingolipids, mRNA analyses of the ceramide synthase family in mice testis and skin were performed.

In the testis, *Cers3* was the ceramide synthase member with highest transcript levels (Figure 18A). The expression of *Cers5* was the most abundant following *Cers3* with about 40% decrease in its transcript levels. Murine testicular mRNA additionally expressed *Cers2* and *Cers6*, however their mRNA levels were about 7 and 10 fold downregulated in relation to *Cers3*, respectively. The mRNA expression of *Cers1* and *Cers4* could not be detected in mouse testis.

In murine neonatal skin, *Cers2* and *Cers3* mRNA transcripts were the most prominent, although the expression of *Cers5* and *Cers4* were fairly abundant (Figure 18B). Here the relative gene expression levels of the ceramide synthases were determined in the combined endothelial and epithelial layers, and thus *Cers* levels reflect an average of their mRNA transcripts in the different cell types present in the skin.

Sphingolipids with ULC-FA moieties are exclusively found in the epidermis, where they play an essential role in the formation and maintenance of the epidermal permeability barrier. Determining whether *Cers3 or Cers2* is the major *Cers* mRNA expressed in the epidermis would still require further investigations. However, both enzymes could potentially be responsible for the transfer of ULC-acyl-CoAs to ceramides.

Cers5 and *Cers4* were additionally expressed in murine neonatal skin. Their relative expression levels were found over 2 and 3 fold times downreagulated, respectively, in relation to the mRNA concentration of *Cers2*. The transcript levels of *Cers6* and *Cers1* were barely detectable.

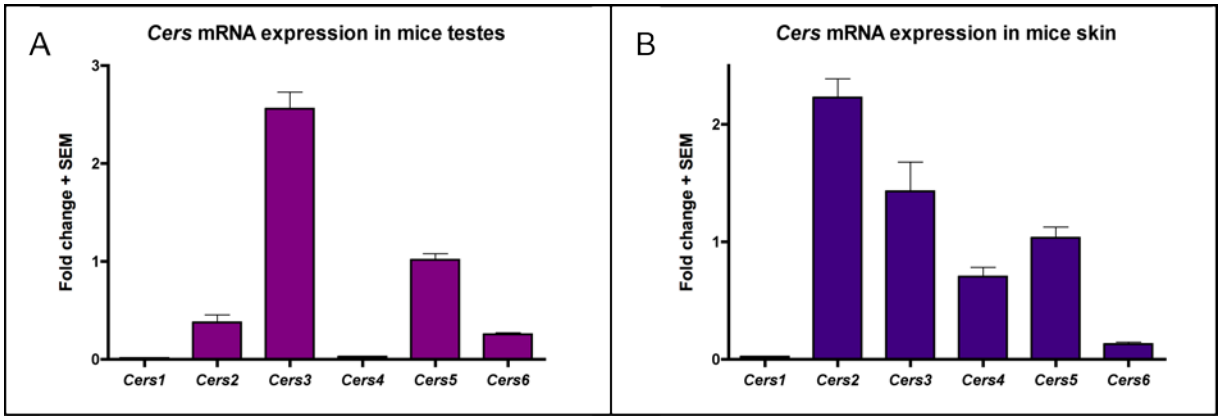

Figure 18. *Cers3* is highly expressed in murine testis and skin.
Quantitative RT-PCR was performed to evaluate Cers transcript expression profile in mice testes (A) and skin (B). Isolated mRNA from juvenile (PN 25) testes and newborn (PN 0) skin were transcribed into cDNA and subsequently evaluated for relative gene expression using specific primers for each homologue. Cers expression levels were calculated according to the $\Delta\Delta C_t$ method normalizing values relative to the expression of a housekeeping gene, here Gapdh. Normalized ΔC_t values were compared to normalized ΔC_t of Cers5-mRNA of each tissue.

Taking into account the expression levels of the ceramide synthase members in the primary tissues containing ULC-sphingolipids, and their reported preferences for acyl-CoA species, it was deducted that *Cers2* and *Cers3* are the only possible candidates that might be responsible for the biochemical transfer of ULC-acyl-CoAs into sphingoid bases (for detailed discussion see section 4.1).

3.1.2. *Cers3* and ULC-PUFA sphingolipid expression simultaneously increase during testicular maturation

Detailed mass spectrometric analyses of testicular sphingolipids according to their acyl residues revealed the lack of ULC-PUFA during the earlier stages of the first spermatogenic cycle. ULC-PUFA moieties were first incorporated into sphingolipids at PN 15, with their levels increasing during the progress of spermatogenesis (Rabionet et al., 2008).

To further investigate whether CerS2, CerS3 or any other CerS member could be responsible for the synthesis of ULC-sphingolipids in testis, stage specific mRNA analysis of the ceramide synthase family was performed. The aim was to correlate the expression of any of the *Cers* genes to the expression of ULC-sphingolipids during the progress of the first spermatogenic cycle in mice. Therefore, mRNA from mice testes of different stages of juvenile development were isolated, subsequently transcribed into cDNA and subjected to quantitative RT-PCR.

The expression profile of the ceramide synthase gene family revealed *Cers2, Cers3, Cers5 and Cers6* to be present in murine juvenile testes, whereas the levels of *Cers4* and *Cers1* were extremely low and almost undetectable, respectively. At the earlier stages of testicular development mRNA of *Cers5*, followed by *Cers2* and *Cers6*, exhibit the most abundant transcript levels. Despite an initial increase from PN 5 to 10, their expression levels were kept roughly constant with no significant changes throughout testicular maturation.

On the contrary, *Cers3* exhibited a distinctive mRNA expression pattern during the progression of the first spermatogenic cycle. Whereas transcript levels prior to PN 10 were low, mRNA was strongly and continuously upregulated from PN 14 onward. *Cers3* mRNA analyses revealed a noteworthy 700 fold change increase during the first wave of spermatogenesis in mice.

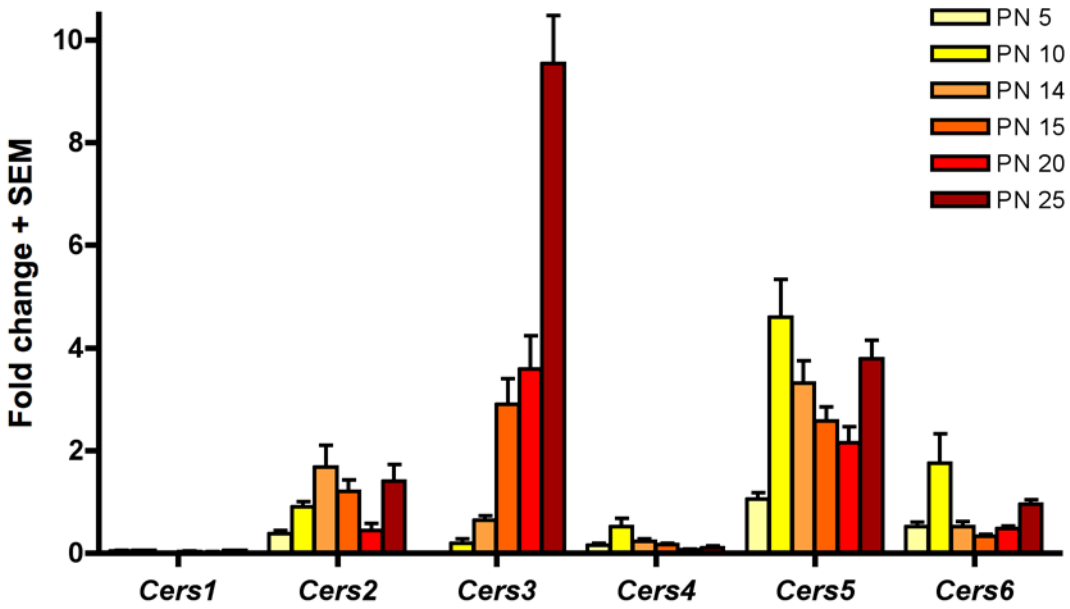

Figure 19. Testicular *Cers3* mRNA is strongly upregulated during the first wave of spermatogenesis in mice.

Cers mRNA expression of isolated cDNA from mice testes at PN 5 to 25 was determined by quantitative RT-PCR. Relative fold expression was calculated using the $\Delta\Delta C_T$ method. ΔC_T represents the normalized threshold cycle (C_T) value corresponding to the difference between C_T of each Cers and the C_T of the housekeeping gene, here Gapdh. Normalized ΔC_T values were compared to normalized ΔC_T of Cers5-mRNA at PN 5. Data represents isolated mRNA of minimum 3 animals per group with technical duplicates. Error bars represent the SEM.

Cers3 mRNA exhibited a tremendous upregulation of over 4.5-fold change during PN 14 to 15, which coincided shortly afterwards with the onset of ULC-sphingolipid expression. Subsequently, the levels of sphingolipids containing ULC-PUFA moieties remarkably increase simultaneously with the mRNA levels of *Cers3*. Contrarily, *Cers2, Cers5* and *Cers6* mRNA concentrations exhibited a moderate downregulation.

Collectively, these findings evidence a correlation between *Cers3* transcriptional levels and the biosynthesis of ULC-sphingolipids.

3.1.3. *Cers3* and ULC-PUFA sphingolipid expression are restricted to differentiated male germ cells

Previous immunohistological studies by Sandhoff et al. localized fucosylated GSLs solely in testicular germ cells, excluding their localization in both Sertoli and interstitial cells (Sandhoff et al., 2005). Taking into consideration that FGSLs mainly contain ULC-PUFA residues, the enzyme responsible for the incorporation of these residues must be likewise localized in germ cells.

In order to provide additional evidence supporting the requirement of CerS3 for the synthesis of ULC-sphingolipids, the ceramide synthase expression levels were determined in germ cells. In this regard, a mouse model lacking intact differentiated germ cells, *i.e.* preleptotene and leptotene spermatocytes, was used for these studies. Kit^{W-v}/Kit^{W} mutant mice lack the c-kit receptor, which is necessary for the stem cell factor ligand in order to regulate the proliferation and differentiation of stem cells. Consequently, Sertoli cells and only a few undifferentiated spermatogonia reside at the basal lamina, while further differentiated germ cells undergo apoptosis. Besides Sertoli cells, other cell types localized in the interstitium, *e.g*. Leydig cells, were unaffected by the lack of the c-kit receptor, as histological analysis of mutant seminiferous tubules revealed (Rabionet et al., 2008).

Cers expression levels were determined in mRNA isolated from testes of Kit^{W-v}/Kit^{W} mutant and control mice, and further subjected to quantitative RT-PCR for transcriptional analysis.

The mRNA profile of control murine testes revealed the expression of *Cers2, Cers3, Cers5* and *Cers6*, corroborating previous findings. The transcripts of all four ceramide synthases were decreased in mutant testes, however significant amounts of *Cers2*, *Cers5* and *Cers6* could still be detected in Kit^{W-v}/Kit^{W} mutant testes. These results indicate that *Cers2*, *Cers5* and *Cers6* are not exclusively expressed in differentiated germ cells. Particularly, *Cers5* mRNA was barely decreased in mutant testicular mRNA, which might indicate a major expression of this ceramide synthase homologue in testicular somatic cells. On the other hand, *Cers2* and *Cers6* were decreased to 20% and 45% of control values, respectively, suggesting their expression in either somatic cells and/or residual spermatogonia in addition to differentiated germ cells.

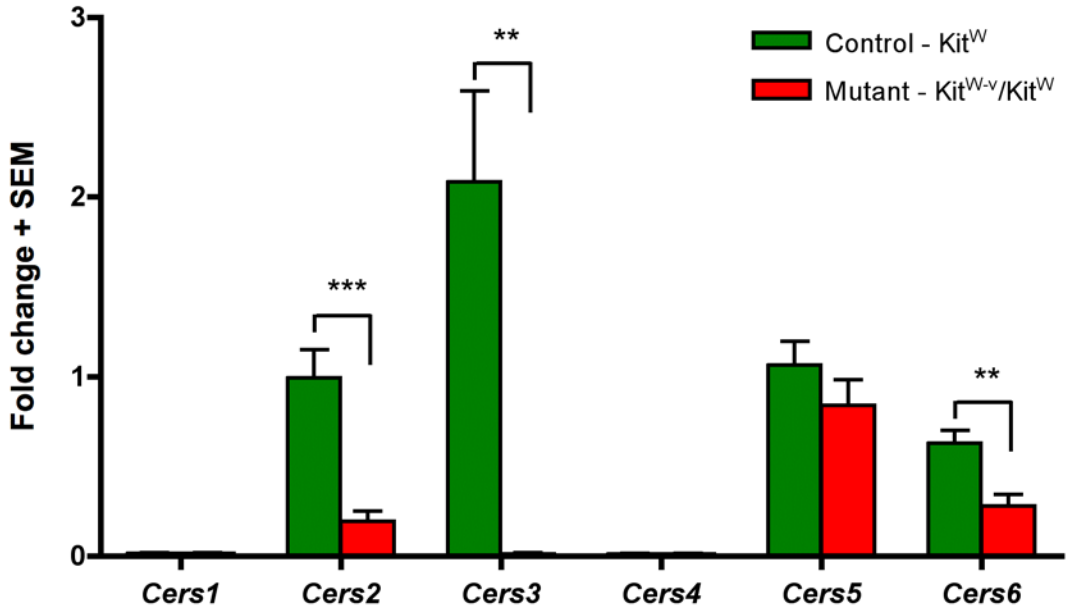

Figure 20. "Germ-cell free" testes of Kit^{W-v}/Kit^{W} mice are devoid of *Cers3* mRNA expression.

Quantitative RT-PCR analysis of Cers mRNA of isolated cDNA from mutant mice testes that lack differentiated germ cells. Relative fold expression was calculated using the comparative C_T method. Normalized ΔC_T values were compared to normalized ΔC_T of control Cers5-mRNA.

In contrast, mutant Kit^{W-v}/Kit^{W} testes were completely depleted of *Cers3* mRNA, implying that *Cers3* expression is restricted to differentiated germ cells.

The testicular sphingolipid pattern of mutant mice determined by ESI-MS/MS revealed the complete lack of sphingolipids containing ULC-PUFA moieties, thus indicating their localization in differentiated germ cells (Rabionet et al., 2008). Hence, the complete loss of *Cers3* mRNA expression correlates with the absence of ULC-sphingolipids in testis. Taking all these results into account and the overall decrease of *Cers* mRNA in infertile mutant mice, the only significant decrease that could be responsible for the loss of ULC-sphingolipids is that of *Cers3* transcript.

In summary, the transcriptional analysis of the ceramide synthases in combination with the ULC-SL expression in juvenile and mutant Kit^{W-v}/Kit^{W} mice testes strongly suggested a leading role of CerS3 in the synthesis of these unconventional sphingolipids.

3.2. Characterization of ceramide synthase 3

Understanding the biosynthetic requirements of these unusual ULC-sphingolipids is a *sine qua non* condition to gain deeper insight into their functional role in spermatogenesis and the epidermal permeability barrier. In this regard, genetic, topological and enzymatic localization analyses, in conjunction with enzymatic assays were performed.

3.2.1. The ceramide synthase 3 gene

Ceramide synthase 3 (*Cers3*, officially denominated *Lass3*) mRNA was first isolated from mouse testis in our department (Sandhoff et al., unpublished results). The identified amino acid sequence could be corroborated by a succeeding study, which in addition identified 36 amino acid residues at the *N*-terminus (Mizutani et al., 2006).

Phylogenetically, *Cers3* is highly conserved in all vertebrates, exhibiting a 78% homology between the mouse and the human protein, as determined by sequence alignment (ClustalW v 1.83, Figure A1). The mouse *Cers3* gene encodes for 419 amino acids in 11 coding exons, with a predicted molecular weight of 50.0 kDa. The additional 5'-prime coding exon of the mouse genome is lacking in the homologous human protein. Therefore, the human *Cers3* gene encodes for 383 amino acids with a predicted molecular weight of 46.1 kDa.

The ceramide synthase genes are characterized by the lag1 motif, a highly conserved stretch of 52 amino acids required for the catalytic activity of these enzymes (Spassieva et al., 2006). The lag domain in mouse is comprised of the totality of exon 8, spanning to the last 2 amino acids of exon 7 and the first seven of exon 9 (exons 6 to 8 in humans). In a broader manner, the lag1 motif has been described to reside in the Tram-Lag-CLN8 (TLC) domain, a region of 201 amino acids contained in 16 additional proteins besides *Cers3* (Winter and Ponting, 2002). The TLC domain is flanked by exon 4 to 10 in the mouse protein, and exon 3 to 9 in the human *Cers3*.

A shortened homeobox (or hox) domain is present in all ceramide synthases except for *Cers1*. In *Cers3*, the hox domain is composed of 44 residues (according to Prosite database) located between exon 3 and 4 (exon 2 and 3 for humans).

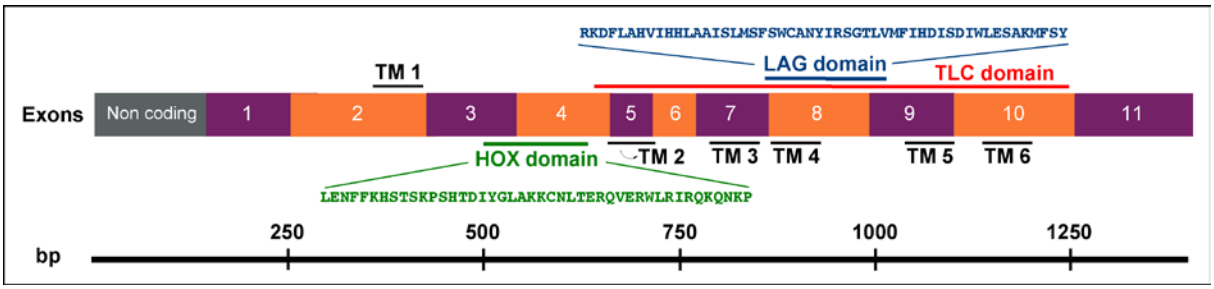

Figure 21. Genomic organization of mouse *Cers3*.

Cers3 (Gene ID mouse: 545975 and human 204219) *is composed of 11 exons in mice and 10 exons in humans. Likewise its family homologues, Cers3 is characterized by the lag1 domain included in the broader Tram-Lag-CLN8 (TLC) domain. Topology analysis predicted 6 transmembrane (TM) domains, with about half of the lag1 motif residing in TM4. Additionally, the homeobox domain is predicted to face the cytosolic side between TM1 and TM2.*

3.2.2. The transmembrane topology of ceramide synthase 3

Hydrophobicity profile analysis was performed in order to predict the membrane-spanning segments of CerS3. The topology of CerS3 as predicted by TopPred II *(Claros and von Heijne, 1994)* revealed 6 transmembrane spanning (TM) domains, as shown in the upper cutoff (red) of the following graph:

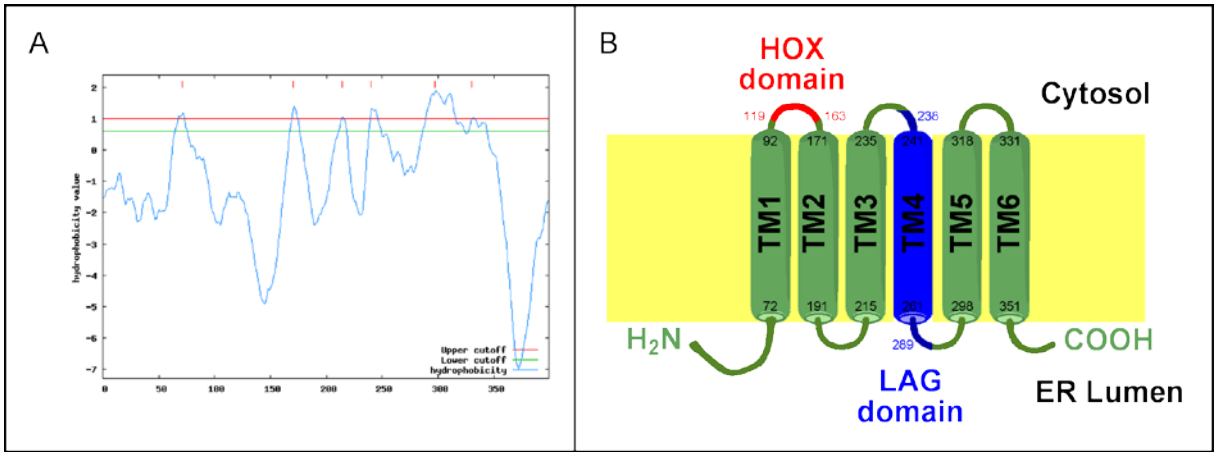

Figure 22. Topology analysis and proposed model for CerS3.

A) Hydrophobicity plot of murine Cers3 as predicted by TopPred. B) Membrane topology model of CerS3 indicating the predicted localization of the transmembrane domains, as well as the HOX and the LAG domain. The first and last amino acid positions are indicated for each domain.

Less restringent algorithms have suggested up to 8 TM for the yeast ceramide synthases and 7 TM for all mammalian CerSs (Kageyama-Yahara and Riezman, 2006; Teufel et al., 2009). Accordingly, the hox domain might reside in the cytosolic loop between TM1 and TM2, and both *N*- and the *C*-termini are predicted to face the luminal side of the endoplasmic reticulum (ER).

Presumably, the lag1 domain may be located in the entire TM4, and additionally exposed to both cytosolic and luminal sides of the ER. This model is partially in agreement with the model suggested by Mizutani and coworkers, however they proposed 5 transmembrane spanning domains to be present in CerS3 (Mizutani et al., 2006).

3.2.3. CerS3 is an ER-resident protein

The subcellular localization of CerS3 has not yet been reported. To address this issue, overexpression of CerS3 with a *C*-terminal EGFP tag was conducted in HeLa cells by means of lipofection. The fluorescence signals of mCerS3-EGFP were compared to those generated by the lysosomal, the golgi compartment and the ER protein-specific markers.

CerS3-EGFP exhibited no colocalization with neither Lamp1 nor Golgin-97 markers, the distribution of whose indicates the location of lysosomes and the Golgi apparatus, respectively. In contrast, CerS3-EGFP was found to colocalize with the protein disulfide isomerase (PDI), demonstrating that CerS3 is an ER-resident protein. Additionally, CerS3-EGFP fluoresecence signals appeared to be distributed in the nuclear envelope.

These findings are in agreement with previous studies indicating the intracellular localization of the remaining ceramide synthases within the ER (Mizutani et al., 2005; Riebeling et al., 2003; Venkataraman et al., 2002) and the nuclear envelope (Mizutani et al., 2005).

Despite the lack of an ER retrieval motif as determined by SignalIP, CerS3 resides at the site of the elongation of fatty acids and ceramide synthesis (Jakobsson et al., 2006; Teufel et al., 2009).

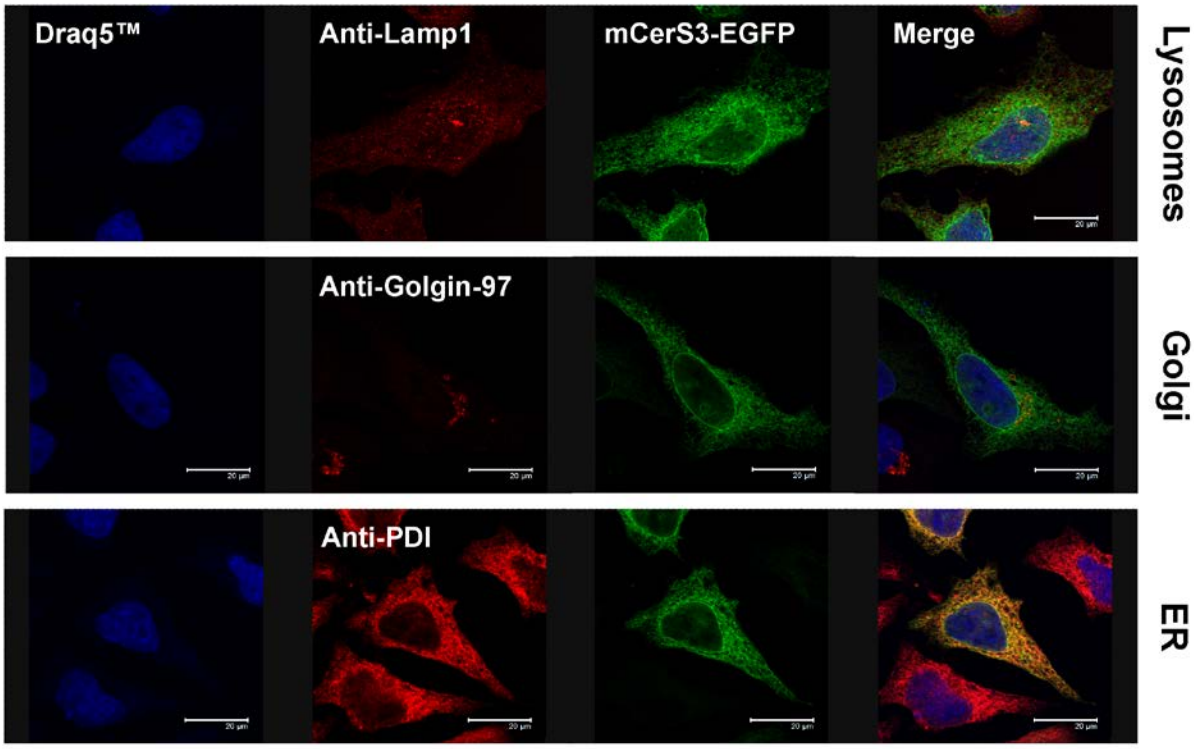

Figure 23. mCerS3-EGFP colocalizes with the ER marker, anti-PDI.
The fluorescence signals detected from the overproduction of CerS3-EGFP in HeLa cells were compared to those generated by the lysosomal marker (anti-Lamp1), the Golgi (anti-Golgin-97) and the ER marker (anti-PDI), shown in red. Nuclear staining with Draq5™dye is shown in blue, while GFP derived fluorescence is shown in green.

3.2.4. CerS3 synthesizes ULC-sphingolipids in living mammalian cells

In the past few years, significant efforts have been made to define the biosynthetic requirements of the ceramide synthases *in vitro*, in order to provide the basis for elucidating the role of specific ceramide species *in vivo*. As described above, each of the six mammalian ceramide synthases have been shown to have affinity for a restricted subset of acyl-CoAs, with the exception of CerS3. Mizutani and colleagues reported a relative broad substrate specificity of CerS3, with certain preference towards long and very long chain acyl-CoAs, namely 18:0-CoA and 24:0-CoA (Mizutani et al., 2006). However, the affinity of CerS3 for ultra long chain acyl residues, as those mainly expressed in skin and testis were not included in those studies.

To address this issue, the *in vitro* specificity of CerS3 towards a wide range of acyl-CoAs including ULC-acyl-CoAs (16:0 to 28:0-CoA) was examined. From the remaining five CerS homologues, CerS2 has been described to best incorporate acyl residues with the longer carbon chain length (22:0 to 26:0-CoA) for the synthesis of the corresponding ceramides (Laviad et al., 2008). All other CerS homologues have been reported to produce ceramides with shorter acyl moieties (Lahiri et al., 2007). Additionally, CerS2 has the highest homology with CerS3, and likewise its mRNA was expressed in skin and testis. However, mRNA and sphingolipid expression analysis performed in testes lacking differentiated germ cells, as well as juvenile mice testes during the first wave of spermatogenesis suggested that CerS3 is the unique enzyme capable of producing ULC-ceramides.

In order to corroborate these findings and to establish whether solely CerS3 incorporates ULC-acyl-CoAs to sphingoid bases, the preference of CerS3 and CerS2 towards acyl-CoAs was tested by means of ceramide synthase assays.

3.2.4.1. CerS3 does not modify the ceramide profile in the absence of ULC-acyl-CoAs

The first approach to demonstrate that CerS3 is the enzyme responsible for the formation of ULC-(PU)FA sphingolipids included an activity study of the enzyme in transient transfected cells. As it has been shown for other ceramide synthase homologues, overexpression of a given CerS in either HEK-293T or HeLa cells produced a change in the ceramide pattern reflecting the specificity of the enzyme towards the fatty acid substrates (Riebeling et al., 2003). In this regard, HeLa cells were transfected with a plasmid encoding for *mCers3* gene in the *N*-terminus of an EGFP tag. However, the sphingolipid profile upon 24 h post transfection exhibited no change in the fatty acid pattern for neither ceramide nor any of its direct metabolites, albeit the expression of the fusion protein in transfected cells was confirmed by immunoblot analysis (Figure 24A). We reasoned that overexpression of CerS3 had no effect in the sphingolipid pattern due to the lack of its fatty acid substrates in these cells, and not due to a lack of activity of the fusion protein. In order to circumvent this issue, we tried to expose the cells with the adequate substrates using different approaches.

First, we attempted to introduce the ULC-FA substrates by performing double transfections with CerS3 together with genes belonging to the elongation of very long chain fatty acid (*Elovl*) gene family. The *Elovl* genes are responsible for the synthesis of activated fatty acids with more than 16 carbons in length via the addition of 2 carbon units from malonyl-CoA to a long chain acyl-CoA substrate. At the starting point of this work, reliable data on the substrate specificity of the seven elongases was limited, therefore we attempted to determine the potential elongase responsible for the synthesis of ULC-acyl-CoAs by means of transcriptional analysis (Figure 24C). *Elovl2* and *Elovl5* mRNA were found to be the most prominent in testis, however *Elovl5* transcript was linked by gene array data (available at www.germonline.org) to be localized in spermatogonia and somatic Sertoli cells (Chalmel et al., 2007). Taking into account that these cells do not contain ULC-sphingolipids, and that its transcript levels were decreased at the onset of ULC-sphingolipid expression (Shima et al., 2004), *Elovl5* was rejected as a potential candidate, leaving *Elovl2* as the most promising candidate.

On the other hand, Elovl4 was additionally included as a possible enzyme for generating ULC-acyl-CoAs, despite the fact that its mRNA levels were not prominent in juvenile murine testes. The rationale behind relies on several studies on Elovl4 deficient mice, where it was shown a complete depletion of epidermal ceramides with FA residues longer than 28 carbon atoms, as well as an accumulation of cerotoyl-ceramide (26:0-Cer) (Li et al., 2007; McMahon et al., 2007b; Vasireddy et al., 2007). Taken together, these results point out Elovl4 as an additional candidate enzyme for the synthesis of ULC-acyl-CoAs, which we hypothesized to be the substrates for CerS3.

However, neither Elovl2 nor Elovl4 double transfections with CerS3 exhibited increased levels of montanoyl-ceramides (28:0-Cer) or any other sphingolipid species containing ULC-acyl moieties. Although overexpression of both fusion proteins could be confirmed by Western blot, as shown with Elovl2 and CerS3 co-transfections (Figure 24B), the sphingolipid pattern of these cells did not exhibit any significant changes. In particular, no increase for m/z 692.7 or 854.7 corresponding to Cer(d17:1, 28:0) and GlcCer(d17:1, 28:0) could be detected.

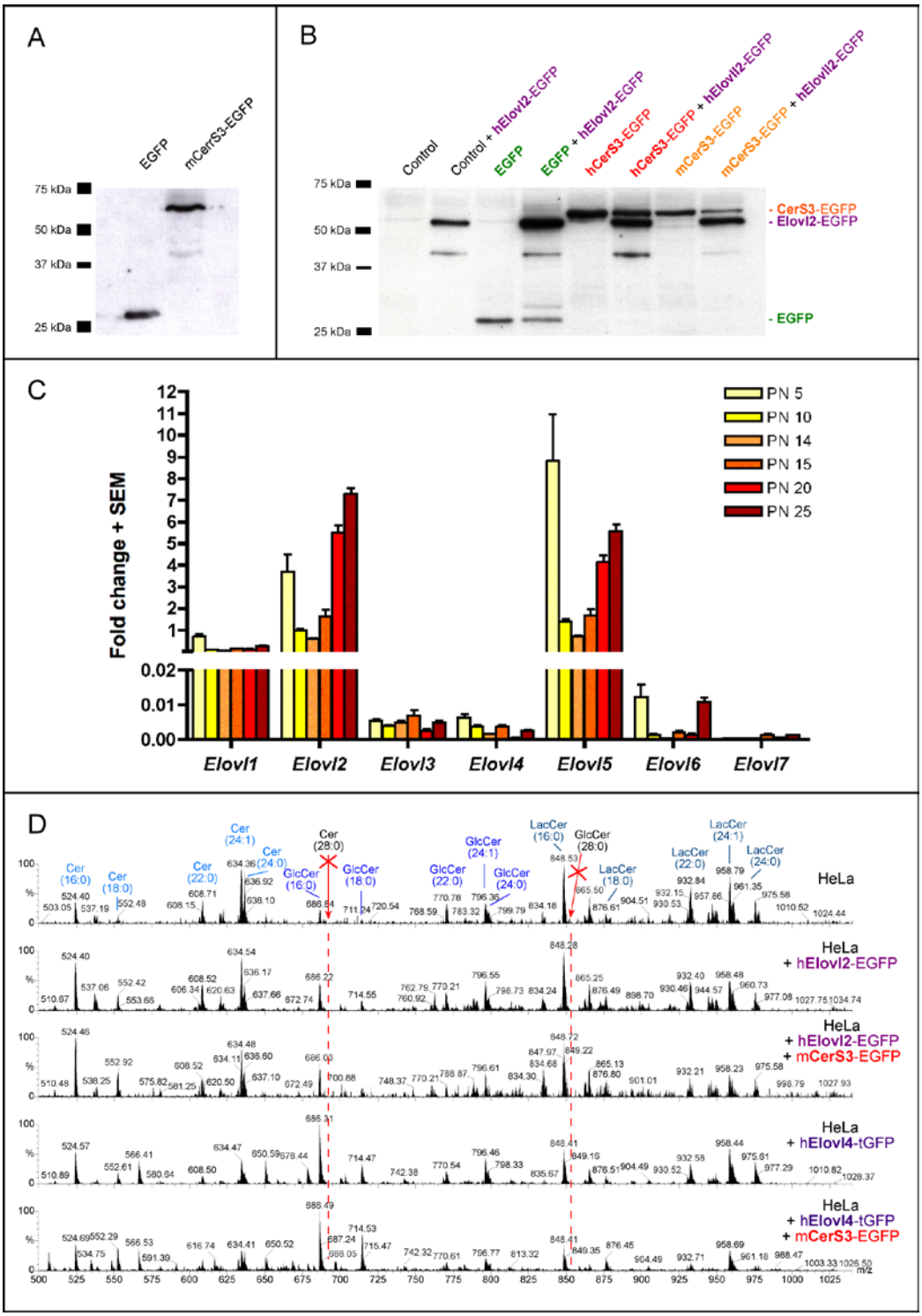

Figure 24. Coexpression of Elovl2/4 and CerS3 does not produce ULC-SLs.
(A) Immunoblot analyses demonstrating overexpression of CerS3-EGFP and control EGFP, and (B) cotransfections with Elovl2-EGFP in HeLa cells. (C) Transcript analyses of the Elovl genes during murine testicular development, as determined by qRT-PCR. (D) Mass spectrometric analyses of ceramide, glucosylceramide and lactosylceramide species in HeLa overexpressing Elovl2/4 and CerS3.

These results provide evidence for the requirement of additional metabolites/enzymes being involved in the production and/or transport of ULC-acyl-CoAs that might be necessary for the complete biosynthesis of ULC-sphingolipids, besides of Elovl2/4 and CerS3. Taking into consideration that with the current stage of knowledge many of the processes regarding the activation and transport of fatty acids, particularly of ULC-FA, are still elusive, we decided to establish the ceramide activity assay by a different approach.

The major difficulty in establishing an adequate assay for CerS3 was the lack of availability of the fatty acid substrates. As stated above, ULC-FAs are restricted to testis, epidermis, and in lesser extent are expressed in the rod outer segments of the retina. The latter have been reported to be incorporated into membrane phospholipids, mainly phosphatidylcholine (Aveldano and Sprecher, 1987). Therefore, we attempted to overexpress CerS3 in an immortalized cell culture system originated from these tissues, expecting that their fatty acid pattern might contain the suitable substrates for CerS3. The immortalized testicular cell types TM4 (Sertoli cells) and K9 (Leydig cells) were studied upon transfection with a CerS3 encoding plasmid. In neither cell lines the concentration of ULC-FAs reached 1%, and thus this minimal amount of substrate was obviously not sufficient to detect an increment of montanoyl- and longer acyl chain ceramides due to the activity of CerS3 overexpression. Retinoblastoma Y79 suspension cells were also subjected to transfection by means of magnetofection or liposome-based transfection, however the gene delivery rates achieved were not sufficient for a quantitative production of the enzyme.

Additional efforts were made to obtain the ULC-FA substrates by means of fatty acid isolation from GM2 activator protein (GM2AP) deficient mice testis. This cofactor is required in conjunction with the lysosomal β-hexosaminidase isoenzymes for the degradation of GM2 and Gg_3Cer, which are intermediate products of FGSL degradation in testis (Liu et al., 1997). Correspondingly, the testes from these mutant mice accumulate both GM2 and Gg_3Cer containing mainly ULC-FA residues. Therefore, fatty acids were extracted from $GM2AP^{-/-}$ mice testes by acid hydrolysis, and subsequently exposed to K9 or HeLa cells overexpressing CerS3. However, the sphingolipid analysis from these cells revealed no incorporation of fatty acids longer

than 26 carbon atoms into ceramide or sphingomyelin (Figure 25). Presumably, the insolubility of these highly hydrophobic compounds in the aqueous culture medium, and/or the deficiency of an effective fatty acid transporter across the plasma membrane, caused the failure of this CerS3 transfection assay.

Considering that ULC-acyl-CoAs are not commercially available, and that all attempts to obtain these substrates via biochemical methods led to failure, we aimed to synthesize ULC-acyl-CoAs chemically.

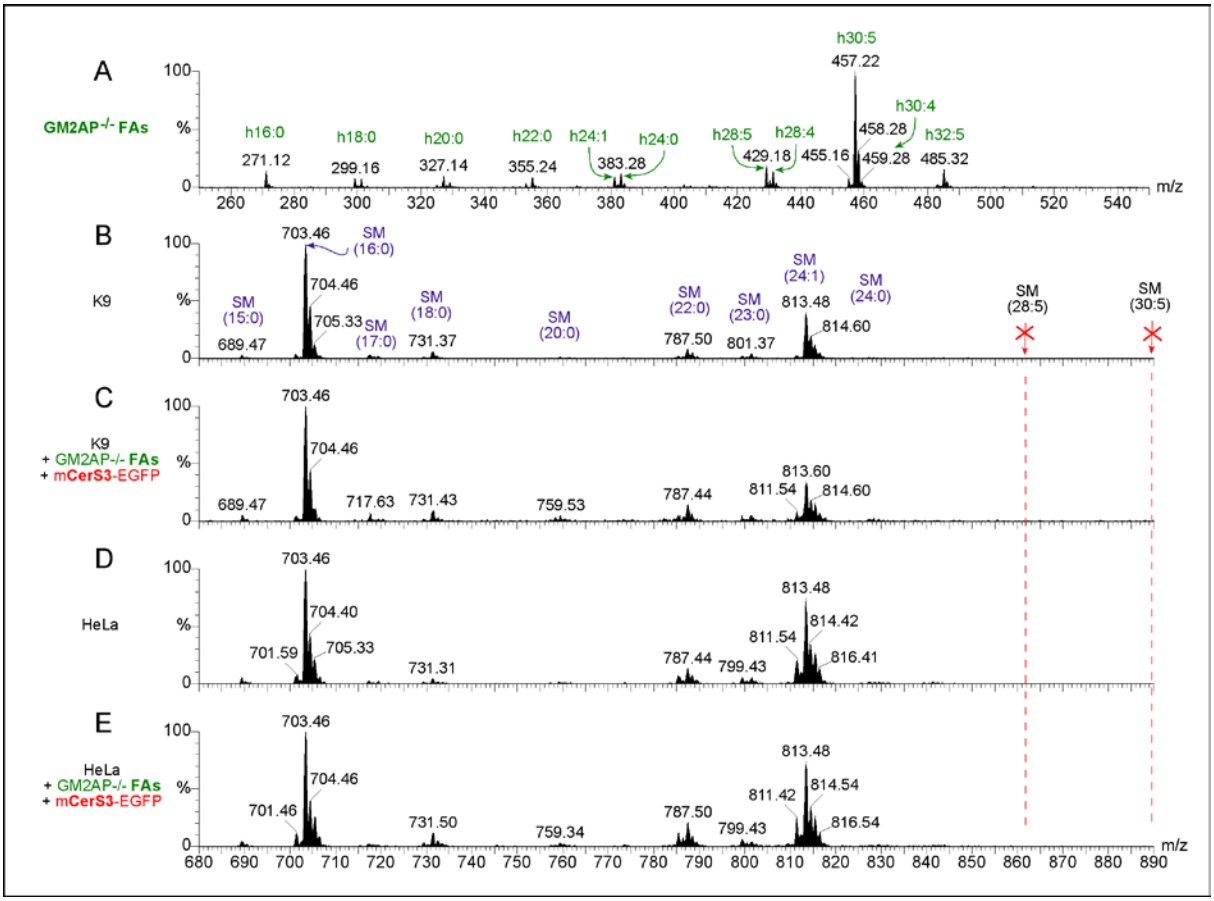

Figure 25. CerS3 overexpressing K9/HeLa cells with media supplementation rich in ULC-FAs do not produce ULC-ceramides.

(A) Mass spectrometric analyses of fatty acids isolated from GM2AP$^{-/-}$ mice testes. The base peak corresponded to hydroxylated fatty acid with 30 carbon atoms in length with 5 olefinic residues. Media supplementation of GM2AP$^{-/-}$ derived FAs into K9 (C) and HeLa cells (E) transfected with CerS3-EGFP did not alter the sphingolipid pattern in relation to control K9 (B) and HeLa (D) endogeneous sphingolipids. For MS, sphingomyelin was detected with parent scan at m/z +184 and fatty acids with neutral loss of m/z +46.

3.2.4.2. Synthesis of ULC-acyl-CoAs

Epidermal and testicular ULC-sphingolipids exhibit a structural diversity, which might reflect their functional specialization. The majority of epidermal ceramides incorporate ω-hydroxylated ULC-acyl-CoAs, which are mainly saturated. Contrary, in testis, ceramide incorporates mostly polyenoic ULC-acyl resiudes, which to a great extent are α-hydroxylated. Regardless of this existent heterogeneity within testicular and epidermal ULC-sphingolipids, we assumed that the enzymatic specificity of the ceramide synthases relies primarily on the hydrocarbon length of the acyl donor, subjugating modifications by hydroxylation or saturation to negligible levels. The basis for this assumption is that: i) CerS2 have been reported to incorporate saturated and monosaturated acyl-CoA substrates with comparable CerS activities (Laviad et al., 2008), and that ii) all CerS homologues could produce α-hydroxy-ceramides with similar chain length preferences as their respective non-hydroxy substrates (Mizutani et al., 2008). Taking this into consideration, saturated acyl-CoAs longer than 26 carbon atoms in length should be adequate substrates for CerS3.

The synthesis of ULC-acyl-CoAs involved a three-step reaction. First, fatty acids were activated with *N*-hydroxysuccinimide in the presence of dicyclohexylcarbodiimide (DCC) to generate the *N*-hydroxysuccinimide esters of the fatty acids, which will be used as the acylating reagent. Subsequently, the activated fatty acids were coupled to coenzyme A (CoA) in two consecutive one-pot reactions to yield the acyl-CoAs.

The coupling of CoA was performed via the *in situ* transformation of coenzyme A into its polysilylated form, which is non polar and thus especially suitable for the formation of highly lipophilic long chain acyl-CoAs, such as the ULC-acyl-CoAs. This method developed by Lucet-Levannier and coworkers (Lucet-Levannier et al., 1995) avoids the use of a water-organic solvent binary mixture that had been previously used as the classical synthetic methodology (Al-Arif and Blecher, 1969). The cosolubilization of the highly hydrophophic acylating reagent containing the ULC-acyl residue in the binary mixture is the limiting factor, which could be bypassed by the use of the lipophilic derivative of coenzyme A under anhydrous conditions. Fluoro-desilylation of the polysilylated CoA under phase-transfer conditions with cesium

fluoride yielded the polyanionic form of CoA, which was subsequently coupled with the *N*-hydroxysuccinimide ester of the fatty acid to give the final acyl-CoAs.

The synthetic strategy of the non-aqueous in comparison with the classical aqueous method is illustrated in the following scheme:

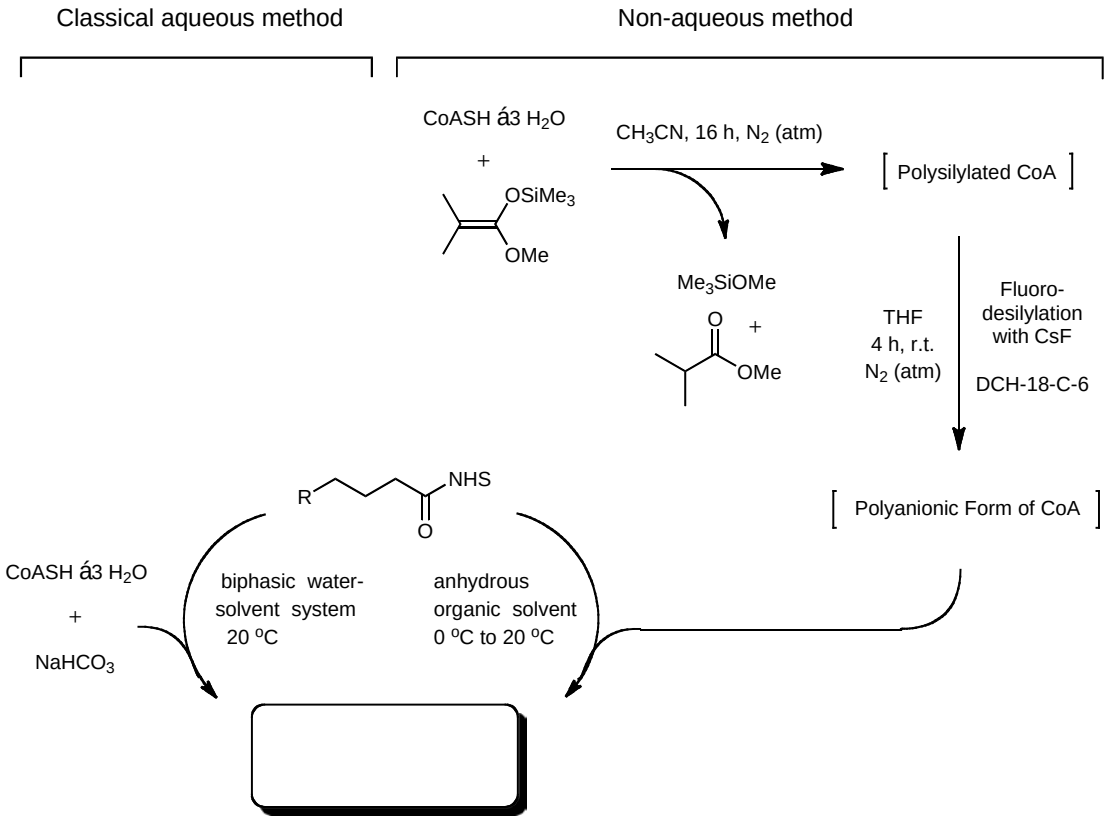

Figure 26. Synthetic scheme comparing classical aqueous and non-aqueous methods for the generation of acyl-CoAs.
ULC-acyl-CoAs were synthesized according to the non-aqueous procedure. This scheme has been modified from (Lucet-Levannier et al., 1995).

The crude product was partially purified by reverse-phase column chromatography, prior to quantification by mass spectrometry analyses with an acyl-CoA mixture of known concentration.

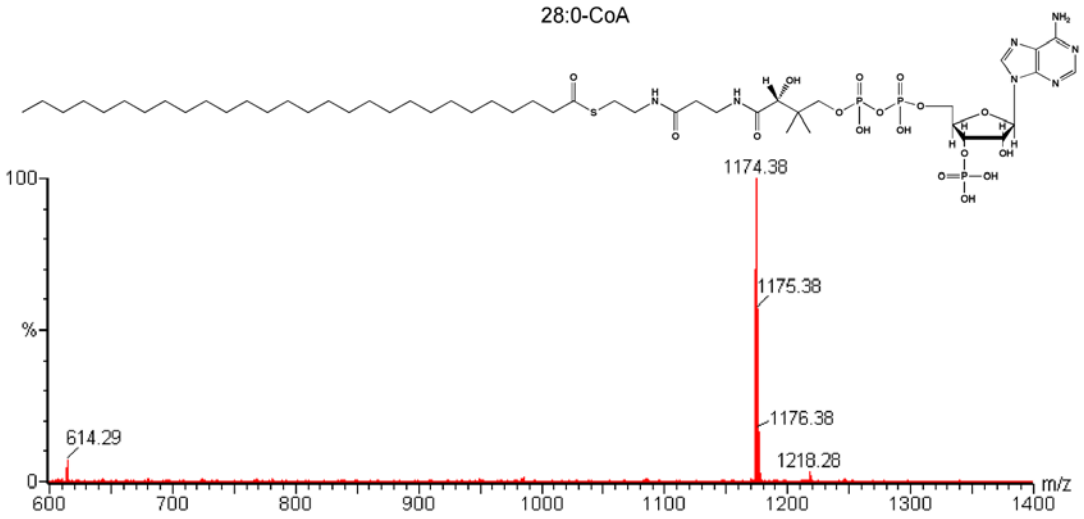

Figure 27. Mass spectrometric characterization of montanoyl-CoA.
Acyl-CoAs were detected with neutral loss of m/z +507.

3.2.4.3. Synthesis of ceramide internal standards

The substrate preference of CerS3 and CerS2 towards a wide range of acyl-CoAs, was established by means of a non-radioactive enzymatic assay in mammalian cells. Thus, the addition of a non-endogeneous sphingoid base (d17:1) enabled to distinguish the various ceramide species generated by CerS overexpression from those ceramides produced by the CerSs conventionally expressed in HeLa cells.

For quantification of *de novo* ceramides by electrospray ionization tandem mass spectrometry (ESI-MS/MS), ceramide internal standards with an appropriate d17:1-sphingoid base and appropriate acyl composition were synthesized. These internal standards were designed in a way that their *m/z* values could not interfere with those of the ceramide species to be analyzed.

Specifically, Cer(d17:1; 19:0) and Cer(d17:1; 25:0) were prepared via a two-step reaction. First, fatty acids were derivatized with *N*-hydroxysuccinimide (NHS) in order to activate the carboxylic acid by transforming into an ester with a good leaving group. Subsequently, sphingosine(d17:1) was coupled to the activated fatty acids, generating an amide bond through nucleophilic displacement of NHS.

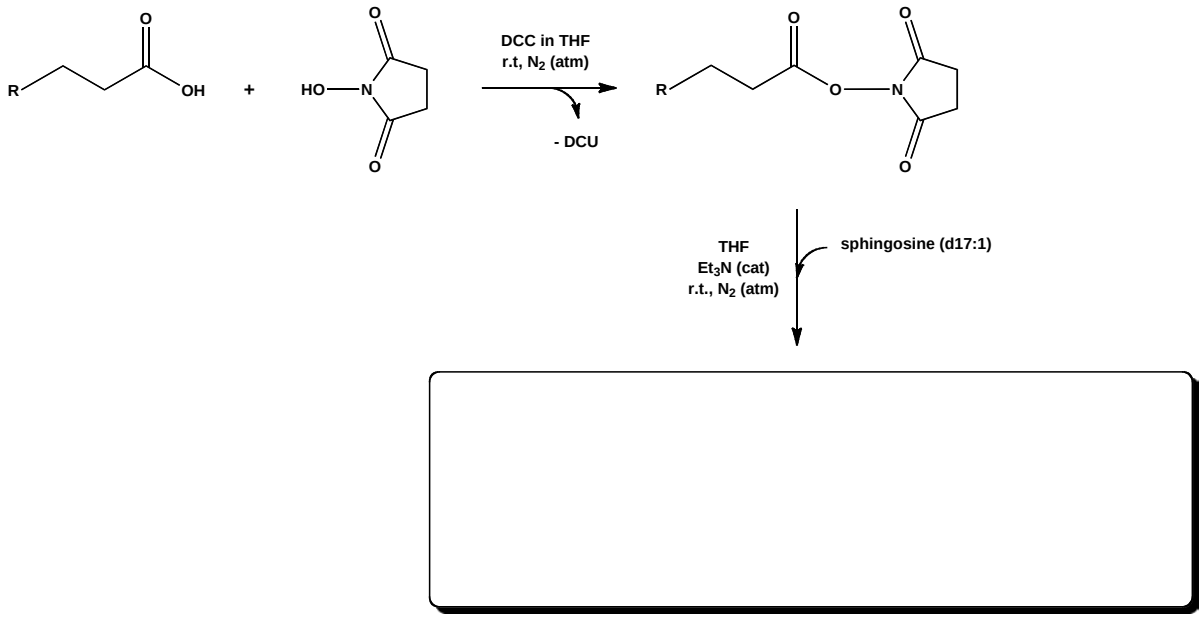

Figure 28. Synthetic scheme describing the preparation of ceramide internal standards.
Syntheses were performed as previously described with slight modifications (Sandhoff et al., 2002).

Crude ceramide products required purification by flash-column chromatography in order to remove excess of fatty acids and other unreactive species (supplemental Figure A2A). Subsequently, final products were characterized by ESI-MS/MS with precursor ion scan corresponding to the d17:1 shingoid base, and their quantification was performed by densitometric analyses via thin layer chromatography (supplemental Figure A2B). For that, a series of dilutions of the synthesized standards were spotted in parallel with ceramide standards with a conventional sphingoid base (d18:1).

For quantification of ceramide species produced by overexpression of specific CerSs, a 14 pmol mixture of each d17:1-ceramide internal standard was added into equivalent lipid aliquots corresponding to 80–100 mg of protein.

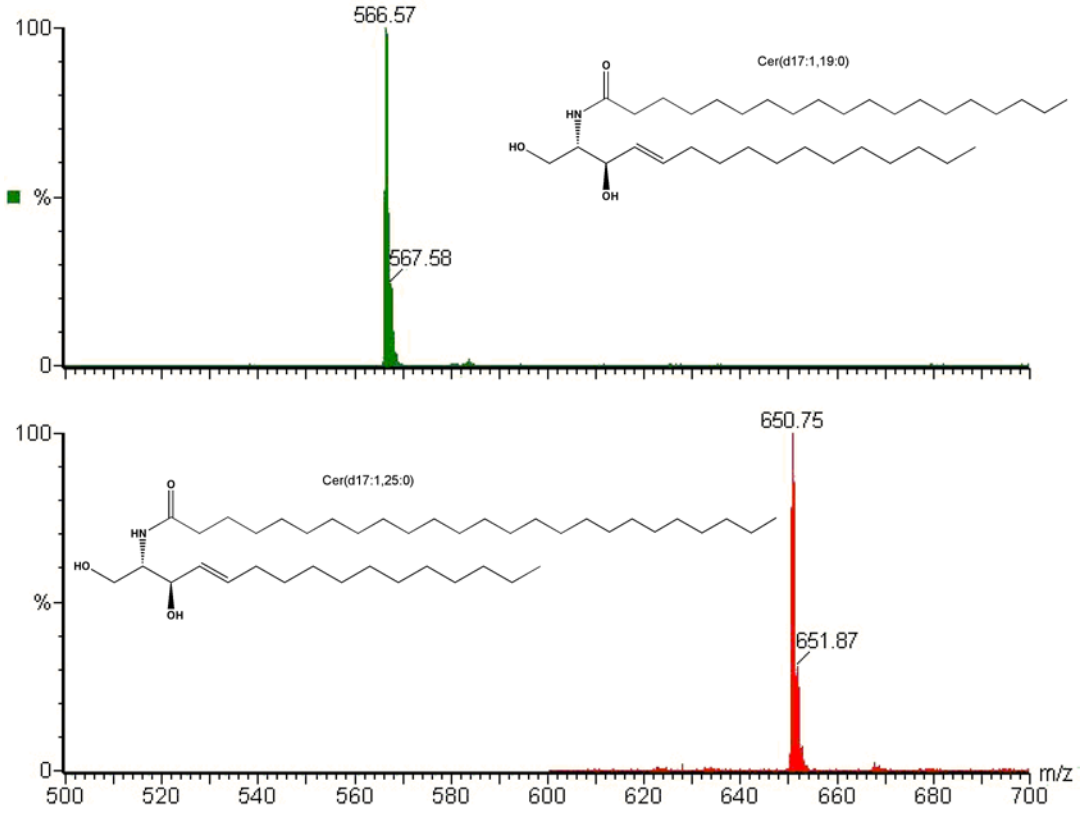

Figure 29. Mass spectrometric characterization of internal standards.
Ceramides were detected with precursor ion scan of m/z +250 corresponding to the sphingoid base (d17:1).

3.2.4.4. The ceramide synthase assay

To definitely establish the role of CerS3 in the biosynthesis of ULC-ceramides, a non-radioactive enzymatic assay in living mammalian cells was established. To accomplish this, stable HeLa cells expressing either the mouse or the human CerS3 with a *C*-terminal EGFP tag were generated by retroviral transduction.

Thus, virions were produced in the packaging cell line HEK-293T following a triple transfection with a vector encoding for the gene of interest (CerS3-EGFP or control EGFP), in addition to two vectors responsible for the formation of the viral proteins (pVPack-GP and pVPack-Eco). To enable the infection of HeLa cells, CerS3 or control EGFP cDNA were inserted into a murine leukemia derived retroviral vector. The assembled retroviral particles in the packaging cell line were collected and used for infecting genetically modified $HeLa_{MCAT1\text{-}rtTA2\text{-}M2}$ cells. These HeLa cells were

previously modified to stably express the murine receptor protein (mCAT1), which is required to achieve the infection by the murine leukemia derived retroviral particles.

In addition, $HeLa_{MCAT1\text{-}rtTA2\text{-}M2}$ cells expressed the doxycycline-sensitive transactivator (rtTA2-M2). This transcription factor binds to the tetracycline-responsive element, which is encoded upstream of CerS3 (or control), and thereby enabling the expression of the gene of interest exclusively under doxycyline induction. HeLa cell lines expressing mCerS3-EGFP, hCerS3-EGFP and control EGFP were generated according to this procedure. For more details refer to the corresponding section in the material and methods (2.2.2.4.).

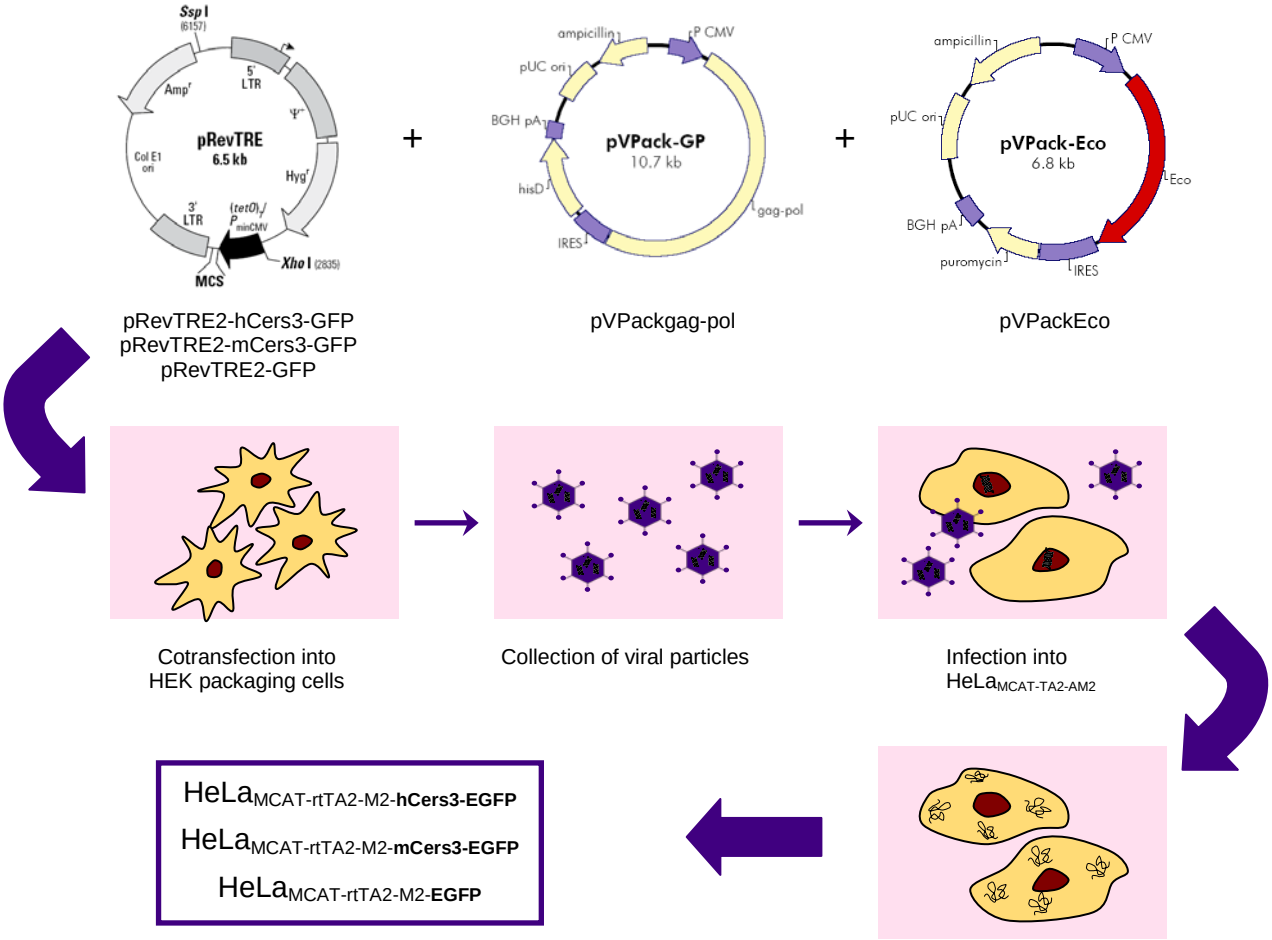

Figure 30. Schematic representation of the generation of stable cell lines by retroviral transduction.

pRevTRE plasmid map was acquired from Clonetech, whereas pVPackgag-pol and pVPackEco were obtained from Stratagene.

The inducible transgene expression of the recombinant mCerS3, hCerS3, and control EGFP, as well as hCerS2 were confirmed by flow cytometric analyses and immunoblotting (supplemental Figure A3 and Figure 31). Using Western blot analyses, fusion proteins were detected using an anti-GFP antibody. Although, both mouse and human CerS3 homologues were detected as one single band at about 63 kDa (Figure 31A), the recombinantly expressed human CerS2 cells exhibited four specific bands that very likely arise from *N*-glycosylation heterogeneities (Figure 31B).

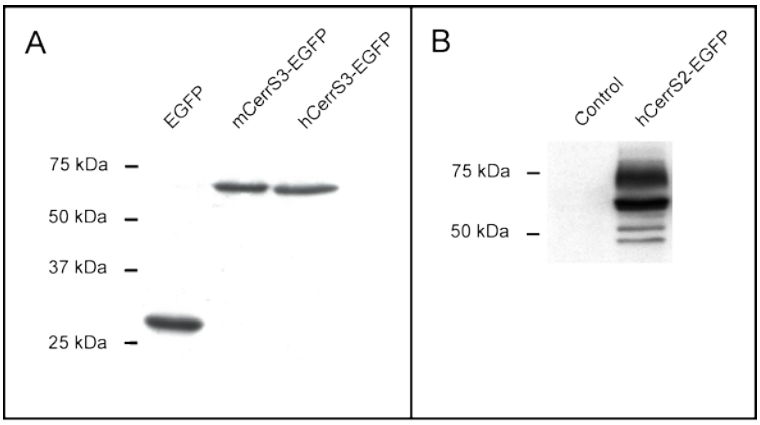

Figure 31. Confirmation of CerS3 and CerS2 recombinant protein expression in HeLa cells by immunoblotting.
Total cell lysates of overexpressing HeLa cells were separated on a 10% SDS-PAGE, and transferred onto nitrocellulose membranes. Fusion proteins were detected using an anti-GFP antibody.

The ceramide synthase activities of the CerS2 and CerS3 homologues were tested in living HeLa cells (Figure 32A). Following 52 h of transgene induction with doxycycline, HeLa cells expressing CerS2 or CerS3 were exposed to a mixture of a wide range of saturated acyl-CoAs, which included the ULC-acyl-CoA, montanoyl-CoA (28:0-CoA). Simultaneously, the non-endogeneous d17:1-sphingosine substrate was supplemented into the culture medium for the duration of the assay in order to monitor newly synthesized ceramides (see above).

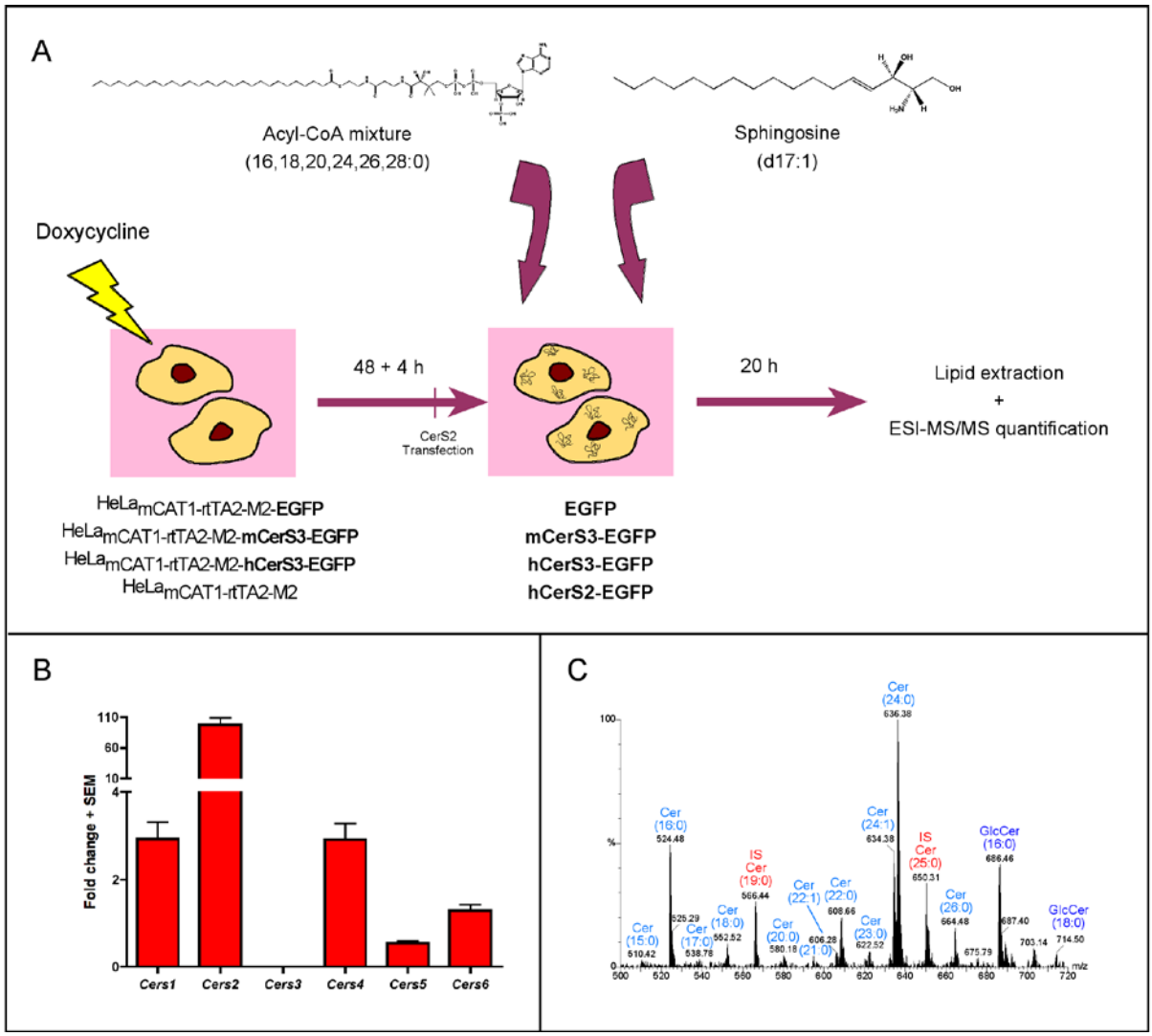

Figure 32. The ceramide synthase assay in living HeLa cells.

(A) Schematic respresentation of the experimental setup. Stable HeLa cell lines were induced for CerS3 (human and mouse) and EGFP expression by incubation with doxycycline, which binds to the tetracycline-controlled transactivator (rtTA2-M2), and ultimately activates transgene expression of the gene of interest downstream of the tetracycline-responsive element. Forty-eight hours after seeding untreated HeLa$_{mCAT1\text{-}rtTA2\text{-}M2}$ cells were transfected with an hCerS2-EGFP encoding plasmid. Ceramide synthase activity towards acyl-coA substrates was tested by addition of a saturated acyl-CoA mixture (16 to 28-CoA). Simultaneously, the addition of sphingosine (d17:1) enabled to monitor newly synthesized ceramides, which were extracted after 20 h of assay and quantified by ESI-MS/MS. (B) Transcript expression and (C) Cer/GlcCer profile of HeLa$_{mCAT1\text{-}rtTA2\text{-}M2}$ cells exposed to the acyl-CoA mixture and d17:1-sphingosine substrate.

Uninduced HeLa cells expressed all *Cers*-mRNA except of *Cers3,* which expression levels were barely detectable. The major transcript levels corresponded to those of *Cers2* (Figure 32B). Correspondingly, the main ceramide species expressed in HeLa cells were lignoceroyl- (24:0) and nervonyl-ceramide (24:1). Despite relatively low expression levels of *Cers5* and *Cers6*, the amount of palmitoyl-ceramide (16:0) was fairly high (Figure 32C). The levels of 18:0-Cer, 20:0-Cer, 22:0-Cer and 26:0-Cer were below the 7% of the total ceramide concentration.

Quantification of *de novo* ceramides produced by either the recombinantly expressed human or murine CerS3 upon incubation of the acyl-CoA mixture (16,18,20,24,26,28-CoA) to the cell culture media, demonstrated that both enzymes were able to synthesize ceramides using cerotoyl- (26:0) and montanoyl-CoA (28:0) as acyl donors (Figure 33B and 33D). Expression of CerS3 strongly induced the synthesis of ultra long chain acyl ceramides. Together the concentration of newly synthesized 26- and 28-ceramides accounted for over 25% of the total ceramides produced by the transgenic CerS3 (Figure 33A and 33C). Mass spectrometric analyses revealed that the absolute cerotoyl-ceramide concentration was increased by 5 fold, while montanoyl-ceramide was over 16 fold increased for the hCerS3 (Figure 33B and 33D). These results indicate that CerS3 has a higher affinity for 28:0- than for 26:0-acyl donors.

Although stearoyl-ceramide (18:0-Cer) and lignoceroyl-ceramide (24:0-Cer) were reported to be the substrates with the highest CerS3 affinity in studies lacking of ULC-CoAs, neither of them exhibited a significant increase in their concentrations upon CerS3 expression with the current conditions. Our results provide evidences that the cell-specific ceramide pattern not only depends on the expression levels of the ceramide synthases, but importantly is also based on the availability of the corresponding substrates. In the presence of ULC-acyl donors, solely cerotoyl-CoA and montanoyl-CoA were preferentially incorporated, demonstrating that they are *bona fide* substrates of CerS3.

In contrast, CerS2 or EGFP-control overexpressing cells generated significant amounts of ULC-ceramides upon induction of these proteins. The levels of lignoceroyl and cerotoyl-ceramides were neither significantly increased with CerS2 expression. However, the relative *Cers2* transcript levels account for over 90% of the

Cers-mRNA, and therefore an increased expression level did not differ significantly the concentration of its reported substrates.

In conclusion, our findings indicate that CerS3 acylates sphingoid bases with acyl-CoAs of 26 or longer carbon atom chains, exhibiting a preferential specificity for the longer acyl substrates in living mammalian cells.

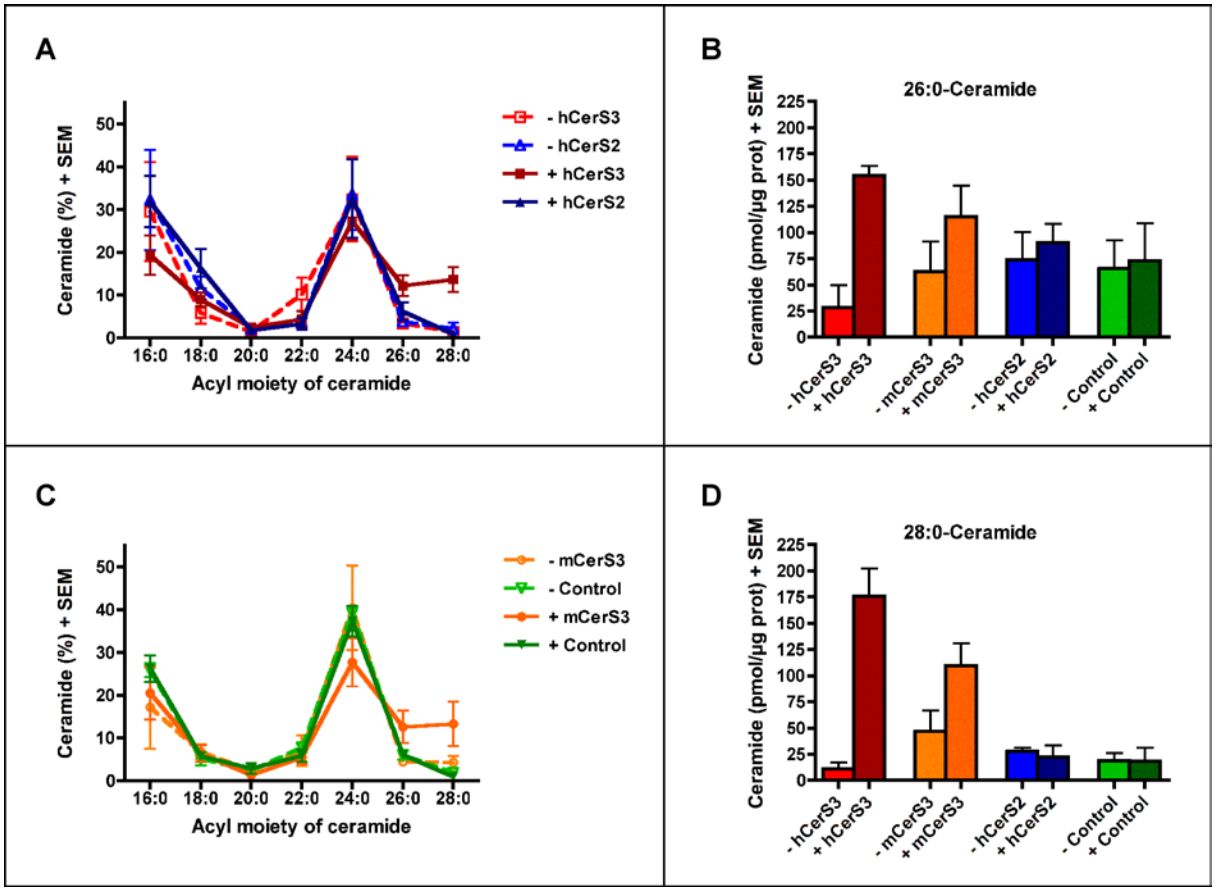

Figure 33. CerS3 synthesizes ULC-ceramides in living HeLa cells.
(A) Relative de novo acyl-ceramide (d17:1) concentrations in non expressing (-), as well as expressing (+) human CerS2 and CerS3 HeLa cells, and (C) mouse CerS3 and EGFP-control HeLa cells. Lipid isolation was performed after cells were incubated for 20 h with a saturated acyl-CoA mixture (16–28-CoA). Mass spectrometric quantification was performed using d17:1 long chain base internal standards. (B) Absolute cerotoyl-ceramide (d17:1, 26:0) and (D) montanoyl-ceramide (d17:1, 28:0) concentrations in CerS2, CerS3 and control cells.

3.3. Disturbed epidermal permeability barrier and keratinocyte differentiation facilitates microbial invasion in CerS3 deficient mice

3.3.1. Characterization of CerS3 deficient mice with a targeted disruption of *Cers3*-exon 7.

In order to confirm the *in vitro* findings and to elucidate the functional role of CerS3 and ULC-sphingolipids *in vivo*, characterization of CerS3$^{d/d}$ mice were conducted. The constitutive depletion of *Cers3* was achieved via the *Cre*-loxP-mediated recombination. In this regard, germline transmission CerS3-floxed mice with loxP sites flanking exon 7 were mated with *Cre*-deleter mice to generate a systemic deletion of exon 7 of the *Cers3* gene.

To verify the appropriate homologous recombination of mutant *Cers3,* PCR analyses with mouse genomic DNA were performed. Wild type and mutant bands were detected at 315 and 272 bp, respectively, corroborating the deletion of exon 7 in mutant mice (Figure 34A, bands 1 and 2).

In skin, CerS3 deficient mice exhibited expression of *Cers3* mRNA lacking exon 7, as analyzed by PCR. The targeted disruption of *Cers3* was confirmed with the control and mutant bands at 686 and 593 bp, respectively, corresponding to the lack of 93 bp of exon 7 in mutants (Figure 34B, bands 3 and 4). Consequently, the gene rearrangement led to complete loss of expression exclusively when amplifications were performed using primers within exon 7 (Figure 34C). The truncated CerS3 transcript was finally confirmed by nucleotide sequencing.

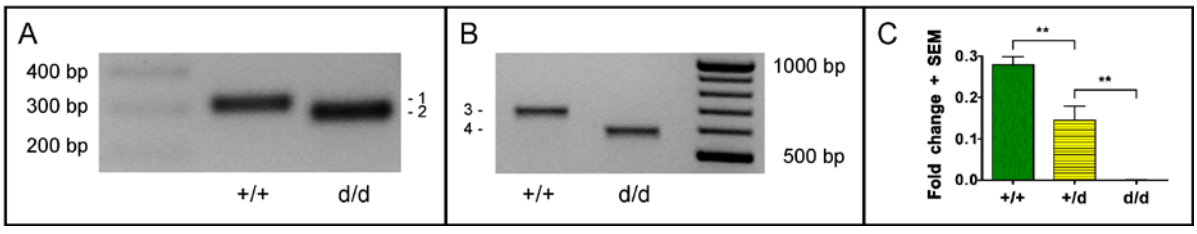

Figure 34. Targeted disruption of *Cers3*-exon 7 in CerS3 deficient mice.
(A) PCR analysis from genomic tail DNA of newborn mice confirming the amplification of the corresponding allelic products of CerS3$^{+/+}$ and CerS3$^{d/d}$. (B) Skin cDNA analysis demonstrating the synthesis of a truncated CerS3 transcript lacking 93 bp due to the targeted deletion of exon 7 in CerS3 deficient mice, as

*demonstrated by PCR. (C) Quantitative RT-PCR verifying the complete loss of CerS3 mRNA expression when amplifying a product within exon 7. Error bars represent the SEM. ** indicate p value < 0.01.*

3.3.2. Defective epidermal barrier function of CerS3$^{d/d}$ mice leads to premature neonatal death

The offspring of CerS3$^{+/d}$ mice were born with Mendelian distribution, indicating that CerS3 might not be essential for embryonic development. Phenotypically, CerS3$^{+/d}$ could not be distinguished from wild type mice, however the skin of CerS3$^{d/d}$ appeared unwrinkled, shiny, sticky and intensively red colored (Figure 35A). Mutant offsprings were not accepted and fed by their progenitors. Loss of CerS3 caused universal neonatal lethality within 3 to 4 hours after birth.

In order to examine the epidermal barrier function, skin permeability assays were carried out. Staining of control and mutant mice with hemalaun revealed a clear impairment of the skin barrier formation at birth (Figure 35B) and at embryonic stage E19 (Figure 35C). Whereas control mice could effectively exclude the dye after several throughout washes, mutant skin exhibited a strong penetration of the dye, indicating a defective epidermal permeability function.

To determine whether an additional outward permeability defect existed, transepidermal water loss (TEWL) rates were measured. Skin of newborn CerS3$^{d/d}$ mice exhibited an over two fold increase in transepidermal fluid evaporation, confirming the compromised skin barrier of mutant mice (Figure 35D). Correlating with the fluid loss, the body weight of newborn CerS3$^{d/d}$ mice was reduced by 30% (Figure 35E). As diminished body weight very likely is a result of dehydration, CerS3 embryos of one litter were collected at E18.5 ± 0.5, sacrificed and freeze dried after determination of wet body weight. With these mice, no differences in body wet or dry weight were observed, supporting that differences in wet body weight of newborns were exclusively due to water loss (Figure 35F and 35G).

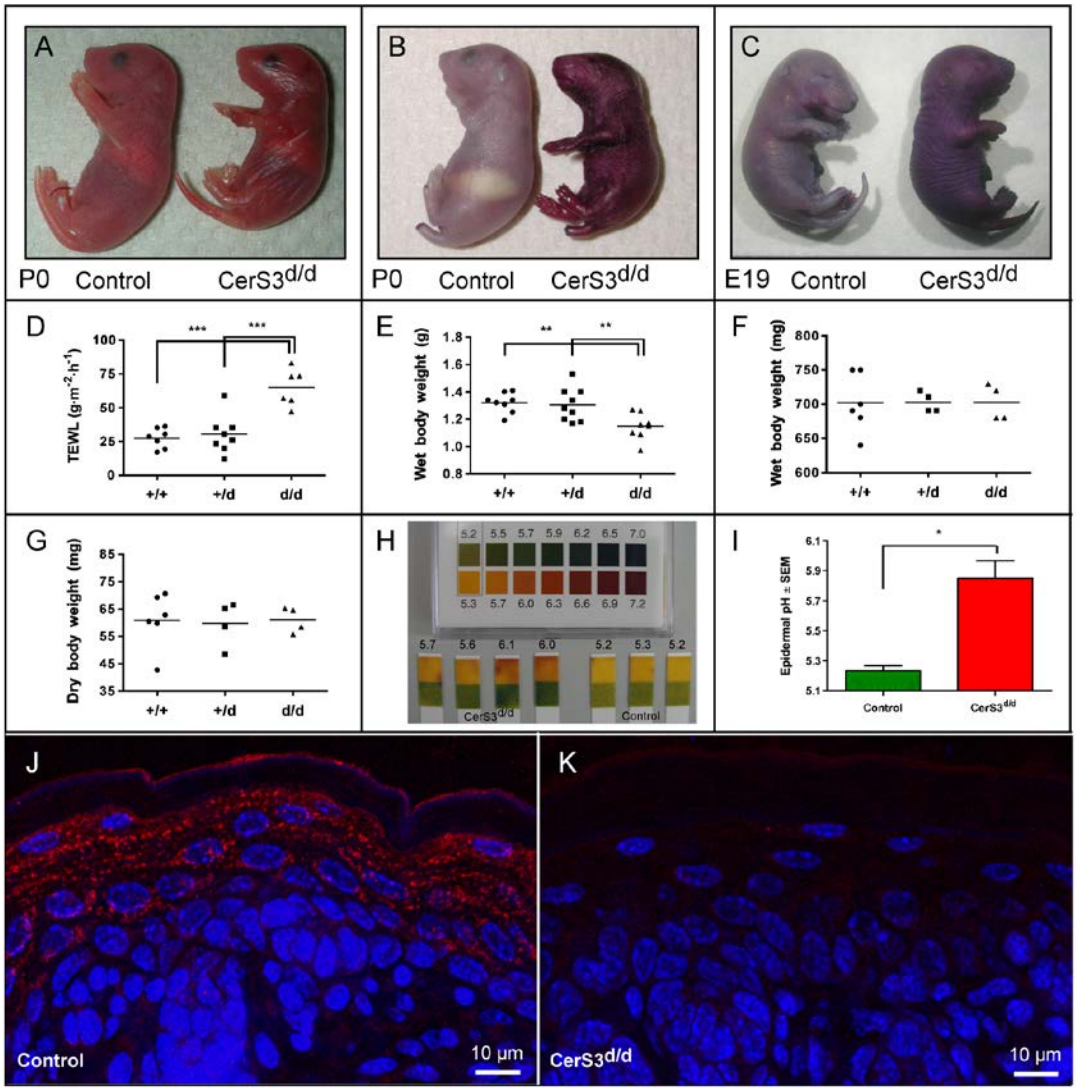

Figure 35. Defective epidermal barrier function of CerS3$^{d/d}$ mice.

(A) Epidermis of newborn CerS3$^{d/d}$ appears intensively red and shiny compared to control littermates. (B) Defective epidermal permeability barrier of CerS3-deficient mice shown with the persistence of hematoxylin dye of newborns, and (C) of embryonic stage E19 ± 0.5 CerS3$^{d/d}$ mice. (D) Significant increase of TEWL and (E) reduced wet body weight of mutant CerS3 mice measured within 3 hours postnatally. (F) No significant difference was observed in wet or (G) dry body weight of E18.5 ± 0.5 mutant CerS3 embryos compared with control littermates. (H) Increased surface pH of mutant CerS3 mice as determined by pH-indicator strips. (I) Quantification of epidermal surface pH revealed a 0.6 pH units increase of mutant epidermis. Immunofluorescence of paraffin sections of skin from the back of control (J) and mutant CerS3$^{d/d}$ (K) mice with anti-CerS3 polyclonal antibody. CerS3 is concentrated as distinct dots within the cytoplasm of keratinocytes of the upper SS and SG, whereas no signal could be detected in the mutant epidermis.

The epidermal permeability barrier is directly regulated by pH, therefore skin surface pH of newborn mutant and control littermates was determined by direct contact with humidified pH-indicator strips. Control mice exhibited an acidic pH of about 5.2, whereas mutant epidermal pH was increased by roughly 0.6 pH units (Figure 35H and 35I).

The lack of a functional CerS3 protein appeared to have direct implications at the epidermal barrier function. Although CerS3 expression in the skin have been demonstrated at the mRNA level, its exact distribution within the epidermal cell layers have not yet been described. Therefore, specific antibodies against the carboxy terminus of the CerS3 protein were generated and used for immunofluorescence labelling of control and CerS3$^{d/d}$ skin biopsies. In control epidermis, CerS3 was distributed in the SS and the SG, concentrated as distinct dots within keratinocytes of the upper epidermal layers (Figure 35J). On the contrary, CerS3 expression was not detected in any strata of mutant epidermis (Figure 35K), thereby corroborating that the lack of exon 7 renders the synthesis of CerS3 dysfunctional. In summary, these results demonstrate the pivotal role of CerS3 for a proper epidermal barrier function.

3.3.3. Epidermal “hyper”keratosis and delayed keratinocyte differentiation of CerS3 deficient mice

Light microscopical analyses of semithin sections of mutant CerS3$^{d/d}$ skin revealed a strikingly thick and compact *stratum corneum*, as observed postnatally (Figure 36A and 36B) as well as at embryonic stage E18.5 ± 0.5 (supplemental Figure A4A and A4B). Thus, the corneocyte layers exhibited a hyperkeratotic phenotype and lacked the “basket-weave” appearance typically observed in control skin. Mutant *stratum corneum* exhibited solely *stratum compactum*, lacking the less cohesive upper layers of the *stratum disjunctum*, which were prominent in control skin. The nucleated epidermal layers appeared relatively normal both prenatally and at birth. However, large keratohyalin granules (KG) of the uppermost *stratum granulosum* cells, which predominantly contain profilaggrin aggregates, were significantly smaller in CerS3 deficient mice, both at birth (Figure 36A and 36B, yellow arrows) and at E18.5 (supplemental Figure A4A and A4B).

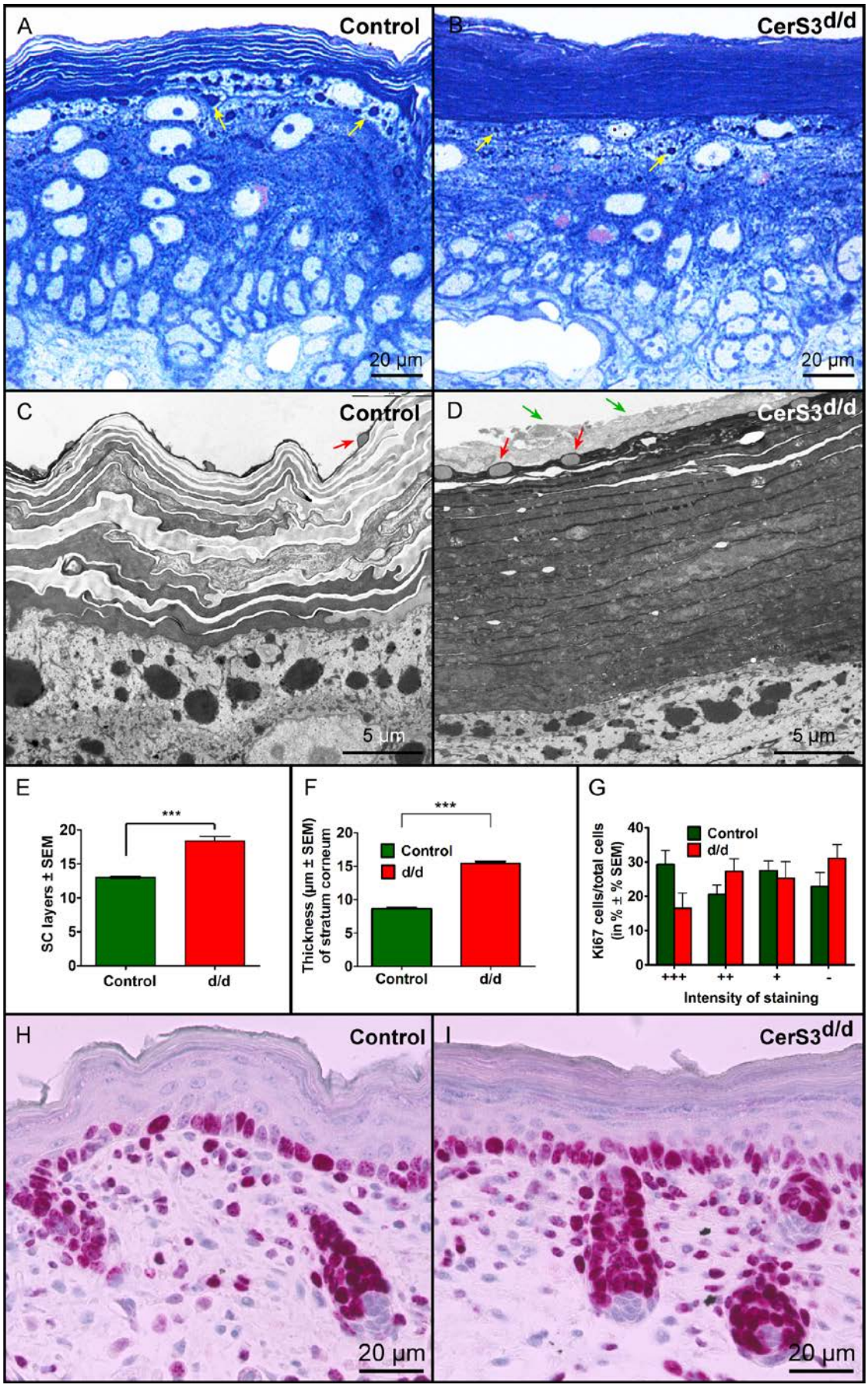
A
Control
20 µm
B
CerS3d/d
20 µm
C
Control
5 µm
D
CerS3d/d
5 µm
E
***
SC layers ± SEM
20
15
10
5
0
Control
d/d
F
***
Thickness (µm ± SEM) of stratum corneum
20
15
10
5
0
Control
d/d
Control
Control
d/d
G
Ki67 cells/total cells (in % ± % SEM)
40
30
20
10
0
Control
d/d
+++
++
+
-
Intensity of staining
H
Control
20 µm
I
CerS3d/d
20 µm

Figure 36. Alterations of keratinocyte differentiation in CerS3$^{d/d}$ mice.
(A) Semithin sections of neonatal skin of control and (B) CerS3$^{d/d}$ mice stained with PAS and methylene blue-Azur II demonstrating "hyper"keratotic mutant SC. Yellow arrows indicate keratohyalin granules reduced in size in CerS3$^{d/d}$ skin. Electron micrographs treated with tannic acid of (C) control and (D) mutant upper epidermal layers exhibiting the persistence of periderm in mutant skin (green arrows), adjacent to the uppermost layer of corneocytes marked by electron-lucent inclusion bodies (red arrows). (E) Quantification of SC layers and (F) SC thickness. (G) Quantification of Ki67-positive keratinocytes according to the staining intensity. (H) Control and (I) CerS3$^{d/d}$ proliferation of basal keratinocytes assessed with Ki67 labelling on paraffin embedded sections. No significant increase in proliferation could be observed in mutant epidermis.

To investigate in detail the anomalies observed in the mutant epidermis, ultrastructural analyses were performed (Figure 36C and 36D). The increased number of corneocyte layers upon CerS3 deficiency could be confirmed and quantified. At birth, no corneocyte layer in either control or mutant mice was shed. This could be determined by the presence of the uppermost corneocytes decorated by electron-lucent inclusion bodies in both mutant and control skin (Figure 36C and 36D, red arrows and supplemental Figure A5). Furthermore, the most stricking feature of mutant epidermis was the persistence of a continuous periderm (Figure 36D and supplemental Figure A5, green arrows). The presence of the most superficial corneocyte layer in both control and mutant SC, and of the periderm in mutant skin indicated that desquamation did not yet occurred in neither both SCs. Control mice exhibited about 13 corneocyte layers, whereas mutant SC had over 40% more of these cell layers (Figure 36E). Additionally, quantification of CerS3$^{d/d}$ SC thickness was found to be almost double to its respective control (Figure 36F).

To address whether mutant epidermis exhibited an enhanced proliferation rate of basal keratinocytes that could result in a thickened SC, the expression of the proliferative marker Ki67 was examined. No significant alteration of the cellular proliferation rates was found associated with CerS3 deficient skin (Figure 36H and 36I), as quantification of Ki67 immunostaining did not reveal a significant overall increase of proliferation in mutant neonatal epidermis (Figure 36G).

Epidermal ultrastructural confirmed the reduced size of profilaggrin-containing keratohyalin granules in CerS3 deficient epidermis (Figure 36C and 36D).

The transition of SG keratinocytes to enucleated corneocytes requires drastic morphological changes, including the degradation of nuclei, organelles and the plasma membrane. However, CerS3 deficiency resulted in a delay of the terminal differentiation program of keratinocytes. Mutant epidermis exhibited an incomplete degradation of organelle structures within the first and up to the third corneocyte layers (supplemental Figure A4C and A4D). Some of these immature corneocytes exhibited a TUNEL-positive staining, which indicate the presence of residual DNA in the progress to its complete degradation (supplemental Figure A4E and A4F). These observations were confirmed by DAPI-postive DNA-containing remmants in the lower SC of mutant skin (compare with Figure 41F, yellow arrows). In addition, glycogen could be observed in CerS3$^{d/d}$ SC, whereas glycogen in control skin was restricted to the viable layers of the epidermis (supplemental Figure A4G and A4H).

The defective cornification process in dysfunctional CerS3 skin was additionally obvious by the presence of the peridermal cell layer overlaying mutant SC (Figure 36D, supplemental A4B and A5, green arrows). Some of these cells even contained nuclear remmants (compare with Figure 39D, 41D and 41J). Although skin of control mice displayed a few remnants of these peridermal cells, mutant skin exhibited a continuous intact periderm.

3.3.4. Defective corneodesmosomal degradation causes elevated intercellular cohesion and persistence of the periderm in CerS3 deficient *stratum corneum*

To further investigate the defects in the terminal keratinocyte differentiation induced by the lack of CerS3, a detailed analysis of SC ultrastructure was performed. While no intact peridermal cell layer could be observed in control epidermis (Figure 37A), the presence of this transitional layer was confirmed in neonatal CerS3 depleted epidermis (Figure 37B-F, **P**). A closer look at the peridermal architecture revealed the presence of desmosomes (Figure 37D and 37F, red arrows), as well as tight junctions (Figure 37F, red star). Therefore, no degradation, disaggregation or shedding of periderm cells was initiated neither at E18.5, nor at birth of CerS3 mutant

mice. Together with the hyperkeratotic phenotype of CerS3$^{d/d}$, these findings might suggest a defect in the proper desquamation of mutant epidermis.

Consistent with this hypothesis, corneodesmosomes were found to persist in defective CerS3 epidermis. In mutant mice, corneodesmosomes remained abundant at all cell layers of the SC (supplemental Figure A5, red arrows), including the most superficial corneocyte layer (Figure 37B, black arrow), and were observed along the whole corneocyte surface. In contrast, corneodesmosomes were restricted to immature, inner corneocytes adjacent to the SG (*stratum compactum*) in control epidermis, and they were lacking at the uppermost SC layers (Figure 37A). As expected, the corneodesmosomal degradation as an important step of desquamation was initiated at the non-peripheral (basal and apical) surface of inner corneocytes and progressed also at the peripheral/lateral intercellular spaces concomitantly with cornification in control SC (data not shown).

The SC of mutant CerS3 mice occasionally exhibited a pair of thin electron-dense bands located within the intercellular space (ICS) parallel to the surface of the CE (Figure 37C, yellow arrows). In CerS3$^{d/d}$ mice, the space between the limits of the CE was much less than 13 nm, which would correspond to the typical ICS occupied by lipid lamellae (White et al., 1988). Instead these thin bands, which were visible to the uppermost corneocyte layer, seem to correspond to a phospholipid bilayer.

The defective corneodesmosomal degradation was further analyzed by immunolocalization of junctional proteins together with their total quantification by immunoblotting. To address whether the loss of CerS3 lead to an aberrant expression of desmosomal proteins, the transmembrane cadherin desmoglein 1/2, as well as the plaque proteins desmoplakin and plakoglobin were examined. Among these studies, the immunolocalization of desmoglein 1/2 exhibited a striking difference between mutant and control epidermis. Whereas the expression of this cadherin was restricted to desmosomes of keratinocytes within the SS and the SG in control mice (Figure 38A), mutant skin expressed desmoglein 1/2 at all the epidermal layers including the complete SC and the periderm (Figure 38B). Although the overall protein levels were found to be decreased in CerS3$^{d/d}$ mice (Figure 38G), its distribution decorating the complete periphery of corneocytes suggests a defective or delayed degradation of mutant corneodesmosomes.

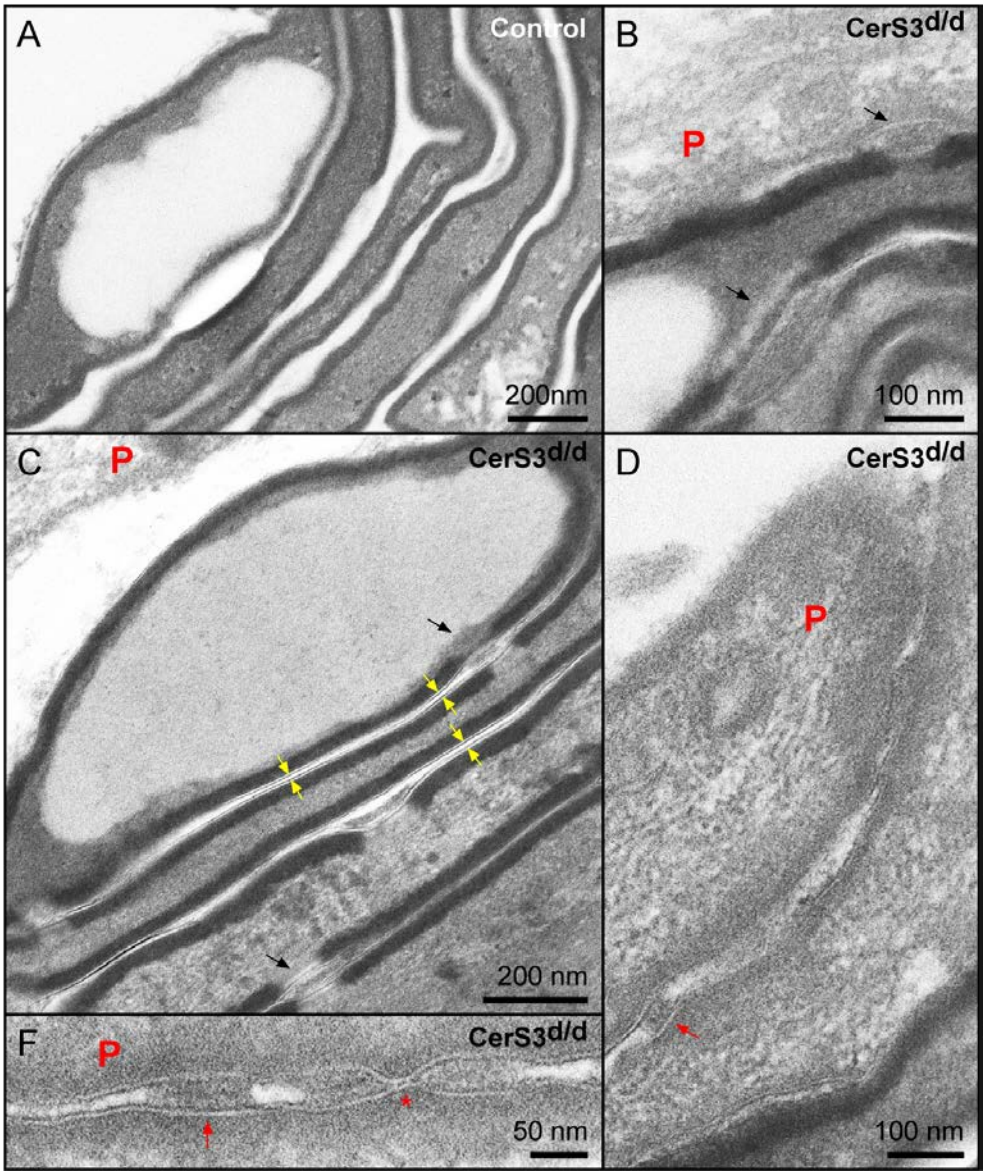

Figure 37. Persistence of periderm and corneodesmosomes in newborn CerS3 depleted mice.

*(A) Superficial corneocytes decorated with inclusion body of control mice lacking adjacent peridermal remmants or non-peripheral corneodesmosomes. A persistant peridermal layer (**P**) was observed in mutant CerS3 mice (B-F). Non-peripheral corneodesmosomes (black arrows) were present between peridermal cells and the most superficial corneocytes (B), as well as between the most superficial corneocytes and lower adjacent layers (C) of CerS3 depleted mice. Typical phospholipid bilayers appeared to be present in the intercellular space between corneocytes of mutant SC (C, yellow arrows). Intact periderm in mutant epidermis exhibited desmosomes (D and F, red arrows), as well as tight junctions (F, red star). Epoxy-embedded sections were treated with tannic acid.*

In contrast, the expression and concentration of the desmosomal plaque proteins, desmoplakin and plakoglobin, were found to be not significantly altered (Figure 38G). As expected, desmoplakin expression was found to be restricted to the nucleated layers of the epidermis (Figure 38C-D). In addition, the epidermal localization of plakoglobin and the cytoskeletal keratins associated with desmosomal complexes, K1 and K10, were found similarly expressed in control and mutant CerS3 mice (data not shown).

Regarding the defective degradation of non-peripheral/central corneodesmosomes in mutants, our results indicate desmoglein 1/2 to be essential for corneocyte cohesions and responsible for persistent cohesions of periderm cells. In addition, these findings suggested an impaired proteolysis of the corneocyte plasma membrane and consequently a defective formation of a mature cornified cell envelope.

To examine whether the defective degradation of corneodesmosomes in mutant SC was caused by the reduced expression of proteolytic enzymes, levels of epidermal proteases of the kallikrein and the cathepsin family were analyzed. The total protein levels of either cathepsin D and KLK5 were found not significantly altered (Figure 38G). However, the epidermal distribution of cathepsin D in $CerS3^{d/d}$ mice remarkably differed from their control littermates. Whereas cathepsin D was found expressed in all the epidermal layers of control mice including the SC (Figure 38E), its expression was markedly decreased at the upper cell layers of the SG and the SC of mutant epidermis (Figure 38F). The reduced expression of this protease, which has been involved in the degradation of desmosomes during desquamation may account for the persistence of corneodesmosome remmants in mutant epidermis.

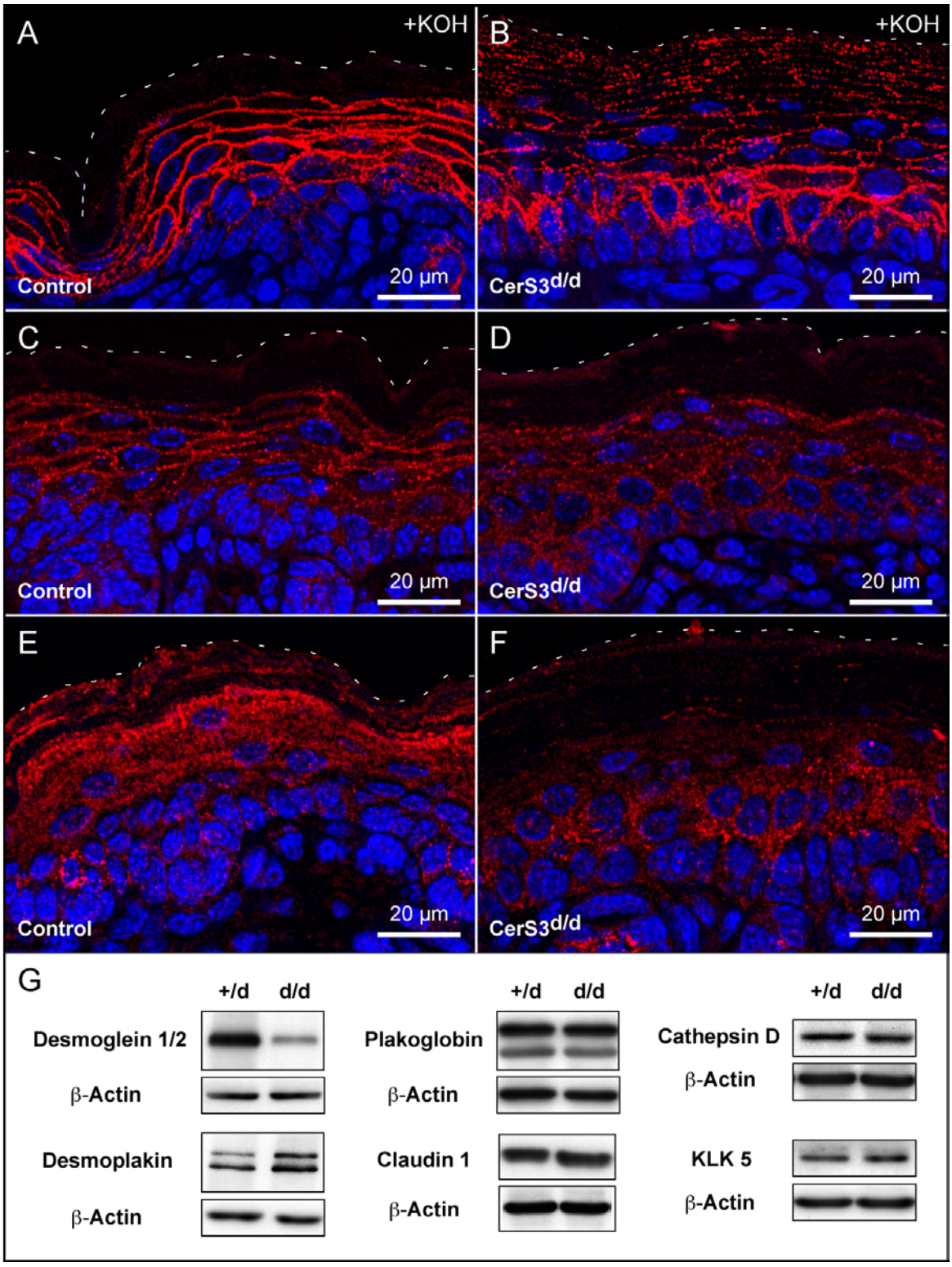

Figure 38. Impaired corneodesmosomal degradation in CerS3$^{d/d}$ epidermis.
(A) Desmoglein 1/2 is strongly expressed in the SS and SG of control mice. (B) In addition, the SC of mutant mice had a prominent staining at the periphery of all corneocyte layers. To assure that the lipid lamellae do not mask the epitope in

control mice, both preparations were subjected to mild alkaline treatment prior to immunolabelling. (C-D) No differences in desmoplakin distribution could be observed in control and mutant epidermis. (E) Cathepsin D distribution was localized at all epidermal cell layers. The uppermost granular keratinocytes displayed the strongest immunofluorescence. (F) In CerS3$^{d/d}$ mice, the strongest cathepsin D signal intensity was in the SS fading towards the SC. (G) Immunoblot analyses of desmosomal and tight junction associated proteins, as well as epidermal proteases. Blots are representative of at least 3 animals per group. β-actin was used to normalize protein levels.

Immunohistochemical analyses of tight junctional proteins were additionally performed in order to determine whether in addition to impaired degradation of the corneodesmosomal protein desmoglein 1/2, a defect in other types of cell junctional complexes existed. The immunolocalization of the tight junctional transmembrane protein claudin 1 and the cytoplasmic associated plaque protein cingulin was found within keratinocytes of the SS and the SG in both control and mutant epidermis (Figure 39A-B and 39C-D). Neither junctional proteins did show a significant difference in their signal intensity and main distribution pattern between control and mutant epidermis, however claudin 1 expression was distinctively and additionally observed in the periderm at the skin surface of mutant mice (Figure 39B, white stars) confirming the ultrstructural observations about the presence of intact tight junctions between peridermal cells (Figure 37F, red star).

Regarding the organization of TJs, cingulin expression in CerS3$^{d/d}$ mice exhibited conspicuous differences. Whereas typical *zonulae occludentes* were established in control epidermis appearing as continuous fluorescent linear structures at the plasma membrane of the upper cell layers of the SG, mutant epidermis displayed weaker fluorescent punctuated signals within the uppermost granular keratinocytes.

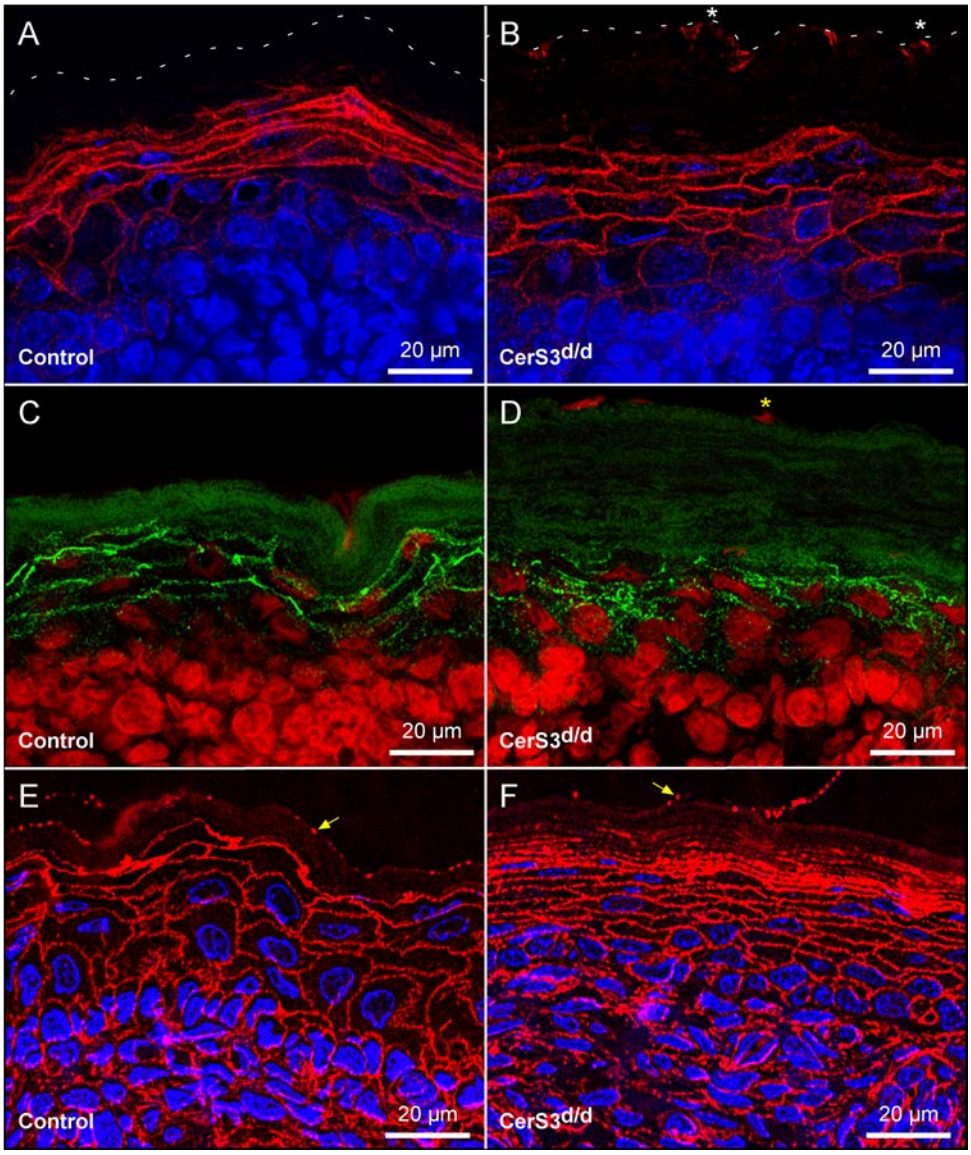

Figure 39. Distribution of tight junctions and associated proteins.

TJs were visualized with claudin 1 (A-B) and cingulin (C-D). No significant differences were observed in their distribution, however claudin 1 exhibited staining on the surface of mutant epidermis marking the periderm (white star). Cingulin expression exhibited a punctated distribution around keratinocytes of the SS and SG of CerS3$^{d/d}$ skin (D), whereas control skin exhibited linear distribution around the cell borders. A residual nuclear staining within some peridermal cells could also be detected on the surface of CerS3$^{d/d}$ skin (yellow star). (E) F-actin was mainly expressed in the nucleated layers of the epidermis in control mice CerS3$^{d/d}$. (F) F-actin distribution differed to control by being also strongly expressed in the lower layers of the SC and progressively fading towards the upper corneocytes. Both control and mutant epidermis exhibited distinct punctated staining in the outer most corneocyte layer (yellow arrows).

The distribution pattern of the cytoskeletal protein F-actin, which is associated with TJs and adherens junctions, was additionally examined by immunolabeling. Besides the intense expression of F-actin at the cell-cell borders of all viable layers of the control epidermis (Figure 39E), its distribution in CerS3$^{d/d}$ mice additionally included the lower layers of the SC (Figure 39F) indicating a delay or a defect in the final cornification process. Furthermore, a pearl-like staining at the surface of both control and CerS3 deficient skin was observed. This distinct punctated expression of F-actin corresponds to the inclusion bodies observed at the ultrastructural level marking the uppermost corneocyte layer (Figure 36C-D and 37A-C).

Considered together, the findings obtained by the ultrastructural and the immunohistochemical analyses indicate an alteration of terminal keratinocyte differentiation particularly of the corneodesmosomal degradation upon deficiency of CerS3. The reduced expression of specific proteolytic enzymes might account totally or partially for the lack of processing of corneodesmosomes, and thereby conserving the intercellular cohesion leading to “hyper”keratosis and persistence of the periderm.

3.3.5. Impaired maturation of granular keratinocytes correlates with altered expression of cornified envelope proteins

Previous light microscopical and low magnification ultrastructural analyses revealed distinct morphological differences between control and mutant CerS3 epidermis with regard to the size of keratohyalin granules both at birth (Figure 36A-D) and at E18.5 (Figure A4A and A4B). To gain deeper insight into these anomalies, higher magnification electronmicrographs were performed. These analyses evidenced the pronounced size reduction of keratohyalin granules (KG) in the neonatal mutant epidermis as compared to epidermis of control littermates (Figure 40, red arrows).

The main constituents of KGs are structural proteins required for the formation of the CE, namely profilaggrin, which is associated with the large KGs (or F-granules) and loricrin, associated with the small KGs (or L-granules). F-granules displayed a fine granular structure of medium electron density (Figure 40A-B, red arrows), whereas L-granules appeared as electron-dense granules found often at the periphery of F-granules, as well as in the nucleoplasm (Figure 40A-B, yellow arrows). CerS3 deficiency resulted in both a significant decrease in the size of F-granules and

in the number of L-granules particularly at the periphery of F-granules (Figure 40A-B).

To examine whether the expression and processing of these proteins was altered upon CerS3 deficiency, immunoblot analyses were performed (Figure 40C). Profilaggrin was processed from its high molecular weight polyprotein to the monomeric filaggrin (~ 28 kDa) in control skin. In contrast, an aberrant processing of profilaggrin was detected in CerS3$^{d/d}$ mice. The expression of the trimeric form and especially the filaggrin dimer (~ 55 kDa) were increased, whereas the expression levels of the monomeric form appeared significantly reduced. The expression levels of loricrin were additionally altered. Loricrin is the most prominent structural protein of the CE accounting for about 65 to 85% of the total protein mass of the cornified layer (Steven and Steinert, 1994). Correspondingly, control mice exhibited high expression levels of loricrin (~ 55 kDa), which were greatly diminished in CerS3 deficient skin.

These anomalies in correlation with the morphological data of profilaggrin and loricrin-containing KGs suggested a defective/delayed maturation of keratinocytes of the upper SG layer due to CerS3 deficiency.

To evaluate whether the defective formation of KGs affected the distribution of structural proteins of the cornified layer, immunolabeling of the key players involved in the formation of the CE were performed. As expected, profilaggrin/filaggrin was primarily localized to the entire SG layer, where it filled the F-granules of the uppermost granular keratinocytes of control epidermis (Figure 41A, white arrows). At the SC, filaggrin levels faded along with cornification leaving a residual staining in mature corneocytes indicative of the proteolytically cleaved filaggrin molecules. In contrast, profilaggrin/filaggrin expression was equally distributed at the uppermost granular keratinocytes, as well as within the entire SC of CerS3 deficient skin. At the cornified layer, profilaggrin/filaggrin expression did not exhibit a decreased expression towards the most superficial corneocytes, as seen in control skin (Figure 41B). Taken together these morphological findings confirmed a defective or delayed profilaggrin processing, which might be a consequence of a delayed maturation of granular keratinocytes.

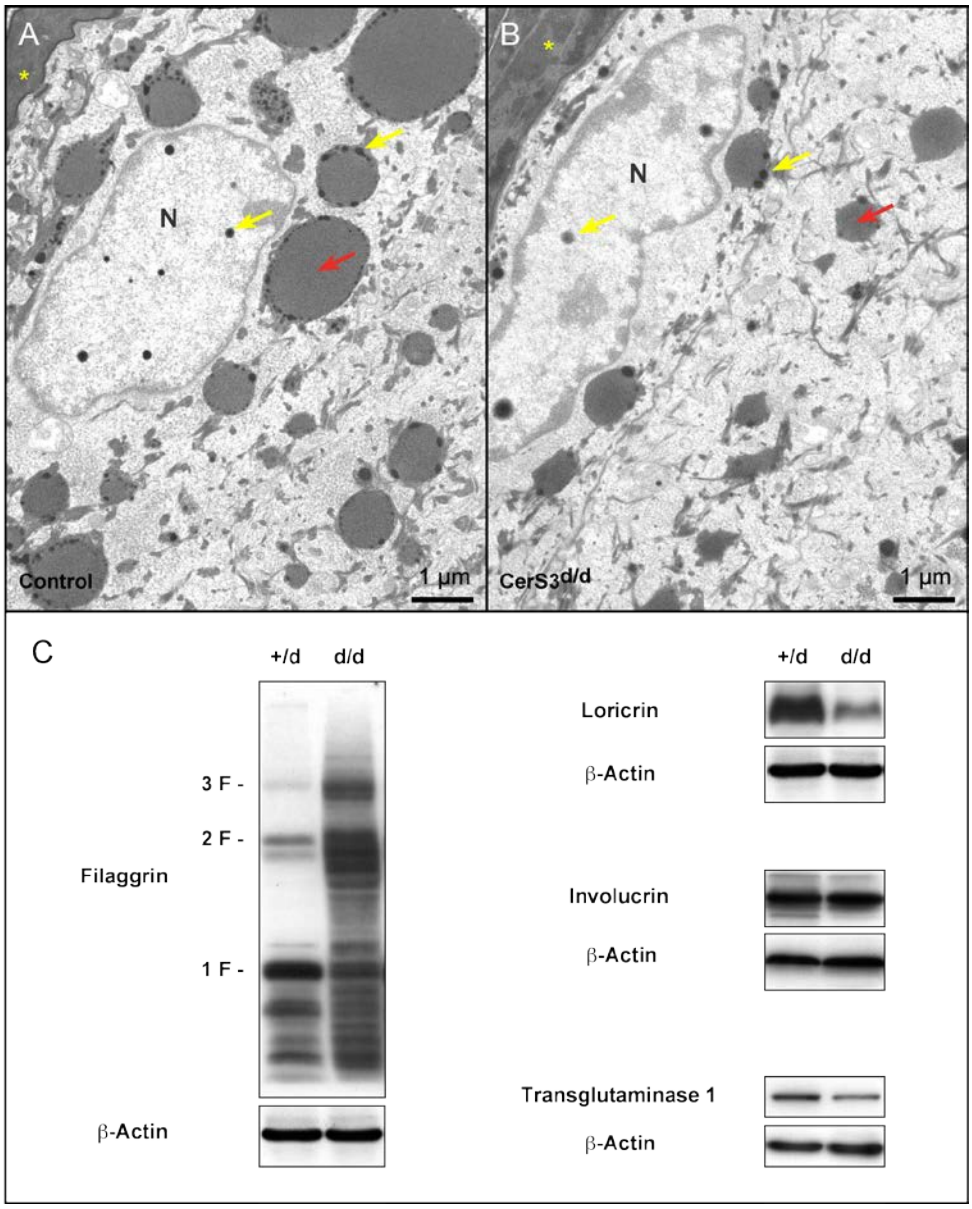

Figure 40. Diminished size of F-granules and reduced number of L-granules correlates with impaired expression of CE proteins.

*Higher magnification electron micrographs treated with tannic acid of control (A) and mutant (B) CerS3$^{d/d}$ keratinocytes of the uppermost SG layer demonstrating altered development of KGs. First corneocyte layer is indicated (yellow star). F-granules (red arrows) were pronouncedly reduced in size, whereas L-granules (yellow arrows) were strongly decreased in number in mutant epidermis. L-granules were also localized within the nucleus (**N**). (C) Defective development of KGs accompanied diminished expression levels of monomeric filaggrin, loricrin and transglutaminase 1 in CerS3 deficient mice. Equal loading of immunoblots was assessed by β-actin expression. Blots shown are representative of at least 3 animals per group.*

In control epidermis, loricrin expression was identified at the granular layer with increased concentration in keratinocytes residing at the border between SG and SC (Figure 41C). Ultracryosemithin sections enabled to detect its distribution distinctively around the periphery of F-granules (white arrows), as well as within the nuclear compartment (white arrowheads). Despite that loricrin has been identified as the major component of the CE, most current literature exhibits its expression exclusively at the SG. We also failed to detect immunolabeling of loricrin at the cornified layer of control skin. However, we assumed that the protein-lipid matrix in the corneocyte interstices might mask the epitope recognized by the antibody. Therefore, we applied an *in situ* methanolic mild alkaline treatment on paraffin sections to cleave protein-bound ceramides and thereby release the antigen. This kind of antigen retrieval unveiled the loricrin at all cornified layers of control epidermis (Figure 41E), as compared with paraffin sections without methanolic treatment (Figure 41E, inset).

In addition to loricrin expression in the SG, CerS3 deficient epidermis exhibited loricrin immunolabeling decorating the cornified cell envelope without requiring antigen retrieval (Figure 41D). As a control, paraffin-embedded sections of mutant epidermis were subjected to methanolic alkaline treatment (Figure 41F) or without this treatment (Figure 41F, inset), resulting in no alteration of loricrin distribution with neither of these procedures. Similar to control, loricrin contained in L-granules was localized at the rim of large F-granules of the SG and within nuclei of granular keratinocytes (Figure 41D, white arrows and arrowheads).

In addition, our data demonstrated the necessity of alkaline hydrolysis to visualize loricrin within the nuclear compartment. A weak nuclear signal was already observed in the lower granular cell layers compared to the strong signal of the uppermost SG in control epidermis. However, only a comparably weak nuclear immunofluorescence was found in CerS3 deficient skin (Figure 41F).

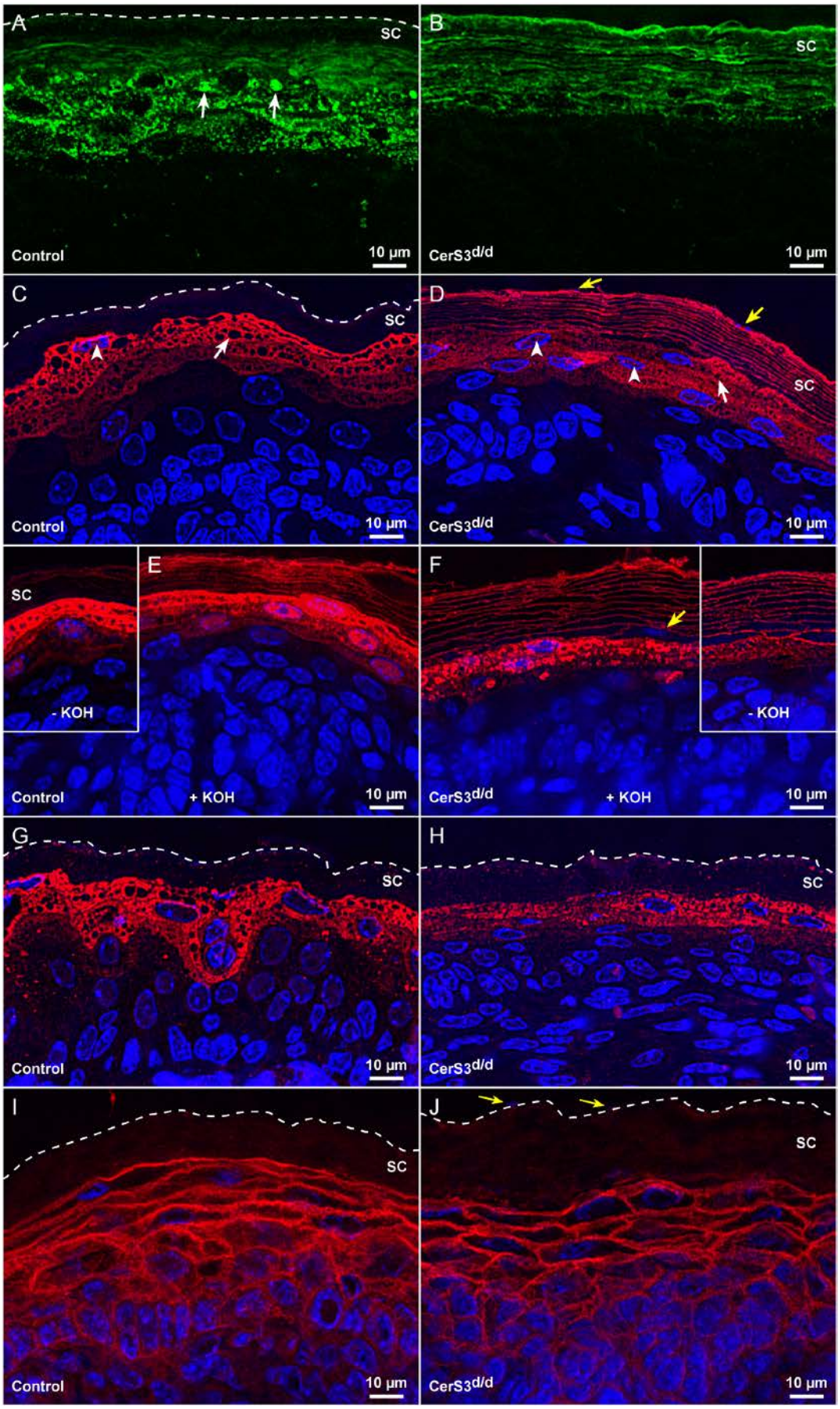
A
SC
Control
10 µm
B
SC
CerS3d/d
10 µm
C
SC
Control
10 µm
D
SC
CerS3d/d
10 µm
SC
- KOH
E
Control
+ KOH
10 µm
F
- KOH
CerS3d/d
+ KOH
10 µm
G
SC
Control
10 µm
H
SC
CerS3d/d
10 µm
I
SC
Control
10 µm
J
SC
CerS3d/d
10 µm

Figure 41. Epidermal distribution of CE proteins.
Control epidermis exhibited the highest profilaggrin/filaggrin intensity at the SG layer (A), whereas in mutant epidermis in addition a strong expression was found in the SC (B). F-granules are indicated with white arrows. Semithin sections indicating loricrin expression of control (C) and CerS3 dysfunctional epidermis (D) without alkaline treatment. Loricrin nuclear localization is indicated with white arrowheads, whereas residual nuclei at the SC (F) and periderm (D) are indicated with yellow arrows. Paraffin-embedded sections stained with loricrin antibody with prior methanolic alkaline hydrolysis to expose antigens residing at the SC of control (E) and mutant (F) epidermis. Control paraffin sections without alkaline antigen retrieval (E and F insets). Involucrin distribution did not differ pronouncedly between control (G) and CerS3$^{d/d}$ (H) skin. In situ transglutaminase activity assay with monodansylcadaverine exhibited no pronounced alterations of control (I) and deficient (J) skin. Note residual nuclei at the periderm layer are indicated with yellow arrows.

In agreement with ultrastructural analyses of mutant keratohyalin granules, loricrin distribution confirmed the reduced dimensions of F-granules.

Together these results indicate that although the expression levels of loricrin were reduced with CerS3 deficiency, its general epidermal distribution was not altered. Nevertheless, the altered maturation of granular keratinocytes was evidenced by the reduced dimensions of KGs, which might be associated with a delayed differentiation of keratinocytes as suggested by the presence of residual nuclear contents at the first corneocytes and the peridermal layer.

To further investigate the phenotypic alterations exhibited in a dysfunctional CerS3 epidermis, focus was shifted towards analyzing the expression and distribution of another key CE protein, involucrin. Although no alteration at the total protein level was detected by immonoblotting (Figure 40C), a slight delay in expression at the SG was observed at the immunofluorescence level in mutant skin (Figure 41G and 41H). Our *in situ* methanolic mild alkaline treatment was additionally performed to visualize involucrin in the CE, considering the published covalent interactions of ceramides with involucrin. However, involucrin immunolabeling did not exhibit any change in their distribution neither with control or mutant epidermis (data not shown).

The total protein content of transglutaminase 1 was moderately decreased in CerS3$^{d/d}$ epidermis. *In vitro*, transglutaminase 1 has demonstrated its capability for catalyzing the crosslinkage of CE proteins, in addition to potentially catalyze the transesterification of ω-hydroxy-ceramides with the carboxy residue of CE proteins. To examine whether alterations in transglutaminase 1 activity existed in mutant epidermis, an *in situ* activity assay with monodansylcadaverine as a substrate were performed on freshly prepared epidermal cryosections. Although the fluorescence intensity associated with the monodansylcadaverine antibody was slightly diminished in mutant epidermis, its distribution at the viable layers of the skin did not differ from controls (Figure 41I and 41J).

3.3.6. Drastic reduction of epidermal ceramides is associated with altered lipid lamellar structures upon CerS3 deficiency

Cholesterol, as well as polar and neutral lipids, were examined on skin sections of CerS3$^{d/d}$ by fluorescence labeling with filipin and nile red, respectively. Both probes revealed a pearl-like distribution of lipids in the SC of mutant epidermis, while their distribution in the lower epidermal layers did not seem to be altered (Figure 42A and 42B). In control epidermis, the transition of the polar lipids present at the SG to the *golden* lamellae of neutral lipids at the SC could be clearly seen with nile red staining. On the contrary, punctual concentration of lipid species was nicely observed predominantly at the upper layers of the SC of CerS3 deficient mice (Figure 42B inset, red arrow).

The non-lamellar lipid agglomerates correlated at the ultrastructural level with electron-light intercellular lentil-like structures in mutant SC. Absence of lamellar unit structures that are required for the establishment of a mature lipid barrier was obvious between these lipid agglomerates (Figure 42C, red arrow), as the intercellular space between corneocytes was maximally reduced. The length between the limits of the electron dense CE of two adjacent corneocytes was estimated to be about 3 to 4 nm in CerS3$^{d/d}$ mice (Figure 42C, yellow arrow), which is less than a third of the determined 13 nm occupied by the intercellular unit lamellar structures (White et al., 1988).

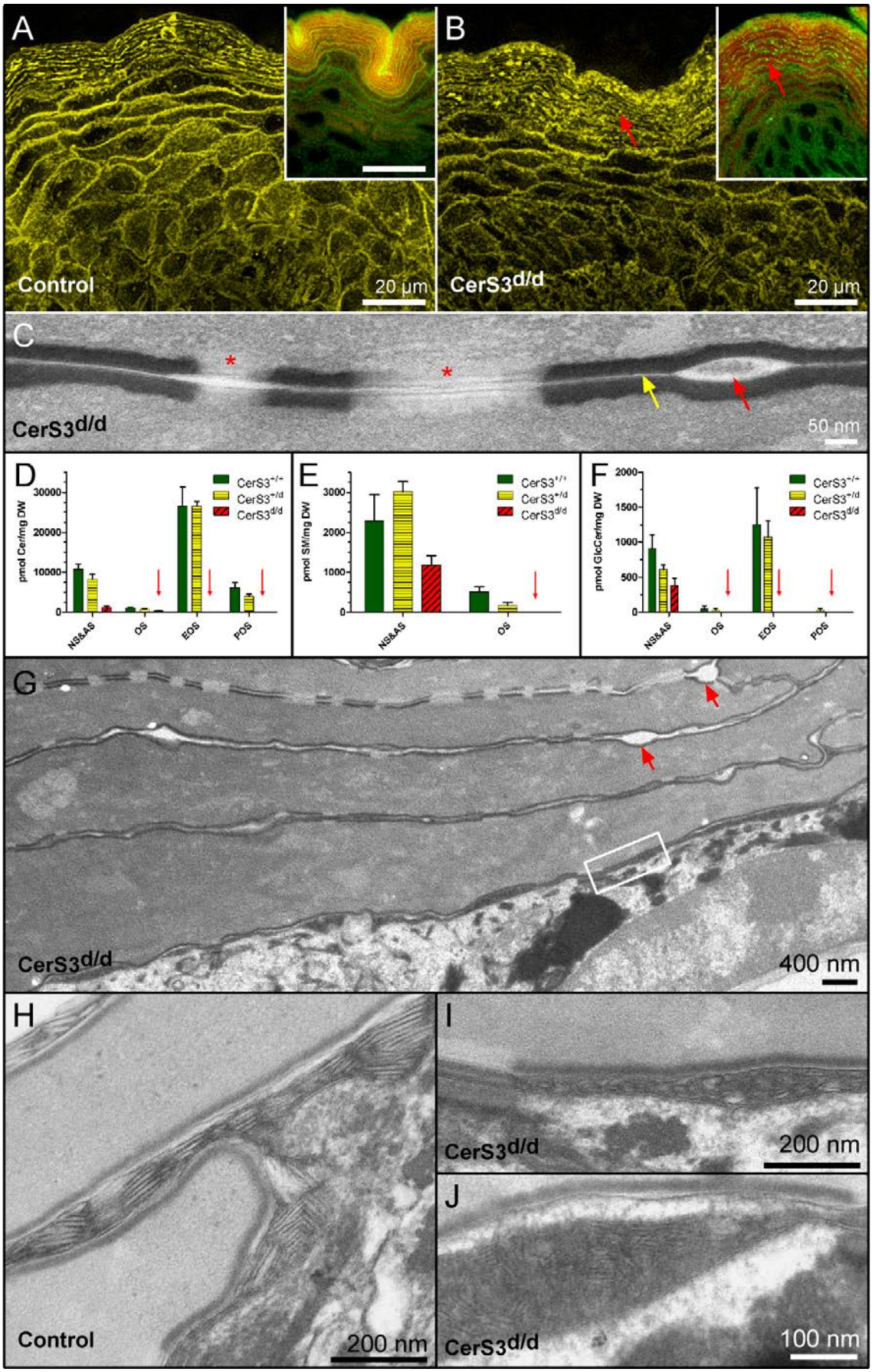
A
Control
20 µm
B
CerS3d/d
20 µm
C
CerS3d/d
50 nm
D
pmol Cer/mg DW
CerS3+/+
CerS3+/d
CerS3d/d
NS&AS
OS
EOS
POS
E
pmol SM/mg DW
F
pmol GlcCer/mg DW
G
CerS3d/d
400 nm
H
Control
200 nm
I
CerS3d/d
200 nm
J
CerS3d/d
100 nm

Figure 42. Altered epidermal lipid content and secretion of CerS3$^{d/d}$ mice.
Labelling of cholesterol with filipin and polar and netral lipids with nile red (inset) revealed the proper linear formation of lipid lamellae on skin sections of control mice (A), while exhibiting a dot-like pattern on CerS3$^{d/d}$ skin (B). Ultrastructure of focalized lipid agglomerates located within the intercellular space of CerS3$^{d/d}$ SC (C, red arrow), as seen at the electron microscopical level in skin sections treated with tannic acid. The intercellular space (yellow arrow) was estimated to be about 3–4 nm, where mature lamellar membrane unit structures were absent. The presence of clearly visible corneodesmosomes (red stars) in mutant SC is also indicated. Mass spectrometric quantification of epidermal ceramides (D), glucosyl-ceramides (E) and sphingomyelins (F) of wild type, heterozygous and homozygous CerS3 mice. Sphingolipids were analysed as non-hydroxy fatty acids (NS), α-hydroxy fatty acids (AS), ω-hydroxy fatty acids (OS), linoleic acid esterified ω-hydroxy fatty acids (EOS) and protein bound ω-hydroxylated fatty acids (POS). Error bars indicate the SEM from 3 animals analyzed per group. Low magnification electron micrograph of CerS3 mutant interface (G) and corresponding higher magnification mutant interface from white-marked rectangle (I). Lipid agglomerates were present in mutant epidermis particularly at tri-cellular contact sites or previous contact sites at the SG (red arrows). Abundant lamellar material packed in small stacks composed of short lamellar discs (I and J) were observed in mutant SC, whereas the interface of control mice (H) displayed stacks consisting of lamellar discs with a larger diameter and showing initial transformation into lamellar unit structures.

To evaluate which lipid species were altered due to the lack of CerS3, thin layer chromatography of free extractable lipids was performed (Figure A6A). Most TLC bands derived from ceramide (Cer) and glucosylceramide (GlcCer) species were extremely reduced or abolished in mutant mice, whereas no stricking differences could be observed for heterozygous mice. The structural differences within the Cer or GlcCer species resulted in several bands, which differences in the length of their acyl chains and hydroxylation produced an unequal mobility through the silica plate. Taking into account the different retention of the lipid species, we could distinguish between low migrating bands containing hydroxylated lipid species, and upper migrating bands with no hydroxylation and increasing mobility with increasing acyl chain length. Furthermore, the most fast migrating bands appeared with Cer and GlcCer being ω-esterified with another acyl chain, mainly linoleic acid. Both lower

migrating bands of Cer and GlcCer appear to be the only ones to be increased with CerS3 deficiency. These bands could be associated with α-hydroxylated LC-Cers and GlcCers. No major differences of other lipid species were evident.

To obtain a detailed lipid profile of epidermal extracts, quantitative mass spectrometric analyses were performed. CerS3 deficient mice exhibited a general drastic reduction of Cers, GlcCers and SMs (Figure 42D-F). Free extractable ceramides with no hydroxylation (NS) or with hydroxylation at the α-position (AS) were strongly reduced but still present in deficient skin. The majority of epidermal ceramides are a special class containing ultra long chain ω-hydroxylated acyl moieties (OS). Most of these OS-ceramides are esterified at the ω-position with another fatty acid (EOS), predominantly linoleic acid. The second major group is ω-esterified to CE-proteins (POS). All three forms of OS-sphingolipid species were absent in mutant epidermis. Similar changes were observed for SM and GlcCer species in CerS3$^{d/d}$ mice. Wild type and heterozygous mice did not differ significantly for any class of sphingolipid analyzed.

Mass spectrometry enabled us to determine quantitatively the profile of acyl moieties linked by an amide bond to the LCB of Cers, GlcCers and SMs (Figure A6B). In agreement with TLC analyses, LC-Cer and GlcCer primarily containing palmitate (16:0) or hydroxylated palmitic acid (h16:0) residue were slightly elevated in CerS3$^{d/d}$ mice. Acyl residues containing lignoceroyl (24:0) were significantly diminished, whereas Cers, GlcCers and SMs containing cerotoyl (26:0) or ULC-FA residues were completely absent in homozygote CerS3 mutants. The latter ULC-acyl moieties are the only source of ω derived sphingolipids. In composite, mass spectrometric analyses revealed that CerS3 depleted mice lacked about 90% of all epidermal ceramides.

Continuous lamellar sheets oriented in parallel and filling the intercellular spaces of the intermediate and upper SC are built up by fusion from nascent lamellar stacks secreted by lamellar bodies (LB) at the SG-SC interface (see section 1.4.2.5.). In control mice, these stacks were composed of large discs (Figure 42H), which were progressively transformed into the typical lamellar basic structures organized in parallel to the PM. In contrast, LB-derived stacks of CerS3 deficient epidermis were smaller and lamellar discs displayed a shortened diameter (Figure 42I and 42J).

Furthermore, in the upper SC layers non-lamellar material clustered forming agglomerates particularly at the tri-cellular contact sites (Figure 42G, red arrow), and the intercellular spaces between corneodesmosomes were maximally reduced lacking mature lamellar unit structures.

3.3.7. Loss of CerS3 but not of CerS2 function results in a drastic reduction of epidermal ceramides/sphingolipids.

In vitro ceramide synthase assays demonstrate the requirement of CerS3 activity for the biosynthesis of ULC-ceramides/sphingolipids, while excluding the role of CerS2 for their biosynthesis. However, CerS2 transcript levels were significantly expressed in murine skin, as observed by quantitative RT-PCR (Figure 43A). To assure our *in vitro* findings and thereby rule out the involvement of CerS2 in the formation of essential epidermal sphingolipids *in vivo*, the epidermal lipid composition of $CerS2^{gt/gt}$ mice were analyzed and compared with $CerS3^{d/d}$. In $CerS2^{gt/gt}$ mice, no decrease was observed for any kind of epidermal ceramide species, not even for ceramide containing a lignoceroyl residue (24:0), the preferred product of CerS2 activity (Figure 43B). In contrast, epidermal ceramides with an acyl chain of 24–28 carbon atoms in length were moderately increased by 15 and 35% in heterozygote and homozygote mutant CerS2 mice, respectively (Figure 43C), thus demonstrating that CerS2 is not required for the biosynthesis of ω-hydroxy-ceramides with ultra long chain acyl residues.

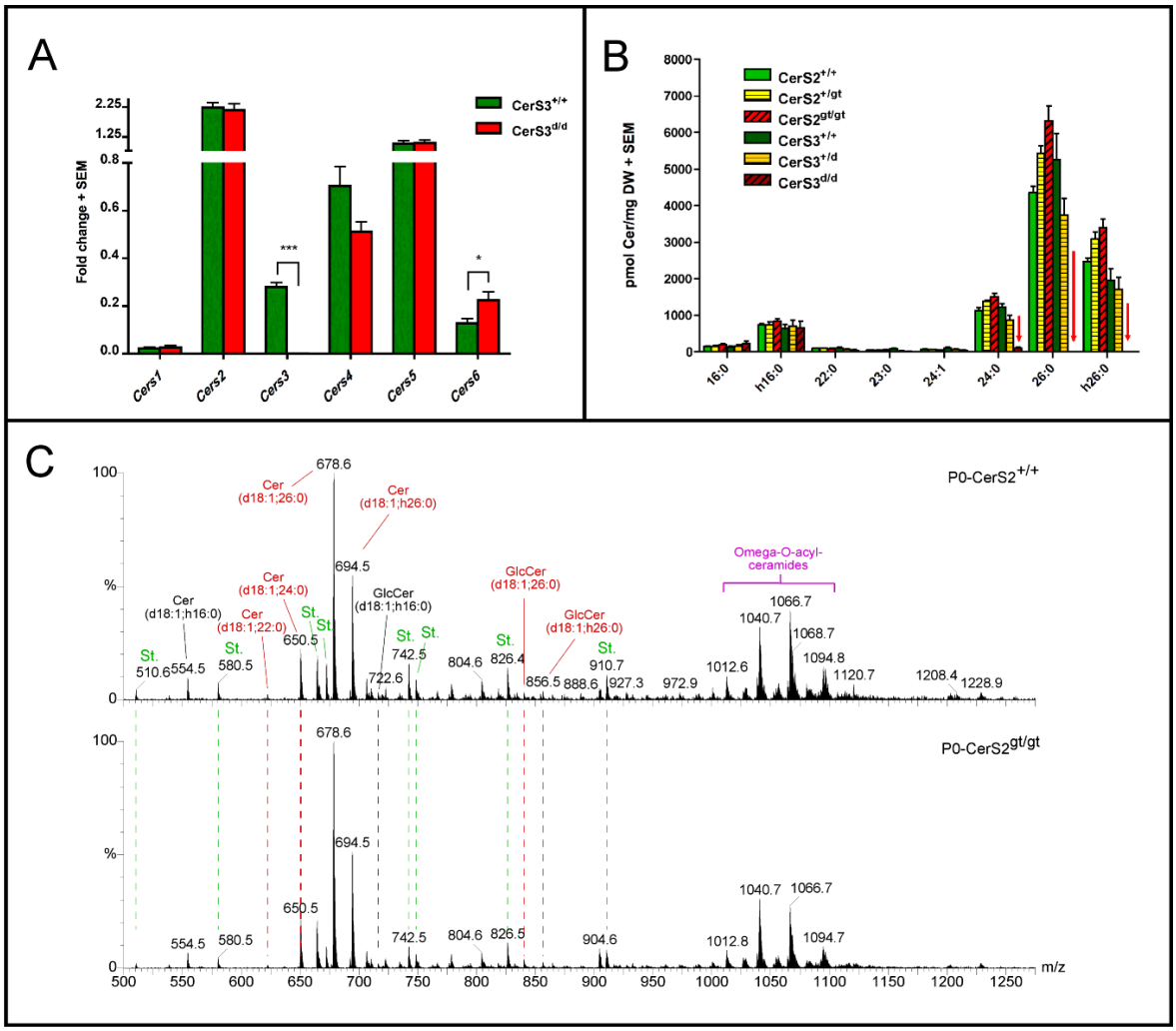

Figure 43. Loss of CerS2 activity does not account for reduction in epidermal ULC-ceramides.

*(A) Quantitative RT-PCR of Cers transcripts in wild type and mutant CerS3 mice. (B) Ceramide profile of CerS2 and CerS3 mutants as compared with their respective wild type and heterozygous littermates. No reduction of any ceramide species was observed in CerS2$^{gt/gt}$ mice. (C) Mass spectrometry of ceramides and glucosylceramides in neonatal wild type and CerS2 deficient epidermis indicating no alterations for EOS-ceramides. Error bars indicate SEM with *** for p<0.001 and * for p<0.05.*

3.3.8. Severe pathogenic infection on cultured skin biopsies of CerS3 deficient mice

A specific ratio of SC lipids is critical for proper epidermal barrier function. Alterations within this ratio, as well as differences between their lipid species have been implicated in multitude of diseases, particularly in atopic dermatitis and psoriasis (Coderch et al., 2003). Besides, certain SC have been suggested to have antimicrobial activity (Arikawa et al., 2002; Bibel et al., 1992). Among them, decreased sphingosine levels have been suggested to play a significant role in the vulnerability of microbial infections in patients suffering atopic dermatitis. This reduction in sphingosine concentration in diseased SC is probably a consequence of diminished ceramide levels. In order to establish whether the lack of major ceramides had an influence on the susceptibility of pathogenic infections, skin biopsies of CerS3 deficient mice were infected with *Candida albicans,* which is a common opportunistic pathogen infecting epidermis of patients with compromised skin integrity.

Control skin infected with 1×10^6 cells of C.*albicans* exhibited only sporadically and in low concentration these pathogens attached to the surface of the skin biopsies independently from the incubation time (Figure 44A). In contrast, an extensive growth could be already observed as early as 6 h after inoculation of the pathogen in CerS3 deficient skin (Figure 44B). Histological examinations with increasing incubation times with the fungi, demonstrated a prominent increase of *C.albicans* after 24 h in mutant skin (Figure 44C-D), which was more pronounced after 66 h (Figure 44E-F). In addition, skin biopsies from mutant embryos at stage of E18.5 ± 0.5 exhibited increased pathogenic growth after 24 h post inoculation, as compared with control littermates. Pathogenic growth was determined by quantification of the colony forming units (CFU) generated from the yeast that infected the skin biopsies (Figure A7A). Addition of pathogens onto the SC of cultured skin resulted in a 3.5 fold increase of CFU in CerS3 deficient skin.

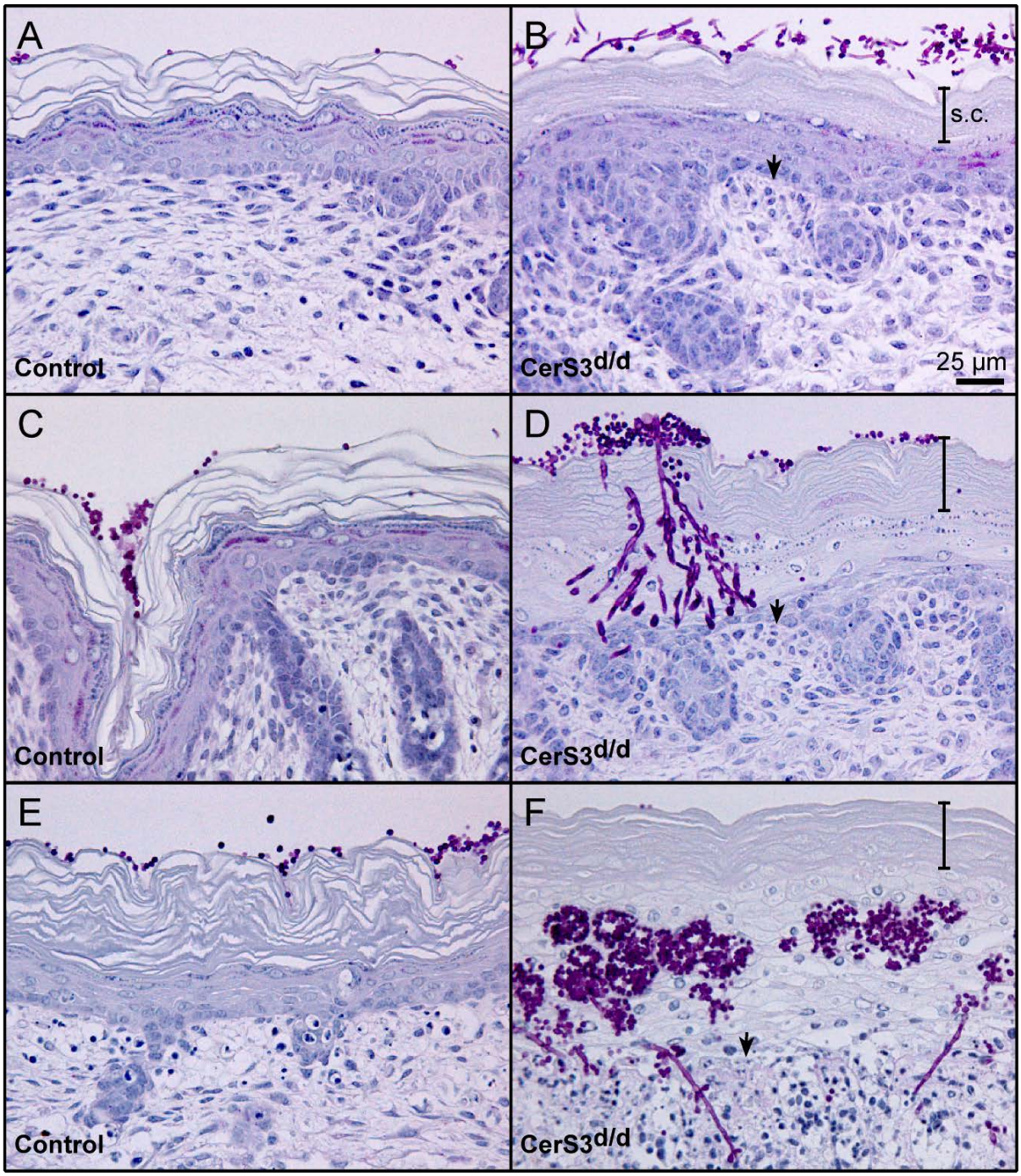

Figure 44. Severe pathogenic infection on cultured skin of CerS3 deficient mice.

Cultured skin from neonatal control and CerS3$^{d/d}$ mice were inoculated with C. albicans and incubated for 6 h (A and B), 24 h (C and D) and 66 h (E and F) at 30 ºC. Paraffin sections of 1 µm thickness were stained with periodic acid-Schiff (PAS). Localization of the basement membrane in mutant skin is indicated (black arrows).

With increasing incubation time, *Candida albicans* developed pseudohyphae, which penetrated the SC and invaded the living epidermal layers down into the dermis only in mutant skin. Upon 24 h incubation, deficient CerS3 skin exhibited extensive invasive pathogen infiltration into the suprabasal layers (Figure 44D), which could not be observed in cultured control skin (Figure 44C). Following the invasion phase, increased bud morphology and colony formation could be observed within the nucleated epidermal layers (Figure 44F). At 66 h, mutant epidermis exhibited pseudohyphae that crossed the basement membrane migrating into the dermis, which was marked by the abundance of infiltrated immune cells (Figure 44F).

In addition to the lipid barrier, microbial growth is greatly inhibited by specialized peptides and proteins that serve as an additional defense mechanism. These antimicrobials peptides are generally packed and extruded by LB in the intercellular space of the SC. Upon recognition of the pathogens by the innate immune response, antimicrobial peptides are activated and secreted in order to combat pathogenic invasion primarily by disrupting the microbial membrane (Yamasaki and Gallo, 2008). To examine whether the increased microbial growth in mutant skin was a consequence of an alteration in the expression of these antimicrobial peptides, quantification of their transcript levels was determined (Figure A7B). However, murine β-defensins, as well as the unique murine cathelicidin expression levels were comparable in CerS3 deficient skin and control. Therefore, antimicrobial peptides could not account for the differences in microbial growth between control and mutant CerS3 skin.

4. Discussion

4.1. Coexpression of *Cers3* and ULC-sphingolipids in mature male germs cells and skin

Sphingolipids containing a fatty acid moiety ranging between 16 and 24 carbon atoms in length have been found constitutively expressed in the plasma membrane of all mammalian cells. However, testicular and epidermal cells additionally express high concentrations of sphingolipids with ultra long chain acyl moieties. In testis, polyenoic (4 to 6 double bonds) ULC-CoAs of 28 to 32 carbon atoms are incorporated into ceramides, which can be further modified generating sphingomyelins or complex glycosphingolipids. Sphingolipids containing ULC-PUFA residues might be exclusively expressed in maturing male germ cells, since the depletion of ULC-PUFA complex GSLs causes azoospermia due to an arrest of the spermatogenic cycle at the stage of spermatid formation in GM2S/Galgt1$^{-/-}$ mice (Sandhoff et al., 2005). On the other hand, mainly saturated and monounsaturated ω-hydroxylated ULC-CoAs of 26 to 36 carbon atoms in length are expressed in highly abundant ceramides of the *stratum corneum* (Sandhoff, 2009). There, ULC-sphingolipids are required from the late embryonic stage on (E16.5-18.5 in mice) for the formation and maintenance of the epidermal permeability barrier, as demonstrated with the specific deletion of the glucosylceramide synthase under the promoter of keratin 14 (Jennemann et al., 2007). However, the functional role of polyenoic ULC-sphingolipids in testicular cells is still elusive. To unveil the molecular mechanism by which ULC-sphingolipids enable the progress of spermatogenesis, it is a prerequisite to fully understand their biosynthetic requirements. Therefore identifying the ceramide synthase/s responsible for their biosynthesis is mandatory.

Currently the six members of the ceramide synthase family have been characterized regarding their substrate affinity towards a range of acyl-CoAs whose length varied from 14 to 26 carbon atoms. From these studies, CerS2 and CerS3 were reported to best incorporate the longest subset of acyl-CoAs (Laviad et al., 2008; Mizutani et al., 2006).

Analysis of the tissue distribution of CerS3 demonstrated its high expression in murine testis and skin, the only tissues reported to contain major concentrations of ULC-ceramides. On the other hand, CerS3 could not be detected in brain, liver and

colon. These organs express sphingolipids exclusively with conventional acyl moieties ranging from 16 to 24 carbon atoms. These results were further confirmed by two independent studies (Laviad et al., 2008; Mizutani et al., 2006). In contrast, CerS2 has been reported to be ubiquitously expressed, with its highest transcript levels found in kidney and liver (Laviad et al., 2008).

In order to correlate the expression of ULC-sphingolipids with the ceramide synthase/s responsible for their biosynthesis, detailed transcript analyses of the *Cers* family were performed in mature mouse testes and neonatal skin. With the exception of *Cers1*, the expression levels of the remaining *Cers* homologues could be detected in either one or both tissues to various extents.

Cers3 was the most prominent *Cers* expressed in testis and the second most abundant in skin, only overtaken by 1.5-fold upregulation of *Cers2*. In addition to ULC-acyl moieties, epidermal sphingolipids contain large quantities of VLC-acyl residues with 26 carbon atoms, which have been shown to be acylated to produce ceramides by CerS2 *in vitro* (Laviad et al., 2008). Therefore, it would be expected to have abundant *Cers2* levels in the epidermis. Whether exclusively CerS2 or in addition CerS3 are able to synthesize sphingolipids with cerotoyl moieties will require further studies. Nevertheless, it seemed plausible that CerS3 might be the enzyme required for the biosynthesis of ULC-sphingolipids, since its mRNA and tissue expression correlates with the presence of sphingolipids containing ULC-acyl moieties.

On the other hand, *Cers2* mRNA was also expressed in testis, although its transcript levels only accounted for 15% of those of *Cers3*. Since recent studies have demonstrated that CerS2 can incorporate acyl-CoAs of 20 to 26 carbon atoms in length (Laviad et al., 2008), CerS2 still was a potential candidate capable of producing ceramides with unconventional ULC-acyl residues.

Both testis and skin expressed fairly abundant levels of *Cers5*, whereas the relative *Cers6* expression levels were rather low. Nevertheless, CerS5 and CerS6 have been reported to incorporate acyl-CoAs with a chain length ranging from 14 to 18 but not more carbon atoms (Mizutani et al., 2005; Riebeling et al., 2003). Hence, it seems unlikely that neither of these two enzymes could catalyze the synthesis of sphingolipids using acyl-CoAs with 28 and longer carbon atom chains as substrates.

Cers4 exhibited a moderate expression in mouse skin, however its mRNA concentration was barely detectable in testis. In skin, *Cers4* has been reported to be mainly expressed in acinar cells of the sebaceous glands (Meixner, 2009). Besides, the highest ceramide synthase activity of CerS4 was achieved with acyl-CoA substrates ranging from 18 to 22 carbon atoms, with negligible activities for longer fatty acid substrates (Riebeling et al., 2003). Likewise CerS5 and CerS6, it would be rather unexpected that CerS4 could catalyze the condensation of ULC-acyl-CoAs with a sphingoid base to produce ULC-ceramides.

Consistent with the correlation of mRNA and tissue expression of the *Cers* homologues in the major tissues expressing ULC-sphingolipids, it was concluded that CerS2 and CerS3 are the only potential candidates that might be involved in the synthesis of ULC-ceramides. In order to confirm or reject their role in this pathway, their transcript expression levels were compared to the concentration of ULC-sphingolipids during the progress of the first spermatogenic cycle.

Levels of testicular sphingolipids containing ULC-PUFA moieties were found to be increased during juvenile maturation. In particular, mass spectrometric analyses of all types of sphingolipids according to their fatty acid residues revealed the presence of exclusively conventional fatty acid moieties (of 16 to 24 carbon atoms) during the earlier stages of postnatal testicular development (Rabionet et al., 2008). LC- and VLC-sphingolipid expression correlated with the elevated mRNA content of *Cers5* and *Cers6*, as well as of *Cers2*, whose highest substrate specificities have been reported to be precisely acyl-CoAs of 16 and 24 carbon atoms, respectively (Lahiri and Futerman, 2005; Laviad et al., 2008). In contrast, *Cers3* mRNA levels prior to PN 14 were barely detectable.

From PN 14 to PN 15, *Cers3* mRNA was exceptionally upregulated, coinciding shortly afterwards with the detection of the first ceramides, sphingomyelins and glycosphingolipids containing ULC-PUFA residues. To the contrary, the transcript levels of all *Cers* expressed in murine testis were simultaneously downregulated.

The concentration of polyenoic ULC-sphingolipids increased progressively until steady state levels were reached between PN 25 and PN 30. In addition, detailed analyses of complex fucosylated GSLs demonstrated the concomitantly increase of the neutral subset, which exclusively incorporate ULC-PUFAs. On the other hand,

fucosylated ganglioside GM1 (FucGM1) was already present from the early stages of the first spermatogenic cycle and its concentration increased moderately from PN 14. FucGM1 was composed of ULC-PUFAs and a major portion of LC-FAs (h16:0) (Rabionet et al., 2008).

Whereas the overall levels of *Cers2*, *Cers5* and *Cers6* remained relatively constant from PN 14 to PN 25, *Cers3* transcript expression prominently increased correlating with the elevated levels of ULC-sphingolipids. The total increase of *Cers3* mRNA from PN 5 to PN 25 was calculated to be more than 700 fold.

Additionally, *Cers3* mRNA was unique among *Cers* transcript levels to be completely depleted in mutant Kit^{W-v}/Kit^{W} mice testes that lacked ceramides, sphingomyelins, and GSLs including FGSLs with ULC-PUFA residues. Infertile Kit^{W-v}/Kit^{W} mice testes are devoid of intact differentiated germ cells, by that underpinning that the latter are the source of polyenoic ULC-sphingolipids. Moreover, neutral FGSL – which are extremely rich in ULC-PUFAs – were localized by immunohistochemistry to differentiated germ cells, *i.e*. pachytene spermatocytes, spermatids and spermatozoa (Sandhoff et al., 2005). Thus, the lack of fertility-essential neutral FGSL carrying ULC-PUFA residues in conjunction with the absence of *Cers3* mRNA in infertile Kit^{W-v}/Kit^{W} mice provided evidence of their requirement in differentiating male germ cells and to be crucial for the proper development of complete spermatogenesis.

Furthermore, the acidic subset of FGSL was reduced in mutant mice (Rabionet et al., 2008). Previously, its major component FucGM1 was mainly localized in spermatogonia stem cells. As a result, FucGM1 additionally was composed of significant amounts of palmitic acid (16:0 and h16:0) besides of ULC-PUFA residues (Sandhoff et al., 2005). The incorporation of the palmitic acid moiety might be catalyzed primarily by *Cers6* and/or *Cers5 (Mizutani et al., 2005; Riebeling et al., 2003)*. In Kit^{W-v}/Kit^{W} mice, significant transcript levels of both *Cers5* and *Cers6* were detected, thus suggesting their localization in either somatic cells and/or residual spermatogonia. Taking into consideration that all *Cers* expression levels were decreased in infertile Kit^{W-v}/Kit^{W} mice, we additionally determined the percentatge of *Cers* mRNA relative to the total *Cers* mRNA levels per mice (data not shown). Neither *Cers5* nor *Cers6* relative transcript levels were reduced in mutant testicular

mRNA, which might indicate a major role of these ceramide synthase homologues in the synthesis of LC-sphingolipids in testicular somatic cells or type A spermatogonia.

Relative transcript levels of *Cers2* were decreased in sterile $Kit^{W\text{-}v}/Kit^{W}$ mice testes. This suggests an expression in basal and eventually adluminal differentiated germ cells, although its residual mRNA levels suggest in addition a somatic and/or spermatogonial origin. In the latter, CerS2 accounts for the synthesis of non-fucosylated VLC-sphingolipids.

In summary, *Cers3* mRNA concentration strongly correlates with the expression of ULC-sphingolipids in murine skin and differentiated male germ cells, suggesting its unique role in the synthesis of these unconventional sphingolipids. During the first spermatogenic cycle in mice, their onset of expression coincided beyond PN 14–15, simultaneously with the migration of the first primary spermatocytes through the blood testis barrier (BTB) and the formation of early pachytene spermatocytes at the adluminal compartment of the seminiferous epithelium.

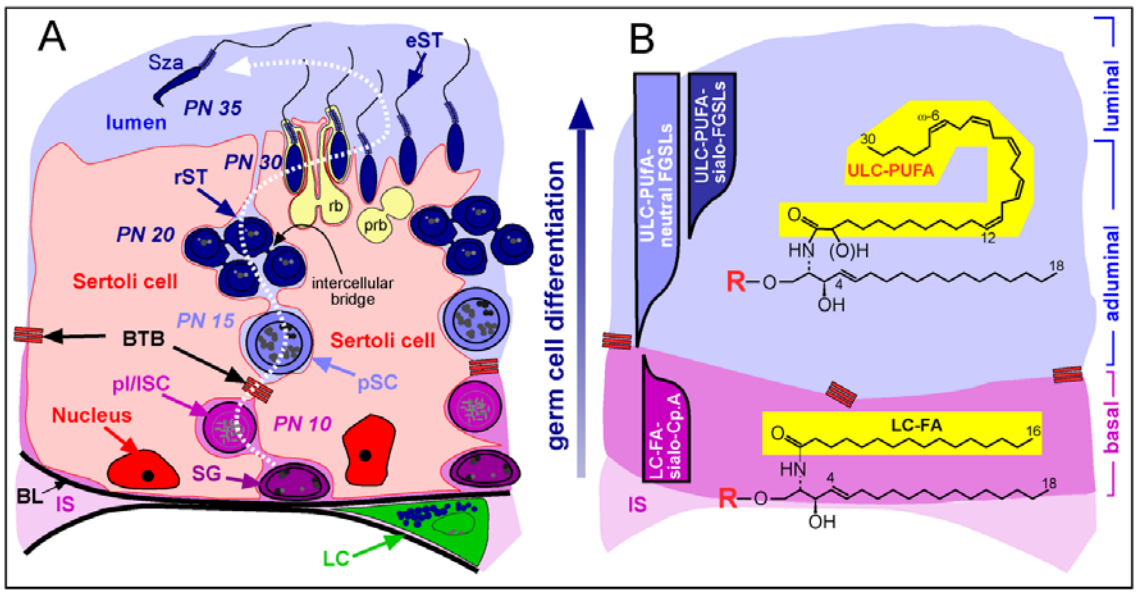

Figure 45. Murine spermatogenesis and associated sphingolipid expression. *Interstitial cells, Sertoli cells and germ cells of the basal compartment express sphingolipids with LC- and VLC-FAs, mainly palmitic acid, whereas adluminal germ cells and spermatozoa express primarily sphingolipids with ULC-PUFA moieties. PN: post natal; SG: spermatogonia; pl/l SC: preleptotene/leptotene spermatocytes; rST: round spermatids; eST: elongated spermatids; Sza: spermatozoa; BL: basal lamina; IS: interstitial cells; LC: Leydig cells. Scheme modified from (Rabionet et al., 2008).*

The physiological role of ULC-sphingolipids in spermatogenesis and male fertility is currently unknown. However, some indications might suggest their requirement for the proper maintenance of the BTB dynamics. The BTB is constituted by an array of specialized junctional complexes established by polarized Sertoli cells. Lack of polyenoic LC-FAs due to the specific disruption of the Δ6-fatty acid desaturase (Fads2) leads to a disruption of the BTB and loss of Sertoli cell polarity, resulting in spermatogenesis arrest at the stage of round spermatid formation and ultimately to azoospermia (Stoffel et al., 2008). Fads2 blocks the rate-limiting step in the desaturation of linoleic (ω6-18:2) to γ-linoleic (ω6-18:3) and of α-linoleic (ω3-18:3) to stearidonic acid (ω3-18:4), precursors required for the subsequent elongation and further desaturation steps yielding ULC-PUFA synthesis. Although ULC-PUFAs and corresponding sphingolipids were not investigated by the authors, in the context of their findings, it could be derived that depletion of polyenoic ULC-sphingolipids might also alter the structural plasma membrane tight junctional complexes leading to an impaired assembly and disassembly of the BTB.

Besides tight junction and gap junction complexes, the BTB is additionally constituted of actin-based adherens junctions, and intermediate filament-based desmosome-like junctions. These two latter types of cell-cell adhesion junctions are crucial for maintaining the close association between nourishing Sertoli cells and developing meiotic germ cells and spermatids. Throughout spermatogenesis, a great restructuring of these junctional complexes is required. Their defective remodeling/disassembly might lead to the formation of the multinucleated giant cells observed upon disruption of the GM2S/Galgt1 gene, wich lack all FGSLs containing ULC-PUFA moieties (Rabionet et al., 2008; Sandhoff et al., 2005).

The functional role of ULC-PUFA sphingolipids might as well be interpreted by alternative hypotheses. During the progress of spermatogenesis, developing germ cell clones at different stages of differentiation must remain connected by intercellular bridges sharing one unique cytosol and plasma membrane. These intercellular bridges are lost and multinucleated giant cells are formed in GM2S/Galgt1 deficient mice (Sandhoff et al., 2005). Hence, the stability, maintenance and regulation of this incomplete cytokinesis, as well as the complex membrane processes during

proliferation and elongation of spermatids, could be modulated by this unconventional lipid class.

Structurally, the multiple cis-olefinic moieties might reduce the intercellular Van der Waals forces probably driving the local deformation of the lipid bilayer, thus reducing the lipid packaging, which might ultimately lead to an increase in membrane flexibility. In addition to be relevant for membrane fusion events, the elevated membrane fluidity in mature germ cells is believed to be required for motility (Nolan and Hammerstedt, 1997; Stoffel et al., 2008). In this regard, polyenoic fucosylated GA1 could be localized at the tail of developing spermatozoa by immunolabeling with anti-Fuc-GA1 (Sandhoff et al., 2005). In a further study, Furland and coworkers linked polyenoic ULC-sphingomyelins and ceramides to the head of spermatozoa. The authors reported high levels of sphingomyelin degradation favoring ceramide formation upon spermatozoa capacitation. This hydrolysis could play a role in prefertilization events required for the correct consummation of the following acrosomal reaction (Furland et al., 2007).

Alternatively, the homeobox domain encoded within the *Cers3* gene might have a key role in regulating germ cell differentiation, as have been already observed for other homeobox-containing genes (Wolgemuth et al., 1987).

To unveil the functional role of CerS3 and polyenoic ULC-sphingolipids, novel *in vivo* models with germ cell specific depletion of these unconventional lipids will be necessary. In this regard, our efforts are currently focused on the conditional depletion of CerS3 in premeiotic male germ cells *in vivo*.

Future perspectives regarding the modulation of ULC-sphingolipids might have an impact in male contraception. In this context, the newly identified CerS3 as a key enzyme for the biosynthesis of fertility-essential ULC-ceramides could be targeted to induce reversible infertility.

4.2. ULC-sphingolipids are *bona fide* substrates of CerS3 in living mammalian cells

To confirm the role of CerS3 in the biosynthesis of testicular and epidermal ULC-sphingolipids, enzymatic assays with recombinantly expressed CerS3 in mammalian

cells were performed with acyl-CoAs ranging from 16 to 28 carbon atoms in length. In contrast to previous CerS assays where either cellular lysates or microsomes were used to assess CerS activity, we have established for the first time a CerS assay in living mammalian cells. Former *in vitro* enzymatic assays made extensive use of detergents to solubilize cellular membranes (Mandon et al., 1992; Mizutani et al., 2005; Mizutani et al., 2006; Shimeno et al., 1998). However, it is well established that use of detergents might induce artifacts due to aggregation or even inactivation of membrane-bound enzymes (Zhou et al., 2001). By establishing a detergent-free assay we have been able to preserve the biochemical environment of the enzyme with minimal alterations of its *in vivo* conditions.

Due to the lack of commercial availability of activated fatty acids longer than 26 carbon atoms, ULC-acyl-CoAs had to be chemically synthesized. For this synthesis, the elegant approach of Lucet-Levannier and coworkers, which is especially designed for the preparation of highly lipophilic acyl-CoAs was employed (Lucet-Levannier et al., 1995). By derivatizing the hydrophilic CoA to the polysilylated CoA, the coupling with the extremely hydrophobic ULC-FAs could take place under anhydrous organic conditions. This type of preparation differed conspicuously from the classical methods, which required the use of a binary mixture of water-organic solvent in order to solubilize both the CoA and the activated fatty acids with *N*-hydroxysuccinimide (Al-Arif and Blecher, 1969). The employment of binary mixtures leads either to a biphasic system in which the contact of reactants is not optimal, or to a homogeneous solution in which the solubilities of both reactants are diminished. In either case, the reaction proceeds in an inefficient manner thereby drastically reducing its chemical yield. Although the classical methods have been employed for the preparation of activated fatty acids in the range of 16 carbon atoms, we assumed that the synthesis of ULC-CoAs with an additional 12 carbon atoms and its increased accompanying hydrophobicity would render the conventional synthethic approach virtually impossible. Additionally, the usage of water results in undesired competing reactions due to the hydrolysis of the NHS-activated fatty acids by water.

Previous to the ceramide synthase assay, overexpression of recombinantly expressed proteins was confirmed by flow cytometric analyses, as well as by immunoblotting. Although CerS3 could be detected by Western blot as one single

band corresponding to the expression of the fusion EGFP protein, CerS2 exhibited four specific bands. These various protein products very likely arise from diverse post-translational modifications. A similar finding was observed with the detection of mCerS2-HA in overexpressed HEK-293T cells by Mizutani et al., who linked this to various *N*-glycosilation microheterogenities (Mizutani et al., 2005). In addition, the authors reported that CerS5 and CerS6 are also *N*-glycosylated proteins, whereas CerS1 and CerS4 are not. Here, we reported that CerS3 produced in overexpressing HeLa cells exhibited one unique band, likely indicating the absence of post-translational glycosilations.

The ceramide synthase activity was examined by exposing CerS3, as well as CerS2 and control EGFP expressing HeLa cells to an acyl-CoA mixture (16:0,18:0,20:0,24:0,26:0,28:0), simultaneously with d17:1-sphingosine for 20 h. To determine the *de novo* synthesized ceramides, we took advantage of the lack of sphingosine (d17:1) in our mammalian cell culture system. Although sphingosine (d18:1) is predominant in most mammalian tissues due to the preference of serine palmitoyl transferase towards palmitoyl-CoA (Hanada, 2003), minor amounts of various long chain bases including d17:1 have been detected in several tissues, *e.g.* skin (Farwanah et al., 2007). Using this non-endogeneous sphingoid base as a substrate, we were able to quantify ceramides with a d17:1 backbone that corresponded to newly synthesized metabolites. Quantification of d17:1-ceramides could only be carried out with suitable internal standards that were synthesized specifically for this purpose in this thesis.

Upon availability of an equimolar mixture of acyl-CoAs that included an ULC-acyl-CoA, CerS3 exclusively produced cerotoyl- (26:0-Cer) and montanoyl-ceramides (28:0-Cer) in a significant manner, thereby demonstrating its capability for ULC-ceramide synthesis. Formerly, *in vitro* CerS3 activity assays performed with overexpressed cell lysates indicated that CerS3 has very broad substrate specificity. With acyl-CoAs ranging from 16 to 26 carbon atoms, CerS3 exhibited the highest activity towards stearoyl-CoA (18:0), with an additional affinity towards behenoyl-CoA (20:0) and lignoceroyl-CoA (24:0) (Mizutani et al., 2006).

In our living cell model, besides the observed affinity of CerS3 towards 26- and 28-CoAs, no other acyl-CoA substrate did exhibit a significant increase upon CerS3

expression. However, preliminary results of our own *in vitro* CerS3 activity assays using cell lysates indicated increased production of lignoceroyl-ceramide (Rabionet and Sandhoff, unpublished results), thus partially supporting the findings obtained by Mizutani and coworkers. The CerS3 affinity towards shorter chain substrates might be overruled in our model by the high levels of endogenously expressed CerS2, which has been demonstrated to catalyze primarily the formation of 22- and 24-ceramides (Laviad et al., 2008). Nevertheless, the present CerS assay demonstrated that CerS3 in contrast to CerS2 could catalyze the acylation of sphingosine using ULC-CoAs as substrates in living human cells.

These findings could successfully be confirmed in a yeast model in collaboration with Prof. Dr. Howard Riezmann from the University of Geneva (Epstein and Riezmann, *personal communication*). In their model, the ceramide synthase specificity of CerS2 and CerS3 was assayed in a mutated yeast strain capable of synthesizing montanoyl-CoA. In particular, the mammalian mCerS2 or hCerS3 proteins were introduced in a *S. cerevisiae* strain, which was previously depleted of the yeast ceramide synthases Lag1p and Lac1p. These strains were further transformed with a plasmid encoding a mutated version of the yeast fatty acid elongase protein, Sur4p. In this context, the major ceramide species generated by expression of CerS2 contained VLC-acyl moieties ranging from 22 to 26 carbon atoms in length, as previously reported. However, availability of 28:0-CoA did not produce any effect on the relative inositolphosphorylceramide (IPC) concentration, and thus supporting our findings that CerS2 is not capable of synthesizing sphingolipids with acyl moieties longer than 26 carbon atoms.

In contrast, CerS3 produced ceramides with stearoyl and cerotoyl moieties in the absence of ULC-CoAs, again partially confirming the results of Mizutani and coworkers. However, the presence of montanoyl-CoA in the fatty acid pool lead to a strong increase of ULC-ceramides, hence corroborating the capability of CerS3 for synthesizing ceramides with ultra long chain acyl moieties.

The specific depletion of CerS3 *in vivo* definitely established the role of CerS3 in the biosynthesis of ULC-ceramides. Quantitative mass spectrometric analyses of epidermal extracts revealed the complete lack of sphingolipids containing acyl moieties ranging from 26 to 36 carbon atoms in length. Additionally, the

concentration of lignoceroyl-sphingolipids was significantly decreased, thus indicating CerS3 to have certain affinity towards 24-CoA. Shorter chain acyl residues did not show any significant decrease upon CerS3 deficiency.

Besides, the epidermal sphingolipid profile of CerS2 depleted mice was additionally investigated. These investigations lead to the conclusion that CerS2 does not play a role in the biosynthesis of ULC-sphingolipids, evidenced by the lack of reduction of ULC-ceramides.

In summary, the *in vitro* and *in vivo* findings demonstrated that in the presence of ULC-acyl-CoAs, CerS3 preferentially incorporates acyl residues of 24 to 36 carbon atoms in length. In contrast, CerS2 is unable to produce ceramides using ULC-CoAs as acyl donors. The reported specificities of the remaning ceramide synthase homologues that were not included in the present study have all been reported to incorporate shorter acyl-CoA substrates. CerS5 and CerS6 primarily incorporate palmitic acid, whereas CerS1 incorporates stearic acid, and CerS4 produces ceramides ranging from 18 to 22 carbon atoms in length. Taken all together, we provide evidence that CerS3 is the only mammalian ceramide synthase capable of synthesizing ULC-sphingolipids. With these findings at hand, we are finally able to attribute the complete spectrum of acyl chain residue specificities to their respective members of the ceramide synthase family (Figure 46).

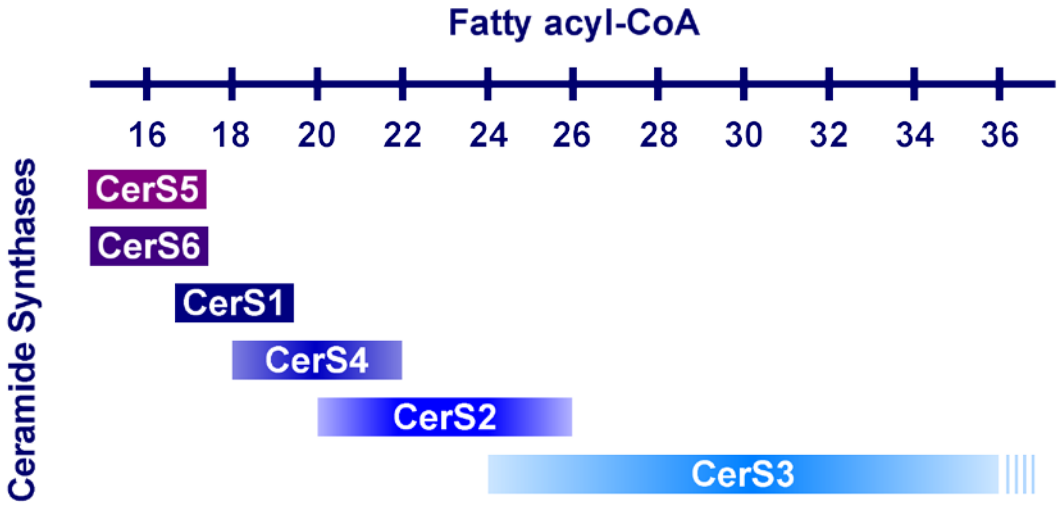

Figure 46. Substrate affinity of the ceramide synthases.
Proposed correlation of the ceramide synthases with their respective substrates, according to previous reported affinities and the current study.

4.3. CerS3 is essential for epidermal barrier function and survival

To unveil the physiological role of CerS3 and ULC-sphingolipids *in vivo*, we investigated the impact of CerS3 deficiency in mice with a targeted disruption of exon 7. This exon includes highly conserved amino acids of the lag1 motif, which has been shown to be required for the enzymatic activity of the ceramide synthase proteins (Spassieva et al., 2006). Furthermore, the majority of amino acids that constitute the floxed exon 7 are predicted to localize within a transmembrane domain (Figure 22, TM3), therefore its deletion most probably invers the topology of the subsequent protein sequence including the residual part of the lag1 domain containing the catalytic activity. In addition and in contrast to control mice, CerS3 could not be detected in skin biopsies of mutant mice. CerS3 immunolocalization analysis performed with a self-designed polyclonal antibody against the last 25 amino acids of the *C*-terminus revealed CerS3 expression within keratinocytes of the upper SS and SG of control epidermis. However, CerS3 immunolabeling failed to detect the epitope in the skin of mutant mice, thus suggesting a misfolding and/or degradation of the truncated protein of which the mRNA is expressed. Together with the confirmed deletion of exon 7 by means of PCR, transcript sequencing and Southern blot analyses, these results indicate that exon 7 deletion renders CerS3 dysfunctional.

CerS3$^{d/d}$ mice exhibited universal premature death within 3 hours postnatally. Severe defects of the epidermal barrier function were associated with the neonatal mortality in CerS3 deficient mice, evidenced by the rapid body weight loss concomitantly with transepidermal water loss, and increased skin permeability. According to the current stage of knowledge, the epidermal permeability barrier primarily resides in the enucleated layers of the SC, as well as within the typical TJs (*zonulae occludentes*) localized within the SG of the epidermis (Brandner, 2009; Kirschner et al., 2010b). The lipid lamellar sheets and the cornified lipid envelope, which surround each corneocyte, play a crucial role in maintaining the epidermal barrier homeostasis. In particular, abundant and epidermis-unique ceramides with hydrophobic ω-hydroxylated-ULC-acyl residues, which to a great extent are esterified with linoleic acid (EOS) or with proteins of the CE (POS), have been implicated as

critical regulators of the epidermal integrity and barrier function. For instance, decreased levels of epidermal ceramides with acyl moieties longer than 26 carbon atoms in mice with a targeted disruption of the fatty acid transport protein (Fatp4) resulted in severe impairment of the epidermal barrier (Herrmann et al., 2003). In Elovl4 deficient mice, lack of ω-hydroxylated-ULC-ceramides, due to the requirement of the enzyme for generating fatty acids longer than 28 carbon atoms, lead to early postnatal lethality, abnormally compact SC and defective permeability barrier (Li et al., 2007; McMahon et al., 2007a; Vasireddy et al., 2007). Furthermore, a harlequin ichthyosis mouse model bearing a non functional member of the ABCA family of transporters, Abca12, exhibited a thickened epidermis presumably due to lack of desquamation caused by a profound reduction of EOS-ceramides, consistent with a deficiency for the transport of EOS-ceramide precursors (Zuo et al., 2008). Finally, CGI-58 deficient mice lacking EOS- and to great extent also POS-ceramides, revealed this enzyme to be critical in the esterification process of OS-(Glc)Cer, with the consequent lethal defect of the epidermal permeability barrier (Radner et al., 2009).

In concert with the previous mouse models, drastic reduction of major epidermal ceramide species led to an impairment of the permeability barrier function in CerS3 deficient mice. In our CerS3$^{d/d}$ mice, all ceramide classes containing ω-hydroxylated-ULC-acyl residues, *i.e*. EOS-Cer, POS-Cer and OS-Cer were lacking in mutant epidermis. Consequently, the corresponding sphingomyelin and GlcCer species, which serve as precursors for the extracellularly secreted ceramides, were accordingly diminished. On the other hand, non-hydroxylated and α-hydroxylated-ceramides that contain acyl residues up to 26 carbon atoms in length with cerotoyl-ceramide (26:0 and h26:0) as the dominating species, were profoundly decreased in CerS3$^{d/d}$ epidermis. Detailed mass spectrometric analysis of the ceramide species according to their acyl residue revealed the completely lack of cerotoyl-ceramides (26:0 and h26:0) and the strong reduction of lignoceroyl-ceramides (24:0 and h24:0) in mutant epidermis, besides the mentioned depletion of ULC-ceramides. Therefore, these findings definitely evidenced the broad substrate affinity of CerS3, which primarily acylates sphingoid bases with fatty acids ranging from 26 to 36 carbon atoms in length, and to a lesser extent additionally with 24 carbon atoms. The

substrate specificity of CerS3 according to this *in vivo* model perfectly correlates with the increased cerotoyl- (26:0) and montanoyl-ceramide (28:0) levels observed upon induction of CerS3 in our living cell model, as well as the higher levels of lignoceroyl-ceramide (24:0) detected using *in vitro* CerS activity assays with overexpressed CerS3 cell lysates. From these results, we concluded that CerS3 is essential for the synthesis of ULC-ceramides as they are found in testis and skin.

The inability to maintain the epidermal barrier homeostasis upon CerS3 deficiency could be additionally contributed by the increased or altered paracellular permeability due to the presence of immature tight junctions. Instead of typical *zonulae occludentes* with a continuous distribution at the cell-cell borders, the intracellular plaque protein cingulin exhibited a discrete and focal distribution at the PM of SG keratinocytes of mutant epidermis. The presence of these *maculae occludentes* presumably maintains local but not zonular intercellular sealing at the SG, and thus combined with the lack of ω-hydroxylated-ULC-ceramides lead to a severe impairment of the epidermal permeability barrier.

Loss of functional CerS3 resulted in a markedly thick and compact SC that lacked the less cohesive layers of the *stratum disjunctum*. This increased intercellular adhesion in mutant SC was associated with the persistence of non-peripheral/central corneodesmosomes that abundantly decorate the cell-cell borders of corneocytes at all the layers of the SC, and also between the uppermost superficial corneocyte layer and the periderm. Immunofluorescence analysis of desmosomal associated proteins indicated an impaired degradation of the intercellular cadherin desmoglein 1/2, the distribution of which appeared at all layers of mutant epidermis, including a distinctive expression at the entire cornified layer and between peridermal cells. In contrast, its distribution was restricted to the viable layers in control epidermis. Whereas desmosomal cadherins provide the anchoring sites for cell adhesion, intracellular plaque proteins are required for proper binding to the intermediate filaments. The distribution of the plaque proteins, *e.g.* desmoplakin and plakoglobin, were not significantly altered in mutant epidermis as compared to control. Therefore, the persistence of corneodesmosomes appeared to be linked to the defective degradation of the transmembrane corneodesmosomal cadherins. Taking into consideration that the epitope recognized by the desmoglein 1/2 antibody is localized

at the cytoplasmic *C*-terminal region, it could be assumed that not only the extracellular domain, but also the cytoplasmic *C*-terminal portion of these cadherins are still intact. In this regard, the lack of degradation of the phospholipid bilayer in the mutant SC might interfere with the proteolytic degradation of the transmembrane cadherins. The aberrant persistence of the conventional PM in the intercellular space between corneocytes could be occasionally detected at the ultrastructural level. This findings were supported by the diminished intercellular space within mutant corneocytes that could be estimated around 3 to 4 nm, which might corresponds to the hydrophobic core of a phospholipid bilayer.

The highly regulated terminal cornification leading to desquamation of the uppermost corneocytes requires the proteolytic cleavage of these corneodesmosomal-associated proteins. From the epidermal proteases investigated, specifically the limited distribution of cathepsin D appeared to be involved in the thickening of the *stratum compactum* and the lack of formation of the *stratum disjunctum* of CerS3 deficient epidermis. Besides its constitutive role in the proteolytic degradation of intracellular proteins within the lysosomal compartment (Zaidi et al., 2008), epidermal cathepsin D has been localized in the intercellular space within adjacent corneocytes and has been implicated in the degradation of corneodesmosomes (Igarashi et al., 2004). Our findings were further confirmed by recent results showing a remarkable increase in the number of corneocyte layers resulting from the disruption of the cathepsin D gene in mice (Egberts et al., 2004). At the SG, nascent lamellar bodies carrying cathepsin D among other enzymes and lipids are predominantly delivered to the apical side of keratinocytes where they secrete their contents at the upper SG layers and between the SG-SC interface (Ishida-Yamamoto et al., 2004; Raymond et al., 2008). Consistent with the reported expression of cathepsin D, its immunolocalization in control skin was found in all the epidermal cell layers with the strongest expression at the SG. Contrarily, cathepsin D expression remarkably decreased at the SG and was absent in the SC of mutant epidermis. Therefore, a reduction in cathepsin D activity at the SG and SC layers of CerS3 deficient skin might lead to the impaired degradation of corneodesmosomal associated cadherins, and ultimately to a defective formation of the *stratum disjunctum* and persistence of the periderm.

At the extracellular space, LB secreted GlcCer and SM species are hydrolyzed to generate SC ceramides (Holleran and Takagi, 2006). This final lipid processing takes place at the optimum acidic pH of the SG-SC interface. Simultaneously with the extrusion of lipids, cathepsin D is secreted to the extracellular space, where the acidic pH is additionally required for its proteolytic activity. Previously, it has been demonstrated that ceramide directly interacts with cathepsin D resulting in the activation of the latter *in vitro* (Heinrich et al., 1999). Hence, it is reasonable to assume that extracellular ceramides might as well activate LB-derived cathepsin D. Taking this into consideration, the major lack of ceramide species upon the *in vivo* deficiency of CerS3 might result in the inactivation of the epidermal protease, which in turn leads to the persistence and defective degradation of the corneodesmosomes. Following this hypothesis further, the major deficiency of epidermal ceramides in Elovl4, Fatp4, CGI-58 and Abca12 deficient mice, besides our CerS3$^{d/d}$ mice, could explain the thickened and compact SC via the inactivation of the protease cathepsin D. However, no survey of the activities of the epidermal proteases in particular of cathepsin D, has been conducted yet in the specified mouse models. To further develop this hypothesis, the analysis of epidermal proteases should be the topic of future investigations.

The loss of function of cathepsin D could in addition be partially or totally contributed by the increased epidermal pH in CerS3 mutant mice. This reduced SC acidity might result from a reduced concentration of extracellular free fatty acids, which might be derived from the lack of hydrolysis of phospholipids and eventually of ceramides. In order to provide more insight into the augmented SC pH in CerS3 deficient mice, detailed mass spectrometric analysis of isolated SC free fatty acids would be required.

As a consequence of the defective degradation of corneodesmosomes, the transient embryonic peridermal layer was found to persist in CerS3 mutant mice. The inmmunolocalization of the TJ associated claudin 1 and the demonstration of TJ structures at the ultrastructural level, directly proved the presence of the periderm in mutant epidermis. In addition, the periderm-specific TJ-associated claudin 6 was exclusively detected at the mutant SC (data not shown). These findings were additionally supported by the residual nuclear remnants detected within peridermal

cells, which could be visualized with the immunolocalization using DAPI as a nuclear marker.

In Abca12$^{-/-}$ mouse skin, the characteristic features of the lack of desquamation in corneocytes and the expanded thicknening of the SC, in correlation with no signs of enhanced keratinocyte proliferation, are entirely consistent with our observations in CerS3 deficient epidermis (Zuo et al., 2008). However, the lack of desquamation in CerS3 deficient mice could not explain the increased number of SC layers, considering that corneocyte shedding has not yet been initiated at birth, not even in control epidermis. This could be proven by the presence of inclusion bodies decorating the outermost corneocyte layer in both control and mutant mice. Taking into account that the proliferation rate of basal keratinocytes was not increased in mutant epidermis, the origin of the augmented corneocyte layers has to be differently reasoned. Currently, we hypothesize that the increase in adhesion at the SC due to the persistence of non-peripheral/central, as well as the peripheral/lateral corneodesmosomes results in an increased lateral interdigitation surface between corneocytes. Therefore, the count of corneocytes in mutant epidermis yields a higher virtual number of cell layers than actually are present.

The *in vivo* disruption of CerS3 in addition led to defects in the regulation of keratinocyte differentiation within the nucleated layers of the epidermis. Impaired maturation of SG keratinocytes could be identified by the reduced size of filaggrin-containing F-granules and by the reduced number of loricrin-containing L-granules. These alterations within keratohyalin granules were accompanied by decreased levels of loricrin and the aberrant processing of profilaggrin to monomeric filaggrin in CerS3$^{d/d}$ mice. In combination with the presence of immature *zonulae occludentes* indicated by the immunolocalization of cingulin, these phenotypic alterations evidenced a delayed or defective keratinocyte differentiation at the granular layers of mutant epidermis.

The terminal cornification of keratinocytes is a remarkably coherent process involving pronounced morphological changes. Thus, the impaired maturation of granular keratinocytes presumably has severe repercussions on their transformation to enucleated corneocytes. CerS3 deficient epidermis exhibited various alterations that indicate a disturbed or delayed terminal differentiation of corneocytes. At mutant

SC, remnants of nuclear material and organelle structures could be detected up to the third corneocyte layer. In addition, F-actin expression and residual PAS-positive glycogen were also found within the first corneocyte layers. The molecular nature leading to these phenotypic alterations might underlie in the presence of the homeobox domain encoded in the *Cers3* gene. In general, homeobox-containing genes regulate embryonic development and cell differentiation by encoding transcription factors capable of modulating gene expression (Mark et al., 1997). Although reports regarding the regulation of epidermal development and keratinocyte differentiation are scarce, several genes of the hox family have been identified to influence normal mammalian skin development, *i.e.* Hoxb13, Hoxa7 and Hoxc4 (La Celle and Polakowska, 2001; Mack et al., 2005; Rieger et al., 1994). Considering the outstanding alterations due to its dysfunctionality, we suggest that CerS3 could also transcriptionally regulate keratinocyte differentiation by targeting proteins required for the adequate maturation of granular keratinocytes. In this regard, subcellular immunolocalization studies of CerS3 possibly indicate the expression of its EGFP-recombinant protein in both the endoplasmic reticulum (ER) and the nuclear envelope. Previously, Mizutani and coworkers additionally detected CerS2 and CerS6 to the nuclear envelope and the perinuclear region, besides of the ER (Mizutani et al., 2005). Whether CerS3 could behave as a master regulator for proper development in the skin and may be in other tissues were it could be expressed in minor amounts will be the focus of our future investigations. Currently, no ceramide synthase homologue containing the homeobox domain, *i.e.* CerS2–6, has been described to influence gene expression. In order to provide insight into the biochemical mechanism by which CerS3 could modulate the activity of its target genes, specific mutations at the *Cers3*-homeobox domain, that do not affect ceramide synthase activity, should definitely clarify the functional role of CerS3 in mammalian epidermis.

In addition to the defective development of keratinocytes at the SG and SC, various abnormalities could also be identified within the corneal layer. The extracellular lipid lamellae as well as the CE and the CLE were altered in mutant CerS3 mice. Regarding the CE, loricrin and transglutaminase 1 concentrations were diminished as determined by immunoblot analysis, whereas involucrin levels remain

unaltered upon CerS3 deficiency. The decreased levels of transglutaminase 1 might be justified considering that its activation could depend on the activity of the epidermal protease cathepsin D (Egberts et al., 2004). Assuming that extracellular ceramides alter the activation of cathepsin D, this could sequentially lead to transglutaminase 1 inactivity. Although the covalent attachment of ω-hydroxy-ULC-ceramides to involucrin has been demonstrated *in vitro* via transglutaminase 1 transesterification (Nemes et al., 1999), involucrin expression could not be detected at the SC of neither mutant or control CerS3 mice even after a harsh *in situ* alkaline hydrolysis on paraffin sections (2 h, 1 M KOH, data not shown). Therefore, it is at least questionable whether involucrin is involved in the linkage of these specific epidermal ceramides to the CE *in vivo*. Furthermore, mice lacking involucrin did not reveal alterations of the CE integrity, neither showing a significant compromised epidermal barrier function (Djian et al., 2000). On the other hand, loricrin distribution at the cornified layer could be detected after mild alkaline hydrolysis in paraffin sections (1 h, 0.1 M KOH) in both control and mutant CerS3 mice, and its total concentration was reduced accordingly with transglutaminase 1 in deficient epidermis. However, neither absence of loricrin or the CE proteins envoplakin and periplakin resulted in severe alterations of the CLE (Jarnik et al., 2002; Sevilla et al., 2007). All together these findings suggest a compensatory redundancy of the CE components. Whether transglutaminase 1 is capable to attach epidermal ceramides to either involucrin, loricrin, envoplakin, periplakin or other CE proteins *in vivo* remains elusive.

The metabolic defect of CerS3 mice resulted in a critical reduction of secreted LB-derived sphingolipids that gave rise to shorter discs, smaller stacks and disorganized lamellar sheets, which failed to align in parallel to the PM and to transform into the lamellar basic unit structures. At the upper SC interstices, focal and non-lamellar lipid agglomerates were sporadically localized within the cornified layers, predominantly at the tricellular contact sites. The complete lack of lamellar basic unit structures in mutant SC could be associated with the increased cohesion between corneocytes established by both central and lateral corneodesmosomes, that may inhibit the homogeneous distribution and the establishment of a continuous lipid layer.

Likewise, loss of transglutaminase 1 function in mice also leads to incomplete and irregularly deformed lipid lamellae that were sparsely distributed within the extracellular space (Kuramoto et al., 2002). Both lack of EOS-ceramides and transglutaminase 1 presumably results in an abnormal formation of the CLE due to the impaired attachment of ceramides to proteins of the CE, thus leading to the absence of POS-ceramides. Therefore, one might speculate that POS-ceramides confer stability to the lipid lamellae providing the adequate membrane fluidity, which might be required for lamellar fusion events in order to form the continuous lamellar sheets. Otherwise, disorganized lamellar sheets yielding severe dysregulations of the permeability barrier might take place.

Similarly to CerS3 deficiency, mice devoid of transglutaminase 1 exhibited reduced desquamation (Kuramoto et al., 2002). Whether this pseudohyperkeratosis is a “physical compensation for the defective cutaneous permeability barrier” as suggested by Kuramoto and colleagues remains elusive. However, if the defective corneocyte shedding in transglutaminase 1 deficient mice is as well due to the persistence of corneodesmosomes spread over the entire corneocyte surface, these could in addition contribute to the altered distribution of the lamellae giving rise to lipidic aggregates.

In conjunction, the epidermal abnormalities described here for CerS3 deficient mice evidenced a severe impairment of the epidermal barrier function. Alterations within the cornification process leading to loss of barrier function have been described in the pathogenesis of various skin disorders, *e.g*. ichthyosis and atopic dermatitis (Jungersted et al., ; Schmuth et al., 2007). Several of these pathologies exhibiting an imbalance of extracellular lipid species at the cornified layer have been associated with an increased vulnerability towards microbial infections (Arikawa et al., 2002). As shown here, dysfunctional CerS3 skin exhibited a drastic increase in pathogenic growth upon infection of biopsies with *Candida albicans*. Pathogens appear to adhere eagerly on the surface of mutant mice, which apparently exert no resistance to invasion. Following surface attachment, yeast cells developed polarized pseudohyphae and infected the living layers down to the dermis, where they initiated colonization of the tissue. Considering that expression levels of murine antimicrobial peptides, *i.e.* defensins and cathelicidin, were not altered in CerS3 mutant mice, we

therefore assumed that lack of epidermal ceramides or its direct metabolites might primarily instigate the pathogenic microbial activity. In this regard, sphingosine levels have been distinguished from SC lipids with respect to provide a barrier against pathogens at the skin surface. Extracellular sphingosines concentrate in the SC towards the *stratum disjunctum*, arising from the permanent degradation of lamellar ceramide. Sphingosine, as well as phytoshingosine and sphinganine, efficiently inhibited the growth of various bacteria and yeast strains – namely *Staphylococcus aureus, Streptococcus pyogenes, Micrococcus luteus, Propionibacterium acnes, Brevibacterium epidermidids* and *Candida albicans*, but not *Escherichia coli* and *Serratia marcescens* –, whereas various phospholipids and sphingolipids, among them ceramide(d18:1,18:0) and mixed galactocerebrosides, demonstrated to be ineffective *in vitro* (Bibel et al., 1992). Furthermore, decreased levels of sphingosine were associated with increased acquired vulnerability to colonization by *S. aureus* in patients suffering from atopic dermatitis (Arikawa et al., 2002). In these patients, reduced levels of protein-bound ω-hydroxy-ULC-ceramides (POS) have been demonstrated (Macheleidt et al., 2002). In CerS3 deficient mice, 90% reduction of epidermal ceramides, including POS-ceramides, presumably results in extremely reduced levels of sphingosine. In order to corroborate this hypothesis, future investigations should include the determination of sphingosine concentration in mutant SC as compared with controls. Additionally, an increased SC pH might contribute to the severe pathogenic infection exhibited by CerS3 deficient mice (Fluhr and Elias, 2002).

In summary, the present study provides conclusive evidences regarding the essential role of CerS3 for the biosynthesis of epidermal ULC-ceramides and the epidermal barrier function.

5. Conclusion

Despite the remarkable progress of the last two decades in defining the enzymatic requirements of the major sphingolipid biosynthethic pathways, few metabolic key steps still remain elusive at the molecular level. To ensure our full understanding of how sphingolipids modulate cellular functions, it is necessary to completely resolve their metabolism. In this context, the present thesis aimed to elucidate the biosynthethic requirements of ULC-sphingolipids in order to gain insight into their functional roles.

Within the ceramide synthase family, CerS3 expression levels distinctively correlated with the presence of ULC-sphingolipids in skin and testis. Using *in vitro* CerS3 overexpression studies in living human cells, combined with *in vivo* deficiency studies in mice, we demonstrated CerS3 substrate specificity towards acyl-CoAs ranging from 24 to 36 carbon atoms. Hence, we concluded that the biosynthesis of ULC-sphingolipids exclusively requires a functional CerS3 with no redundancy provided by any other ceramide synthase member.

The physiological role of CerS3 in the formation and maintenance of the epidermal permeability barrier was conclusive. Although ULC-sphingolipids were first described in human epidermis in 1975 (Gray and Yardley, 1975), interest in their functionality did not arise until recent reports associated skin pathologies with imbalances in epidermal lipids. In particular, decreased levels of ceramides have been demonstrated to contribute to the pathology of atopic dermatitis, psoriasis, ichthyosis, and xerosis (Coderch et al., 2003). Despite that no human epidermal disorder has yet been associated with alterations of the *Cers3* gene, the present thesis revealed several important findings that should contribute to its prognosis. This unidentified skin disorder might be characterized by a drastic increase of transepidermal water loss, a markedly thick and compact *stratum corneum* with eventually reduced levels of epidermal proteases, altered expression of cornified envelope proteins and reduced levels of ω-hydroxy-ULC-ceramides as the symptomatic hallmark. Various pathologies classified within the heterogeneous family of ichthyoses share several of these features, for instance harlequin ichthyosis and lamellar ichthyosis. Currently, the genetic factor of some of these ichthyoses has not yet been identified (Oji et al., 2010). In order to correlate a skin disorder to alterations within the *Cers3* gene, future

investigations should focus on analyzing epidermal human biopsies from patients with symptomatic similarities as here described for CerS3.

The complex molecular events presumably altered upon CerS3 deficiency might as well contribute to the pathogenesis of other skin diseases. In this regard, the homeobox domain encoded in the CerS3 gene might transcriptionally regulate the expression of crucial genes involved in the maturation and terminal differentiation of keratinocytes. Furthermore, mutations within the homeobox domain not affecting enzymatic activity could contribute to developmental abnormalities in other organs where CerS3 is expressed only in traces.

In addition, the homeobox domain might as well play a crucial role in modulating the expression of genes associated with male germ cell differentiation. Although we previously reported the essential role of complex ULC-sphingolipids for proper development of the spermatogenic cycle (Rabionet et al., 2008; Sandhoff et al., 2005), the premature death of CerS3$^{d/d}$ mice prevented the characterization and specific identification of its functional role in mature male germ cells. Future studies with germ cell specific depletion of CerS3 might clarify the physiological role of this enzyme in male fertility and thus could provide new perspectives on human disorders characterized by male sterility.

6. References

Abraham, W., Wertz, P.W., and Downing, D.T. (1985). Linoleate-rich acylglucosylceramides of pig epidermis: structure determination by proton magnetic resonance. Journal of lipid research *26*, 761-766.

Aerts, J.M., Ottenhoff, R., Powlson, A.S., Grefhorst, A., van Eijk, M., Dubbelhuis, P.F., Aten, J., Kuipers, F., Serlie, M.J., Wennekes, T.*, et al.* (2007). Pharmacological inhibition of glucosylceramide synthase enhances insulin sensitivity. Diabetes *56*, 1341-1349.

Agbaga, M.P., Brush, R.S., Mandal, M.N., Henry, K., Elliott, M.H., and Anderson, R.E. (2008). Role of Stargardt-3 macular dystrophy protein (ELOVL4) in the biosynthesis of very long chain fatty acids. Proceedings of the National Academy of Sciences of the United States of America *105*, 12843-12848.

Akiyama, M., Sugiyama-Nakagiri, Y., Sakai, K., McMillan, J.R., Goto, M., Arita, K., Tsuji-Abe, Y., Tabata, N., Matsuoka, K., Sasaki, R.*, et al.* (2005). Mutations in lipid transporter ABCA12 in harlequin ichthyosis and functional recovery by corrective gene transfer. The Journal of clinical investigation *115*, 1777-1784.

Al-Arif, A., and Blecher, M. (1969). Synthesis of fatty acyl CoA and other thiol esters using N-hydroxysuccinimide esters of fatty acids. Journal of lipid research *10*, 344-345.

Ardail, D., Popa, I., Bodennec, J., Louisot, P., Schmitt, D., and Portoukalian, J. (2003). The mitochondria-associated endoplasmic-reticulum subcompartment (MAM fraction) of rat liver contains highly active sphingolipid-specific glycosyltransferases. The Biochemical journal *371*, 1013-1019.

Arikawa, J., Ishibashi, M., Kawashima, M., Takagi, Y., Ichikawa, Y., and Imokawa, G. (2002). Decreased levels of sphingosine, a natural antimicrobial agent, may be associated with vulnerability of the stratum corneum from patients with atopic dermatitis to colonization by Staphylococcus aureus. The Journal of investigative dermatology *119*, 433-439.

Aveldano, M.I., and Sprecher, H. (1987). Very long chain (C24 to C36) polyenoic fatty acids of the n-3 and n-6 series in dipolyunsaturated phosphatidylcholines from bovine retina. The Journal of biological chemistry *262*, 1180-1186.

Bauer, R., Voelzmann, A., Breiden, B., Schepers, U., Farwanah, H., Hahn, I., Eckardt, F., Sandhoff, K., and Hoch, M. (2009). Schlank, a member of the ceramide synthase family controls growth and body fat in Drosophila. The EMBO journal *28*, 3706-3716.

Bibel, D.J., Aly, R., and Shinefield, H.R. (1992). Antimicrobial activity of sphingosines. The Journal of investigative dermatology *98*, 269-273.

Bradford, M.M. (1976). A rapid and sensitive method for the quantitation of microgram quantities of protein utilizing the principle of protein-dye binding. Analytical biochemistry *72*, 248-254.

Brandner, J.M. (2009). Tight junctions and tight junction proteins in mammalian epidermis. Eur J Pharm Biopharm *72*, 289-294.

Brandner, J.M., Haftek, M., and Niessen, C.M. (2010). Adherens Junctions, Desmosomes and Tight Junctions in Epidermal Barrier Function. The Open Dermatology Journal *4*, 14-20.

Brandner, J.M., and Proksch, E. (2006). Epidermal Barrier Function: Role of Tight Junctions. Skin Barrier, 191-210.

Brock, R., Hamelers, I.H., and Jovin, T.M. (1999). Comparison of fixation protocols for adherent cultured cells applied to a GFP fusion protein of the epidermal growth factor receptor. Cytometry *35*, 353-362.

Brush, R.S., Tran, J.T., Henry, K.R., McClellan, M.E., Elliott, M.H., and Mandal, M.N. (2010). Retinal Sphingolipids and their Very Long Chain Fatty Acid Containing Species. Investigative ophthalmology & visual science *51*, 4422-4431.

Candi, E., Schmidt, R., and Melino, G. (2005). The cornified envelope: a model of cell death in the skin. Nature reviews *6*, 328-340.

Chalmel, F., Rolland, A.D., Niederhauser-Wiederkehr, C., Chung, S.S., Demougin, P., Gattiker, A., Moore, J., Patard, J.J., Wolgemuth, D.J., Jegou, B.*, et al.* (2007). The conserved transcriptome in human and rodent male gametogenesis. Proceedings of the National Academy of Sciences of the United States of America *104*, 8346-8351.

Chomczynski, P., and Sacchi, N. (1987). Single-step method of RNA isolation by acid guanidinium thiocyanate-phenol-chloroform extraction. Analytical biochemistry *162*, 156-159.

Claros, M.G., and von Heijne, G. (1994). TopPred II: an improved software for membrane protein structure predictions. Comput Appl Biosci *10*, 685-686.

Coderch, L., Lopez, O., de la Maza, A., and Parra, J.L. (2003). Ceramides and skin function. American journal of clinical dermatology *4*, 107-129.

D'Mello N, P., Childress, A.M., Franklin, D.S., Kale, S.P., Pinswasdi, C., and Jazwinski, S.M. (1994). Cloning and characterization of LAG1, a longevity-assurance gene in yeast. The Journal of biological chemistry *269*, 15451-15459.

Djian, P., Easley, K., and Green, H. (2000). Targeted ablation of the murine involucrin gene. The Journal of cell biology *151*, 381-388.

Doering, T., Holleran, W.M., Potratz, A., Vielhaber, G., Elias, P.M., Suzuki, K., and Sandhoff, K. (1999a). Sphingolipid activator proteins are required for epidermal permeability barrier formation. The Journal of biological chemistry *274*, 11038-11045.

Doering, T., Proia, R.L., and Sandhoff, K. (1999b). Accumulation of protein-bound epidermal glucosylceramides in beta-glucocerebrosidase deficient type 2 Gaucher mice. FEBS Lett *447*, 167-170.

Dorschner, R.A., Lin, K.H., Murakami, M., and Gallo, R.L. (2003). Neonatal skin in mice and humans expresses increased levels of antimicrobial peptides: innate immunity during development of the adaptive response. Pediatric research *53*, 566-572.

Egberts, F., Heinrich, M., Jensen, J.M., Winoto-Morbach, S., Pfeiffer, S., Wickel, M., Schunck, M., Steude, J., Saftig, P., Proksch, E.*, et al.* (2004). Cathepsin D is involved in the regulation of transglutaminase 1 and epidermal differentiation. Journal of cell science *117*, 2295-2307.

Elias, P.M., Feingold, K.R., and Fartasch, M. (2006). The Epidermal Lamelar Body as a Multifunctional Secretory Organelle. Skin Barrier, 261-272.

Elias, P.M., Schmuth, M., Uchida, Y., Rice, R.H., Behne, M., Crumrine, D., Feingold, K.R., Holleran, W.M., and Pharm, D. (2002). Basis for the permeability barrier abnormality in lamellar ichthyosis. Experimental dermatology *11*, 248-256.

Elias, P.M., Williams, M.L., Maloney, M.E., Bonifas, J.A., Brown, B.E., Grayson, S., and Epstein, E.H., Jr. (1984). Stratum corneum lipids in disorders of cornification. Steroid sulfatase and cholesterol sulfate in normal desquamation and the pathogenesis of recessive X-linked ichthyosis. The Journal of clinical investigation *74*, 1414-1421.

Engling, A., Backhaus, R., Stegmayer, C., Zehe, C., Seelenmeyer, C., Kehlenbach, A., Schwappach, B., Wegehingel, S., and Nickel, W. (2002). Biosynthetic FGF-2 is targeted to non-lipid raft microdomains following translocation to the extracellular surface of CHO cells. Journal of cell science *115*, 3619-3631.

Farwanah, H., Pierstorff, B., Schmelzer, C.E., Raith, K., Neubert, R.H., Kolter, T., and Sandhoff, K. (2007). Separation and mass spectrometric characterization of covalently bound skin ceramides using LC/APCI-MS and Nano-ESI-MS/MS. Journal of chromatography *852*, 562-570.

Fluhr, J.W., and Elias, P.M. (2002). Stratum corneum pH: Formation and Function of the 'Acid Mantle'. Exog Dermatol *1*, 163-175.

Freinkel, R.K., and Traczyk, T.N. (1985). Lipid composition and acid hydrolase content of lamellar granules of fetal rat epidermis. The Journal of investigative dermatology *85*, 295-298.

Furland, N.E., Oresti, G.M., Antollini, S.S., Venturino, A., Maldonado, E.N., and Aveldano, M.I. (2007). Very long-chain polyunsaturated fatty acids are the major acyl groups of sphingomyelins and ceramides in the head of mammalian spermatozoa. The Journal of biological chemistry *282*, 18151-18161.

Furuse, M., Furuse, K., Sasaki, H., and Tsukita, S. (2001). Conversion of zonulae occludentes from tight to leaky strand type by introducing claudin-2 into Madin-Darby canine kidney I cells. The Journal of cell biology *153*, 263-272.

Furuse, M., Hata, M., Furuse, K., Yoshida, Y., Haratake, A., Sugitani, Y., Noda, T., Kubo, A., and Tsukita, S. (2002). Claudin-based tight junctions are crucial for the mammalian epidermal barrier: a lesson from claudin-1-deficient mice. The Journal of cell biology *156*, 1099-1111.

Futerman, A.H., and Pagano, R.E. (1991). Determination of the intracellular sites and topology of glucosylceramide synthesis in rat liver. The Biochemical journal *280 (Pt 2)*, 295-302.

Geilen, C.C., Wieder, T., and Orfanos, C.E. (1997). Ceramide signalling: regulatory role in cell proliferation, differentiation and apoptosis in human epidermis. Archives of dermatological research *289*, 559-566.

Germain, L., Rouabhia, M., Guignard, R., Carrier, L., Bouvard, V., and Auger, F.A. (1993). Improvement of human keratinocyte isolation and culture using thermolysin. Burns *19*, 99-104.

Goritz, C., Thiebaut, R., Tessier, L.H., Nieweg, K., Moehle, C., Buard, I., Dupont, J.L., Schurgers, L.J., Schmitz, G., and Pfrieger, F.W. (2007). Glia-induced neuronal differentiation by transcriptional regulation. Glia *55*, 1108-1122.

Gray, G.M., and Yardley, H.J. (1975). Lipid compositions of cells isolated from pig, human, and rat epidermis. Journal of lipid research *16*, 434-440.

Greenspan, P., Mayer, E.P., and Fowler, S.D. (1985). Nile red: a selective fluorescent stain for intracellular lipid droplets. The Journal of cell biology *100*, 965-973.

Grimm, M.O., Grimm, H.S., Patzold, A.J., Zinser, E.G., Halonen, R., Duering, M., Tschape, J.A., De Strooper, B., Muller, U., Shen, J.*, et al.* (2005). Regulation of cholesterol and sphingomyelin metabolism by amyloid-beta and presenilin. Nature cell biology *7*, 1118-1123.

Guillou, H., Zadravec, D., Martin, P.G., and Jacobsson, A. (2009). The key roles of elongases and desaturases in mammalian fatty acid metabolism: Insights from transgenic mice. Progress in lipid research.

Haftek, M., Simon, M., and Serre, G. (2006). Corneodesmosomes: Pivotal Actors in the Stratum Corneum Cohesion and Desquamation. Skin Barrier, 171-189.

Hakomori, S. (1981). Glycosphingolipids in cellular interaction, differentiation, and oncogenesis. Annual review of biochemistry *50*, 733-764.

Hakomori, S. (1996). Tumor malignancy defined by aberrant glycosylation and sphingo(glyco)lipid metabolism. Cancer research *56*, 5309-5318.

Hama, H. (2009). Fatty acid 2-Hydroxylation in mammalian sphingolipid biology. Biochimica et biophysica acta.

Hanada, K. (2003). Serine palmitoyltransferase, a key enzyme of sphingolipid metabolism. Biochimica et biophysica acta *1632*, 16-30.

Hanada, K., Kumagai, K., Yasuda, S., Miura, Y., Kawano, M., Fukasawa, M., and Nishijima, M. (2003). Molecular machinery for non-vesicular trafficking of ceramide. Nature *426*, 803-809.

Hardman, M.J., and Byrne, C. (2006). Skin Structural Development. Skin Barrier, 273-288.

Hardman, M.J., Sisi, P., Banbury, D.N., and Byrne, C. (1998). Patterned acquisition of skin barrier function during development. Development (Cambridge, England) *125*, 1541-1552.

Heinrich, M., Wickel, M., Schneider-Brachert, W., Sandberg, C., Gahr, J., Schwandner, R., Weber, T., Saftig, P., Peters, C., Brunner, J.*, et al.* (1999). Cathepsin D targeted by acid sphingomyelinase-derived ceramide. The EMBO journal *18*, 5252-5263.

Herrmann, T., van der Hoeven, F., Grone, H.J., Stewart, A.F., Langbein, L., Kaiser, I., Liebisch, G., Gosch, I., Buchkremer, F., Drobnik, W.*, et al.* (2003). Mice with targeted disruption of the fatty acid transport protein 4 (Fatp 4, Slc27a4) gene show features of lethal restrictive dermopathy. The Journal of cell biology *161*, 1105-1115.

Holleran, W.H., and Takagi, Y. (2006). Stratum Corneum Lipid Processing: The Final Steps in Barrier Formation. Skin Barrier, 231-259.

Holleran, W.M., Ginns, E.I., Menon, G.K., Grundmann, J.U., Fartasch, M., McKinney, C.E., Elias, P.M., and Sidransky, E. (1994a). Consequences of beta-glucocerebrosidase deficiency in epidermis. Ultrastructure and permeability barrier alterations in Gaucher disease. The Journal of clinical investigation *93*, 1756-1764.

Holleran, W.M., Takagi, Y., Menon, G.K., Jackson, S.M., Lee, J.M., Feingold, K.R., and Elias, P.M. (1994b). Permeability barrier requirements regulate epidermal beta-glucocerebrosidase. Journal of lipid research *35*, 905-912.

Hornemann, T., Wei, Y., and von Eckardstein, A. (2007). Is the mammalian serine palmitoyltransferase a high-molecular-mass complex? The Biochemical journal *405*, 157-164.

Huitema, K., van den Dikkenberg, J., Brouwers, J.F., and Holthuis, J.C. (2004). Identification of a family of animal sphingomyelin synthases. The EMBO journal *23*, 33-44.

Igarashi, S., Takizawa, T., Takizawa, T., Yasuda, Y., Uchiwa, H., Hayashi, S., Brysk, H., Robinson, J.M., Yamamoto, K., Brysk, M.M.*, et al.* (2004). Cathepsin D, but not cathepsin E, degrades desmosomes during epidermal desquamation. The British journal of dermatology *151*, 355-361.

Igarashi, Y. (2010). Studies of SMS2 or CerK defiency mice and their relations to diet-induced obesity and mast cell activation. personal communication *ICBL Conference*.

Imokawa, G., Abe, A., Jin, K., Higaki, Y., Kawashima, M., and Hidano, A. (1991). Decreased level of ceramides in stratum corneum of atopic dermatitis: an etiologic factor in atopic dry skin? The Journal of investigative dermatology *96*, 523-526.

Ishida-Yamamoto, A., Simon, M., Kishibe, M., Miyauchi, Y., Takahashi, H., Yoshida, S., O'Brien, T.J., Serre, G., and Iizuka, H. (2004). Epidermal lamellar granules transport different cargoes as distinct aggregates. The Journal of investigative dermatology *122*, 1137-1144.

Jakobsson, A., Westerberg, R., and Jacobsson, A. (2006). Fatty acid elongases in mammals: their regulation and roles in metabolism. Progress in lipid research *45*, 237-249.

Jarnik, M., de Viragh, P.A., Scharer, E., Bundman, D., Simon, M.N., Roop, D.R., and Steven, A.C. (2002). Quasi-normal cornified cell envelopes in loricrin knockout mice imply the existence of a loricrin backup system. The Journal of investigative dermatology *118*, 102-109.

Jeckel, D., Karrenbauer, A., Burger, K.N., van Meer, G., and Wieland, F. (1992). Glucosylceramide is synthesized at the cytosolic surface of various Golgi subfractions. The Journal of cell biology *117*, 259-267.

Jennemann, R., Sandhoff, R., Langbein, L., Kaden, S., Rothermel, U., Gallala, H., Sandhoff, K., Wiegandt, H., and Grone, H.J. (2007). Integrity and barrier function of the epidermis critically depend on glucosylceramide synthesis. The Journal of biological chemistry *282*, 3083-3094.

Jungersted, J.M., Scheer, H., Mempel, M., Baurecht, H., Cifuentes, L., Hogh, J.K., Hellgren, L.I., Jemec, G.B., Agner, T., and Weidinger, S. (2001). Stratum corneum lipids, skin barrier function and filaggrin mutations in patients with atopic eczema. Allergy.

Kageyama-Yahara, N., and Riezman, H. (2006). Transmembrane topology of ceramide synthase in yeast. The Biochemical journal *398*, 585-593.

Karlsson, K.A. (1970). On the chemistry and occurrence of sphingolipid long-chain bases. Chemistry and physics of lipids *5*, 6-43.

Kelsell, D.P., Norgett, E.E., Unsworth, H., Teh, M.T., Cullup, T., Mein, C.A., Dopping-Hepenstal, P.J., Dale, B.A., Tadini, G., Fleckman, P.*, et al.* (2005). Mutations in ABCA12 underlie the severe congenital skin disease harlequin ichthyosis. American journal of human genetics *76*, 794-803.

Kirschner, N., Bohner, C., Rachow, S., and Brandner, J.M. (2010a). Tight junctions: is there a role in dermatology? Archives of dermatological research *302*, 483-493.

Kirschner, N., Houdek, P., Fromm, M., Moll, I., and Brandner, J.M. (2010b). Tight junctions form a barrier in human epidermis. European journal of cell biology *89*, 839-842.

Kolter, T., and Sandhoff, K. (1999). SphingolipidsÐTheir Metabolic Pathways and the Pathobiochemistry of Neurodegenerative Diseases. Angew Chem Int Ed *38*, 1532-1568.

Komljenovic, D., Sandhoff, R., Teigler, A., Heid, H., Just, W.W., and Gorgas, K. (2009). Disruption of blood-testis barrier dynamics in ether-lipid-deficient mice. Cell and tissue research *337*, 281-299.

Kuramoto, N., Takizawa, T., Takizawa, T., Matsuki, M., Morioka, H., Robinson, J.M., and Yamanishi, K. (2002). Development of ichthyosiform skin compensates for defective permeability barrier function in mice lacking transglutaminase 1. The Journal of clinical investigation *109*, 243-250.

La Celle, P.T., and Polakowska, R.R. (2001). Human homeobox HOXA7 regulates keratinocyte transglutaminase type 1 and inhibits differentiation. The Journal of biological chemistry *276*, 32844-32853.

Lahiri, S., and Futerman, A.H. (2005). LASS5 is a bona fide dihydroceramide synthase that selectively utilizes palmitoyl-CoA as acyl donor. The Journal of biological chemistry *280*, 33735-33738.

Lahiri, S., and Futerman, A.H. (2007). The metabolism and function of sphingolipids and glycosphingolipids. Cell Mol Life Sci *64*, 2270-2284.

Lahiri, S., Lee, H., Mesicek, J., Fuks, Z., Haimovitz-Friedman, A., Kolesnick, R.N., and Futerman, A.H. (2007). Kinetic characterization of mammalian ceramide synthases: determination of K(m) values towards sphinganine. FEBS Lett *581*, 5289-5294.

Landmann, L. (1986). Epidermal permeability barrier: transformation of lamellar granule-disks into intercellular sheets by a membrane-fusion process, a freeze-fracture study. The Journal of investigative dermatology *87*, 202-209.

Lang, T. (2007). SNARE proteins and 'membrane rafts'. The Journal of physiology *585*, 693-698.

Langbein, L., Grund, C., Kuhn, C., Praetzel, S., Kartenbeck, J., Brandner, J.M., Moll, I., and Franke, W.W. (2002). Tight junctions and compositionally related junctional structures in mammalian stratified epithelia and cell cultures derived therefrom. European journal of cell biology *81*, 419-435.

Lannert, H., Gorgas, K., Meissner, I., Wieland, F.T., and Jeckel, D. (1998). Functional organization of the Golgi apparatus in glycosphingolipid biosynthesis. Lactosylceramide and subsequent glycosphingolipids are formed in the lumen of the late Golgi. The Journal of biological chemistry *273*, 2939-2946.

Laviad, E.L., Albee, L., Pankova-Kholmyansky, I., Epstein, S., Park, H., Merrill, A.H., Jr., and Futerman, A.H. (2008). Characterization of ceramide synthase 2: tissue distribution, substrate specificity, and inhibition by sphingosine 1-phosphate. The Journal of biological chemistry *283*, 5677-5684.

Lee, N.P., Mruk, D.D., Xia, W., and Cheng, C.Y. (2007). Cellular localization of sphingomyelin synthase 2 in the seminiferous epithelium of adult rat testes. The Journal of endocrinology *192*, 17-32.

Leonard, A.E., Pereira, S.L., Sprecher, H., and Huang, Y.S. (2004). Elongation of long-chain fatty acids. Progress in lipid research *43*, 36-54.

Li, W., Sandhoff, R., Kono, M., Zerfas, P., Hoffmann, V., Ding, B.C., Proia, R.L., and Deng, C.X. (2007). Depletion of ceramides with very long chain fatty acids causes defective skin permeability barrier function, and neonatal lethality in ELOVL4 deficient mice. International journal of biological sciences *3*, 120-128.

Liu, Y., Hoffmann, A., Grinberg, A., Westphal, H., McDonald, M.P., Miller, K.M., Crawley, J.N., Sandhoff, K., Suzuki, K., and Proia, R.L. (1997). Mouse model of GM2 activator deficiency manifests cerebellar pathology and motor impairment. Proceedings of the National Academy of Sciences of the United States of America *94*, 8138-8143.

Livak, K.J., and Schmittgen, T.D. (2001). Analysis of relative gene expression data using real-time quantitative PCR and the 2(-Delta Delta C(T)) Method. Methods (San Diego, Calif *25*, 402-408.

Lowry, O.H., Rosebrough, N.J., Farr, A.L., and Randall, R.J. (1951). Protein measurement with the Folin phenol reagent. The Journal of biological chemistry *193*, 265-275.

Lucet-Levannier, K., Lellouche, J., and Mioskowski, C. (1995). Polysilylated Coenzyme A for a High-Yielding. Preparation of Very Lipophilic Acyl Coenzymes A in Anhydrous Organic Solvents. J Am Chem Soc *117*, 7546-7547.

Lüllmann-Rauch, R. (2003). Histologie.

Macheleidt, O., Kaiser, H.W., and Sandhoff, K. (2002). Deficiency of epidermal protein-bound omega-hydroxyceramides in atopic dermatitis. The Journal of investigative dermatology *119*, 166-173.

Mack, J.A., Li, L., Sato, N., Hascall, V.C., and Maytin, E.V. (2005). Hoxb13 up-regulates transglutaminase activity and drives terminal differentiation in an epidermal organotypic model. The Journal of biological chemistry *280*, 29904-29911.

Madison, K.C. (2003). Barrier function of the skin: "la raison d'etre" of the epidermis. The Journal of investigative dermatology *121*, 231-241.

Majoul, I., Schmidt, T., Pomasanova, M., Boutkevich, E., Kozlov, Y., and Soling, H.D. (2002). Differential expression of receptors for Shiga and Cholera toxin is regulated by the cell cycle. Journal of cell science *115*, 817-826.

Mandal, M.N., Ambasudhan, R., Wong, P.W., Gage, P.J., Sieving, P.A., and Ayyagari, R. (2004). Characterization of mouse orthologue of ELOVL4: genomic organization and spatial and temporal expression. Genomics *83*, 626-635.

Mandon, E.C., Ehses, I., Rother, J., van Echten, G., and Sandhoff, K. (1992). Subcellular localization and membrane topology of serine palmitoyltransferase, 3-dehydrosphinganine reductase, and sphinganine N-acyltransferase in mouse liver. The Journal of biological chemistry *267*, 11144-11148.

Marekov, L.N., and Steinert, P.M. (1998). Ceramides are bound to structural proteins of the human foreskin epidermal cornified cell envelope. The Journal of biological chemistry *273*, 17763-17770.

Mark, M., Rijli, F.M., and Chambon, P. (1997). Homeobox genes in embryogenesis and pathogenesis. Pediatric research *42*, 421-429.

Masukawa, Y., Narita, H., Shimizu, E., Kondo, N., Sugai, Y., Oba, T., Homma, R., Ishikawa, J., Takagi, Y., Kitahara, T.*, et al.* (2008). Characterization of overall ceramide species in human stratum corneum. Journal of lipid research *49*, 1466-1476.

McMahon, A., Butovich, I.A., Mata, N.L., Klein, M., Ritter, R., 3rd, Richardson, J., Birch, D.G., Edwards, A.O., and Kedzierski, W. (2007a). Retinal pathology and skin barrier defect in mice carrying a Stargardt disease-3 mutation in elongase of very long chain fatty acids-4. Molecular vision *13*, 258-272.

McMahon, A., Jackson, S.N., Woods, A.S., and Kedzierski, W. (2007b). A Stargardt disease-3 mutation in the mouse Elovl4 gene causes retinal deficiency of C32-C36 acyl phosphatidylcholines. FEBS Lett *581*, 5459-5463.

Meixner, M. (2009). Untersuchungen zur Funktion der alpha-hydroxylierten Sphingolipide im Nervensystem und in der Haut. Dissertation.

Melton, J.L., Wertz, P.W., Swartzendruber, D.C., and Downing, D.T. (1987). Effects of essential fatty acid deficiency on epidermal O-acylsphingolipids and transepidermal water loss in young pigs. Biochimica et biophysica acta *921*, 191-197.

Menuz, V., Howell, K.S., Gentina, S., Epstein, S., Riezman, I., Fornallaz-Mulhauser, M., Hengartner, M.O., Gomez, M., Riezman, H., and Martinou, J.C. (2009). Protection of C. elegans from anoxia by HYL-2 ceramide synthase. Science (New York, NY *324*, 381-384.

Michel, C., and van Echten-Deckert, G. (1997). Conversion of dihydroceramide to ceramide occurs at the cytosolic face of the endoplasmic reticulum. FEBS Lett *416*, 153-155.

Mitsutake, S., Yokota, H., Zama, K., Yamashita, T., Okazaki, T., Watanabe, K., and Igarashi, Y. (2010). SMS2 deficiency prevents diet-induced obesity. ICBL Conference *Poster presentation*.

Mizutani, Y., Kihara, A., Chiba, H., Tojo, H., and Igarashi, Y. (2008). Synthesis of 2-hydroxy-ceramide by ceramide synthase family members: enzymatic basis for the preference of fatty acid chain length in cultured cell models. Journal of lipid research *49*, 2356-2364.

Mizutani, Y., Kihara, A., and Igarashi, Y. (2005). Mammalian Lass6 and its related family members regulate synthesis of specific ceramides. J Biochem *390*, 263-271.

Mizutani, Y., Kihara, A., and Igarashi, Y. (2006). LASS3 (longevity assurance homologue 3) is a mainly testis-specific (dihydro)ceramide synthase with relatively broad substrate specificity. J Biochem *398*, 531-538.

Morita, K., Furuse, M., Yoshida, Y., Itoh, M., Sasaki, H., Tsukita, S., and Miyachi, Y. (2002). Molecular architecture of tight junctions of periderm differs from that of the maculae occludentes of epidermis. The Journal of investigative dermatology *118*, 1073-1079.

Morita, K., Itoh, M., Saitou, M., Ando-Akatsuka, Y., Furuse, M., Yoneda, K., Imamura, S., Fujimoto, K., and Tsukita, S. (1998). Subcellular distribution of tight junction-associated proteins (occludin, ZO-1, ZO-2) in rodent skin. The Journal of investigative dermatology *110*, 862-866.

Motta, S., Monti, M., Sesana, S., Caputo, R., Carelli, S., and Ghidoni, R. (1993). Ceramide composition of the psoriatic scale. Biochimica et biophysica acta *1182*, 147-151.

Muramatsu, T. (2000). Essential roles of carbohydrate signals in development, immune response and tissue functions, as revealed by gene targeting. Journal of biochemistry *127*, 171-176.

Nemes, Z., Marekov, L.N., Fesus, L., and Steinert, P.M. (1999). A novel function for transglutaminase 1: attachment of long-chain omega-hydroxyceramides to involucrin by ester bond formation. Proceedings of the National Academy of Sciences of the United States of America *96*, 8402-8407.

Nolan, J.P., and Hammerstedt, R.H. (1997). Regulation of membrane stability and the acrosome reaction in mammalian sperm. Faseb J *11*, 670-682.

O'Brien, J.S., and Rouser, G. (1964). The fatty acid composition of brain sphingolipids: sphingomyelin, ceramide, cerebroside, and cerebroside sulfate. Journal of lipid research *5*, 339-342.

Oji, V., Tadini, G., Akiyama, M., Blanchet Bardon, C., Bodemer, C., Bourrat, E., Coudiere, P., DiGiovanna, J.J., Elias, P., Fischer, J.*, et al.* (2010). Revised nomenclature and classification of inherited ichthyoses: results of the First Ichthyosis

Consensus Conference in Soreze 2009. Journal of the American Academy of Dermatology *63*, 607-641.

Pakkala, S.G., Fillerup, D.L., and Mead, J.F. (1966). The very long chain fatty acids of human brain sphingolipids. Lipids *1*, 449-450.

Perry, R.J., and Ridgway, N.D. (2005). Molecular mechanisms and regulation of ceramide transport. Biochimica et biophysica acta *1734*, 220-234.

Poulos, A. (1995). Very long chain fatty acids in higher animals--a review. Lipids *30*, 1-14.

Pruett, S.T., Bushnev, A., Hagedorn, K., Adiga, M., Haynes, C.A., Sullards, M.C., Liotta, D.C., and Merrill, A.H., Jr. (2008). Biodiversity of sphingoid bases ("sphingosines") and related amino alcohols. Journal of lipid research *49*, 1621-1639.

Rabionet, M., van der Spoel, A.C., Chuang, C.C., von Tumpling-Radosta, B., Litjens, M., Bouwmeester, D., Hellbusch, C.C., Korner, C., Wiegandt, H., Gorgas, K.*, et al.* (2008). Male germ cells require polyenoic sphingolipids with complex glycosylation for completion of meiosis: A link to ceramide synthase-3. The Journal of biological chemistry *283*, 13357-13369.

Radner, F.P., Streith, I.E., Schoiswohl, G., Schweiger, M., Kumari, M., Eichmann, T.O., Rechberger, G., Koefeler, H.C., Eder, S., Schauer, S.*, et al.* (2009). Growth retardation, impaired triacylglycerol catabolism, hepatic steatosis, and lethal skin barrier defect in mice lacking comparative gene identification-58 (CGI-58). The Journal of biological chemistry *285*, 7300-7311.

Raymond, A.A., Gonzalez de Peredo, A., Stella, A., Ishida-Yamamoto, A., Bouyssie, D., Serre, G., Monsarrat, B., and Simon, M. (2008). Lamellar bodies of human epidermis: proteomics characterization by high throughput mass spectrometry and possible involvement of CLIP-170 in their trafficking/secretion. Mol Cell Proteomics *7*, 2151-2175.

Riebeling, C., Allegood, J.C., Wang, E., Merrill, J., A.H., and Futerman, A.H. (2003). Two Mammalian Longevity Assurance Gene (LAG1) Family Members, trh1 and trh4, Regulate Dihydroceramide Synthesis Using Different Fatty Acyl-CoA Donors. The Journal of biological chemistry *278*, 43452-43459.

Rieger, E., Bijl, J.J., van Oostveen, J.W., Soyer, H.P., Oudejans, C.B., Jiwa, N.M., Walboomers, J.M., and Meijer, C.J. (1994). Expression of the homeobox gene HOXC4 in keratinocytes of normal skin and epithelial skin tumors is correlated with differentiation. The Journal of investigative dermatology *103*, 341-346.

Robinson, B.S., Johnson, D.W., and Poulos, A. (1992). Novel molecular species of sphingomyelin containing 2-hydroxylated polyenoic very-long-chain fatty acids in mammalian testes and spermatozoa. The Journal of biological chemistry *267*, 1746-1751.

Ruvolo, P.P. (2003). Intracellular signal transduction pathways activated by ceramide and its metabolites. Pharmacol Res *47*, 383-392.

Sandhoff, R. (2007). Struktur-funktionsbeziehung von Glycosphingolipiden Habilitationsschrift.

Sandhoff, R. (2009). Very long chain sphingolipids: Tissue expression, function and synthesis. FEBS Lett.

Sandhoff, R., Geyer, R., Jennemann, R., Paret, C., Kiss, E., Yamashita, T., Gorgas, K., Sijmonsma, T.P., Iwamori, M., Finaz, C.*, et al.* (2005). Novel class of glycosphingolipids involved in male fertility. The Journal of biological chemistry *280*, 27310-27318.

Sandhoff, R., Hepbildikler, S.T., Jennemann, R., Geyer, R., Gieselmann, V., Proia, R.L., Wiegandt, H., and Grone, H.J. (2002). Kidney sulfatides in mouse models of inherited glycosphingolipid disorders: determination by nano-electrospray ionization tandem mass spectrometry. The Journal of biological chemistry *277*, 20386-20398.

Schmuth, M., Gruber, R., Elias, P.M., and Williams, M.L. (2007). Ichthyosis update: towards a function-driven model of pathogenesis of the disorders of cornification and the role of corneocyte proteins in these disorders. Advances in dermatology *23*, 231-256.

Schnaar, R.L. (1991). Glycosphingolipids in cell surface recognition. Glycobiology *1*, 477-485.

Schorling, S., Vallee, B., Barz, W.P., Riezman, H., and Oesterhelt, D. (2001). Lag1p and Lac1p are essential for the Acyl-CoA-dependent ceramide synthase reaction in Saccharomyces cerevisae. Molecular biology of the cell *12*, 3417-3427.

Schroeder, H.E., Rossinsky, K., and Muller, W. (1980). An established routine method for differential staining of epoxy-embedded tissue sections. Microscopica acta *83*, 111-116.

Sevilla, L.M., Nachat, R., Groot, K.R., Klement, J.F., Uitto, J., Djian, P., Maatta, A., and Watt, F.M. (2007). Mice deficient in involucrin, envoplakin, and periplakin have a defective epidermal barrier. The Journal of cell biology *179*, 1599-1612.

Shima, J.E., McLean, D.J., McCarrey, J.R., and Griswold, M.D. (2004). The murine testicular transcriptome: characterizing gene expression in the testis during the progression of spermatogenesis. Biology of reproduction *71*, 319-330.

Shimeno, H., Soeda, S., Sakamoto, M., Kouchi, T., Kowakame, T., and Kihara, T. (1998). Partial purification and characterization of sphingosine N-acyltransferase (ceramide synthase) from bovine liver mitochondrion-rich fraction. Lipids *33*, 601-605.

Simionescu, N., and Simionescu, M. (1976). Galloylglucoses of low molecular weight as mordant in electron microscopy. II. The moiety and functional groups possibly involved in the mordanting effect. The Journal of cell biology *70*, 622-633.

Spassieva, S., Seo, J.G., Jiang, J.C., Bielawski, J., Alvarez-Vasquez, F., Jazwinski, S.M., Hannun, Y.A., and Obeid, L.M. (2006). Necessary role for the Lag1p motif in (dihydro)ceramide synthase activity. The Journal of biological chemistry *281*, 33931-33938.

Spiegel, S., and Milstien, S. (2003). Sphingosine-1-phosphate: an enigmatic signalling lipid. Nature reviews *4*, 397-407.

Sprong, H., Kruithof, B., Leijendekker, R., Slot, J.W., van Meer, G., and van der Sluijs, P. (1998). UDP-galactose:ceramide galactosyltransferase is a class I integral membrane protein of the endoplasmic reticulum. The Journal of biological chemistry *273*, 25880-25888.

Stark, H.J., Boehnke, K., Mirancea, N., Willhauck, M.J., Pavesio, A., Fusenig, N.E., and Boukamp, P. (2006). Epidermal homeostasis in long-term scaffold-enforced skin equivalents. The journal of investigative dermatology Symposium proceedings / the Society for Investigative Dermatology, Inc *11*, 93-105.

Steven, A.C., and Steinert, P.M. (1994). Protein composition of cornified cell envelopes of epidermal keratinocytes. Journal of cell science *107 (Pt 2)*, 693-700.

Stoffel, W., Holz, B., Jenke, B., Binczek, E., Gunter, R.H., Kiss, C., Karakesisoglou, I., Thevis, M., Weber, A.A., Arnhold, S.*, et al.* (2008). Delta6-Desaturase (FADS2) deficiency unveils the role of omega3- and omega6-polyunsaturated fatty acids. The EMBO journal.

Stratford, S., Hoehn, K.L., Liu, F., and Summers, S.A. (2004). Regulation of insulin action by ceramide: dual mechanisms linking ceramide accumulation to the inhibition of Akt/protein kinase B. The Journal of biological chemistry *279*, 36608-36615.

Teufel, A., Maass, T., Galle, P.R., and Malik, N. (2009). The longevity assurance homologue of yeast lag1 (Lass) gene family (Review). International journal of molecular medicine *23*, 135-140.

Thudichum, J.L.W. (1884). A treatise on the chemical constitution of the brain.

Tsukita, S., Furuse, M., and Itoh, M. (2001). Multifunctional strands in tight junctions. Nature reviews *2*, 285-293.

Uchida, Y., and Hamanaka, S. (2006). Stratum Corneum Ceramides: Function, Origins, and Therapeutic Applications. Skin Barrier, 43-64.

Uchida, Y., Hara, M., Nishio, H., Sidransky, E., Inoue, S., Otsuka, F., Suzuki, A., Elias, P.M., Holleran, W.M., and Hamanaka, S. (2000). Epidermal sphingomyelins are precursors for selected stratum corneum ceramides. Journal of lipid research *41*, 2071-2082.

Valianpour, F., Selhorst, J.J., van Lint, L.E., van Gennip, A.H., Wanders, R.J., and Kemp, S. (2003). Analysis of very long-chain fatty acids using electrospray ionization mass spectrometry. Molecular genetics and metabolism *79*, 189-196.

Vallee, B., and Riezman, H. (2005). Lip1p: a novel subunit of acyl-CoA ceramide synthase. The EMBO journal *24*, 730-741.

Vasireddy, V., Uchida, Y., Salem, N., Jr., Kim, S.Y., Mandal, M.N., Reddy, G.B., Bodepudi, R., Alderson, N.L., Brown, J.C., Hama, H.*, et al.* (2007). Loss of functional ELOVL4 depletes very long-chain fatty acids (> or =C28) and the unique omega-O-acylceramides in skin leading to neonatal death. Human molecular genetics *16*, 471-482.

Veerman, E.C., Valentijn-Benz, M., van't Hof, W., Nazmi, K., van Marle, J., and Amerongen, A.V. (2010). Phytosphingosine kills Candida albicans by disrupting its cell membrane. Biological chemistry *391*, 65-71.

Venkataraman, K., Riebeling, C., Bodennec, J., Riezman□, H., Allegood, J.C., Sullards, M.C., Merrill, J., A.H., and Futerman, A.H. (2002). Upstream of Growth and Differentiation Factor 1 (uog1), a Mammalian Homolog of the Yeast Longevity Assurance Gene 1(LAG1), Regulates N-Stearoyl-sphinganine (C18-(Dihydro)ceramide) Synthesis in a Fumonisin B1-independent Manner in Mammalian Cells. The Journal of biological chemistry *277*, 35642-35649.

Wang, Y., Botolin, D., Xu, J., Christian, B., Mitchell, E., Jayaprakasam, B., Nair, M.G., Peters, J.M., Busik, J.V., Olson, L.K.*, et al.* (2006). Regulation of hepatic fatty acid elongase and desaturase expression in diabetes and obesity. Journal of lipid research *47*, 2028-2041.

Weinmann, A., Galle, P.R., and Teufel, A. (2005). LASS6, an additional member of the longevity assurance gene family. Int J Mol Med *16*, 905-910.

Werzt, P.W. (2006). Biochemistry of Human Stratum Corneum Lipids. Skin Barrier, 33-43.

Westerberg, R., Tvrdik, P., Unden, A.B., Mansson, J.E., Norlen, L., Jakobsson, A., Holleran, W.H., Elias, P.M., Asadi, A., Flodby, P.*, et al.* (2004). Role for ELOVL3 and fatty acid chain length in development of hair and skin function. The Journal of biological chemistry *279*, 5621-5629.

White, S.H., Mirejovsky, D., and King, G.I. (1988). Structure of lamellar lipid domains and corneocyte envelopes of murine stratum corneum. An X-ray diffraction study. Biochemistry *27*, 3725-3732.

Winter, E., and Ponting, C.P. (2002). TRAM, LAG1 and CLN8: members of a novel family of lipid-sensing domains? Trends in biochemical sciences *27*, 381-383.

Wolgemuth, D.J., Viviano, C.M., Gizang-Ginsberg, E., Frohman, M.A., Joyner, A.L., and Martin, G.R. (1987). Differential expression of the mouse homeobox-containing gene Hox-1.4 during male germ cell differentiation and embryonic development.

Proceedings of the National Academy of Sciences of the United States of America *84*, 5813-5817.

Yamasaki, K., and Gallo, R.L. (2008). Antimicrobial peptides in human skin disease. Eur J Dermatol *18*, 11-21.

Yamashita, T., Hashiramoto, A., Haluzik, M., Mizukami, H., Beck, S., Norton, A., Kono, M., Tsuji, S., Daniotti, J.L., Werth, N.*, et al.* (2003). Enhanced insulin sensitivity in mice lacking ganglioside GM3. Proceedings of the National Academy of Sciences of the United States of America *100*, 3445-3449.

Yanagi, T., Akiyama, M., Nishihara, H., Ishikawa, J., Sakai, K., Miyamura, Y., Naoe, A., Kitahara, T., Tanaka, S., and Shimizu, H. (2010). Self-improvement of keratinocyte differentiation defects during skin maturation in ABCA12-deficient harlequin ichthyosis model mice. The American journal of pathology *177*, 106-118.

Yang, L.J., Zeller, C.B., Shaper, N.L., Kiso, M., Hasegawa, A., Shapiro, R.E., and Schnaar, R.L. (1996). Gangliosides are neuronal ligands for myelin-associated glycoprotein. Proceedings of the National Academy of Sciences of the United States of America *93*, 814-818.

Zaidi, N., Maurer, A., Nieke, S., and Kalbacher, H. (2008). Cathepsin D: a cellular roadmap. Biochemical and biophysical research communications *376*, 5-9.

Zhou, Y., Lau, F.W., Nauli, S., Yang, D., and Bowie, J.U. (2001). Inactivation mechanism of the membrane protein diacylglycerol kinase in detergent solution. Protein Sci *10*, 378-383.

Zuo, Y., Zhuang, D.Z., Han, R., Isaac, G., Tobin, J.J., McKee, M., Welti, R., Brissette, J.L., Fitzgerald, M.L., and Freeman, M.W. (2008). ABCA12 maintains the epidermal lipid permeability barrier by facilitating formation of ceramide linoleic esters. The Journal of biological chemistry *283*, 36624-36635.

7. Appendix

Carbon chain length of saturated fatty acids	IUPAC nomenclature	Trivial name
C14	Tetradecanoic	Myristic
C16	Hexadecanoic	Palmitic
C18	Octadecanoic	Stearic
C20	Eicosanoic	Arachidic
C22	Docosanoic	Behenic
C24	Tetracosanoic	Lignoceric
C26	Hexacosanoic	Cerotic
C28	Octacosanoic	Montanic
C30	Triacontanoic	Melissic
C32	Dotriacontanoic	Lacceroic
C34	Tetratriacontanoic	Geddic
C36	Hexatriacontanoic	Henxatriacontylic

Table A1. Nomenclature of saturated fatty acids.

The nomenclature of fatty acids commonly specified in this study are described with their trivial name and according to IUPAC rules.

Carbon chain length of saturated fatty acids	IUPAC nomenclature	Trivial name
C18:1, ω-9	cis-9-octadecenoic	Oleic
C18:2, ω-6	cis-9,12-octadecadienoic	Linoleic
C18:3, ω-6	cis-6,9,12-octadecatrienoic	γ-Linolenic
C20:3, ω-6	cis-8,11,14-eicosatrienoic	Dihomo γ-Linolenic
C20:4, ω-6	cis-5,8,11,14-eicosatretraenoic	Arachidonic
C22:4, ω-6	cis-7,10,13,15-docosatetraenoic	
C24:1, ω-9	cis-15-tetracosaenoic	Nervonic
C24:4, ω-6	cis-9,12,15,18- tetracosaenoic	
C18:3, ω-3	cis-9,12,15-octadecatrienoic	Linolenic
C18:4, ω-3	cis-6,9,12,15-octadecatetraenoic	
C20:4, ω-3	cis-8,11,13,17-eicosatetraenoic	

Table A2. Nomenclature of unsaturated fatty acids.

The nomenclature of fatty acids commonly specified in this study are described with their trivial name and according to IUPAC rules.

Species	Enzyme name	Fatty acyl-CoA substrate
Homo sapiens / Mus musculus	CerS1	18
	CerS2	22-24
	CerS3	18-24 ?
	CerS4	18-22
	CerS5	16
	CerS6	14-16
Caenorhabditis elegans	Hyl-1	24-26
	Hyl-2	20-22
	Lagr-1	?
Saccharomyces cerevisiae	Lag1	26
	Lac1	26
	Lip1	26
Drosophila melanogaster	Schlank	14-18

Table A3. The ceramide synthases in various eukaryotic organisms.
Substrate preferences of H. sapiens and M. musculus (Laviad et al., 2008; Mizutani et al., 2006; Riebeling et al., 2003; Venkataraman et al., 2002; Weinmann et al., 2005), C. elegans (Menuz et al., 2009), S. cerevisiae (Schorling et al., 2001; Vallee and Riezman, 2005), and D. melanogaster (Bauer et al., 2009), as reported according to the current literature.

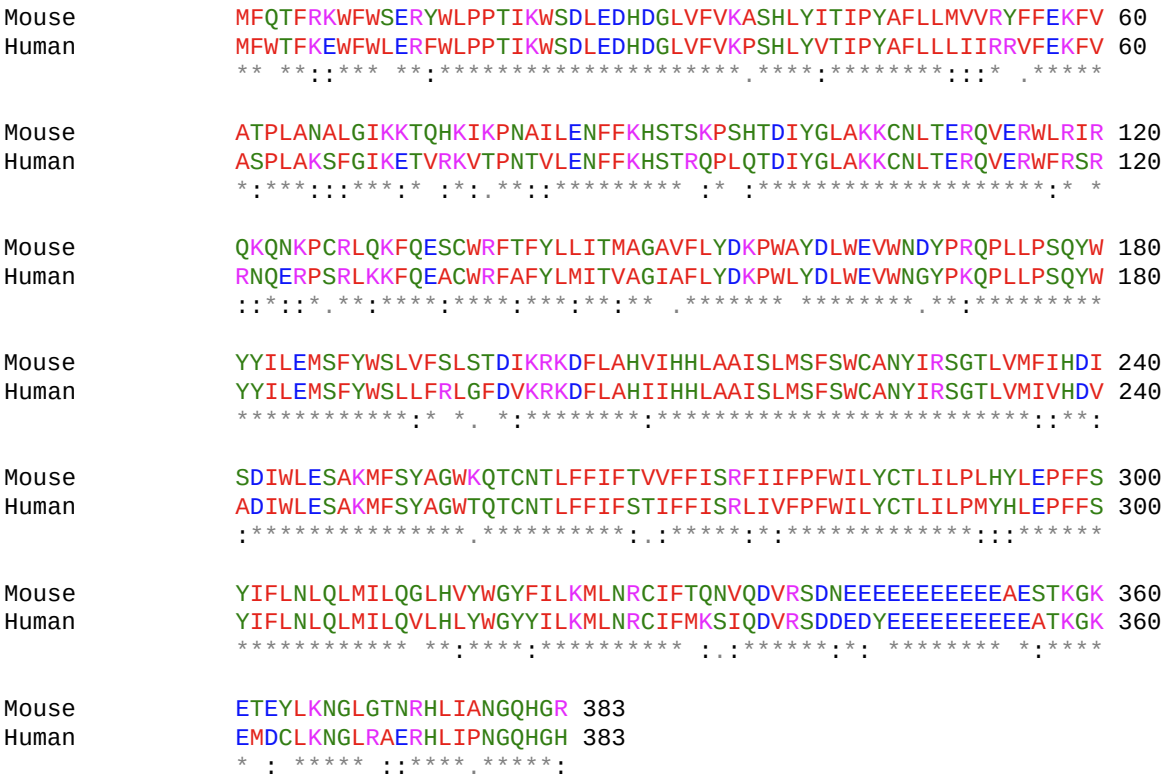

Figure A1. Mouse amino acid sequence of CerS3 compared to human homologue.

CerS3 mRNA isolated from mouse testis was subjected to reverse transcription and subsequently sequenced. The mouse and human protein sequences are compared here together in a blast. Conserved amino acid are annotated (*), as well as observed conserved substitutions (:) and semi-conserved substitutions (.).

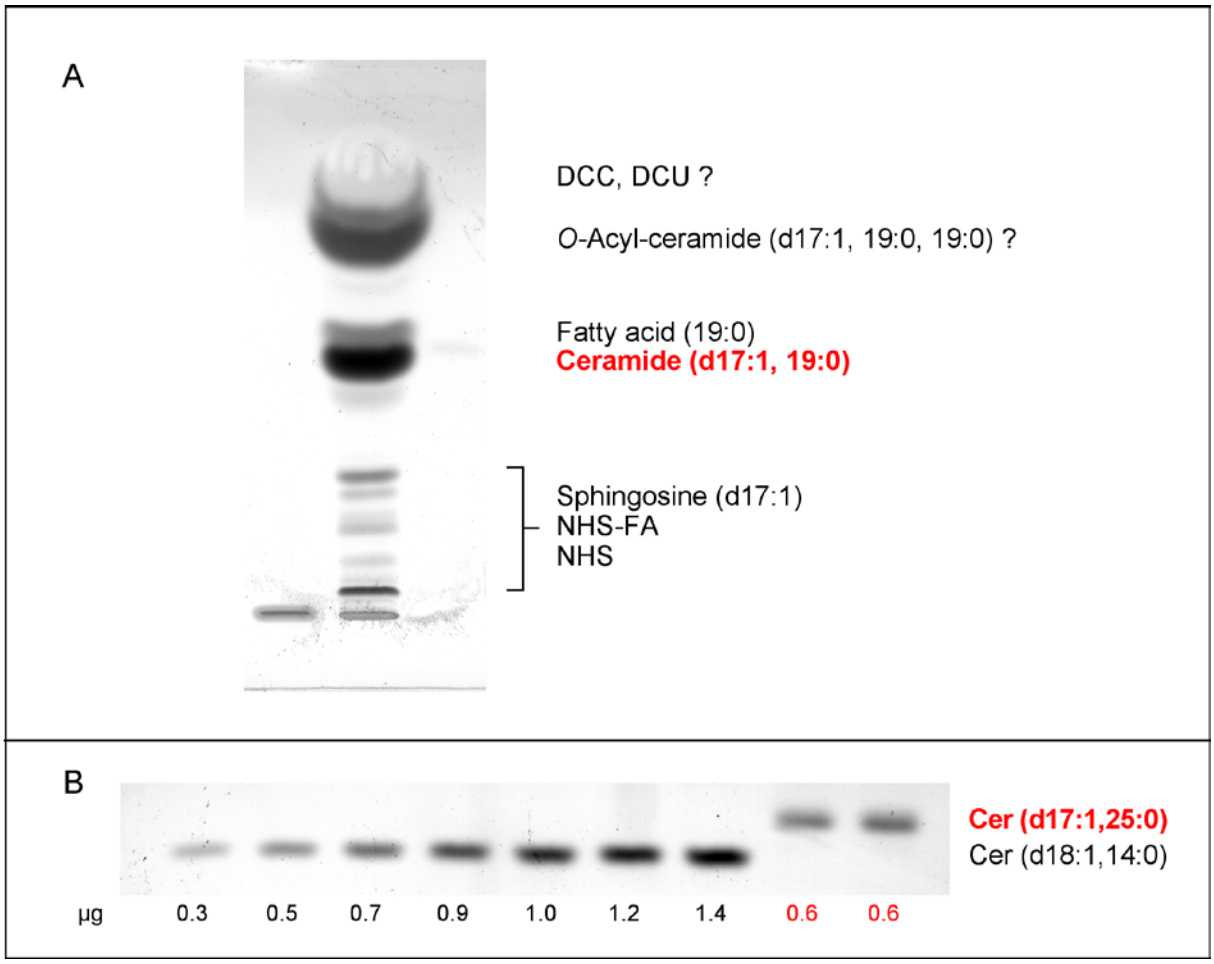

Figure A2. Thin layer chromatography of synthesized internal standard ceramides.

(A) TLC of a crude ceramide product separated with $CHCl_3$/CH_3OH/glacial AcOH (188/11/1) as a solvent system. Residual reactants and side-products are indicated. Bands were visualized by staining with copper reagent. (B) For quantification of purified ceramide standards, a dilution series of ceramide in a known concentration, here Cer(d18:1, 14:0), were spotted next to the ceramide of unknown concentration.

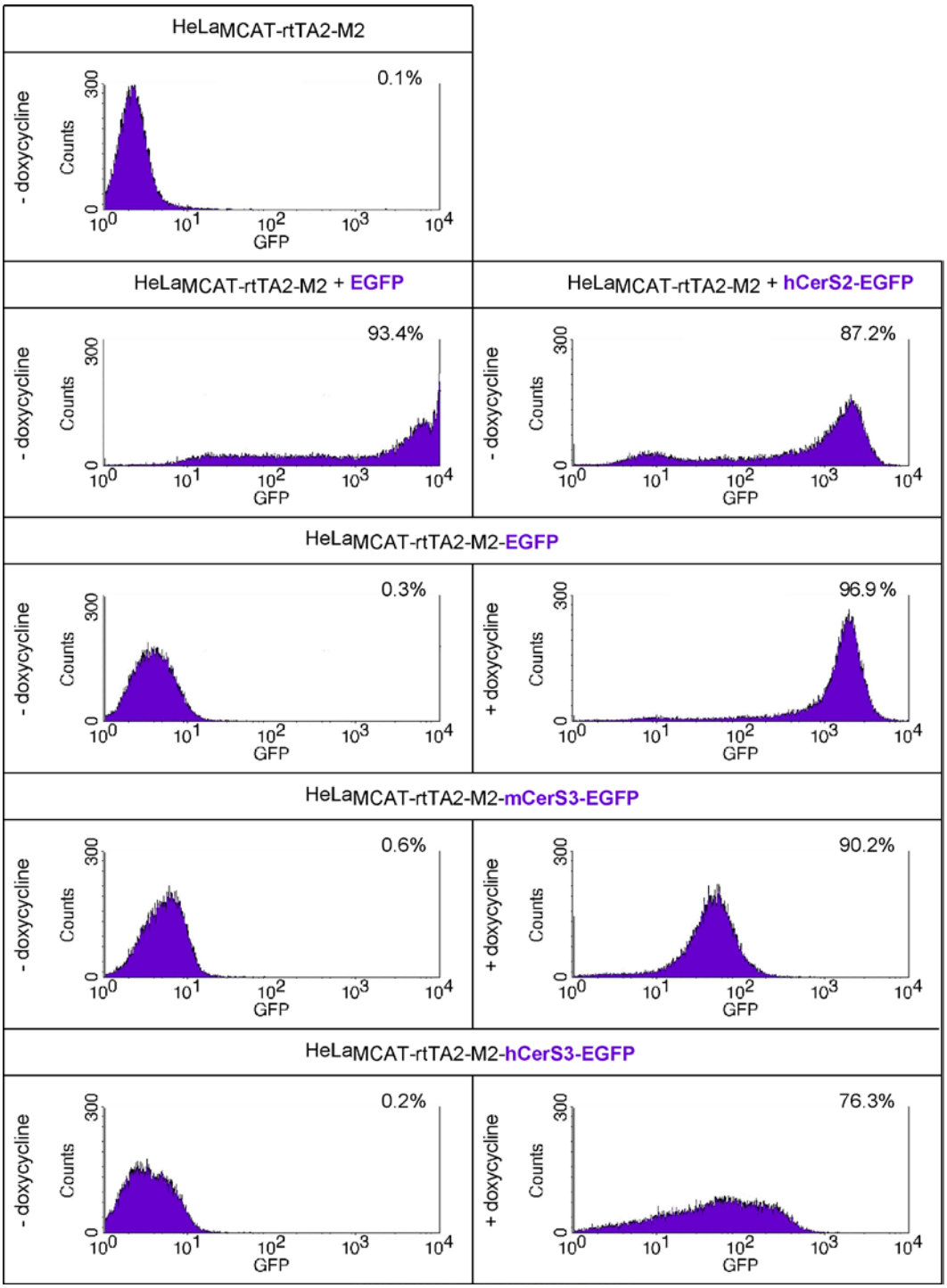

Figure A3. Flow cytometric analyses according to GFP fluorescence of stable cell lines expressing CerS3 and transiently transfected cells expressing CerS2. *HeLa cells expressing CerS2 or CerS3 were subjected to flow cytometric analyses prior to being used for ceramide synthase assays. Transfection efficiency (%) was determined according to relative fluorescence intensity of 1 × 10^4 cells, considering fluorescence positive cells those with signal intensity over ≥10^1.*

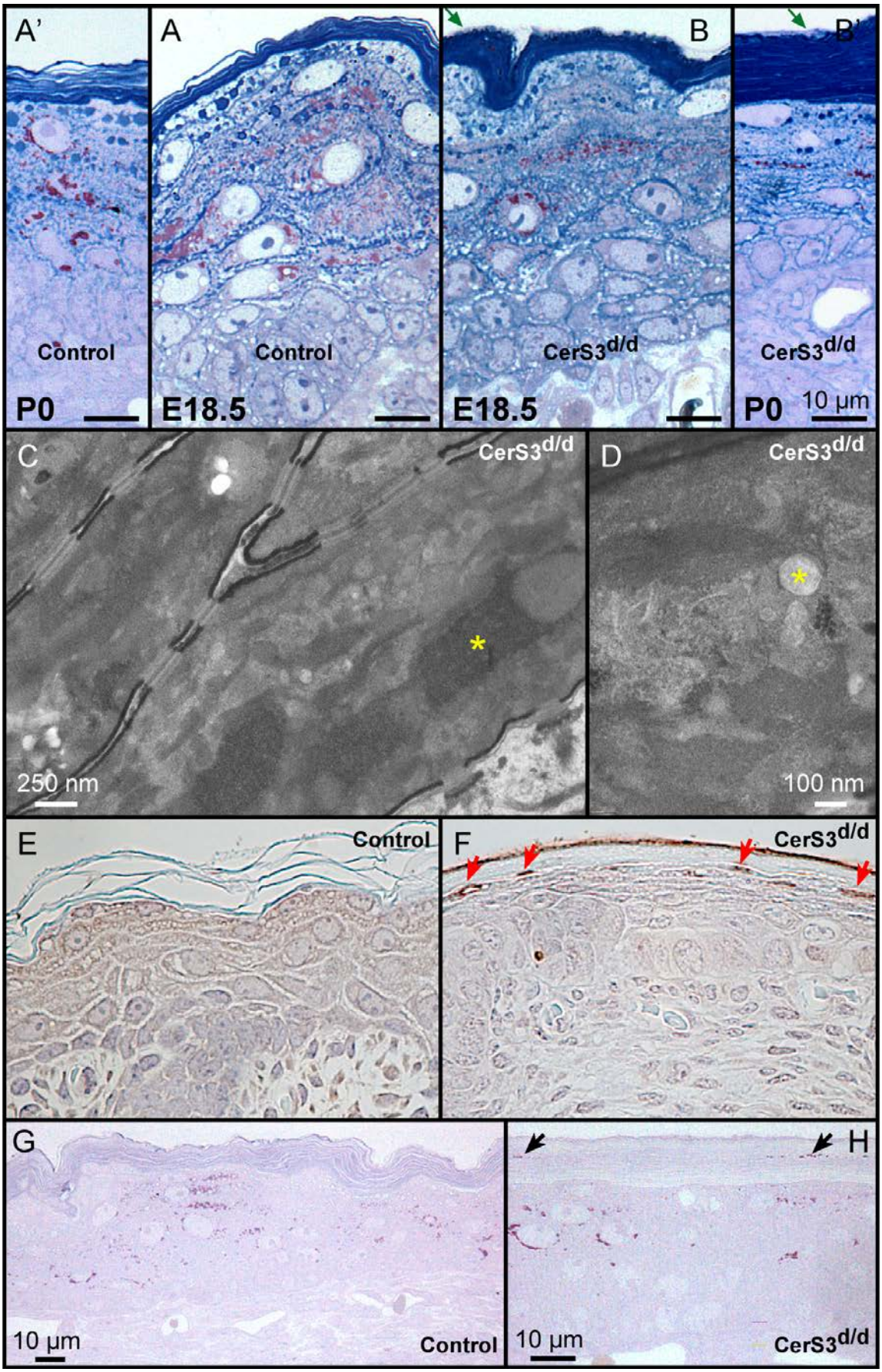
A'
Control
P0
A
Control
E18.5
B
CerS3d/d
E18.5
B'
CerS3d/d
P0
10 µm
C
CerS3d/d
250 nm
D
CerS3d/d
100 nm
E
Control
F
CerS3d/d
G
10 µm
Control
H
10 µm
CerS3d/d

Figure A4. "Hyper"keratosis and delayed keratinocyte maturation in CerS3$^{d/d}$ mice.

Light micrographs of semithin Epon sections of neonatal (A-B) and embryonic (A'-B') skin of control (A) and CerS3$^{d/d}$ (B) mice stained with PAS-methylene blue-Azur II. Mutant SC is distinctively compact and thicker at birth and at embryonic stage E18.5 ± 0.5, as compared to controls. Periderm persisted in mutant skin at E18.5, as well as after birth (green arrows). (C-D) Electron micrographs revealed delayed cornification/degradation of organellar structures (yellow stars) in the first corneocyte layer of CerS3$^{d/d}$ mice. (E-F) TUNEL staining performed on paraffin sections of control and mutant epidermis. TUNEL-positive corneocytes and superficial peridermal layer indicated remnants of nuclear structures in mutant epidermis (red arrows), as compared to control mice (E). PAS staining of semithin Epon sections of control (G) and mutant CerS3$^{d/d}$ (H) skin for detection of glycogen. Residual glycogen was exclusively detected in the superficial layers of mutant SC (black arrows). Comparable staining for both control and mutant was observed predominantly within the SS and SG.

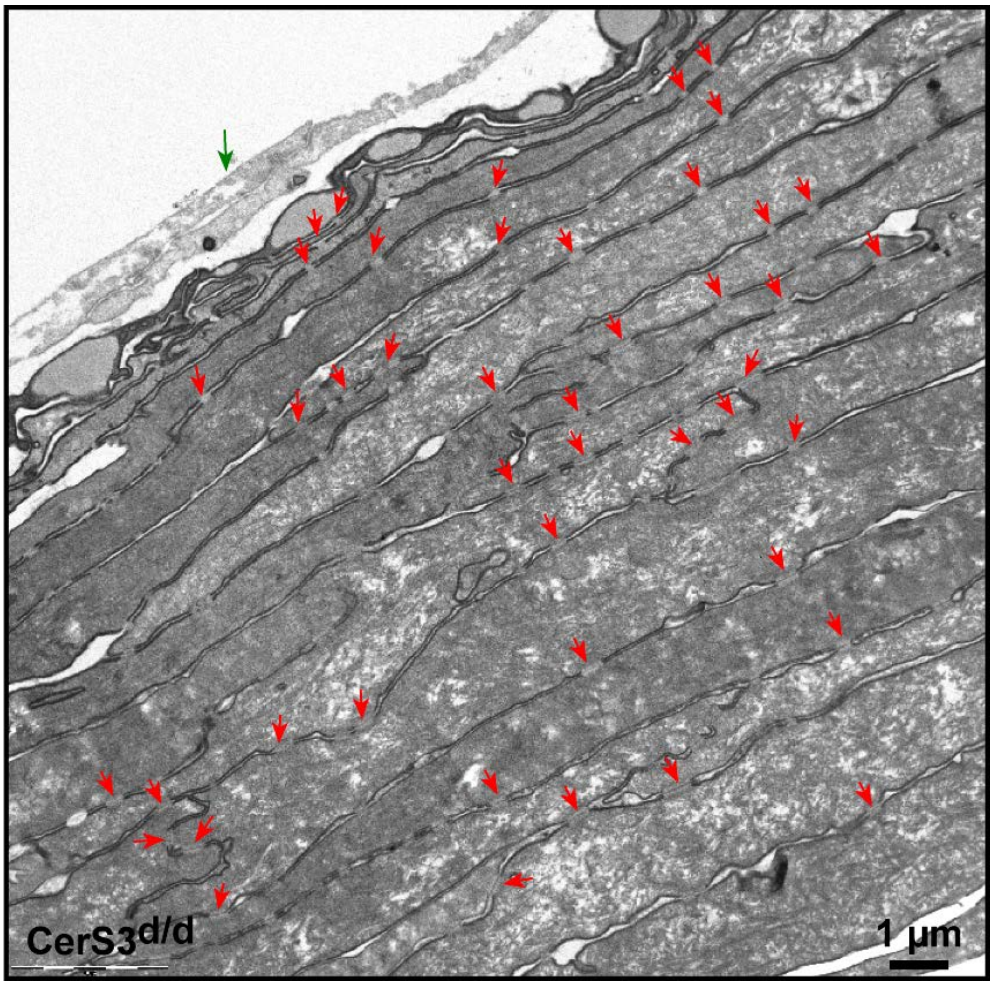

Figure A5. Persistence of corneodesmosomes in the entire SC of CerS3 deficient skin.

Electron micrograph of the upper layers of the neonatal CerS3$^{d/d}$ skin exhibiting the persistant periderm (green arrow) and corneodesmosomes within the enitre SC (red arrows).

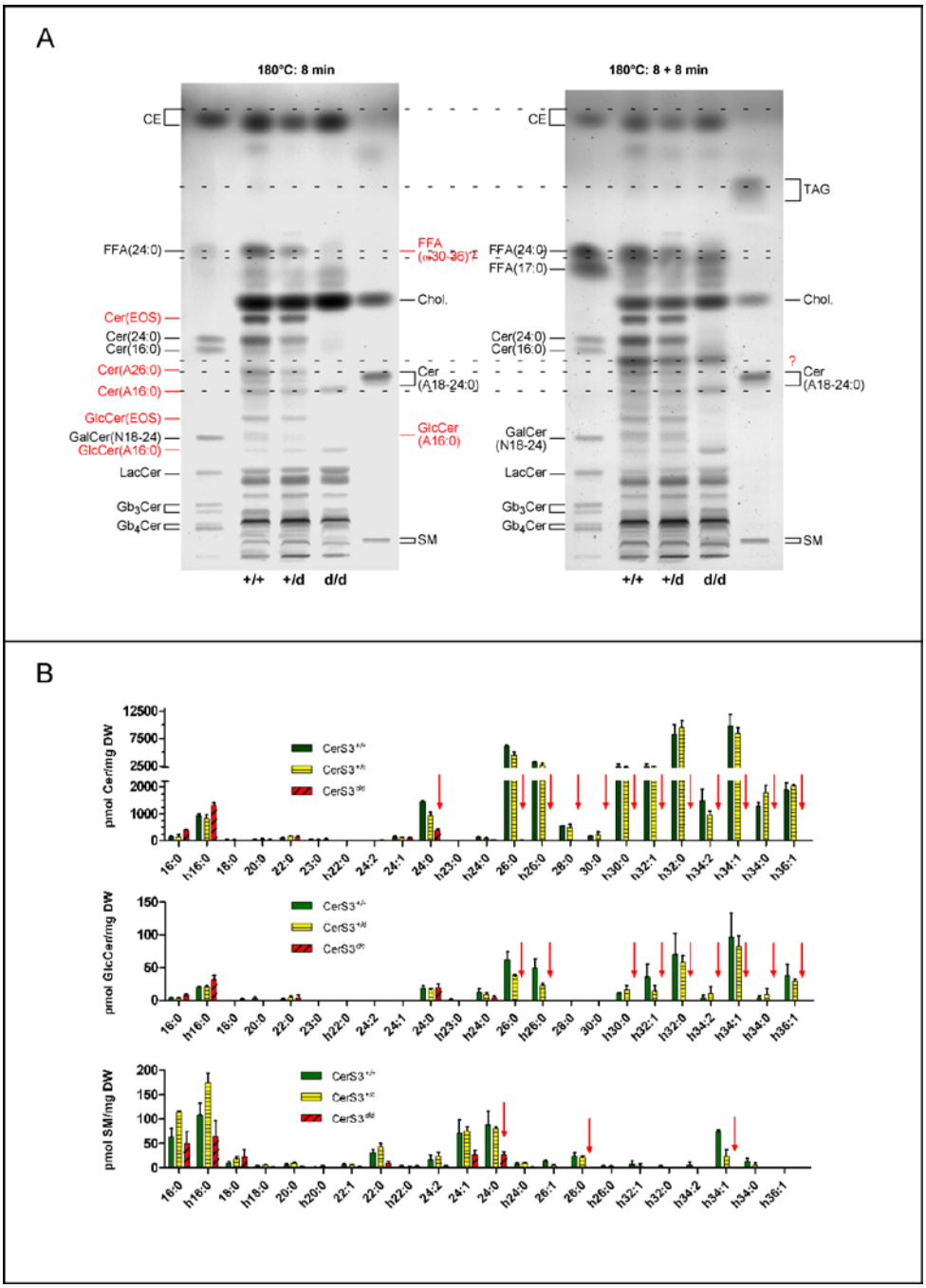

Figure A6. Epidermal sphingolipid profile of CerS3$^{d/d}$ mice.

(A) TLC of epidermal sphingolipids stained with copper sulfate/phosphoric acid and developed at 180 ºC for 8 and 16 min. Each lane corresponds to 0.5 mg dry weight of epidermis. Lipid standards are annotated in black, and epidermal lipids in red. (B) Mass spectromtric quantification of ceramide, glucosylceramide and sphingomyelin species. Lipid species with a fatty acid moiety longer than 24 carbon atoms were strongly reduced or completely missing in CerS3$^{d/d}$ epidermis (red arrows). Error bars represent the SEM of 3 analysed extracts.

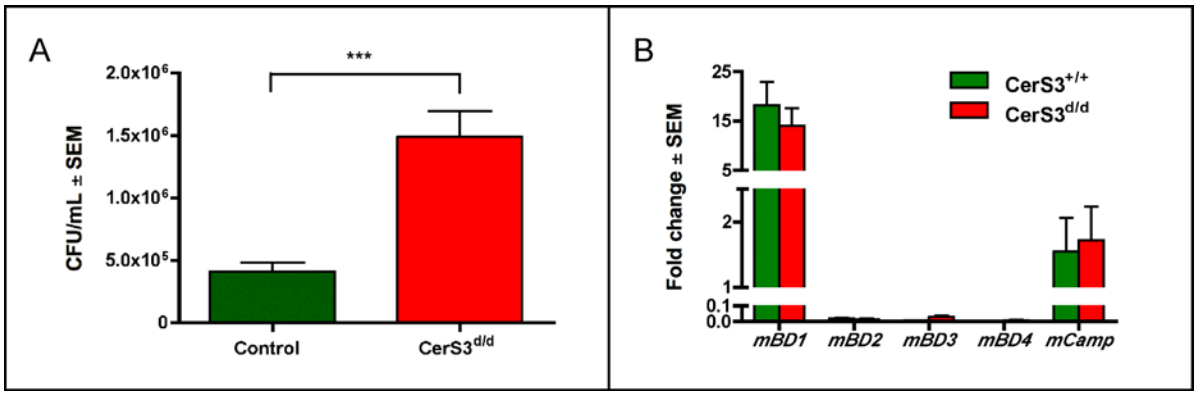

Figure A7. Increased pathogenic growth is not associated with decreased expression rates of antimicrobial peptides in CerS3 mutant mice.

(A) Quantification of C. albicans growth after 24 h infection of cultured skin biopsies of embryonic E18.5 ± 0.5 control and mutant mice. Growth was determined by colony forming units of yeast cultured on Sabouroud agar plates for 48 h at 37 ºC. (B) Transcript expression levels of murine defensins (mBD1–4) and cathelicidin (mCamp) in skin of newborn CerS3$^{+/+}$ and CerS3$^{d/d}$, as determined by qRT-PCR. No significant changes in the expression levels of any of the examined antimicrobial peptides was detected in mutant mice. Relative fold expression was calculated using the $\Delta\Delta C_T$ mtehod. Normalized ΔC_T values were compared to normalized ΔC_T of control wild type mCamp-mRNA.

List of abbreviations

AcOH	Acetate
Amp	Ampicillin
APS	Ammonium persulfate
BL	Basal lamina
BSA	Bovine serum albumin
BTB	Blood-testis barrier
cDNA	Complementary DNA
CE	Cornified envelope
CFU	Colony forming units
CLE	Corneocyte-lipid envelope
Cer	Ceramide
CerS	Ceramide synthase
CoA	Coenzyme A
CTS	Cathepsin
DCC	Dicyclohexylcarbodiimide
DCU	Dicyclohexylurea
DMEM	Dulbecco’s modified Eagle's medium
DMSO	Dimethyl sulfoxide
dNTP	Deoxyribo nucleotide triphosphate
Dox	Doxycycline
dT	deoxyribo thymine
DTT	Dithiothreitol
e.g.	*Exempli gratia*
EB	Eluation buffer
ECL	Enhanced chemiluminescence
EGFP	Enhanced green fluorescent protein
Elovl	Elongation of very long chain fatty acids
EOS	ω-hydroxy-FA esterified to primarily linoleic acid
ER	Endoplasmic reticulum
ESI-MS/MS	Electrospray ionization tandem mass spectrometry

eST	Elongated spermatid
Etc.	*Et cetera*
FA	Fatty acid
FFA	Free fatty acid
FACS	Fluorescence-activated cell sorting
FCS	Fetal calf serum
F-granules	Filaggrin/profilaggrin containing granules
FGSL	Fucosylated glycosphingolipids
GAPDH	Glyceraldehyde 3-phosphate dehydrogenase
Gb	Globo
Gg	Ganglio
GlcCer	Glucosylceramide
GSL	Glycosphingolipid
HP-TLC	High performance TLC
HRP	Horseradish peroxidase
ICS	Intercellular space
i.e.	*Id est*
IS	Interstitium
IS	Internal standard
Kan	Kanamycin
Kbp	Kilo base pair
KG	Keratohyalin granule
KLK	Kallikrein
LacCer	Lactosylceramide
Lass	Longevity assurance
LB	Lamellar body
LB	Lysogeni broth or Luria-Bertani broth
LC	Leydig Cell
LC	Long chain
LCB	Long chain base
L-granules	Loricrin containing granules
lSC	Leptotene spermatocyte

MBS	Modified bovine serum
mCAT1	Murine cationic aminoacid transporter 1
MoMLV	Moloney murine leukemia virus
NHS	*N*-hydroxysuccinimide
NS	Non-hydroxy-FA
OS	ω-hydroxy-FA
PAS	Periodic acid Schiff
PBS	Phosphate buffered saline
PC	Phosphatidylcholine
PCR	Polymerase chain reaction
PDI	Protein disulfide isomerase
PFA	Paraformaldehyde
PGK	Phosphoglycerate kinase
plSC	Preleptotene spermatocyte
PM	Plasma membrane
PN	Postnatal
POS	ω-hydroxy-FA esterified to proteins
PUFA	Polyunsaturated fatty acids
rb	Residual body
rST	Round spermatid
r.t.	Room temperature
RPMI	Roswell park memorial institute medium
rtTA2-M2	Optimized reverse tetracycline-controlled transactivator
SB	*Stratum basale*
SC	*Stratum corneum*
SC	Short chain
SC	Spermatocyte
SDS-PAGE	Sodium dodecyl sulphate polyacrylamide gel electrophoresis
SG	*Stratum granulosum*
SG	Spermatogonia
SL	Sphingolipid
SM	Sphingomyelin

SMS	Sphingomyelin synthase
SOC	Super optimal broth with catabolite repression
ST	Spermatid
Sza	Spermatozoa
T_a	Annealing temperature
TAE	Tris-acetate-EDTA
TE	Tris base-EDTA
TEWL	Transepidermal water loss
THF	Tetrahydrofuran
TLC	Thin layer chromatography
TLC	Tram-Lag-CLN8 domain
TM	Transmembrane
TRE	Tetracycline-responsive element
TUNEL	Terminal dUTP nick-end labeling
ULC	Ultra long chain
VLC	Very long chain
ZO	*Zonulae occludentes*

Acknowledgements

Herewith I would like to acknowledge everyone whose help make this work what it is today.

First and foremost, I would like to express my sincerest gratitude towards my supervisor, Prof. Dr. Roger Sandhoff, for his inspiring guidance and his permanent encouragement in tackling the difficulties encountered throughout this work. His enthusiasm for science, his extensive knowledge and stimulating discussions have been invaluable for the completion of this project, as well as for my personal and scientific development.

I also would like to express my gratitude towards Prof. Dr. Hermann-Josef Gröne for giving me the opportunity to pursue my thesis in his laboratory. His critical and constructive discussions as well as his support have been of great value to me.

Furthermore, I would like to thank my examination committee, especially Prof. Dr. Walter Nickel for being my first supervisor in the Faculty of Biosciences, as well as, and Prof. Dr. Peter Angel and Prof. Dr. Sabine Strahl. In addition, I would like to express my appreciation towards Prof. Dr. Werner W. Franke for his helpful comments and suggestions during the course of this work.

Most especially I would like to thank Prof. Dr. Karin Gorgas for her key suggestions and immense contribution to this work, as well as for her thorough corrections of this thesis. Her constant strive for work perfectly done, as well as her impassionate perspective of life and science have been most inspiring and encouraging.

I also would like to acknowledge the work of Richard Jennemann regarding the generation of the CerS3 deficient mice, which have been one pillar of this thesis.

Additionally, I am very grateful to my collaboration partners Prof. Dr. Alexander Dalpke and Rene Karayilan from the Department of Medical Microbiology and Hygiene of University of Heidelberg, as well as Prof. Dr. Howard Riezman and Sharon Epstein from the University of Geneva. Their contributions have truly enriched the conclusiveness of this thesis.

I would like to thank Thomas Klein from Keyence for providing the fluorescence microscope that enabled us to brilliantly visualize epidermal proteins with simply the best quality and highest detail. From the Biochemie-Zentrum der Universität Heidelberg, I would like to acknowledge PD Dr. Britta Brügger for making available the triple quadrupole nano-ESI-MS/MS, as well as PD Dr. Hans-Michael Müller and Sabine Wegehingel for their suggestions and support regarding the retroviral transduction. I am very thankful to Dr. Steffen Schmitt and Klaus Hexel from the Flow Cytometry Core Facility of DKFZ for sorting of the cells for the generation of stable cell lines. Moreover, I would like to kindly thank Dr. Hans-Jürgen Stark, Dr. Hans Heid and Dr. Lutz Langbein for their knowledge, fruitful discussions and support regarding the analysis of epidermal proteins. Additionally, I would like to thank Prof. Dr. Klaus Willecke and Prof. Dr. Richard L. Proia for kindly supporting the analysis of the CerS2$^{gt/gt}$ and the GM2AP$^{-/-}$ mice, respectively. Finally, I would like to acknowledge Dr. Robert W. Owen for carrying out the purification of the synthesized acyl-CoAs by HPLC/MS.

I would like to express my greatest thanks to Benita von Tümpling-Radosta and Ulrike Rothermel for their technical expertise and important contribution to this work. Also I am thankful to Claudia Schmidt, Gabriele Schmidt, Sylvia Kaden, Mahnaz Bonrouhi and Tjeerd Sijmonsma for their valuable technical assistance. From the department of Anatomy and Cell Biology of University of Heidelberg, I would like to acknowledge the superb technical assistance of Ingrid Kuhn-Krause.

Furthermore, I would like to thank all my colleagues, especially Aaron, Alex and Stefan for their helpful discussions and practical advice, as well as Paula, Milena, Zoran, Christoph, Nicole, Francesca, Viola, Katja, 龍 and Prashant for creating a nice working environment and a good atmosphere inside and outside of the laboratory.

Finally, I would like to thank my family in Catalunya for their endless support and encouragement throughout all these years, as well as my family in Germany and my friends. Especially, I would to thank Michael for simply being there always for me, for his understanding and for immense care and love. Without all of you this thesis would never have been possible!

Publications

- **M. Rabionet**, A. van der Spoel, C. Chuang, B. von Tümpling Radosta, M. Litjens, D. Bouwmeester, C.C. Hellbush, C. Körner, H. Wiegandt, K. Gorgas, F.M. Platt, H.-J. Gröne, R. Sandhoff, "Male germ cells require polyenoic sphingolipids with complex glycosilation for completion of meiosis: A link to ceramide synthase-3", *J. Biol. Chem.,* **2008**, *283,* 13357.

- **M. Rabionet**, J. Arre Toque, A. Ektessabi, "In vitro evaluation of osteoblast-like cells on hydroxyapatite-coated porous stainless steel implants by synchrotron radiation x-ray fluorescence", *X-Ray Spectrometry,* **2009**, *38,* 278.

- Y. Ota, A. Ektessabi, **M. Rabionet**, "Influence of mechanical and electromagnetic stresses upon cells", *Nippon Kikai Gakkai Kansai Shibu Teiji Sokai Koenkai Koen Ronbunshu,* **2005**, *80,* 8.21.

- A. Ektessabi, **M. Rabionet**, "The Role of Trace Metallic Elements in Neurodegenerative Disorders: Quantitative Analysis Using XRF and XANES Spectroscopy", *Analytical Sciences,* **2005**, *21,* 885